University of Alberta

Depositing Ni-WC Wear Resistant Overlays with Hot-Wire Assist Technology

by

Stuart Dan Guest

A thesis submitted to the Faculty of Graduate Studies and Research
in partial fulfillment of the requirements for the degree of

Doctor of Philosophy
in
Materials Engineering

Department of Chemical and Materials Engineering

Spring 2014
Edmonton, Alberta

Abstract

Seven Ni-WC tubular wires utilized in this study were characterized by the nickel sheath area, powder composition, and overall initial carbide volume fraction of the wire prior to welding. The electrical resistivity of steel, stainless steel, and Ni-WC welding consumables were measured from 25-1200 ^{o}C. The electrical resistivity of steel and stainless steel welding consumables are greater than those reported in literature. Tubular Ni-WC resistivity is in good agreement with pure nickel values reported in literature.

A hot-wire electrode extension model was proposed to predict the current necessary to achieve the semi-solid temperature of the welding consumable at the weld pool free surface. The influence of a GTAW and GMAW leading heat source was quantified and found to play a significant role on the hot-wire melting.

The hot-wire GTAW process showed significant challenges due to excessive electrode contamination and it might not be viable for typical oil sands or downhole drilling equipment wear protection. GMAW using tubular Ni-WC wires was investigated as a more practical alternative and a range of welding parameters and shielding gases were explored. A previously undocumented phenomenon of the non-wetting behaviour of tungsten carbide on the molten weld pool free surface was observed with high speed videography. Carbide dissolution and non-wetting resulted in GMAW carbide transfer efficiencies of 20-70% within the range of parameters studied.

Hot-wire GMAW was deemed a viable alternative, with a deposition rate of 5.4 $kg \cdot hr^{-1}$, 33% carbide volume fraction, and ASTM G65 Dry Sand/Rubber Wheel Procedure A mass loss of 0.086 grams. Metallographic analysis did not show indications of carbide dissolution using the hot-wire assist technology with a GMAW leading heat source.

Acknowledgements

My path up to this point can be aptly described as the road less travelled. I was not a star in the classroom by any measure and an advanced degree was never on my radar. I was going straight into industry to work. That is until a chance summer internship sparked something that had laid dormant for most of my undergraduate studies: curiosity. Suddenly, I wanted to know more about this mysterious world of welding. Returning for my final year at the University of Alberta, I stepped into the office of the new “welding professor”. Little did I know that what transpired that day and in the months to follow would change everything.

Prof. Patricio Mendez has a unique and intuitive view of people and the welding industry. What he saw in me in 2010 I will never know but I am extremely grateful to have had the opportunity to glean every bit of his genius during my time at the Canadian Centre for Welding and Joining. Always asking “are you sure?” with his knowing look, Patricio instilled a desire to look past the obvious and go that step further on one’s own. While my professional development has grown exponentially under him, perhaps his biggest contribution is the mindset to never stop being curious. The moments of frustration and elation we shared during my time at the CCWJ will always be cherished for they shaped who I am now and ultimately who I will mature into.

While my name is the only one to appear on this work, the list of people who have helped along the way is a long one. I would like to thank Walter Boddez and Les Dean for helping make some of my crazy hair-brained ideas come to fruition. The CME machine shop deserves special notice for their helpful discussions. A special note to Terry Runyon and Dancy Bogdanovic, problem solver extraordinaires, who continually went that extra mile and made my life much easier at the CCWJ. This work is truly the result of teamwork with my colleagues. Thank you Steven Borle, Gentry Wood, Goetz Dapp, Kevin Scott, Julien Chapuis, Ata Kamyabi, and the many others for always lending a helping hand and being excellent sounding boards whenever I was having brain cramps. I would like to thank Hitachi

Canadian Industries Ltd., the individuals and consumable companies who donated the very expensive Ni-WC wires, Lincoln Electric, Bab-Hitachi, Miller, the CCWJ sponsors, and the many others who made this project possible.

To my friends and colleagues at the CCWJ, it has been quite the adventure. From the personal pitcher nights that left us crying in laughter to the excellent head scratching discussions on the whiteboard, the family atmosphere was infectious and brought out the best in me. I look forward to crossing paths with everyone as we go our separate ways.

To my parents, Dan and Marlene, I owe you many thanks for your unfailing support during my undergraduate and doctoral work. Without the upbeat pep talks and life-saving care packages, this road less travelled would have been far bumpier. Thank you for everything.

Lastly, to Alysha, your support in this journey is totally unquantifiable. Your ability to make me smile and remember the little things in the face of overwhelming dead ends and deadlines will always be cherished and never forgotten.

Stay curious everyone,

Contents

List of Figures

List of Tables

1. Introduction and Background

1.1. Introduction

The highly erosive and corrosive operating environments encountered during oil sands mining and extraction and downhole drilling operations lead to high equipment wear rates [1]. The coating of equipment with wear resistant materials is essential to improving the lifetime of equipment [2]–[4]. Wear rates often vary considerably between equipment components, component service conditions, and between mine or drilling locations. Slurry system piping can wear at a rate of 12mm per thousand hours, slurry pump impeller vanes at a rate greater than 25mm per hundred hours, and ground engaging shovel teeth need to be completely replaced every 2-3 shifts [5].

Nickel matrix, tungsten carbide reinforced (Ni-WC) overlays are typically chosen in industry to protect components against the most severe forms of abrasive wear, such as that experienced in mining environments like the oil sands of Northern Canada. In this paper, the notation Ni-WC signifies any system based on a Ni matrix with Cr-B-Si additions reinforced with externally added tungsten carbide particles. The Ni-WC material system differs considerably from other hardfacing overlay systems such as chrome carbide overlays (CCOs). In CCOs and other complex carbide systems, primary carbides nucleate and grow during the solidification stage. In contrast, in Ni-WC overlays, the tungsten carbides are created externally, and then deposited into the weld pool. Tungsten carbides are very sensitive to heat and readily dissolve at the high temperatures and cooling times seen during welding.

In common industrial practice, low dissolution of tungsten carbides is achieved with powder consumables and Plasma Transferred Arc Welding (PTAW) or laser cladding [6]. These processes can produce excellent quality overlays with desirable 45-50% volume fraction of tungsten carbide. These processes have limitations that make field repairs and some aspects of manufacturing very difficult or impossible. Powder-based processes cannot be used outside the flat position, are sensitive to wind, and have high capital and operating costs.

The development of tubular Ni-WC GMAW wires has enabled field repairs of worn components, and it might enable small fabricators to produce high value-added Ni-WC overlays at a fraction of the capital costs of traditional processes. The relatively small market demand and utilization of tubular Ni-WC consumables compared to worldwide welding and metal manufacturing creates a lack of off-the-shelf solutions or dedicated research for optimizing wear performance.

Hot-wire assist technology, an arc-less welding process, can reduce carbide dissolution by not directly subjecting the tungsten carbides to the hot welding arc. Hot-wire assist technology utilizes resistance or Joule heating to bring the wire to near its melting temperature before addition to the weld pool without creating an arc at the wire tip. The lack of an arc requires a leading heat source such as GTAW, GMAW, PAW, or LBW to melt the base plate material for wetting to occur. The preheated wire allows the leading heat source power to be decreased, lowering the overall weld pool temperatures. The ability to weld Ni-WC overlays with low carbide dissolution in a relatively inexpensive package makes hot-wire assist technology a viable alternative to PTAW or laser cladding. The following sections introduce hot-wire assist welding processes, tubular wires, and matrix metallurgy considerations that will be discussed throughout this thesis.

1.2. Review of Welding Processes

This thesis employs the usage of hot-wire assist technology, Gas Tungsten Arc Welding (GTAW), and Gas Metal Arc Welding (GMAW) welding process. The following sections provide a brief overview of the fundamentals of each process as it pertains to depositing Ni-WC overlays.

1.2.1. Hot-Wire Assist Technology

Hot-wire assist technology utilizes Joule I^2R heating to preheat the filler wire near its melting point without creating an arc at the electrode tip. The formation of an arc is prevented by passing sufficiently low voltages so as to not overcome the anode and cathode fall voltages of a sustainable arc. This electrode melting process was originally patented by Manz in 1964 [7] and is currently used to produce high quality weldments using solid wires for automotive manufacturing and corrosion resistant overlays in the chemical, petrochemical, and offshore industries [8]. The hot-wire is commonly inserted at the rear of the weld pool/arc differing from the conventional front feeding in manual GTAW process, as the wire no longer requires the arc for melting. Figure 1.1 below illustrates a common hot-wire Gas Tungsten Arc Welding (HWGTAW) torch setup.

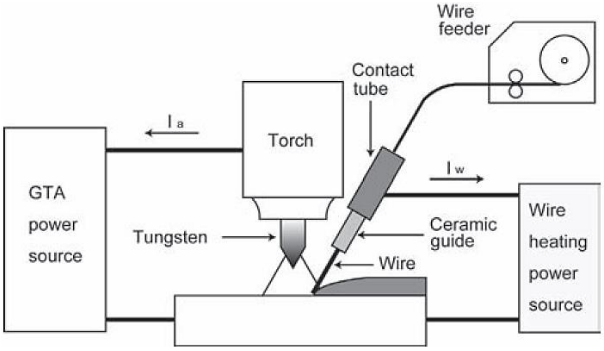

Figure 1.1: Conventional hot-wire assisted GTAW equipment setup [9].

The wire current is typically supplied as direct current (DC) compared to alternating current (AC) to reduce arc instabilities caused the magnetic arc blow and attraction phenomenon in AC. Due to the hot-wire proximity to the welding arc, the polarity and current magnitude passing through the wire interacts with the arcs magnetic field according to Fleming's Rule, leading to arc attraction or deflection relative to the hot-wire. To reduce the effects of arc blow and stabilize the hot-wire at high current and deposition rates, pulsed current power supplies were created [10]. Further mitigation of the sometimes detrimental arc blow phenomenon can be accomplished by synchronized alternated pulsing of the arc and hot-wire. However for typical applications, the pulsed hot-wire is sufficient to maintain high wire feed speeds and process stability. Hori et al. conducted extensive studies including high speed video on the effect of hot-wire polarity, pulsing frequency, and hot-wire power supply design using solid steel wire in hot-wire GTAW (HWGTAW) [10]. It was determined that a pulsing frequency of 100Hz or greater improved productivity while maintaining process stability.

Extensive studies on the effect of wire current, proximity to the arc, voltage drops across the electrified electrode extension, and the regions of stable bead formation for steel wire were conducted by Ueguri et al. for increased productivity [11]. It was found that the effect of arc current on the nearby hot-wire decreased with increasing wire feed speeds which can be attributed to the increased thermal mass.

The usage of pulsed current hot-wire was expanded to include stainless steel and titanium consumables for thick and thin plate materials and narrow-groove joint geometries [11], [12]. Hot-wire assist technology is typically paired with the Gas Tungsten Arc Welding (GTAW) process for exceptional weld bead geometry, weldment quality, and heat input control [9]–[17]. The addition of hot-wire assist technology to consumable electrode processes is scarcely utilized and documented in literature. Tsuyama et al. studied the microstructures formed with steel wire consumables when using hot-wire in conjunction with submerged arc welding (SAW) and GMAW leading heat sources [18]–[20]. The addition of hot-wire assist technology to conventional laser welding systems has seen immense uptake in recent years [21]–[25]. The ability to preheat the filler wire to near the melting temperature allows the laser power to be decreased, preventing excessive evaporation and penetration through the substrate.

Numerous manufacturers and researchers utilize hot-wire assist technology as a tool to attain the required weld metal and heat-affected zone (HAZ) properties; however little publicly available research has been conducted on the process itself. Shinozaki et al. proposed an electrode extension temperature distribution model for the hot-wire GTA welding process [16].

The calculation of the wire temperature distribution to determine the adequate hot-wire current region was completed using Joule heating and heat transfer through the electrode extension length considering boundary conditions of room and melting temperature at the contact tip and electrode tip. The energy contribution from the nearby leading heat source was neglected. Temperature dependent properties of electrical resistivity, density and specific heat capacity were used with an incrementing step of 0.1mm. Shinozaki et al. measured the temperature distribution throughout the length of the hot-wire using a radiation thermometer during feeding using the torch a modified hot-wire torch with machined reliefs [16]. Parametric studies of titanium, mild steel, and stainless steel hot-wire GTAW welding were completed using high speed imaging and temperature distribution measurements. Excessive hot-wire current caused intermittent contact disruptions with the weld pool while too low current cause the wire to contact the bottom of the weld pool and skip underneath the arc. Figure 1.2 below shows the weld bead images, measured hot-wire temperature distribution, and high speed images. The model proposed by Shinozaki et al. corresponds well with the measured temperature distribution [16]. It should be noted that this model was completed for solid wires only.

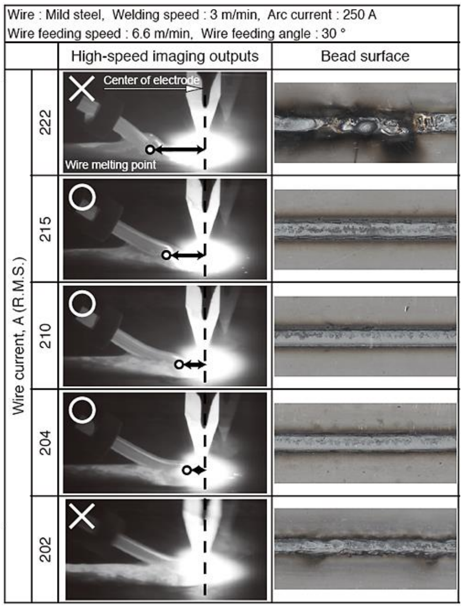

Figure 1.2: High speed images of steel wire HWGTAW indicating optimal wire heating currents to achieve a near-molten condition [11], [15], [16].

1.2.2. Gas Tungsten Arc Welding

Gas Tungsten Arc Welding (GTAW) is a versatile non-consumable, thermionic emission electrode process. An electric welding arc is formed when a potential is applied across a gap between the cathode and anode, ionizing the shielding gas and creating a soft conductor for the current and forming a consistent arc. The arc formed is plasma, often called “the fourth state of matter”, comprised of an electrically conductive ionized gas capable of supporting high welding currents.

The GTAW welding arc is formed between a tungsten electrode cathode (typically of negative polarity) and the anodic base material. The basic schematic of the GTAW system is shown in Figure 1.3 below.

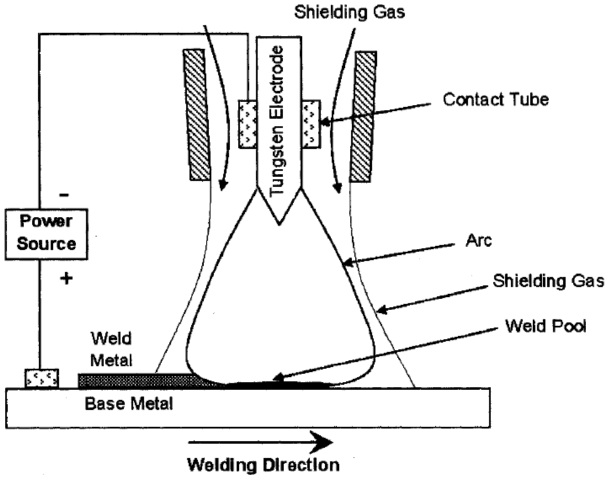

Figure 1.3: Basic schematic of the GTAW process [26].

The welding arc is maintained by an electromagnetic Lorentz force producing a very fast downward plasma jet near the electrode that is approximately 100-500 m/s [27]. This strong plasma jet is a result of arc constriction caused by the interaction between the magnetic field (B) and the current (J), commonly referred to as the Lorentz force. The inward pressure exerted is proportional to the current density [28]. Equilibrium is achieved when the internal outward plasma pressure equals the compressive Lorentz force and the Joule heating balances the radiation losses of the arc [29]. The ionized gas comprising the shielding gas has a large effect on the shape and velocity of the plasma arc, especially important for metal transfer mechanisms in consumable electrode processes such as Gas Metal Arc Welding (GMAW). The formation of the welding arc can lead to temperatures ranging from 5000-50000 K in various regions of the arc depending on shielding gas compositions [30], [31]. These temperatures are extremely high and can cause boiling and evaporation of the weld pool constituents, potentially causing detrimental effects in wear resistant carbide coatings.

The GTA welding process requires the addition of an inert shielding gas to protect the molten weld pool and electrode from oxidation. Shielding gases are typically pure argon or argon-helium blends, occasionally with small amounts of nitrogen or hydrogen added for unique materials. The shielding gas composition can alter the weld penetration profiles due to varying chemical reactions and ionization potentials [32].

The electrode is comprised of tungsten which has a high melting point and low thermionic work function. To further stabilize the welding arc by increasing the electron emission levels, oxides of thorium, cerium, or lanthanum are added. GTAW is typically operated in negative polarity in which 2/3 of the arc energy is directed towards the substrate and 1/3 is subjected to the electrode, making it ideal for welding thick sections [32]. During positive polarity, the energy distribution is reversed with the electrode experiencing 2/3 of the arc energy. Electrode positive polarity can have a tendency to melt the electrode at high current levels however the reversed electron flow is useful for breaking up and “cleaning” tenacious refractory oxides, for example in aluminum welding.

The GTA welding process might or might not involve the addition of filler material to the weld pool. This gives the process good control over the weld pool with a high quality weld; however, at the expense of low productivity. When paired with hot-wire assist technology, the process separates the arc heat input from the deposition rates, an intrinsic issue for consumable electrode processes such as Gas Metal Arc Welding (GMAW). HWGTAW gives improved control of the penetration or dilution of the base material with the weld metal, an important consideration when depositing corrosion or erosion resistant overlays.

1.2.3. Gas Metal Arc Welding

The Gas Metal Arc Welding (GMAW) process differs from GTAW as the arc is established between a consumable wire electrode and the base material, shown in Figure 1.4. GMAW is a flexible welding process that can be utilized in all positions and operated manually, semi-automatically or in automatic modes. The GMAW process can weld many commercially used materials with the proper selection of consumable and shielding gases [33], [34].

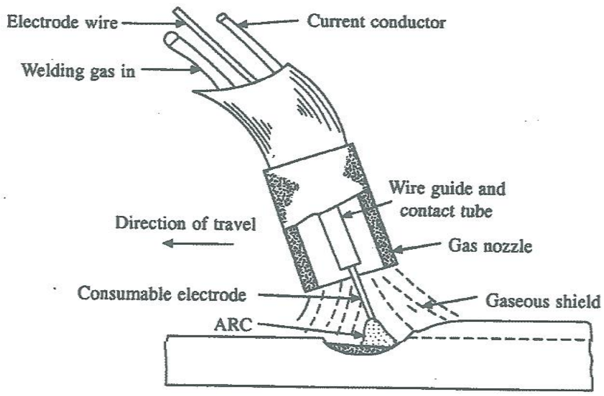

Figure 1.4: Basic schematic of the GMAW process [35].

Typically, electrode positive polarity is used in GMAW over negative polarity due to arc instabilities. Stable transfer in electrode positive polarity is a result of the increased electron emission sites of the weld pool and base metal compared to the relatively small wire electrode surface area in negative polarity. Although negative polarity increases electrode melting rates, the highly mobile cathode spots induce erratic arc forces which de-stabilize the metal transfer. The transfer of electrons leaving the weld pool and coalescing on the electrode melts the continuously fed wire. GMAW can be operated in constant current or constant voltage operating conditions but can be best characterized by the metal transfer mode of the consumable.

The metal transfer modes can be broken into three basic distinct regions: short-circuit, globular, and spray [35]–[38]. Metal transfer modes in GMAW are related to welding current and voltage with short-circuit transfer occurring at low current and voltages, globular forming at higher voltage and low current, and spray transfer at high voltages and currents. Short-circuit transfer can be characterized by the consistent intermittent contact between the electrode and the weld pool, extinguishing the welding arc and transferring the molten droplet on the wire tip to the weld pool. During the short-circuit, the welding power supply will attempt to re-establish the welding arc by rapidly increasing the current. The increasing current simultaneously increases the electromagnetic Lorentz forces, causing a shrinking of the molten droplet neck. Droplet transfer therefore occurs by the liquid metal surface tension and magnetic Lorentz pinch forces. The re-established arc will melt more of the consumable wire electrode, forming a droplet which will eventually contact the weld pool surface. At higher voltages, short-circuit gives way to free-flight globular transfer in which the arc is never extinguished from intermittent contact.

Globular transfer can be characterized by large molten droplets forming on the wire tip. The low welding currents create relatively weak Lorentz forces surrounding the wire, producing a metal droplet transfer dominated by gravitational forces. Globular droplets are approximately 2-3 times larger than the electrode diameter and transfer to the weld pool in an erratic non-axial manner. Metal droplet transfer rates are also much lower than free-flight spray transfer [37]. Spray transfer occurs at currents greater than the globular-spray transition current, which is characteristic of the shielding gas composition, electrode material, and electrode size. The high currents of spray transfer increases the compressive Lorentz force surrounding the electrode. The increased force elongates the molten region at the electrode tip, creating strong parallel plasma jets and small droplets that are transferred axially and at a high frequency.

Shielding gas composition plays an important role in the metal transfer mode. For spray transfer to occur, the gas composition must be argon-rich. Increasing the concentration of gases such as carbon dioxide, oxygen, or helium will not allow the arc to attach above the droplet, preventing spray transfer. The use of 100% inert shielding gases such as argon however does not oxidize the weld pool to provide sufficient electron emission sites at the cathode to stabilize the welding arc. Stabilization is improved when oxygen (1-5%) and CO_2 (5-25%) are added to inert shielding gases.

When the consumable is a tubular Ni-WC wire, the superheating of the molten droplet at the electrode tip before detachment can increase the tungsten carbide dissolution. Previous attempts at welding Ni-WC overlays have resulted in low carbide volume fractions using short-circuit and globular transfers [39]–[47]. Taking advantage of the measured minimum of molten droplet temperature between globular and spray transfers [48], Scott attempted to apply this theory to tubular Ni-WC wires to reduce carbide dissolution [47]. It was found that a minimum of temperature exists for tubular wires however the weld deposits still exhibit low carbide volume fractions and carbide dissolution.

1.2.4. Tubular Welding Consumables

The development of tubular wire manufacturing techniques has enabled the addition of powders to the wire-based welding consumable. Typically, these tubular consumables utilize a metallic sheath that has been formed into a tube and sealed by either crimping, overlapping the metallic sheet ends, or more recently seamless wires manufactured by processes such as Electrical Resistance Welding (ERW) the longitudinal sheath seams together, depicted in Figure 1.5 [49], [50]. During the forming process, powders are introduced into the partially formed tube before the joint is sealed and drawn to the desired diameters in subsequent manufacturing. The internal powders can consist of arc stabilizers, fluxing agents for slag based systems, shielding gas producers, and metallic alloying elements or ceramic powders for different welding applications. The tubular design has increased the application of wire based welding processes to include flux/slag based self-shielded and gas-shielded Flux Cored Arc Welding (FCAW), specialty alloyed Metal Cored Arc Welding (MCAW) consumables, and tubular CCO and Ni-WC hardfacing consumables.

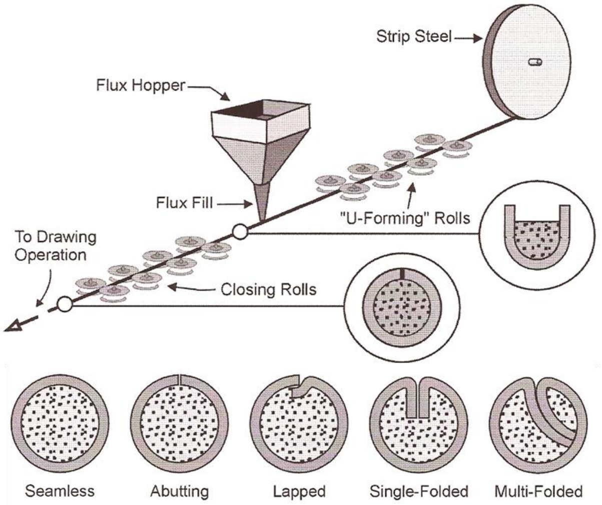

Figure 1.5: General manufacturing process of tubular FCAW, MCAW, and CCO/Ni-WC hardfacing wires. Types of sheath overlap and crimping is indicated.

Tubular consumables can exhibit metal transfer modes differing from GMAW. Literature contains scarce research and documentation of the Ni-WC metal transfer modes however some similarities will exist with FCAW consumables [49], [51]–[54]. Low current globular transfer can be characterized by repelled non-axial droplets while higher arc currents can produce small droplet non-axial metal transfer with the flux column protruding from the electrode tip, leading to separate transfer of the steel sheath and the flux powder, shown in Figure 1.6. Little available research has been published on short-circuit FCAW or MCAW wires. Tubular Ni-WC wires manufactured for wear resistant overlays do not conform to any regulatory consumable standards and therefore can vary considerably in their chemical composition, volume fraction of tungsten carbide, and sheath thicknesses.

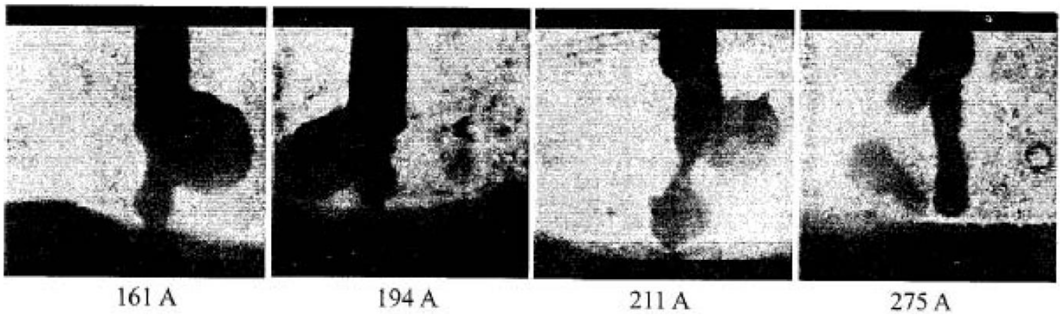

Figure 1.6: FCAW metal transfer modes exhibiting repelled globular transfer at low currents and a small droplet non-axial transfer with protruding flux column at high currents [52].

1.3. Ni-WC Overlay Fundamentals

The performance of the deposited wear resistant Ni-WC overlay has a direct correlation with the microstructure and carbide volume fraction of the overlay. The following sections will highlight the key matrix metallurgy and carbide morphology considerations and the effect of welding on overlay wear resistance.

1.3.1. Ni-based Matrix

The matrix of Ni-WC overlays are comprised of a nickel rich matrix with alloying additions of chromium, boron, and silicon in varying concentrations to obtain the desired weld deposit hardness, welding characteristics, and wear/corrosion performance. The microstructure generally forms as primary nickel dendrites with various borides, carbides, and silicides dispersed throughout the interdendritic regions [55], [56]. The primary nickel dendrites typically are soft (~350 HV) but the formation of CrB, Cr_7C_3, Cr_3C_2, Ni_3B, Ni_3Si and other complex phases can raise the overall matrix hardness to approximately 500-800 HV with individual phases reaching >1000HV [55], [57]–[60]. Figure 1.7 demonstrates a GMAW Ni-WC overlay and the associated phases typical of a NiBSi matrix. The addition of 1-5 wt% boron can drastically lower the melting temperature of the Ni-based alloy, enabling the welding heat input to be decreased and reducing detrimental carbide dissolution [61]–[64]. Silicon plays a lesser role in lowering the alloy melting temperature however its primary purpose is to deoxidize the weld pool [62], [65], [66]. A reaction of boron, silicon, and oxygen in the weld metal has been proposed to form a type of borosilicate glass [64], [67]. Borosilicate glass has a low density and will float to the weld pool surface where it can be removed as a light slag.

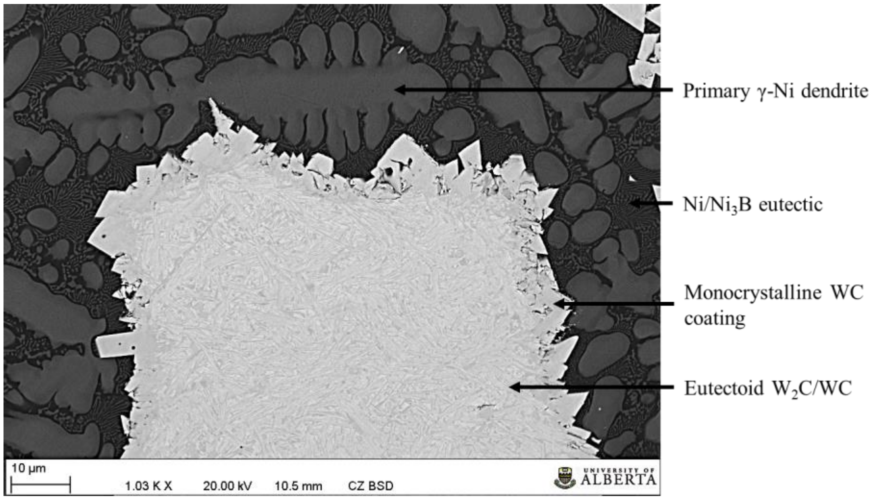

Figure 1.7: Backscattered SEM image of a typical GMAW overlay with WC-coated eutectoid W_2C/WC carbides in a NiBSi matrix. Primary nickel dendrites, interdendritic Ni_3B phases, and lack of carbide dissolution is demonstrated [6].

The addition of chromium to the nickel matrix forms hard chromium carbides [59]; however, it drastically increases the dissolution of tungsten carbides during welding. This is often attributed to chromium having a higher affinity for carbon than tungsten at elevated temperatures, promoting dissolution. In consumables containing high chromium levels (approximately 14 wt%), a blocky Cr-Ni-Si-W-

C phase surrounds the tungsten carbide particles, suggesting that the tungsten carbide particles partially dissolve. The dissolution creates a C-rich region surrounding the remaining primary tungsten carbide, leading to reactions with Cr and other elements and forming secondary carbide phases. This phenomenon was extensively characterized by Liyanage and demonstrated in Figure 1.8 [55]. Although the secondary carbides have high hardness (960-1600 HV) and therefore increase the bulk overlay hardness, they exhibit an extremely brittle behaviour, typically cracking during Vickers hardness testing when loads greater than 50 grams. Figure 1.9 depicts the brittle secondary phases cracking during hardness testing.

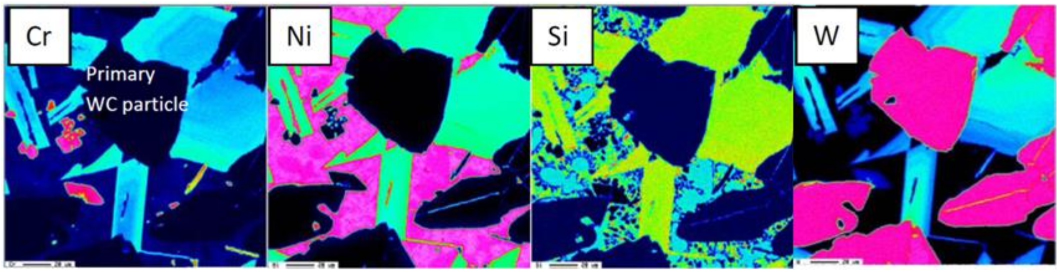

Figure 1.8: EPMA element map showing primary carbide dissolution and re-precipitation of W-containing phases surrounding the carbide [55]. Dark regions indicate low amounts of analyzed element.

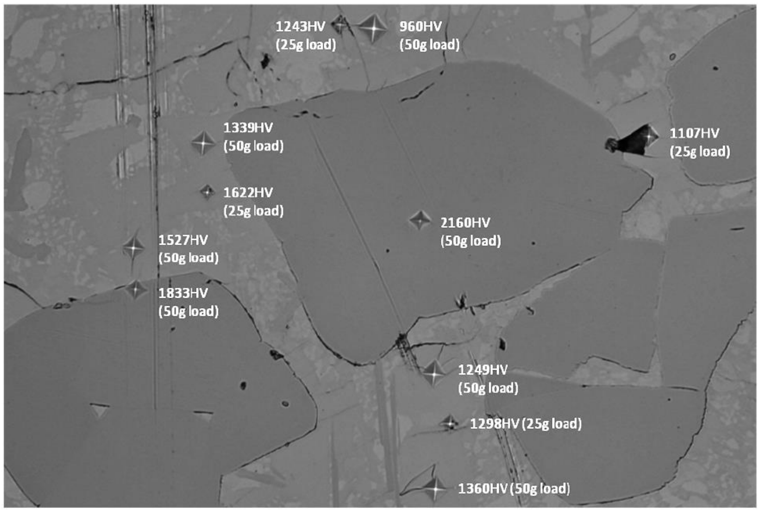

Figure 1.9: PTA welded Ni-WC overlay containing ~14wt% Cr. High carbide dissolution created very brittle complex Cr-Ni-Si-W-C phases surrounding the carbides that fracture during ASTM G65 wear testing, increasing mass loss [55].

It is important to highlight the paradox that chromium typically increases the bulk hardness of the matrix, intuitively suggesting that it increases wear resistance; however the wear resistance decreases as the secondary carbides break easily, further exposing the primary carbides and promoting pull-out. In addition to the brittleness of secondary carbides, the dissolution of tungsten carbides driven by Cr results in increased inter-carbide spacing and exposure of the softer metallic matrix to the abrasive medium [55], [68], [69]. To prevent excessive dissolution and carbide pull-out from overlays deposited with arc welding, a Cr-free matrix should be used in an erosive environment.

The effect of iron or nickel-based matrix alloy compositions on carbide dissolution was discussed by Babu et al. and Zhou et al. [70], [71]. Babu et al. studied the effect of a pure iron and pure nickel matrix on laser cladded overlays with monocrystalline tungsten carbide. Using ThermoCalc software, Babu et al. determined the characteristic dissolution time of tungsten carbide in iron to be twice that of a nickel matrix. Furthermore, any dissolved tungsten in the liquid solution precipitates as monocrystalline WC in the nickel matrix system while the inferior W_6C phase is precipitated in the Fe-based matrix [70]. It is important to note that the reprecipitation of WC predicted by Babu et al. only applies to a pure Ni matrix, not accounting for any B, Si, Cr, or Fe typically present in the weld pool. It has been shown that in commercially used Ni-based alloy systems, the dissolved tungsten does not reprecipitate as WC but rather as a brittle multi-element phase [55], [68]. Zhou et al. conducted a similar trial wherein NiCrFeBSiC and FeNiCrSiC matrix alloy powders reinforced with eutectoid W_2C/WC carbides was deposited on a steel substrate with the laser cladding process [71]. Using similar welding parameters for each matrix alloy, it was determined that the Ni-rich matrix reduced the tungsten carbide dissolution while nearly all of the tungsten carbides were dissolved with the Fe-rich matrix. Zhou et al. utilized a high workpiece preheat (1073 K), leading to a slower cooling rate and increasing the time for precipitated phases to form. Yang et al. conducted a parametric study on the effect of laser power (analogous to heat input) on the non-magnetic properties of an Fe-based monocrystalline WC overlay for downhole drilling tools [72]. Despite the rapid cooling rates of the laser cladding process, carbide dissolution was still observed in the Fe-based overlays within the parameters utilized by Yang et al. In summary, the presence of iron significantly increases the dissolution rate of tungsten carbide and measures should be taken to reduce dilution of the Ni-WC overlay with the steel substrate.

1.3.2. Carbide Morphology

Tungsten carbides exhibit high hardness, low thermal expansion, and relatively high toughness making them ideal for use as a wear resistant particle in a nickel matrix for oil sands and downhole tool applications. The downside to using tungsten carbides is the low heat of formation (-40 $kJmol^{-1}$), which during the welding thermal cycle, promotes the dissolution of the carbides in the weld pool [73].

There are two common tungsten carbide microstructural morphologies: monocrystalline WC and eutectoid W_2C/WC. Eutectoid (often referred to as “cast and crushed”) W_2C/WC carbides are manufactured with a carbon content range of 3.7-4.1 wt% through conventional casting and crushing processes. Eutectoid carbides have a hardness of 2200-2400 HV, melt at 2785 ^oC, and are distinguished by their alternating WC and W_2C lamellae. Monocrystalline tungsten carbides, commonly referred to as macrocrystalline carbides, are formed with carbon contents higher than 6.1 wt%, have an approximate hardness of 1200-2200 HV, and melting point of 2870 ^oC [74]. Monocrystalline carbides are formed through high temperature carburization of eutectoid W_2C/WC carbides as casting at carbon contents >6.1wt% can lead to carbon segregation and formation of graphite. It is important to note that monocrystalline tungsten carbides are not a single crystal.

Recently, a modified type of the traditional W_2C/WC tungsten carbide has been patented and manufactured [75]. These modified eutectoid carbides are partially carburized, creating a thin monocrystalline WC layer on the carbide surface. The monocrystalline WC shell is believed to decrease detrimental carbide dissolution during welding [76]. The fourth type of carbide microstructure is the spherical

WC_{1-x} morphology. Spherical tungsten carbides are manufactured with 3.7-4.1 wt% C, often using eutectoid W_2C/WC carbides as the feedstock, and are manufactured through a plasma spheroidizing process. This process creates a fully dense carbide with a very fine feathery structure that is possibly metastable [77]–[87]. It has been suggested that the relatively large (>10 µm) spherical carbides manufactured for welding consumables are not of the WC_{1-x} phase but rather are comprised of finely spaced W_2C and WC lamellae. This postulation however has not been proven as of this writing. Spherical carbides are more prone to dissolution than eutectoid carbides [88]–[91] however they exhibit a hardness range of 2700-3400 HV and are more resistant to fracture than monocrystalline WC [78]. Figure 1.10 demonstrates the monocrystalline, eutectoid, and spherical carbide regimes on the W-C phase diagram [82]–[84]. Figure 1.11 contains micrographs of the four tungsten carbide microstructures previously discussed. Figure 1.12 demonstrates the angular and spherical morphologies found in monocrystalline, eutectoid, and spherical carbides used in welding.

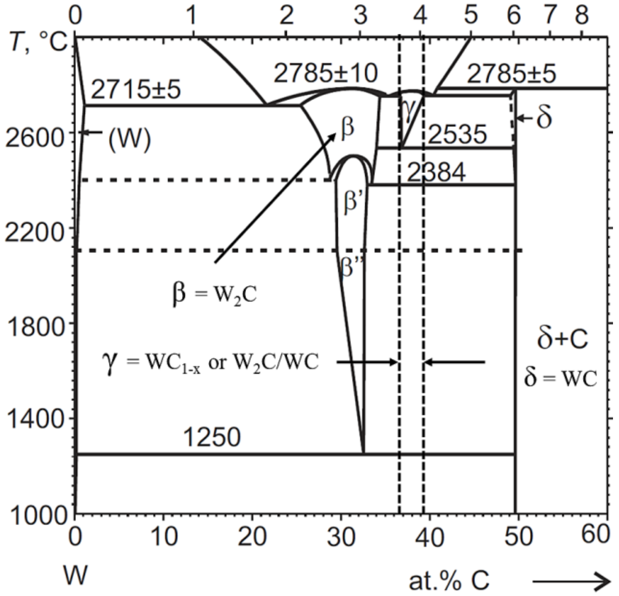

Figure 1.10: Partial W-C phase diagram with monocrystalline WC (δ), eutectoid W_2C/WC and spherical WC_{1-x} (γ) carbide formation regions indicated [82]–[84].

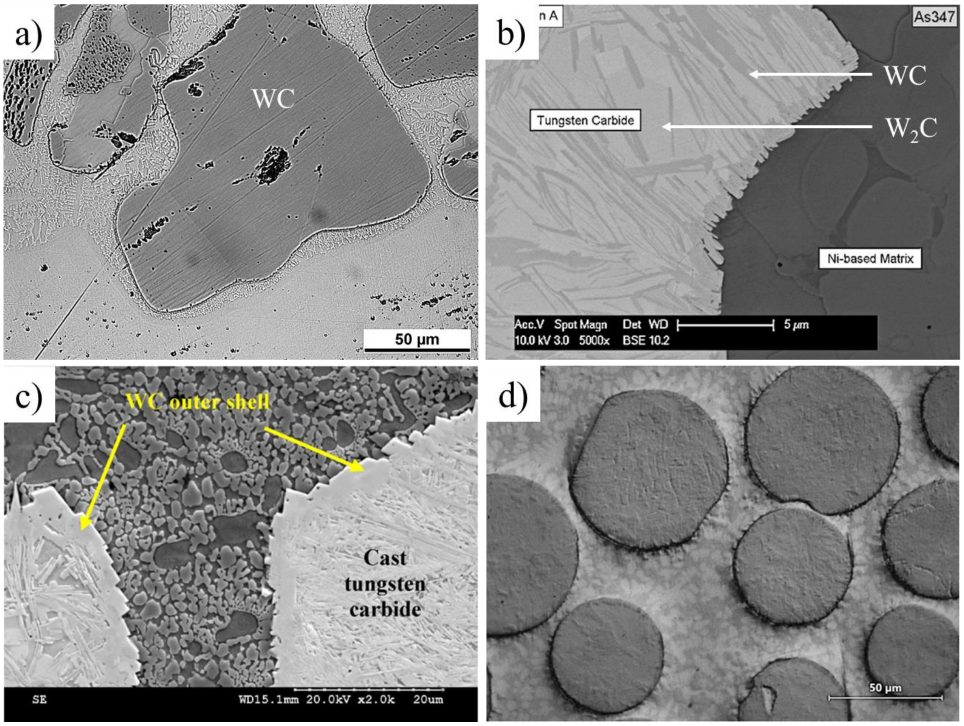

Figure 1.11: Summary of a) monocrystalline WC, b) eutectoid W_2C/WC [92], c) WC-coated eutectoid W_2C/WC [75], [76], and d) spherical WC_{1-x} [6] tungsten carbide microstructural morphologies.

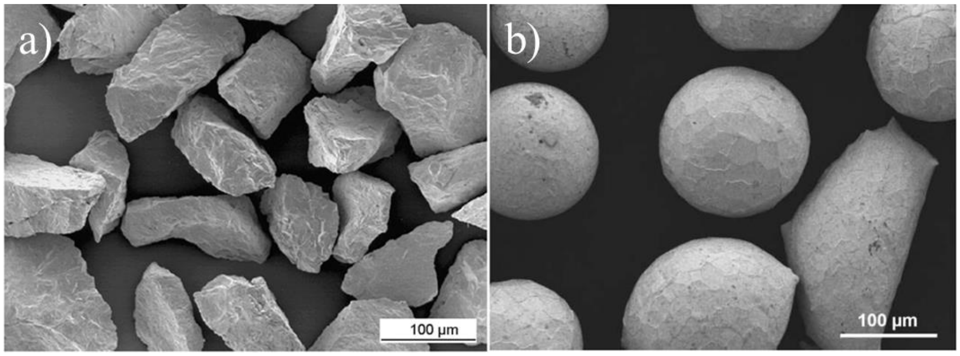

Figure 1.12: Common tungsten carbide shape morphologies of a) angular [45] found in monocrystalline and eutectoid tungsten carbides and b) spherical WC_{1-x} carbides [93].

Gassman et al. stated that eutectoid carbides have inferior tribological traits and are very brittle compared to monocrystalline carbides however this statement was not proven in any manner [94]. The increased resistance to fracture of eutectoid and spherical carbides to monocrystalline carbides during impact loading and high force wear testing was demonstrated by Fisher et al. [78]. Although the eutectoid carbides exhibit higher hardness and greater impact resistance compared to monocrystalline carbides, the W_2C phase is less stable than WC at elevated temperatures. This creates a dissolution band enriched in tungsten and carbon surrounding the carbide periphery [39]–[46], [55], [68], [71], [72], [76], [78], [88]–[92], [94]–[102]. The dissolution band is responsible for the reprecipitation of deleterious W-containing secondary phases that dramatically decrease the overlays wear resistance, exemplified in Figure 1.13. It is important to note that dissolution can be observed in monocrystalline WC overlays despite their higher resistance to dissolution.

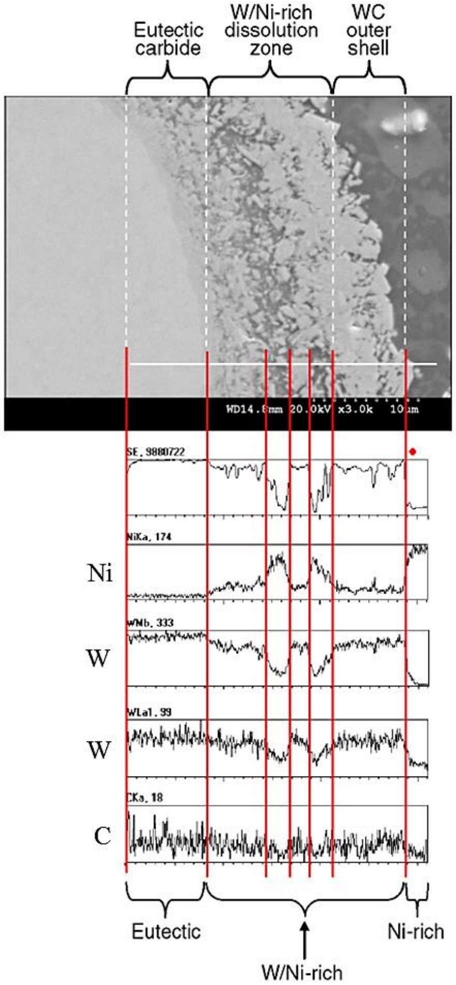

Figure 1.13: Dissolution band surrounding PTA welded spherical tungsten carbide [89].

1.3.3. Performance of Ni-WC Overlays Deposited by Welding

The welding of high quality Ni-WC is difficult and deviations from the ideal matrix chemistries and welding parameters often leads to poor wear resistance due to carbide dissolution, formation of brittle phases, increased inter-particle spacing, and decreased erosion-corrosion resistance. The effect of increasing heat input on carbide dissolution is summarized in Figure 1.14 and Figure 1.15.

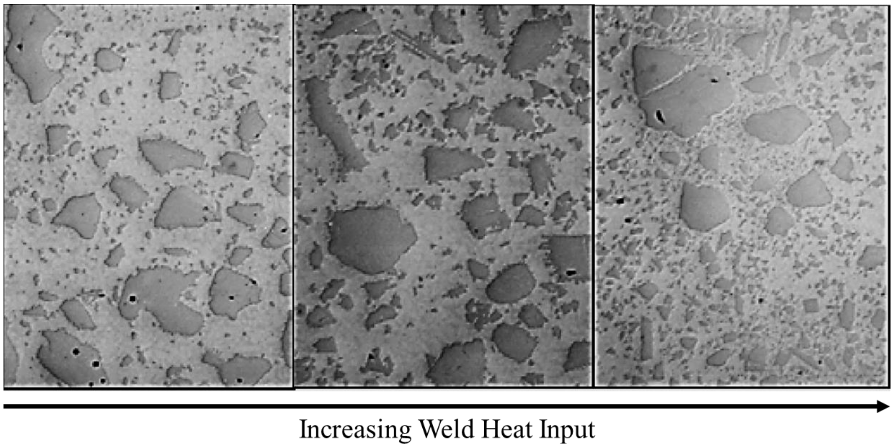

Figure 1.14: Effect of increasing heat input on tungsten carbide dissolution [103].

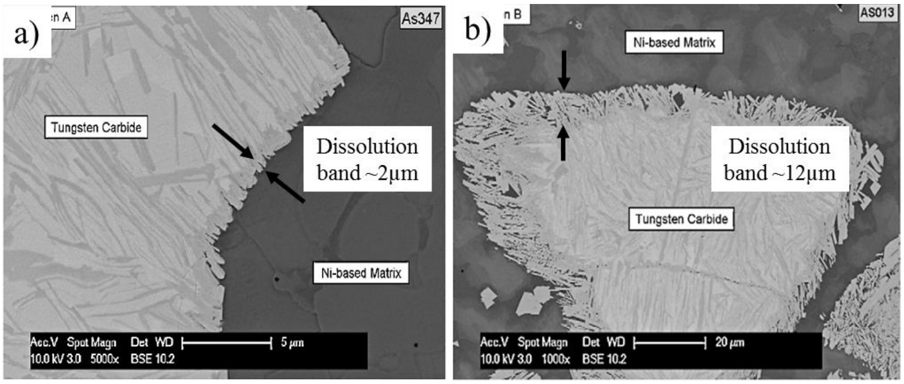

Figure 1.15: PTA welded eutectoid carbides in a NiBSi matrix demonstrating increased dissolution by increasing welding current 25% from a) to b) [92].

Figure 1.16 depicts PTAW overlays welded with the same parameters but with a high-Cr and a Cr-free matrix. Analysis of the ASTM G65 wear scar revealed chipping around the carbides in the high-Cr overlay, indicating the brittle phases expose the carbide periphery to the abrasive media and more than doubling the mass loss [55]. Tungsten carbide is approximately twice the density of nickel and can often settle to the bottom of the weld pool during welding [55], [101]. This can create a non-homogeneous carbide fraction distribution through the overlay thickness, leading to non-linear wear rates. Tungsten carbide settling is shown in Figure 1.16c).

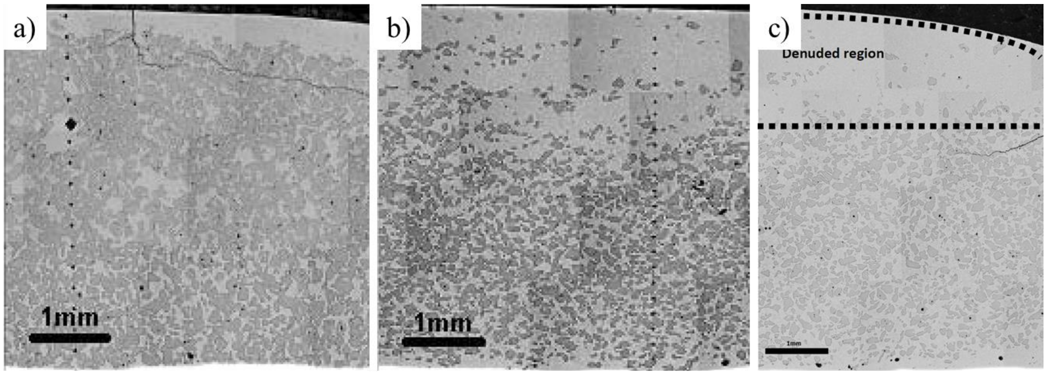

Figure 1.16: PTA welded Ni-WC overlays with the same welding parameters. Image a) is a Cr-free matrix while b) contains approximately 14%Cr leading to high carbide dissolution and lower primary carbide volume fractions. Image c) depicts tungsten carbides settling during welding, creating a denuded zone [55].

The most common test for wear resistance performance in Alberta is the ASTM G65 Dry Sand/Rubber Wheel Procedure A wear test. In this test, a rubber wheel is rotated against the wear specimen with a set force and number of rotations. Ni-WC overlays typically require two Procedure A wear tests; the first removes the nickel matrix and exposes the carbides while the second set of rotations is carried out in the same wear scar and is more representative of in-service wear conditions. The abrasive media is added between the rubber wheel and the specimen and comprised of quartz sand with a U.S. mesh size range of 50/70 (212-300µm). Wear performance for Ni-WC overlays is typically recorded as a mass loss during the second set of rotations in the previous wear scar. A lower mass loss indicates a higher wear resistance. For reference, an appropriately heat treated 60 HRC AISI D2 tool steel loses 0.280 grams, and industrial-scale chromium carbide overlays lose 0.180-0.200 grams during a single set of Procedure A rotations. Appropriately welded PTAW or laser cladded Ni-WC overlays lose ~0.050 grams during the second set of Procedure A rotations.

The wear resistance of Ni-WC overlays declines with the decrease of carbide volume fraction. This can be attributed to the increase of the mean inter-particle spacing, or the distance between the hard tungsten carbide particles, leading to preferential wear of the softer matrix material. Laser cladding can provide excellent control over the carbide dissolution and distribution in the nickel matrix, making it an ideal process to determine the effect of inter-particle spacing on the

ASTM G65 wear test. Polak et al. deposited various carbide size distributions and volume fractions using spherical tungsten carbides and a NiCrBSi matrix. It was determined that the inter-particle spacing is the dominant metric for wear performance over the carbide size for the abrasive media used. Figure 1.17 below indicates that a smaller inter-particle spacing increases the wear resistance in the ASTM G65 wear test [69]. However, it has been shown that tungsten carbide size plays a significant role in wear rate when considering other sizes of abrasive medias [78].

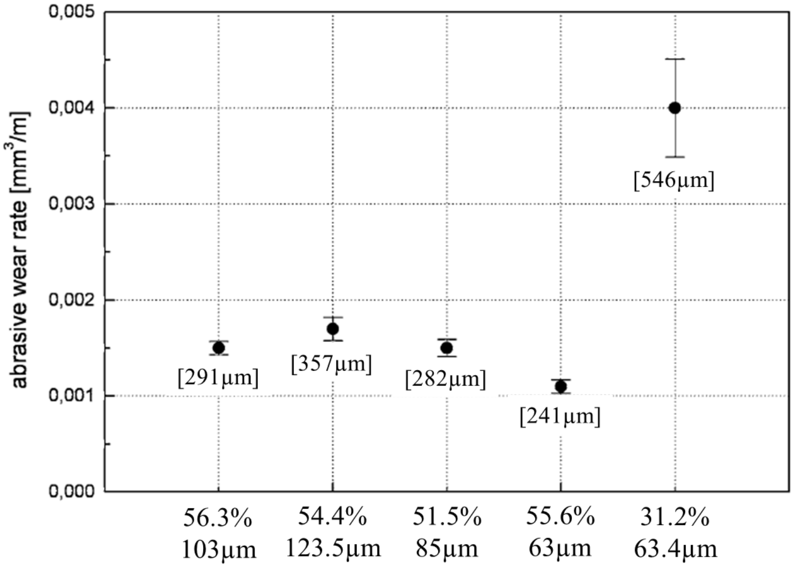

Figure 1.17: ASTM G65 Procedure A volume losses of Ni-WC overlays produced with varying inter-particle spacing's, indicated in brackets. The carbide volume and carbide diameter are indicated [69].

Spherical tungsten carbides are very prone to dissolution in PTAW and GMAW welding processes and provide an excellent illustration of the low wear resistance of secondary W-containing phases. Katsich and Badisch studied the effect of heat input on ASTM G65 wear resistance using PTAW deposited spherical tungsten carbide overlays [91]. High heat inputs led to considerable dissolution of the primary spherical carbides, forming large dissolution bands surrounding the carbide periphery. The brittle re-precipitated phases in the matrix and dissolution bands led to increased mass loss during ASTM G65 wear testing. The brittle secondary phases wore at a similar rate compared to the nickel matrix while the remaining primary spherical carbides exhibited a lower wear rate. Figure 1.18

summarizes the effect of heat input and carbide dissolution on Ni-WC overlay wear resistance. It is important to note that the small re-precipitated secondary carbide phases are traditionally measured during volume fraction measurements. This will give a false prediction of the wear performance of the overlay as the brittle secondary phases do not improve wear resistance.

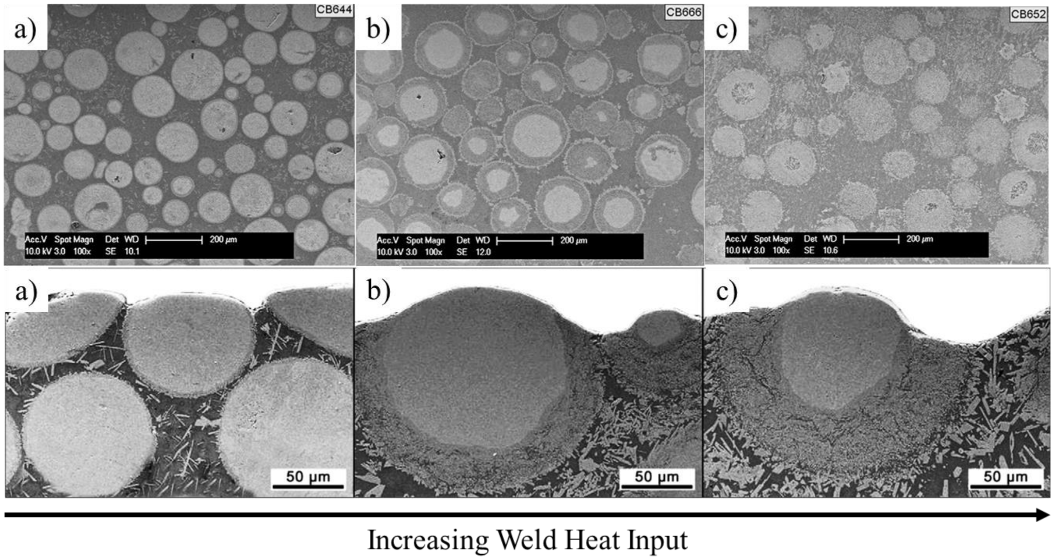

Figure 1.18: Effect of increasing heat input in PTA welded spherical tungsten carbide overlays in a NiCrBSi matrix. Overlay micrographs indicate carbide dissolution has occurred (top images) and preferential wear of dissolution bands following ASTM G65 wear testing (bottom images). Adapted from Katsich and Badisch [91].

Ni-WC overlays are often subjected to a variety of operating conditions including dry low-stress erosion and wet erosion where corrosion can influence the wear rate of the overlay. A variety of erosion-corrosion research has been conducted on PTAW overlays containing eutectoid, monocrystalline, and spherical tungsten carbides and matrices containing various concentrations of Cr, B, and Si [76], [89], [98]–[100], [104], [105]. All the overlays containing chromium exhibited some levels of carbide dissolution and reprecipitation of secondary phases containing W and Cr. The secondary phases did not significantly improve the erosion-corrosion performance of the overlay. The Cr-depleted regions adjacent to the reprecipitated phases and the boron-rich regions acted as the main locations for corrosion. Jones et al. conducted thorough studies on Cr-bearing and Cr-free

PTA welded Ni-WC overlays using angular and spherical eutectoid and monocrystalline carbides [89]. It was found that the eutectoid carbides in a NiBSi matrix showed considerable dissolution and reprecipitation of W-Ni rich bands around the carbide periphery, leading to anodic polarization and increased erosion-corrosion rates compared to the monocrystalline WC/NiCrBSi overlays. The primary damage mechanism of the WC/NiCrBSi overlays was corrosion of the matrix. In order to prevent the preferential erosion-corrosion attack surrounding the eutectoid carbides, carburized WC-coated eutectoid carbides were tested [76]. It was found that the erosion-corrosion rate of the modified carbide was 1/3 that of the eutectoid carbides as the preferential attack of the surrounding dissolution and reprecipitation zones was decreased, making the nickel matrix damage the dominant loss factor [76]. In context, the studies were conducted separately without testing the identical welding parameters or utilizing matching matrix composition to compare the WC-coated eutectoid carbides to the monocrystalline WC carbides in a Cr-bearing matrix. Therefore a direct correlation between carbide morphology on erosion-corrosion wear rates is not possible however the preferential erosion-corrosion degradation of the re-precipitated phases points to the importance of minimizing carbide dissolution.

Previous research on Ni-WC overlays deposited with tubular wires is scarce. Kivineva et al. investigated the effect of tungsten and tungsten carbide powder size distributions and surface coatings on the volume fraction and microstructure following welding using AISI 310 stainless steel sheathed tubular wires and GTAW and GMAW welding processes [106]. It was found that coating the tungsten powders with a SiO_2 film reduced dissolution, while small tungsten carbides (1μm) were immediately dissolved during welding. Klimpel et al. performed extensive parametric heat input studies of GMAW with two different Ni-WC wires and observed high levels of tungsten carbide dissolution throughout the deposits [41], [43]. Badisch and Kirchgassner [45] and Choi et al. [46] observed that dissolution was present independently of whether the overlay was deposited over fresh steel plate or over previous Ni-WC overlays. Vespa et. al. conducted controlled short-circuit GMAW welds with a mechanical wireretraction torch and it was found that increasing heat input increased the carbide dissolution and amount of re-precipitated phases [44]. Scott, in an attempt to reduce dissolution and using the well documented localized minimum molten droplet temperature region between globular and spray transfer modes in solid wires [48], identified a similar region with tubular Ni-WC wires [47]. The measured minimum region identified with Ni-WC wires still provided sufficient driving force for carbide dissolution.

1.4. Purpose of this Thesis

The purpose of this thesis is to determine the viability of the hot-wire assist technology for the deposition of nickel tungsten carbide wear resistant overlays using tubular wires. The hot-wire process is a high quality, high productivity, low cost alternative to the current industry-standard PTA welding system which is distinguished by its high capital cost, high weld quality, and relatively low productivity. The hot-wire process would allow small fabricators to produce high value-added Ni-WC wear resistant coatings for a variety of industries. This study will be the first of its kind utilizing tubular consumables and a GMAW leading heat source.

1.5. Thesis Outline

The following chapters will discuss the characterization of the tubular Ni-WC wires utilized in this study and their effect on the performance of the material system. The electrical resistivity of welding consumables, including tubular Ni-WC wires, will be discussed. After, the heat distribution within the tubular hot-wire was modeled to better predict the welding parameters when various torch assemblies and tubular wires are employed. Finally, the results of hot-wire assisted GTAW and GMAW overlays are discussed with corresponding metallurgical analysis and ASTM G65 wear test results. The appendices contain a summary of the nomenclature used herein, the raw tubular wire analysis data, summary of measured and calculated temperature dependent properties, additional metallurgical analysis, and highlights of high speed videos of selected phenomenon observed during welding.

2. Tubular Nickel Tungsten Carbide Consumables

2.1. Introduction

The development of tubular wire manufacturing techniques has enabled consumable electrode-based welding processes to deposit Ni-WC overlays. There are a variety of manufacturers producing Ni-WC wires in various sizes, typically 1.6mm nominal diameter but larger varieties are also available. The lack of hardfacing overlay consumable code governance has allowed manufacturers to create consumables with the same nominal diameters while different crimp overlaps, nickel sheath thicknesses, and powder compositions and size distributions are observed between the wires studied in this thesis. Characterization of Ni-WC consumables is needed to determine the subtle differences between manufacturers to explain different welding and metallurgical characteristics. The thermal conductivity of the powder core was calculated using an established model, while the electrical resistance of the tubular Ni-WC wires was measured between room temperature and near melting temperature.

2.2. Characterization of Tubular Ni-WC Consumables

The consumables were donated to the CCWJ for research purposes, with six 1.6mm (1/16”) and one 2.0mm (5/64”) coming from 5 different manufacturers. To keep the consumable manufacturer data confidential, the six 1.6mm wires were labelled A-through-F and the 2.0mm wire was labelled G.

2.2.1. Optical Characterization

To characterize the consumables, six sections approximately 1.5cm in length were cut from each wire spool and mounted perpendicular in an epoxy puck for metallurgical preparations. The wires were rough and fine ground, and polished to a 1µm diamond finish. To reduce scratching from the tungsten carbide powders falling out of the wire and marring the nickel sheath surface, the epoxy pucks were ultrasonically vibrated to remove loose carbides between grinding and polishing steps. The diamond polished cross sections were then photographed with an inverted light microscope. Image analysis was conducted using the Measurement tool in Adobe Photoshop CS5 which was calibrated by comparing the number of pixels in a line to a metallurgical scale. The pixel-length measurement obtained was the dimensional size of a single pixel. The region of interest was manually selected in Photoshop CS5 and the selected pixel count was recorded and converted into an area using the pixel-length ratio. Figure 2.1 below shows the wire cross sections for Consumables A-G with the corresponding average nickel sheath, A_S, and internal area, A_I, measured for each wire. The standard deviation of the average areas are shown and calculated from each individual section measurement, found in Appendix 1.

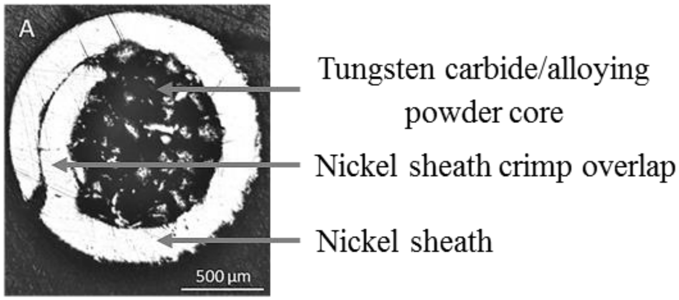

Sheath Area (mm^2) = 0.949 ± 0.085
Internal Area (mm^2) = 0.956 ± 0.115

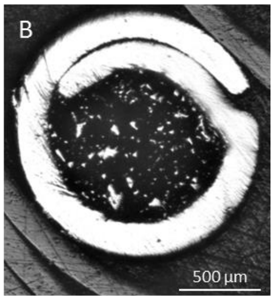

Sheath Area (mm^2) = 1.030 ± 0.007
Internal Area (mm^2) = 0.916 ± 0.018

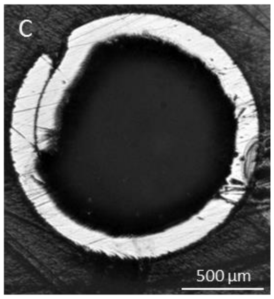

Sheath Area (mm^2) = 0.691 ± 0.023
Internal Area (mm^2) = 1.276 ± 0.031

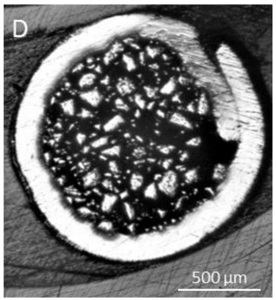

Sheath Area (mm^2) = 0.769 ± 0.013
Internal Area (mm^2) = 1.267 ± 0.031

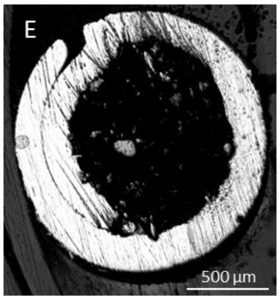

Sheath Area (mm^2) = 1.056 ± 0.030
Internal Area (mm^2) = 0.946 ± 0.030

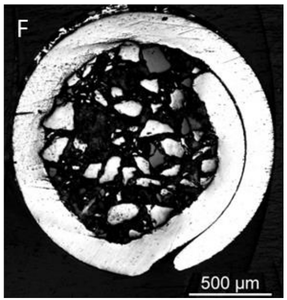

Sheath Area (mm^2) = 0.996 ± 0.019
Internal Area (mm^2) = 0.989 ± 0.007

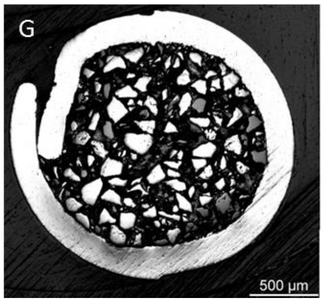

Sheath Area (mm^2) = 1.154 ± 0.037
Internal Area (mm^2) = 1.966 ± 0.081

Figure 2.1: Wire cross sections of Consumables A-G where A-through-F are 1.6mm OD while G is 2.0mm OD. The measured sheath area and internal area are shown.

The relaxation of the sheath crimp is visible in the wire cross sections shown in Figure 2.1 and Figure 2.2. The correction of the internal area was completed by manually estimating the crimp relaxation and "closing" the wire in Photoshop through photo manipulation. The adjusted internal area was measured using the Measurement tool and the characteristic pixel-length ratio and demonstrated in Figure 2.2. The internal area variance between the as-polished and the adjusted measurements is less than 6.4% for Consumables A-G, as seen in Appendix 1. The crimp relaxation can be a result of the manufacturing of the tubular Ni-WC wires as the nickel foil can relax following the mechanical deformation of the drawing operation. To remove any wrinkling, warping, or crimp relaxation from the plastic deformation of cutting the wire sections the wires were ground 3mm from the cut surface before the macrographs of Figure 2.1 and Appendix 1 were taken. The internal areas reported in Figure 2.1 and used in any subsequent calculations were of the as-polished condition.

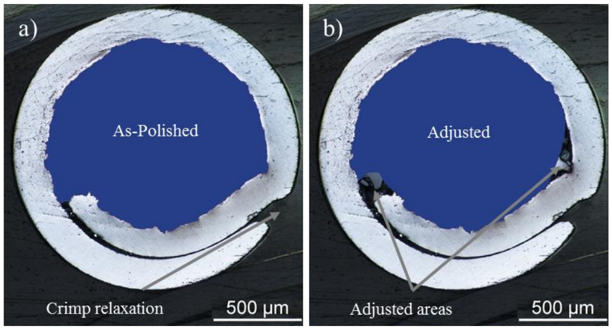

Figure 2.2: Demonstration of crimp relaxation in a) the as-polished condition and b) the manually adjusted region for internal area measurement of Consumable F.

Large variances between manufacturers in the nickel sheath thickness, crimping overlap, and internal carbide carrying area. Consumables A, B, E, and F have a thicker nickel sheath and a larger crimp overlap, decreasing the internal area compared to Consumables C, D and G. An understanding of the sheath thickness is of great importance. In the wires studied, the thicker sheathed consumables have an observed wider range of welding parameters and exhibit a more stable metal transfer in GMAW compared to the thin sheaths of C, D and G. However, a Ni-WC wire with a thick nickel sheath will have a lower carbide fraction compared to thinner sheathed wires for a given wire diameter, leading to potentially lower carbide fractions in the welded deposit. Due to the large variances of the consumables, the linear mass and initial wire carbide volume fraction, $f_{c,max}$, must be measured and calculated.

2.2.2. Mass Characterization

The difference in sheath thickness and crimp overlap between comparable nominal outside diameter consumables warranted further characterization of the consumable in this study. In order to calculate the initial wire carbide volume fraction, the linear mass of the powder and nickel sheath components were measured. The linear mass ($g \cdot cm^{-1}$) of the nickel sheath and powder core was measured by prying apart 0.5-1.0 meter of wire and emptying the powders out of the nickel sheath. Prior to weighing, the nickel sheath sections were thoroughly cleaned in an ultrasonic bath and rinsed in methanol to remove trace powders. The clean nickel sheath sections and powder were measured separately to yield the linear mass (m'_x) for each consumable according to Equation 2.1 below.

$$m'_X = \frac{Mass\ of\ x\ (g)}{Length\ of\ wire\ section\ (cm)}$$

Equation 2.1

Where x denotes the powder mass (P) or nickel sheath mass (S). Table 2.1 contains the measured powder and nickel sheath linear mass values for each consumable. To validate the powder removal method of prying the sheath apart, a sensitivity analysis was conducted using the resolution of the scale used to weight the powders. It was found that over 1000 individual tungsten carbide particles would have to be unaccounted for to be registered on the scale, calculated in Appendix 1. Less than 1000 carbides were lost during the separation process.

Table 2.1 Sheath and powder linear mass values for Consumables A-G.

Consumable	m'_S (g·cm^{-1})	m'_P (g·cm^{-1})	m'_{total} (g·cm^{-1})
A	0.087	0.081	0.168
B	0.088	0.081	0.169
C	0.065	0.118	0.183
D	0.069	0.114	0.183
E	0.094	0.079	0.173
F	0.092	0.086	0.178
G	0.101	0.148	0.249

2.2.3. Initial Wire Carbide Volume Fraction

The carbide volume fraction in the deposited weld overlays is a critical factor in assessing the quality and performance of overlays in-service. It is necessary to characterize the initial wire carbide volume fraction, $f_{c,max}$, of the consumable prior to welding to postulate the amount of carbides lost to dissolution or non-wetting, a new loss mechanism documented for the first time in this work. The initial wire carbide volume fraction is a function of the powder linear mass, density of powder, internal area, and nickel sheath area as calculated below. The initial wire carbide volume fraction is the theoretical upper carbide volume fraction bound or the maximum volume fraction of carbide that can be obtained in the weld pool following welding. Using the linear mass values from Table 2.1, the initial wire carbide volume fraction, $f_{c,max}$, can be calculated using Equations 2.2 and 2.3.

$$A_C = \frac{m'_C}{\rho_C} \approx \frac{m'_P}{\rho_C}$$

Equation 2.2

$$f_{c,max} = \frac{A_C}{A_P + A_S} \approx \frac{A_C}{A_C + A_S} = \frac{1}{1 + \frac{A_S}{A_C}}$$

Equation 2.3

Where A_C is the area of carbide powder, ρ_c is the density of monocrystalline or eutectoid tungsten carbide, and A_S is the area of nickel sheath. A_c approximates the volume of tungsten carbide powder contained in the wire core as a solid area cross section so it can be compared to the area of nickel sheath in $f_{c,max}$. The initial wire carbide volume fraction corresponding to Consumables A-G can be seen in Figure 2.3. Consumables A, C, E, F, and G are comprised entirely of eutectoid W_2C/WC carbides while Consumable B utilizes the monocrystalline WC morphology exclusively. Consumable D contains unique eutectoid carbides that have been carburized to produce a WC shell.

It was approximated that the bulk density of powder was entirely comprised of tungsten carbide as it is in high quantities and denser than the lighter alloying elements of boron and silicon. The density of monocrystalline WC is 15.8 gcm^{-3} and the density of W_2C is 17.15 gcm^{-3} [74], [107]. The density of eutectoid carbides was calculated using a phase balance of 78-80% W_2C and 20-22% WC for a density of 16.87 gcm^{-3} [79]. The WC shell of the Consumable D eutectoid carbides was neglected as the carburization case depth is unknown.

The wire core carbide fraction, $f_{c,core}$,or “packing factor” can be calculated using the area of carbide powder, A_C, and the internal area of the wire core, A_I as seen in Equation 2.4.

$$f_{c,core} = \frac{A_C}{A_I}$$

Equation 2.4

The wire core carbide fraction for all the consumables studied indicates that the powder core has a packing factor of ~0.5, which is reasonable considering maximum packing of same size spheres is 0.74. The calculation of the initial wire carbide volume revealed a correlation with the volume of nickel sheath, demonstrated in Figure 2.3. The consumables which were manufactured with a thick nickel sheath exhibited a large decrease in the initial wire carbide volume fraction. Consumables C, D, and G which utilize a thinner nickel sheath than the other wires show a smaller decrease in volume fraction. The correlation discrepancy caused by the 2mm O.D. Consumable G is from the higher nickel sheath area compared to the smaller 1.6mm O.D. wires despite having a thin sheath. Oil sands operators typically require 45-50% volume fraction carbide in the wear resistant overlays. Based on this criteria, only Consumables C and D and potentially G contain enough carbide to provide sufficient volume fraction and wear resistance following welding.

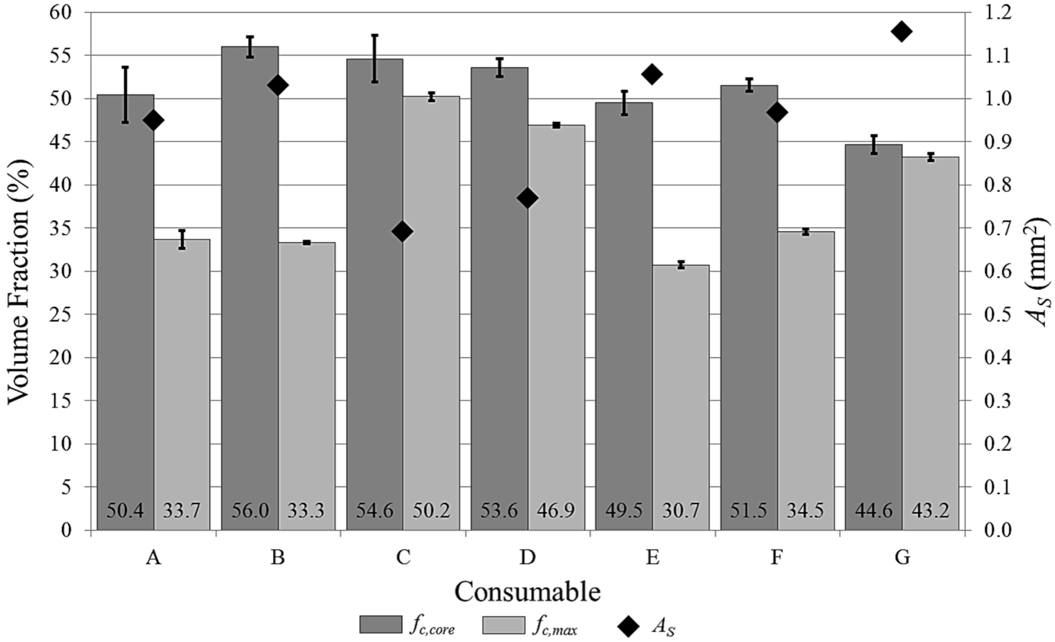

Figure 2.3: The wire core carbide fraction, $f_{c,core}$, and the relationship between initial wire carbide volume fraction, $f_{c,max}$, and nickel sheath area, A_S, is shown for Consumables A-G.

Error analysis was conducted on $f_{c,max}$ and $f_{c,core}$ using Equation 2.5 where x denotes each term. The error analysis will allow direct comparisons of carbide volume fractions between consumables following welding while being certain the observed differences are a result of welding and not the consumables themselves. The terms L_{wire} and m_p are the total length of wire cut for linear density measurement and mass of powder weighed from the total length respectively. The terms m_{error} and L_{error} are the resolution in the measurement of mass (0.01 grams) and wire length (0.1 cm) errors respectively. The error in carbide density, $\rho_{c,error}$, is calculated from the phase balance variance of the eutectoid carbides and is assumed negligible for the single phase monocrystalline WC carbides. The error for eutectoid carbides was calculated at 0.057 g·cm^{-3}. The error in nickel sheath area, $A_{S,error}$, is the standard deviation of the nickel sheath area measurements for the 6 wire sections cut for each consumable. The error of the nickel sheath and carbide powder separation process is negligible compared to the scale error, as demonstrated in Appendix 1. The tabulated error values for all consumables are shown in Table 2.2.

$$\sigma_{f_{c,max}} = \sqrt{\left(\frac{\partial f_{c,max}}{\partial x}\right)^2 \partial_x^2 + \dots}$$

Equation 2.5

Table 2.2: Measured and error values for L_{wire}, m_p, $A_{S,error}$ and the total error in the calculation of the initial wire carbide volume fraction.

Consumable	L_{wire} (cm)	m_P (g)	$A_{S_{error}}$ (mm^2)	$\sigma_{f_{c,core}}$ (%)	$\sigma_{f_{c,max}}$ (%)
A	49.2	4.00	0.085	6.34	2.02
B	52.7	4.27	0.007	2.33	0.21
C	51.4	6.04	0.023	5.39	0.85
D	51.1	5.85	0.013	2.13	0.45
E	37.5	2.98	0.300	2.71	0.64
F	90.8	7.79	0.019	1.46	0.64
G	112.4	16.63	0.037	2.02	0.79

The optical nickel sheath area measurements were validated using mass measurements. The measured nickel sheath area was converted to a calculated nickel sheath linear density (g·cm^{-1}) and compared to the measured sheath linear density (Equation 2.1 and Table 2.1), with the results being summarized in Appendix 1. Although only the measured nickel sheath area for Consumables A, D, E, and G met the criteria, the remaining consumables were very close to being verified. This can be due to the measurement method of the nickel sheath linear density which involved prying the wire sections apart and emptying out the carbide powder before rinsing and ultrasonic bathing. The nickel sheath sections could have retained embedded carbide powder when weighed for the calculation of the nickel sheath linear density, providing a small unquantifiable error.

2.3. Sheath and Powder Chemical Analysis

The chemical makeup of wear resistant overlays plays a critical role in the performance against the aggressive oil sands operating environments. Higher levels of boron and silicon can alter the matrix properties while chromium can increase the dissolution of tungsten carbide [55]. The chemistry can vary between wire manufacturers so it is necessary to quantify the alloying elements present. Chemical analysis was conducted separately on the tungsten carbide powder and the nickel sheath. Analysis was conducted using Inductively Coupled Plasma (ICP) and Energy Dispersive X-ray Spectroscopy (EDS/EDX).

2.3.1. Nickel Sheath

Typical steel tubular welding wires (FCAW and MCAW) contain some small additions of alloying elements such as carbon and silicon in the metallic sheath. To determine the presence of alloying elements in the nickel sheaths, lengths of Consumables A-D were cut into sections and the nickel sheath was separated from the carbide powder. The cut strips of sheath were ultrasonically bathed in methanol prior to drying to remove any carbide powder. Parts of the clean foil strips were sent for ICP testing with the results shown in Table 2.3.

Table 2.3: Chemical compositions of nickel sheaths for Consumables A-D. ICP testing revealed the nickel sheaths are approximately pure nickel.

	Elemental Concentration (wt%)					
Consumable	Ni	C	Mn	Si	Fe	B
A	99.9	0.011	0.03	0.01	<0.01	<0.001
B	99.7	<0.01	0.14	0.05	0.02	<0.001
C	99.9	<0.01	0.05	<0.01	<0.01	<0.001
D	99.9	<0.01	0.05	<0.01	<0.01	<0.001

ICP analysis showed the nickel sheaths of Consumable A-D were almost entirely comprised of nickel, with trace concentrations of manganese and silicon. The detection limits of are less than 0.02 ppm ($2x10^{-6}$ wt%) for the elements analyzed in this study [108]. The sensitivity of the ICP analysis technique validates the above wt% measurements.

2.3.2. Carbide and Alloying Powder

The carbide powders removed from Consumables A-D were analyzed with ICP to determine alloying element concentrations. The ICP test results did not correspond with data provided from the consumable manufacturers and observed microstructures, summarized in Table 2.4. The wire powders should contain measurable amounts of Cr, B, and Si. The testing facility stated that the acid digestion procedure used did not fully dissolve all of the powder, which could explain the discrepancies. As a result, powder from Consumable A was sent to another ICP facility. The results, shown in Appendix 2, indicated that the second ICP digestion technique was not viable as only trace amounts of Cr, B, Si were detected.

Table 2.4: ICP powder analysis of Consumables A-D. Chemical test reports are found in Appendix 2.

	Elemental Concentration (wt%)				
Consumable	W	C	O	Mn, Si, Cr, Fe, Ca, K, Ni	B
A	94.3	4.1	0.39	<0.01	<0.001
B	93.2	6.5	0.16	<0.01	<0.001
C	95.1	4.5	0.25	<0.01	<0.001
D	94.3	5.2	0.35	<0.01	<0.001

The inaccurate results of the ICP analysis prompted characterization of the carbide powders with EDS for Consumables A-G. The EDS analysis technique does not possess the accuracy of ICP for bulk concentration measurements because it has low sensitivity for light elements such as carbon, boron, and silicon but can be useful in determining specific elemental concentrations of individual particles.

The tungsten carbide and alloying powder volumes and size distributions vary considerably between the manufacturers presented in this study. Analysis of the individual particles found in the powder of each consumable was conducted to determine the exact constituents comprising the carbide and alloying powder. This was done to determine what type of powder is being added as well as determine the level of other additions such as arc stabilizers and fluxing agents. It is important to note that powder size and concentration distributions present in the SEM images are not fully representative of the bulk sample as a result of applying the powder to sticky carbon tape and removing the loose excess particles before placing the mounted samples in the SEM-EDS. The micrographs of Consumables A-G are shown in Figure 2.4-Figure 2.10 and the subtleties will be discussed.

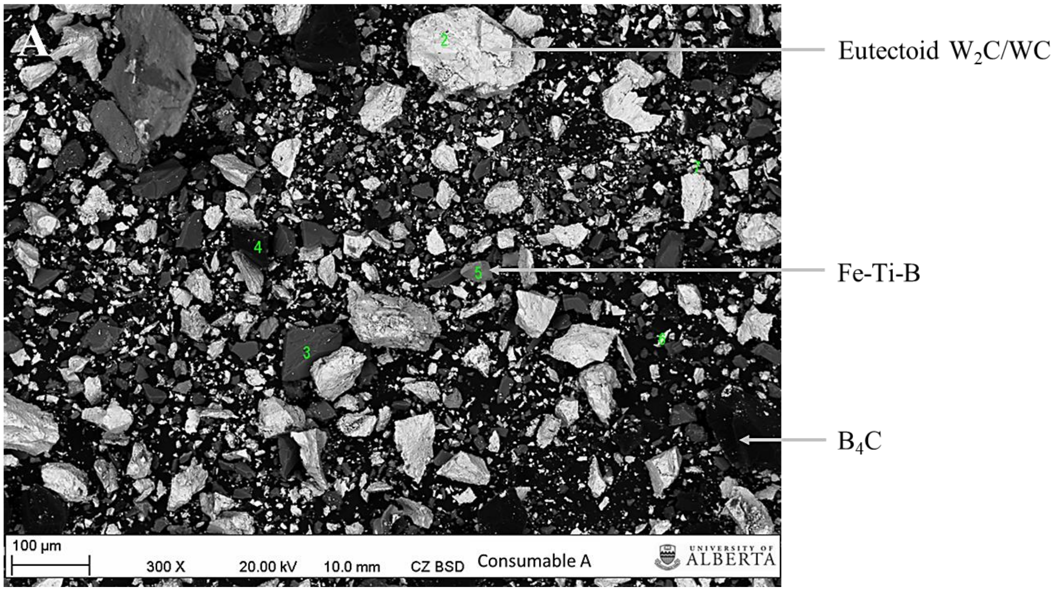

Figure 2.4: Backscattered electron EDS analysis of Consumable A with proposed particle compositions. Complete EDS data found in Appendix 3.

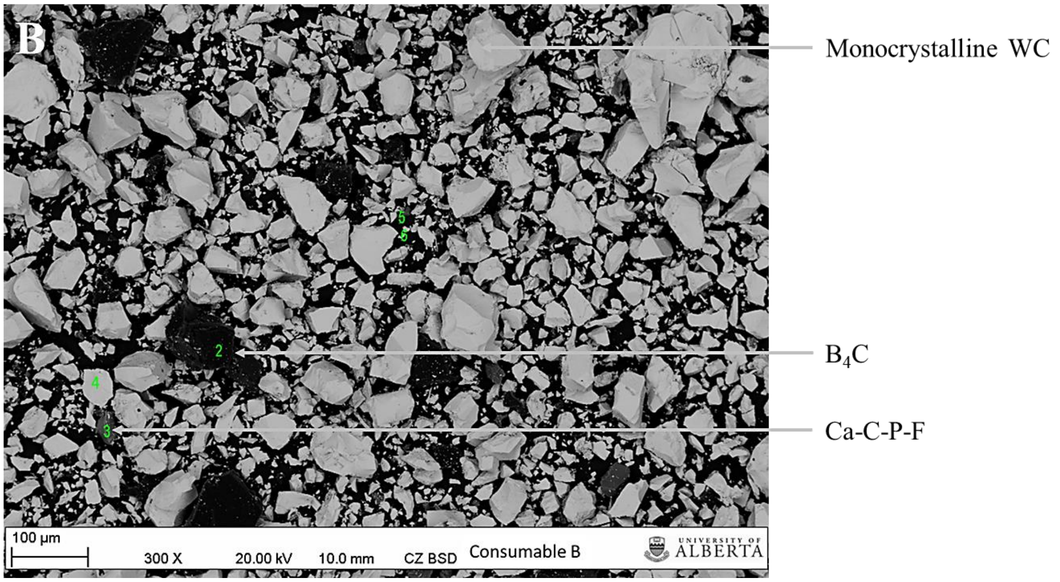

Figure 2.5: Backscattered electron EDS analysis of Consumable B with proposed particle compositions. Complete EDS data found in Appendix 3.

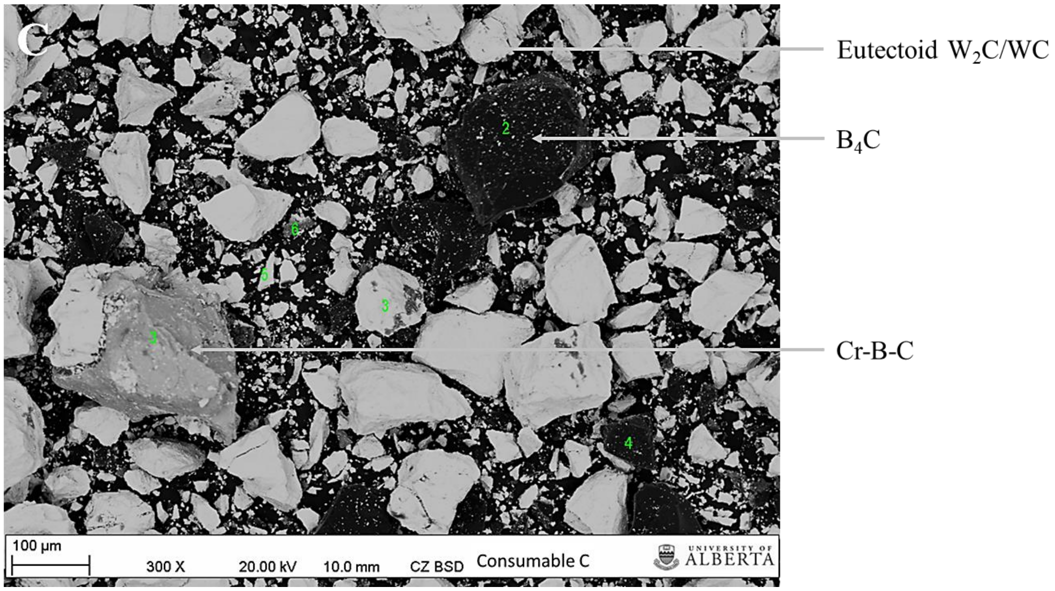

Figure 2.6: Backscattered electron EDS analysis of Consumable C with proposed particle compositions. Complete EDS data found in Appendix 3.

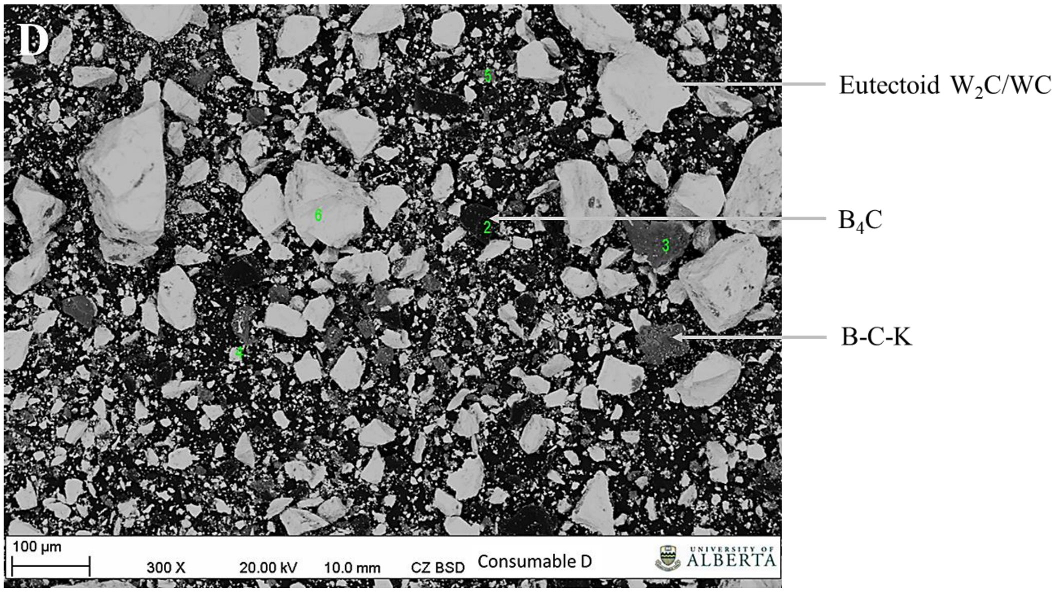

Figure 2.7: Backscattered electron EDS analysis of Consumable D with proposed particle compositions. Complete EDS data found in Appendix 3.

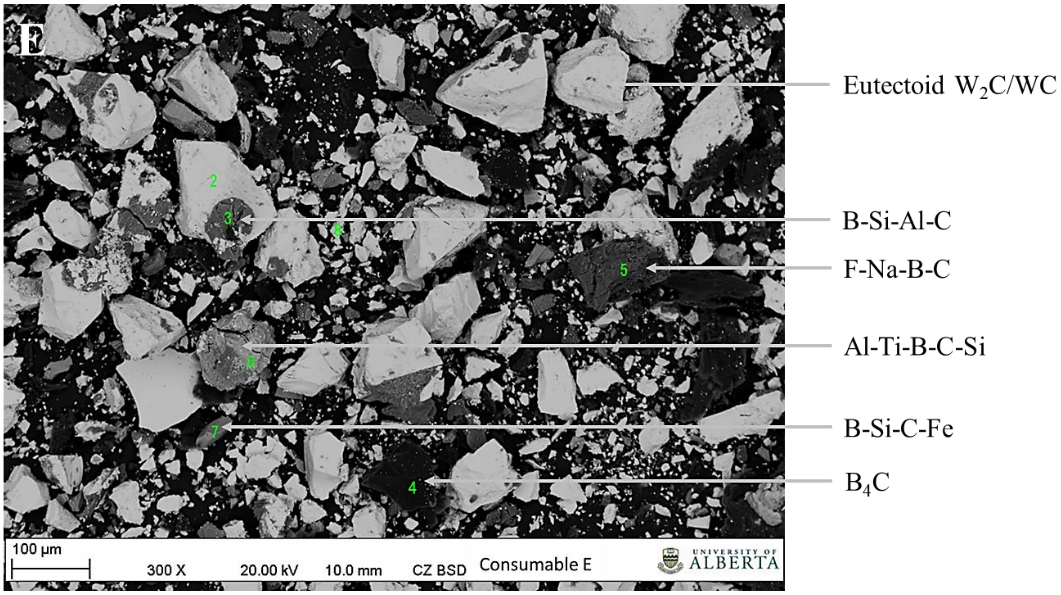

Figure 2.8: Backscattered electron EDS analysis of Consumable E with proposed particle compositions. Complete EDS data found in Appendix 3.

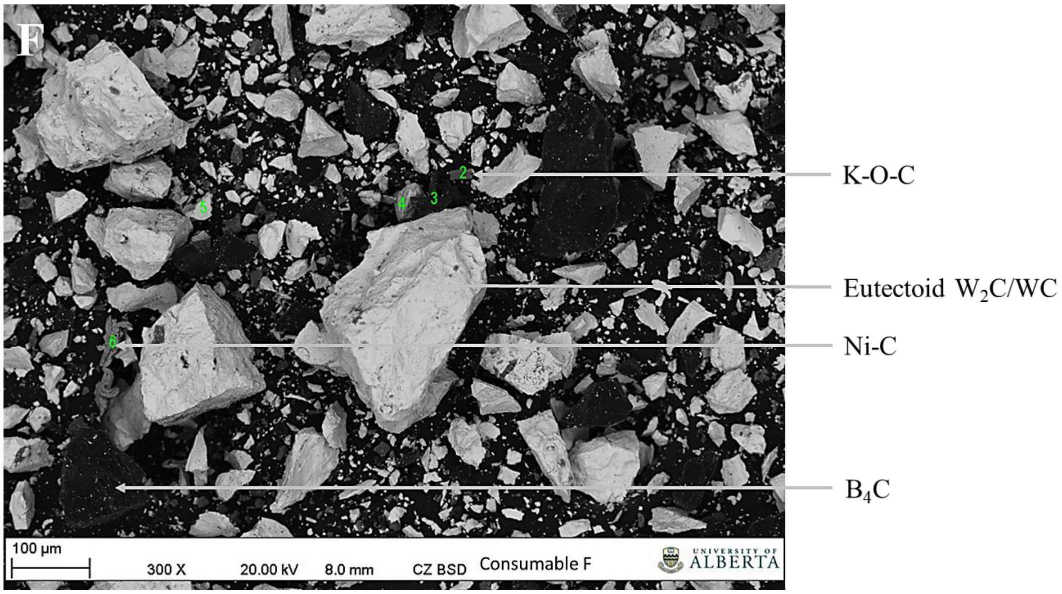

Figure 2.9: Backscattered electron EDS analysis of Consumable F with proposed particle compositions. Complete EDS data found in Appendix 3.

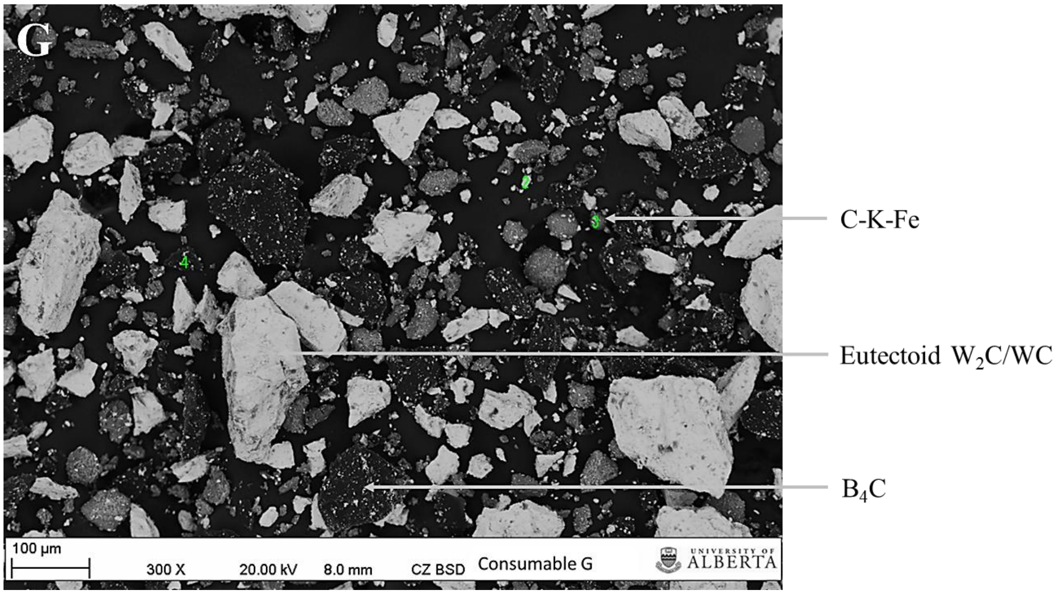

Figure 2.10: Backscattered electron EDS analysis of Consumable G with proposed particle compositions. Complete EDS data found in Appendix 3.

The carbide powder morphology is consistent between consumables, exhibiting an angular shape with sharp edges. The carbide particle size varies considerably between manufacturers with Consumable B having an average size of 70 µm while the other wires contain carbides of 100-120 µm average diameters. Consumable B exhibited a characteristic bimodal carbide size distribution with a large portion of small carbides and a few very large carbides, demonstrated in Appendix 3. The relative amount of fine angular tungsten carbides levels also varies considerably with Consumables A, E, and F containing higher volumes than Consumables C, D, and G. All consumables do however contain some small tungsten carbide fines ranging in size from 5-20 µm. The amount of fines may be a result of the powder size distributions placed in the wires by the manufacturer or a result of the mechanical drawing operation. The reduction in wire nominal diameter might cause fracturing of the tungsten carbides in the wire core. The quantity of alloying powder and chemical composition of the constituents differs considerably between manufacturers. Tubular Ni-WC wire manufacturers add several different elements and compounds in order to alloy the matrix, stabilize the welding arc, and decrease the melting point of the alloy system. The addition of sodium and potassium help stabilize the welding arc while titanium cleans the weld pool of contaminants. Consumable A and E contain silicon, aluminum and magnesium which can serve to reduce the melting point of the matrix and increase weld pool fluidity so the material system can be welded at lower heat inputs. It is suspected that the addition of arc stabilizer powders of Na, K, and F is in a fine powdered form as nearly all carbide and alloy particles had trace amounts detected during EDS testing. All of the manufacturers analyzed added boron in the form of B_4C as determined by the EDS chemical ratio range of 3.6/1-4.8/1 boron/carbon atomic ratio. Table 2.5 contains a summary of the visual and EDS analysis.

Table 2.5: Summary of approximate powder size and constituents from SEM/EDS analysis of Consumables A-G.

	Consumable						
	A	**B**	**C**	**D**	**E**	**F**	**G**
Size (µm)	20-130	20-120	50-120	30-130	30-110	30-110	50-120
Quantity of Alloy Powder	H	L	M	M	M	M	H
B_4C	Y	Y	Y	Y	Y	Y	Y*
Si	Y	-	-	-	Y	-	-
Al/Mg	Y	-	-	-	Y	-	-
Fe	Y	-	-	-	Y	-	Y
Ni	-	-	-	-	-	Y	-
Ti	Y	-	-	-	Y	-	-
Cr	Y	-	Y	-	-	-	-
Na	Y	-	Y	Y	Y	Y	-
Ca	-	Y	-	-	-	-	-
F	Y	Y	Y	Y	Y	Y	Y
K	Y	-	Y	Y	Y	Y	Y
P	-	Y	-	-	-	-	-

(Y) = Yes, (-) = No L = Low, M = Medium, H = High

*: Presence of B_4C not chemically measured however particle is visually recognized from other powders.

2.4. Thermal Conductivity of the Tungsten Carbide Powder Core

The hot-wire electrode extension model proposed in Chapter 3 assumes a 1-D axisymmetric heat flow. Determining the thermal conductivity of the tungsten carbide powder inside the tubular wire will satisfy the assumption that the temperature through the wire cross section is uniform. The following work will utilize an existing powder thermal conductivity model to approximate the wire core thermal conductivity and discuss the validity of the axisymmetric heat flow assumption.

The thermal conductivity of the powder core can be approximated by the Zehner and Bauer model [109]. This model includes three main coefficients: the particle-particle radiation, conduction across the fluidic inter-particle spacing, and conduction from particle to particle at the point of contact. The notation depicted below has been altered from the original version. According to this model, the effective thermal conductivity of the powder, k_{powder}, can be expressed as:

$$k_{powder} = \lambda_{2P} k_{air}$$

Equation 2.6

Where k_{powder} is in W·m^{-1}·K^{-1}, λ_{2P} is the unitless thermal conductivity coefficient of the powder, and k_{air} is the thermal conductivity of the air inside the powder in W·m^{-1}·K^{-1}. The thermal conductivity coefficient of the carbide powder core can be expressed as Equation 2.7.

$$\lambda_{2P} = \left(1 - \sqrt{1-\psi}\right)\psi\left[\left(\psi - 1 + {\lambda_G}^{-1}\right)^{-1} + \lambda_R\right] + \sqrt{1-\psi}\left[\varphi\lambda_P + (1-\varphi)\lambda_C\right]$$

Equation 2.7

The thermal conductivity coefficient of the powder is a function of: ψ is the volume fraction of air in the powder bed, λ_G denotes the unitless conductivity coefficient of the fluid between the particles, λ_R is the radiation coefficient from particle to particle, φ is the flattening coefficient of the powder, λ_P is the conductivity coefficient of the powder constituents, and λ_C is the conductivity coefficient of the tubular wire core.

Simplification of the thermal conductivity of the fluid, λ_G, can be accomplished by assuming the tubular Ni-WC wires are exposed to air during manufacturing and before welding, it can be assumed that the fluid between the particles is air. This makes the coefficient of the fluid equal to 1, as seen in Equation 2.8.

$$\lambda_G = \frac{k_{gas}}{k_{air}} = \frac{k_{air}}{k_{air}} = 1$$

Equation 2.8

The radiation coefficient from particle to particle, λ_R, can be expressed as a function of the temperature, emissivity of the carbide particle, and diameter of the carbide particle, shown in Equation 2.9. The radiation constant for a black body, C_S, is 5.67x10^{-8} W·m^{-2}·K^{-4}. Room temperature was used for calculations and 0.9 was used for the tungsten carbide emissivity [110]. The particle size, d, was found by assuming a monodispersed particle sizing (ie. powder is comprised of only one size) and using a visual average of the SEM images of carbide powders, summarized in Table 2.5. The powders contained within tubular Ni-WC wires are actually comprised of tungsten carbide and boron-silicon alloying powder with polydispersed size distributions ranging from ~10-200 µm. If the exact polydispersed carbide powder distribution is known, Equation 2.10 can be used to determine the particle size.

$$\lambda_R = \frac{4C_s}{\frac{2}{\epsilon} - 1} T^3 \frac{d}{k_{air}}$$

Equation 2.9

$$d = \left(\Sigma \frac{Q_i}{d_i}\right)^{-1} \text{ for polydispersed packings}$$

Equation 2.10

The flattening coefficient, φ, was chosen to be 0.0010 from Table 2.6 based on the shape similarities between the tungsten carbide depicted in Figure 2.4-Figure 2.10 and the broken silica sand in Figure 2.11.

Table 2.6 Shape factor coefficients and flattening coefficients for the Zehner and Bauer model as outlined by Tsotsas and Martin [109].

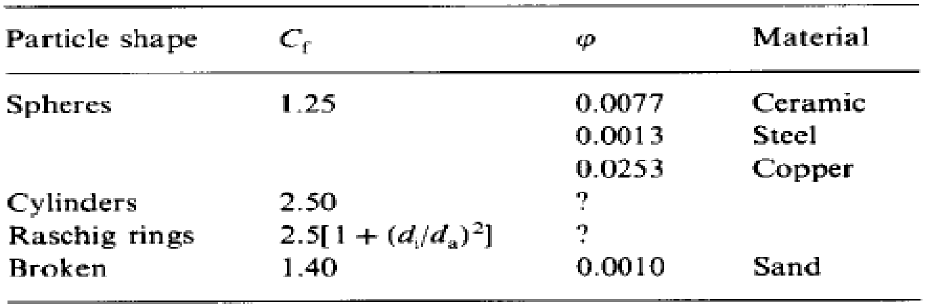

Particle shape	C_f	φ	Material
Spheres	1.25	0.0077 0.0013 0.0253	Ceramic Steel Copper
Cylinders	2.50	?	
Raschig rings	$2.5[1 + (d_i/d_a)^2]$	?	
Broken	1.40	0.0010	Sand

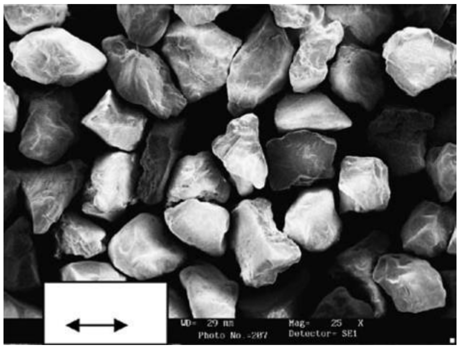

Figure 2.11: Image of broken silica sand for comparison to tungsten carbide morphology to determine flattening coefficient.

The coefficient of thermal conductivity of the powders, λ_P, can be assumed to be the thermal conductivity of tungsten carbide as it is the most prevalent compound found in the powder. The thermal conductivity of monocrystalline WC, $k_{carbide}$, used was 84 W·m^{-1}·K^{-1} [111]. The thermal conductivity of air, k_{air}, is 0.02 W·m^{-1}·K^{-1} at room temperature [112]. The thermal conductivity of the powders is calculated in Equation 2.11.

$$\lambda_P = \frac{k_i}{k_{air}} = \frac{k_{carbide}}{k_{air}}$$

Equation 2.11

The core conductivity coefficient, λ_C, takes into account radiation, fluid conduction, particle-particle contact conduction, and deformation factor of the powder, *B*, which is used to account for various shapes of particles in the fluid bed.

$$\lambda_C = \frac{2}{N}\left\{\frac{B(\lambda_P + \lambda_R - 1)}{N^2\lambda_G\lambda_P}\ln\left(\frac{\lambda_P + \lambda_R}{B\big(\lambda_G + (1-\lambda_G)(\lambda_P + \lambda_R)\big)}\right) + \frac{B+1}{2B}\left[\frac{\lambda_R}{\lambda_G} - B\left(1 + \frac{1-\lambda_G}{\lambda_G}\lambda_R\right)\right] - \frac{B-1}{N\lambda_G}\right\}$$

Equation 2.12

$$N = \frac{1}{\lambda_G}\left(1 + \frac{\lambda_R - B\lambda_G}{\lambda_P}\right) - B\left(\frac{1}{\lambda_G} - 1\right)\left(1 + \frac{\lambda_R}{\lambda_P}\right)$$

Equation 2.13

The deformation factor, *B*, can be generalized as: a sphere represents *B*=1 while *B*<1 depicts elongated needle-like particles and *B*>1 represents cylindrical shapes. The deformation factor can be calculated using the shape factor coefficient, C_f, of 1.40 from Table 2.6 due to the similar shapes of carbide powder and broken silica sand, the bed porosity, ψ, and the distribution function, $f(\zeta)$.

$$B = C_f \left[\frac{(1-\psi)}{\psi}\right]^{10/9} f(\zeta)$$

Equation 2.14

The bed porosity, ψ, is a function of the wire core carbide fraction and is calculated with Equation 2.15.

$$\psi = 1 - f_{c,core}$$

Equation 2.15

The distribution function, $f(\zeta)$, takes into account the various sizing and distribution of particles in the fluid bed. To simplify the calculations, the powder was assumed to be monodispersed. Therefore, Q_i=1 for a monodispersed distribution while d_i is the visual average of carbide powder from Figure 2.4-Figure 2.10 and summarized in Table 2.5.

$$f(\zeta) = 1 + 3\left(\frac{\Sigma \frac{Q_i}{d_i^2}}{\left(\Sigma \frac{Q_i}{d_i}\right)^2} - 1\right)^{0.5}$$

Equation 2.16

Using the above data and assumptions, the thermal conductivity of the carbide powder core for Consumables A-G were calculated, as summarized in Table 2.7.

Table 2.7: Thermal conductivity of the powder core, k_{powder}, for Consumables A-G at 295K.

	Consumable						
	A	**B**	**C**	**D**	**E**	**F**	**G**
$d\ (m)$	0.00007	0.00005	0.00010	0.00010	0.00007	0.00007	0.00010
B	1.530	1.830	1.830	1.750	1.464	1.600	1.172
ψ	0.48	0.44	0.44	0.45	0.49	0.47	0.54
φ	0.001	0.001	0.001	0.001	0.001	0.001	0.001
N	1	1	1	1	1	1	1
λ_p	4200	4200	4200	4200	4200	4200	4200
λ_c	23.175	26.679	26.664	25.736	22.385	23.998	18.838
λ_G	1	1	1	1	1	1	1
λ_R	0.0167	0.0117	0.0233	0.0233	0.0163	0.0163	0.0233
$f(\zeta)$	1	1	1	1	1	1	1
λ_{2P}	20.005	23.341	23.331	22.443	19.257	20.785	15.938
$k_{powder}\ (W \cdot m^{-1} \cdot K^{-1})$	0.400	0.467	0.467	0.449	0.385	0.416	0.319

The thermal conductivity of the tungsten carbide powders is very low and as such, may not satisfy the axisymmetric assumption of the proposed hot-wire electrode extension model. Calculation of the characteristic distance from the electrical contact points to homogeneous cross sectional temperature, x, will provide insight into the temperature distribution of the wire. Figure 2.12 depicts a generalized schematic of the heat flow through the tubular Ni-WC wire after passing through the electrical contact point.

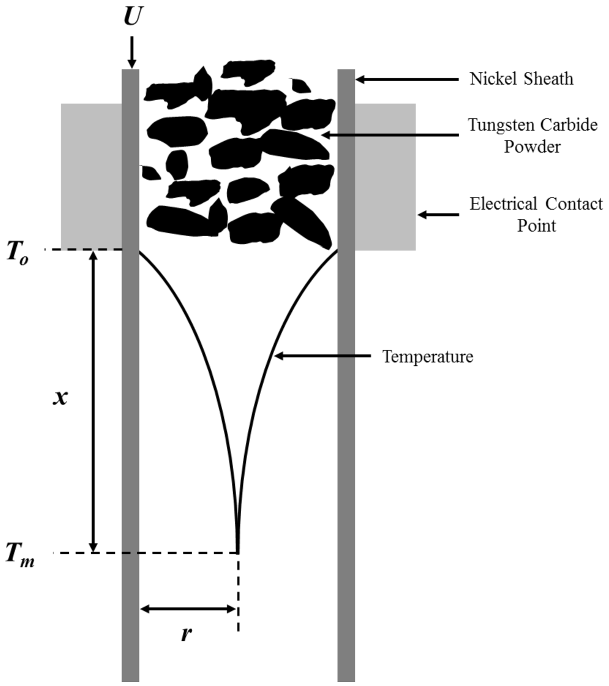

Figure 2.12: Schematic of heat flow through a tubular Ni-WC wire cross section.

Calculation of the distance x following the electrical contact point can be completed using Equation 2.17.

$$r = 2\sqrt{\alpha t} = 2\sqrt{\alpha \frac{x}{U}}$$

$$x = \frac{r^2 U}{4\alpha}$$

Equation 2.17

Where U is the wire feed speed of the hot-wire, r is the radius of the inner powder core of the tubular consumable, and α is the thermal diffusivity of the powders, which can be approximated with Equation 2.18. The powders were assumed to be entirely comprised of tungsten carbide based on the previous wire and powder characterization.

$$\alpha = \frac{k}{\rho C_p} \approx \frac{k_{powder}}{f_{c,core}^2 \rho_C C_{p_{WC}}} \approx \frac{k_{powder}}{f_{c,core}^2 \left(\frac{H_{WC}^m - H_{WC}^o}{T_m - T_o} \right)}$$

Equation 2.18

Where k_{powder} is summarized in Table 2.7, $f_{c,core}$ is the fraction of carbides in the tubular wire core and summarized in Figure 2.3, and the volumetric enthalpy of tungsten carbide is calculated from ThermoCalc and summarized in Table 3.7. The temperature boundary conditions were observed between an initial temperature, T_o, of 200 ^{o}C and the melting temperature of the pure nickel sheath, T_m, of 1455 ^{o}C.

A 1.6mm nominal OD Ni-WC wire has an inner radius, r, of ~0.6 mm and an $f_{c,core}$ of ~0.5. Typical hot-wire Ni-WC wire feed speeds used in this thesis are 0.05 $m \cdot s^{-1}$. Using Equations 2.17 and 2.18, the distance after the contact tip when the wire exhibits a uniform temperature through its cross section is approximately 9 mm. Typical hot-wire electrode extensions utilized in this thesis range from 65-70 mm. As a result, the proposed axisymmetric hot-wire electrode extension model is valid as the electrode exhibits a uniform temperature cross section for a large portion of the electrode extensions utilized in this study.

2.5. Electrical Resistivity of Welding Consumables

2.5.1. Introduction

The hot-wire electrode extension model proposed in Chapter 3 utilizes two important material specific properties: volumetric enthalpy and resistivity. Electrical resistivity data in literature is limited for welding consumables which often have different alloy compositions compared to the bulk base materials. Additionally, the temperature ranges found in literature often do not extend to the semi-solid temperature of the alloy. This section will focus on the fundamentals of measuring the electrical resistivity for steel, stainless steel, and tubular Ni-WC consumables from room temperature to near-melting temperature.

2.5.2. Basics of Electrical Resistivity

Electrical resistance is the resistance to movement of electrons through a material and is characteristic of the material composition, temperature, and to some extent the dislocation density from cold working [113]–[115]. The electrical conductivity of a material is related to its electron band structure and the arrangement of electrons within the valence shells. For a metal to be conductive, an electron must be excited to an energy state higher than the Fermi energy of the material. An applied electric field in metals often easily overcomes the Fermi energy and electrons can move freely to empty conductive bands. The now-free electrons will move in a direction opposite to the applied electric field. In a perfect crystal lattice, the electrons are not scattered and the electric current will continuously increases with time. This is often not observed in materials due to a competing frictional force that results from impurities, dislocations, lattice defects, thermal atom vibrations, and defects [115]. In metals, electrical resistivity of the alloy is the sum of contributions from thermal vibrations, impurities, and plastic deformation. The contribution of each term will vary with the alloy and temperature range of study. A literature study for various low alloy and carbon steels, austenitic stainless steels, and pure nickel was conducted and is included in subsequent sections.

The electrical properties of solid materials can be expressed by Ohm's Law which relates current, I, and voltage, V, to the material's resistance, R, shown in Equation 2.19.

$$R = \frac{V}{I}$$

Equation 2.19

Resistance is dependent on the specimen geometry and is not easily expressed as a universal material property. Resistivity, a function of resistance and expressed in Ω·m, is a function of the specimen cross sectional area, A, and length, l. Rearranging Equation 2.19, we obtain the expression for resistivity, ρ', shown in Equation 2.20.

$$\rho' = \frac{VA}{Il}$$

Equation 2.20

This expression is valid for solid components however additional considerations must be made for multi-component systems such as tubular Ni-WC consumables.

Tubular consumables can be viewed as parallel resistors with both the nickel sheath and powder core capable of carrying the welding current. The total resistance of the tubular wire can be given by Equation 2.21.

$$R = \left(\frac{1}{R_S} + \frac{1}{R_P}\right)^{-1}$$

Equation 2.21

Where R is the effective resistance of the wire, R_S is the resistance of the nickel sheath, and R_P is the resistance of the powder core. The resistance of powders are historically very high compared to a solid metal and the electrical conductivity of ceramics is much lower than the metallic nickel sheath. The tungsten carbide powder core will therefore exhibit a very high resistance and the powder component of Equation 2.21 can be assumed to be infinite. Expressing Equation 2.21 as a function of resistivity, we obtain Equation 2.22.

$$\rho' = \frac{VA_S}{Il}$$

Equation 2.22

High temperature electrical resistivity, while not readily available for some alloys, can be approximated by the Wiedemann-Franz Law [116]. The Wiedemann-Franz Law relates the thermal conductivity of the material to the electrical conductivity using Equation 2.23.

$$\frac{k}{\sigma} = LT$$

Equation 2.23

Where k is the material's thermal conductivity ($W \cdot m^{-1} \cdot k^{-1}$), L is the Lorenz number of the alloy, T depicts the temperature, and σ is the electrical conductivity of the alloy ($\Omega^{-1} \cdot m^{-1}$). Electrical conductivity is the reciprocal of electrical resistivity, denoted by ρ' in this thesis. The Lorenz number is available for a number of material and temperature ranges [117]. For the purpose of any subsequent calculations from literature data, a Lorenz number of 2.44×10^{-8} $W \cdot \Omega \cdot K^{-2}$ is used.

2.5.3. Furnace Heating Method

The furnace heating method is a simple experimental setup utilizing coiled lengths of wire inside a high temperature furnace. Experimental determination of the resistivity of Consumables A-D were carried out by coiling a set length (~1 m) of wire inside a chamber furnace and separating the wires by layers of Fibrefrax furnace insulation to prevent wire contact and short-circuits. The tail ends of the coiled wires were placed at the edge of the furnace door joint to allow the constant current power supply to be attached via alligator clips. The constant current power supply was set to provide 5 A while measuring the voltage drop as the furnace temperature was elevated from room temperature to approximately 1400 K. To monitor the furnace temperature, a K-type thermocouple was placed inside the furnace and the temperature was allowed to stabilize 5 minutes before voltage measurements were taken to ensure homogeneous temperature throughout. In order to ensure experimental accuracy, a standard of 1.14 mm (0.045 in.) solid ER310 stainless steel wire was coiled inside the furnace for comparison against tabulated resistivity data. The voltage drop was measured approximately every 50 ^{o}C through the temperature range studied. The experimental setup can be seen in Figure 2.13 and Appendix 4 contains the raw data.

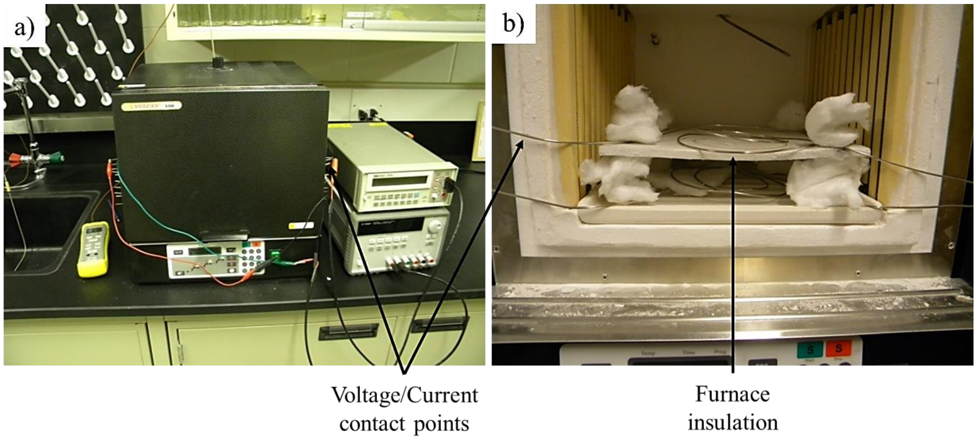

Figure 2.13: Furnace heating method experimental setup for measuring electrical resistivity of welding consumables.

Few repetitions of the tests were completed due to intermittent contact between wires during the testing, attributed to thermal expansion. Resistivity for the

ER310 stainless steel was calculated using Equation 2.18. Analysis of the standardized ER310 stainless steel resistivity revealed a good correlation with values obtained from literature, shown in Figure 2.14.

Analysis of the furnace heating method for the tubular Ni-WC Consumables A-D showed a good correlation with tabulated pure nickel electrical resistivity's, shown in Figure 2.15. Only a single test for each consumable had valid data throughout the temperature range that was devoid of intermittent short-circuits, potentially resulting in the statistical spread in resistivity between Consumables A-D. Due to the low success rate of the furnace heating method for measuring electrical resistivity, the Joule heating method outlined in the subsequent section was utilized.

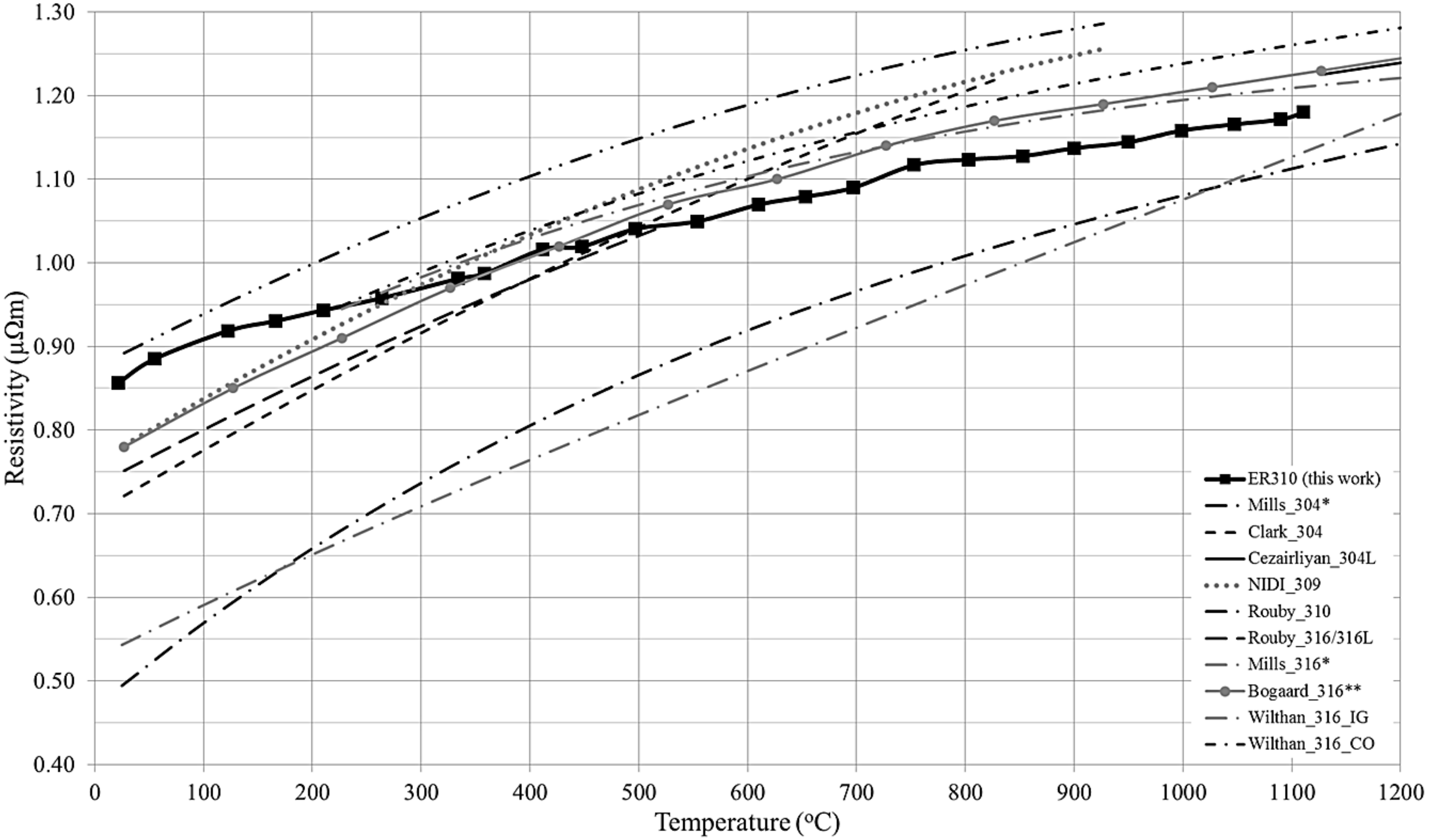

Figure 2.14: Electrical resistivity of ER310 stainless steel wire with comparisons to literature [118]–[124]. *: calculated from the Wiedemann-Franz Law, **: determined from graph as no data table or formula was provided.

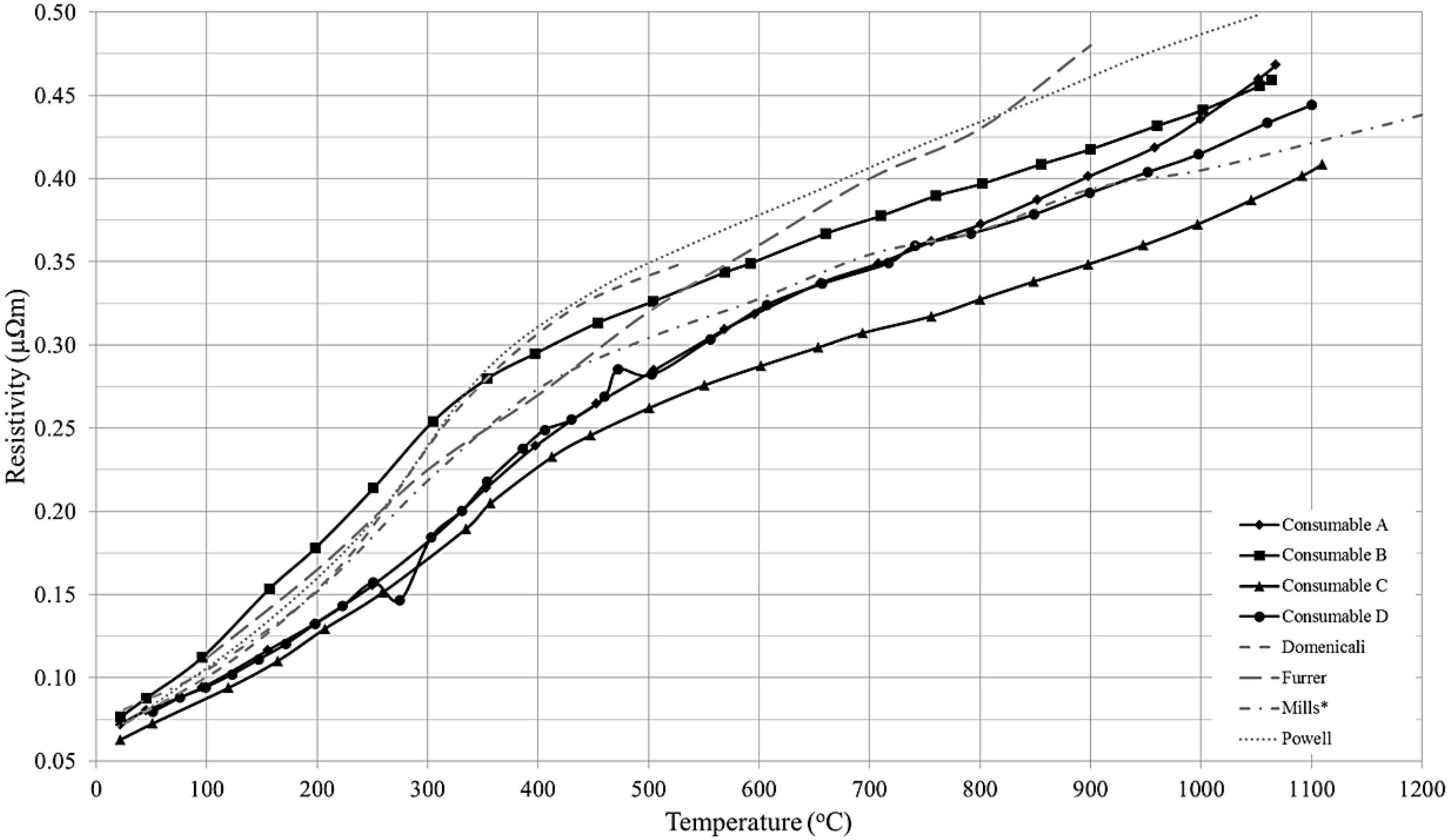

Figure 2.15: Electrical resistivity of Consumables A-D and compared to pure Ni literature [113], [121], [125], [126]. *: calculated from the Wiedemann-Franz Law.

2.5.4. Joule Heating Method

The Joule heating method discussed herein was designed to accommodate a variety of solid and tubular wires and provides sufficient flexibility to measure the electrical resistivity of many welding consumables. It utilizes the 4 point measurement system with current and voltage measurements synchronized with four K-type thermocouples, depicted in Figure 2.16. The four 0.25 mm thermocouples are spot welded to the wire surface at known intervals using a capacitor dump spot welder. Special care is taken to ensure the Alumel and Chromel wires are well bonded to the welding consumables and are not contacting each other away from the consumable surface. A 50 A current shunt was used to measure the current passing through the consumable from a 40 A, 10 V DC power supply. Electrical contact between the DC power supply and the wire consumables was accomplished with high current rated screw terminals. The voltage drop was collected with screw terminals just inside power supply/wire screw terminals. The entire wire extension including thermocouples and screw terminals is surrounded by high temperature Fibrefrax furnace insulation to minimize heat losses.

The voltage drop was measured directly by a National Instruments 6351X USB data acquisition module that was operated via LabView software. The data acquisition module does not natively support thermocouple measurements. Cold junctions (Texas Instruments LM35) were added to the data acquisition module thermocouple channels to provide an accurate reference for the attached 4 thermocouples. All current, voltage, and temperature data was captured and synchronized at 10 Hz by the data acquisition module. The nominal outside diameter for solid wires was measured with calipers and the wire extension between the voltage contact points was recorded for each test. Wire extensions ranged from 28.5-30 cm during all testing. The nickel sheath areas summarized in Figure 2.1 were utilized for the tubular Ni-WC consumables. While the thermocouple voltages were collected at temperatures higher than 1200 ^{o}C, they are not included in the following discussions. K-type thermocouples have a guaranteed accuracy of the voltage-temperature conversion polynomial up to

1200 °C. Future work will create an accurate voltage-temperature conversion polynomial at temperatures greater than 1200 °C so the relatively inexpensive K-type thermocouples can be utilized. For the intents of this thesis, the four thermocouple measurements were averaged along the wire extension.

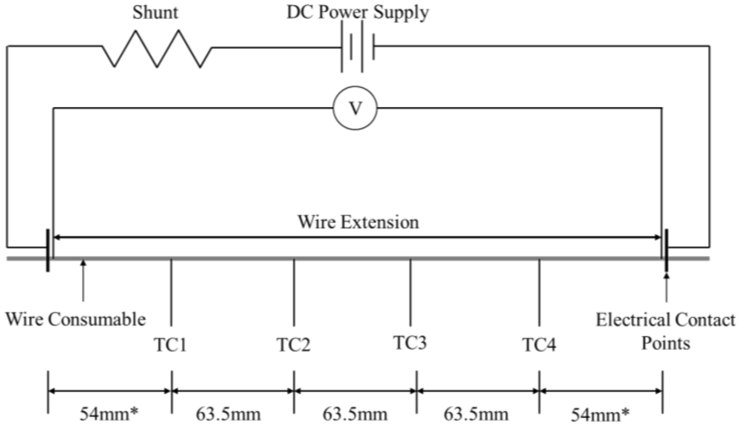

Figure 2.16: 4-point measurement system for Joule heating electrical resistivity tests. Values denoted by * vary slightly between experimental runs.

Standardization of the proposed Joule heating method was completed using AISI 1008 steel wire and comparing to literature values. The AISI 1008 wire utilized featured a measured 1.17 mm outside diameter and a black oxide finish. Nine tests were completed using two heating profiles: a high constant current (CC) and a stepwise current (SWC) during which the current was increased as the wire reached elevated temperatures, graphically depicted in Figure 2.17 below. The difference in heating rate was analyzed to determine the effect of time and temperature on the ferrite-austenite phase transformation characteristic of carbon steel.

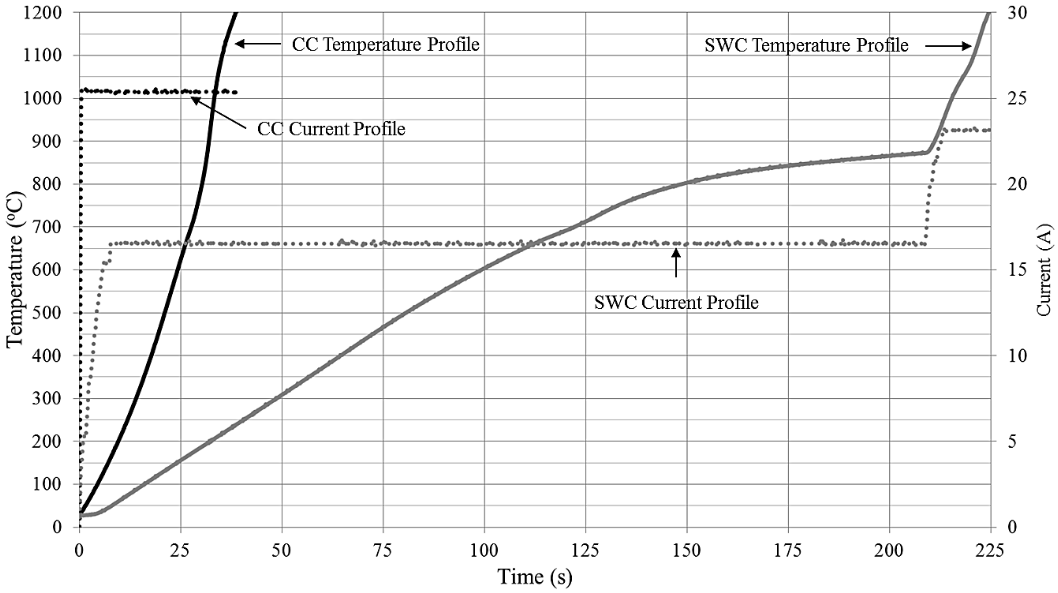

Figure 2.17: Current and temperature profiles for CC and SWC heating of AISI 1008 steel wire.

The results of the experimental setup validation using AISI 1008 steel is shown in Figure 2.18 where four of the nine test runs are compared to literature. Analysis of the measured AISI 1008 resistivity indicated excellent correlations at low and high temperatures with literature. The intermediate temperature region between 600-800 ^{o}C depicts some deviation from the values reported in literature. This can be attributed to the decomposition of ferrite to austenite as a function of time. The constant current (CC) tests exhibited a characteristic ferrite decomposition lag compared to the stepwise current (SWC) tests and literature values. The rapidly increasing temperature did not allow sufficient time for phase equilibrium to be achieved, resulting in a higher resistivity at lower temperatures. Analysis of the AISI 1008 tests and literature data indicates that ferrite has a greater resistivity than austenite, based on the slopes of their respective phase stability regions. Slow heating the wire with variable current provides more time for the ferrite-austenite transformation, leading to the lower resistivity observed in Figure 2.18. The good correlation with literature validates the proposed Joule heating methodology for obtaining high temperature electrical resistivity data for solid and tubular welding consumables.

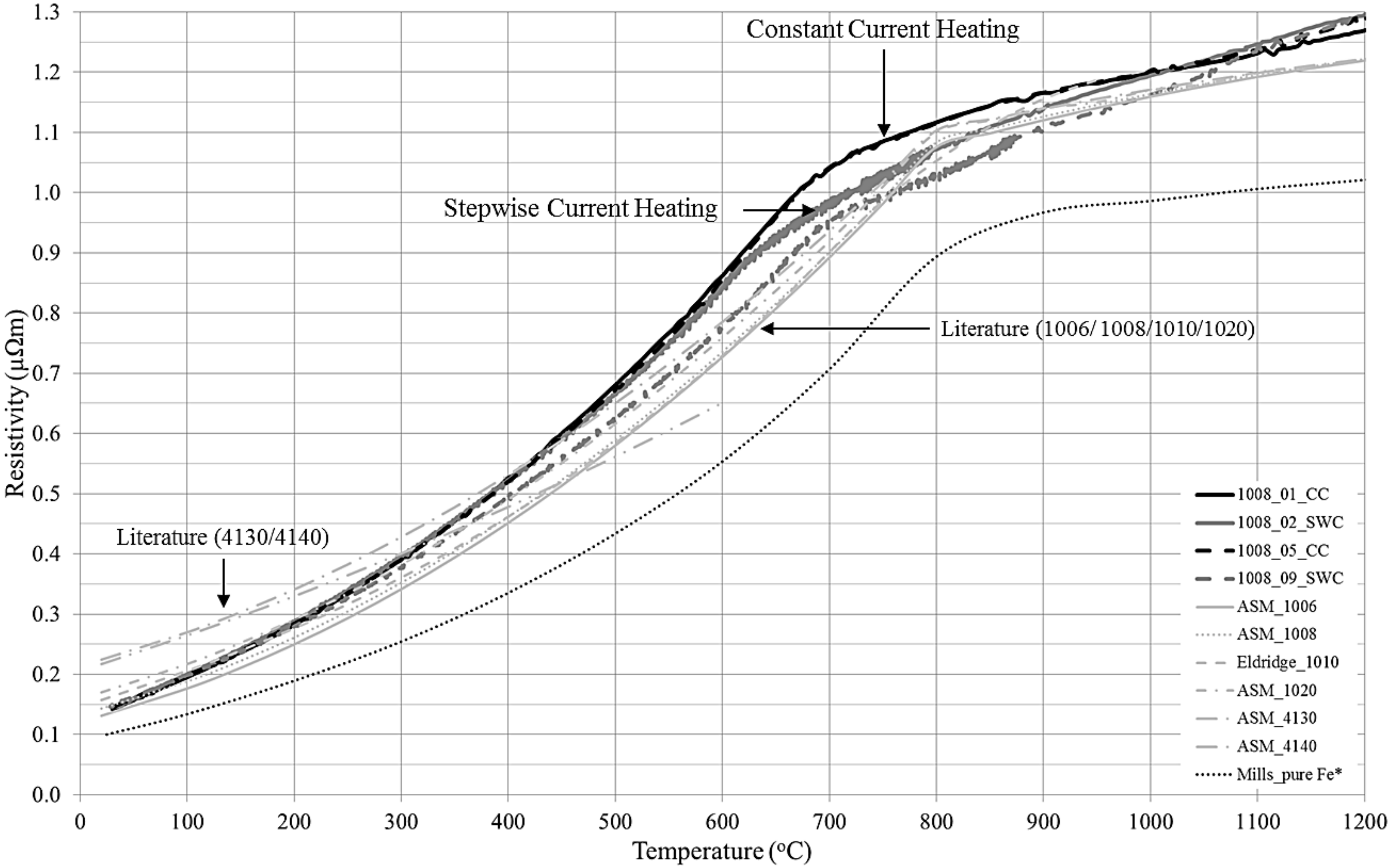

Figure 2.18: Comparison of the electrical resistivity of AISI 1008 steel using the Joule heating method to literature [121], [127]–[129].

Following the good correlation with literature using AISI 1008 steel, the effect of annealing and CC/SWC heating was investigated using solid AWS A5.9 ER309LSi (Lincoln Blue Max 309LSi, 0.045 in. nominal OD) austenitic stainless steel and AWS A5.18 ER70S-6 (Lincoln SuperArc L-56, 0.045 in. nominal OD) steel wire. Full annealing of the ER309LSi wire was completed at 1060 ^{o}C for 5 minutes while a heat treatment procedure of 860 ^{o}C for 5 minutes was used for the ER70S-6 wire [130]. A 0.5 wt%C carbon equivalent was calculated for the ER70S-6 heat treatment parameters based on the nominal wire composition. All wire sections were annealed in an argon-shielded furnace and air-cooled.

A distinct increase in resistivity was observed throughout the temperature range for both steel and stainless steel welding consumables compared to literature. Comparison of the ER309LSi wire to literature data for austenitic stainless steel grades 304, 304L, 309, 310, 316, and 316L was completed in Figure 2.19. Analysis of the ER309LSi data revealed no observable differences between the effect of annealing and stepwise current heating on the electrical resistivity across nine tests. The lack of a phase change in the austenitic wire meant that the heating rate had no effect from room temperature to 1200 ^{o}C. The welding wire resistivity was consistently greater across the temperature range studied than literature. Study of the results of Figure 2.19 showed the lack of change between the as-drawn and fully annealed wires. This indicates that cold-working has a very small secondary effect on the electrical resistivity. Reeves studied the effect of cold working on austenitic grade 316 stainless steel and found that up to 50% cold work had a 3% increase on room temperature electrical resistivity [114]. The difference in electrical resistivity observed in Figure 2.19 can then be traced to chemical composition being the dominant factor in altering resistivity.

Full annealing of the ER70S-6 had no observable effect on the resistivity of ER70S-6 steel wire, shown in Figure 2.20. The ER70S-6 wire exhibited the same ferrite-austenite shift in the 600-800 ^{o}C temperature range previously observed and discussed with the AISI 1008 wire. The effect of chemical composition on resistivity was distinctly observed as the welding consumable exhibited much higher resistivity than the basic C-Mn steels found in literature. ER70S-6 wire is more alloyed than the basic C-Mn AISI 1008, potentially increasing the resistivity of the alloy. This effect will be discussed in more detail in the following section.

Following the validation of the proposed Joule heating experimental apparatus with AISI 1008 steel and studying the effect of heat treatment and heating rate on the resistivity of steel and austenitic stainless steel welding consumables, tubular Ni-WC consumables were studied. Consumable D was utilized during hot-wire GMAW in this thesis for its thin nickel sheath, high 47% $f_{c,max}$, and dissolution resistant WC-coated eutectoid tungsten carbides. The wires were left in their as-drawn condition and stepwise current heating was employed. Equation 2.20 was used in conjunction with the nickel sheath area summarized in Figure 2.1. Six tests were completed and compared to pure nickel values from literature, summarized in Figure 2.21. The electrical resistivity of Consumable D showed a good correlation with tabulated pure nickel. This corresponds with predicted results based on the ICP-verified pure Ni sheath and the measured sheath area.

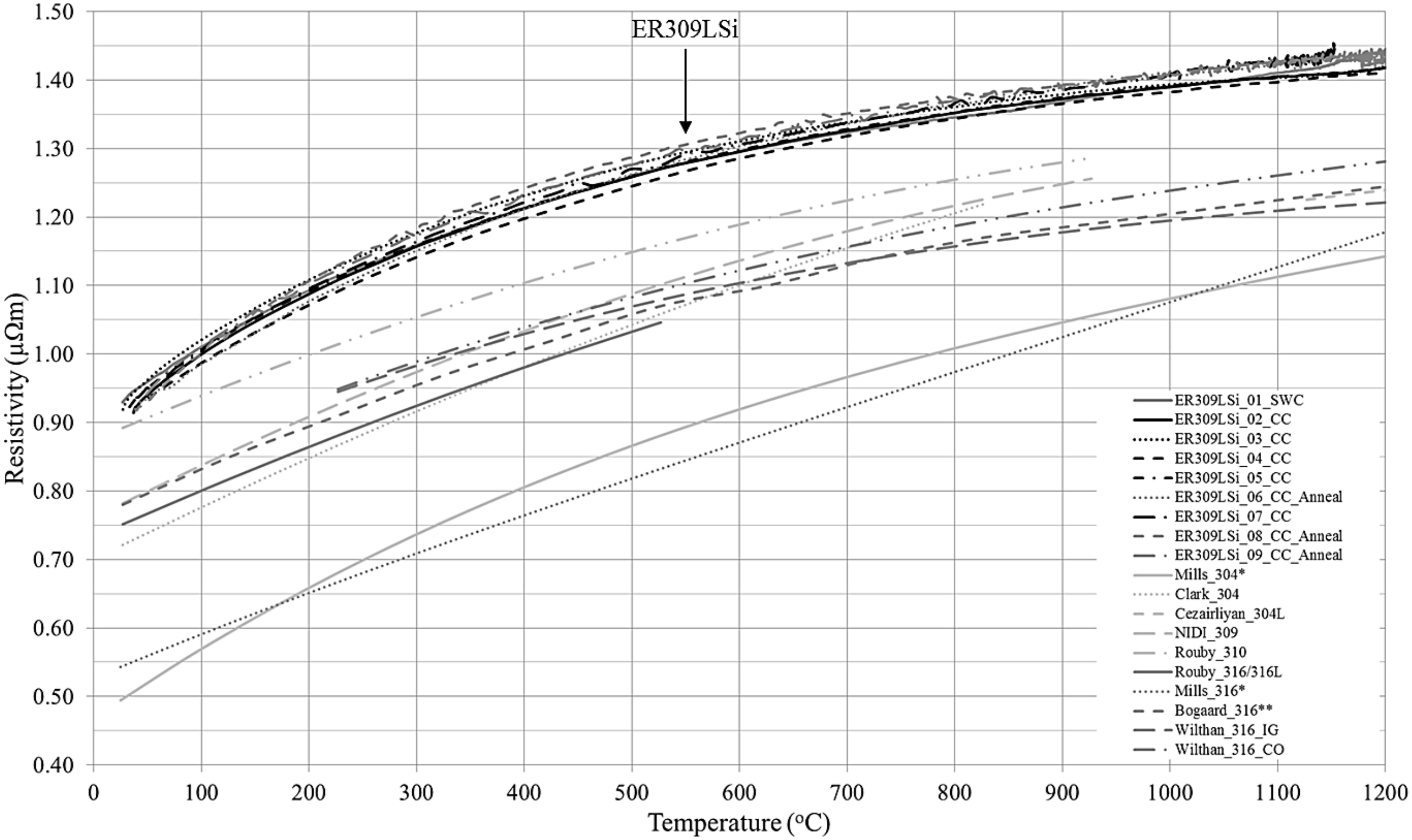

Figure 2.19: Electrical resistivity of ER309LSi stainless steel wire (Lincoln Blue Max 309LSi, 0.045 in. nominal OD) with comparisons to literature [118]–[124]. *: calculated from the Wiedemann-Franz Law, **: determined from graph as no data table or formula was provided.

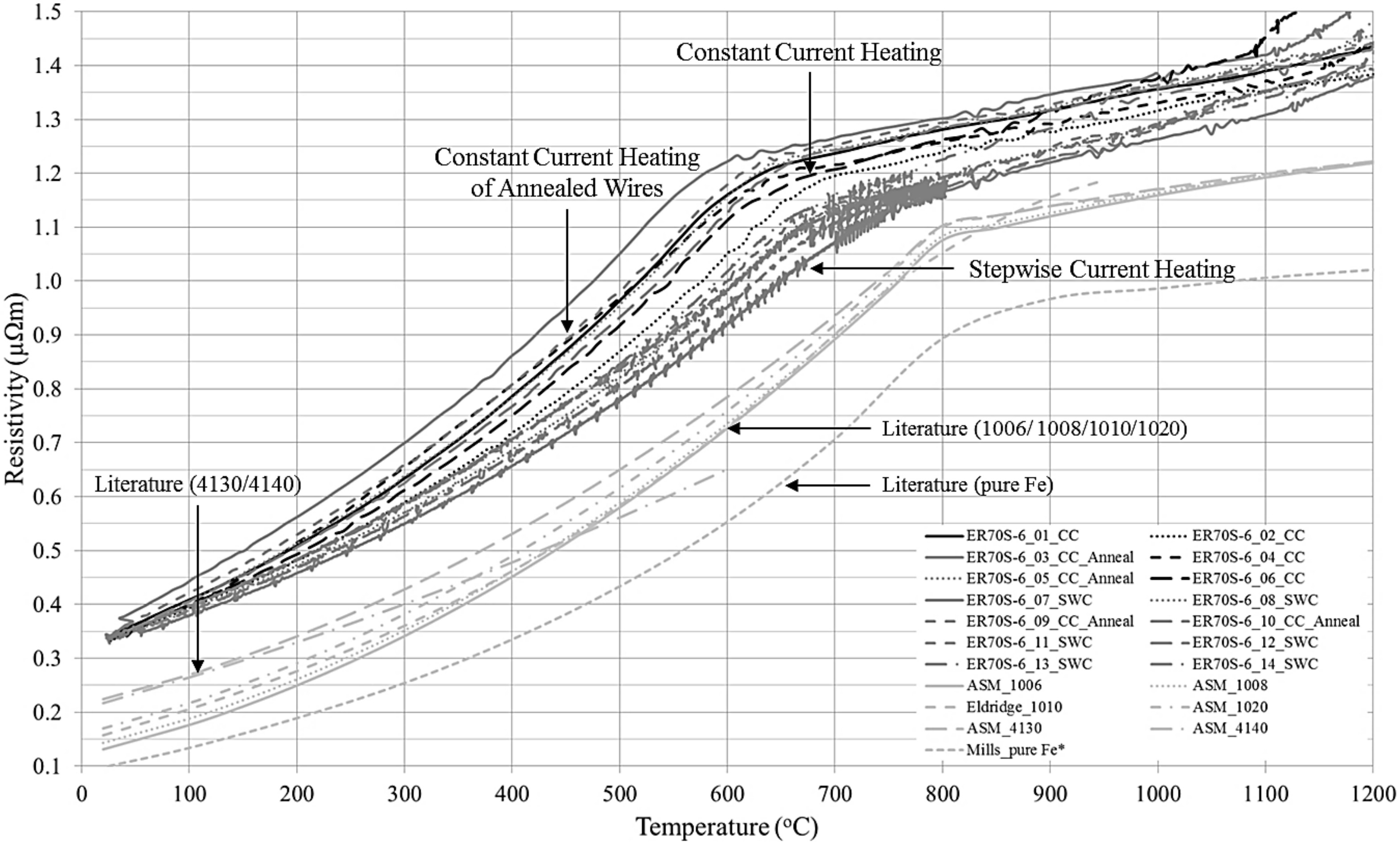

Figure 2.20: Electrical resistivity of AWS A5.18 ER70S-6 steel GMAW wire (Lincoln SuperArc L-56, 0.045 in. nominal OD) with comparisons to literature [121], [127]–[129]. *: calculated from the Wiedemann-Franz Law.

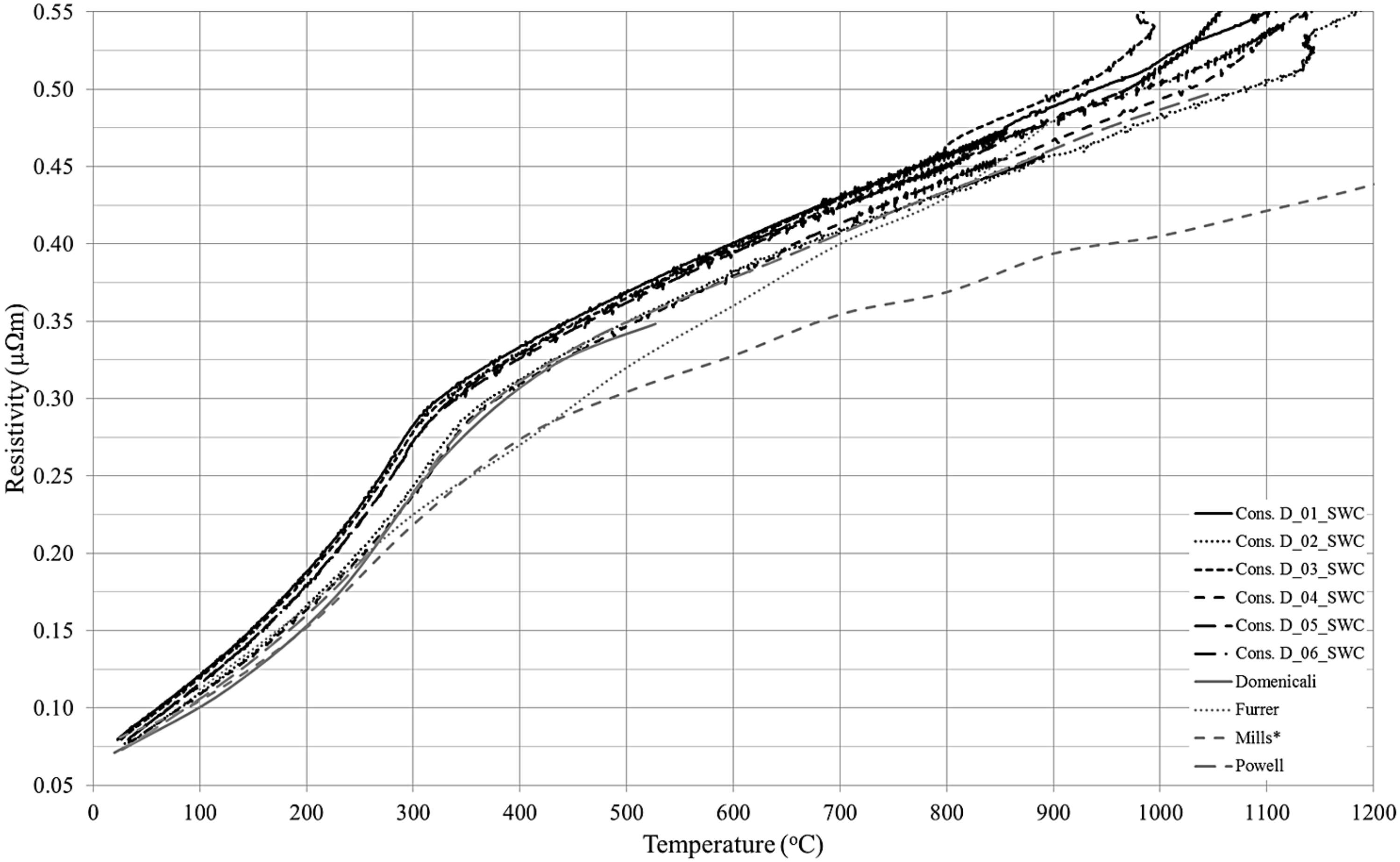

Figure 2.21: Electrical resistivity for Consumable D with comparisons to pure nickel literature [113], [121], [125], [126]. *: calculated from the Wiedemann-Franz Law.

2.5.5. Electrical Resistivity Discussion

Measurement of the high temperature electrical resistivity was conducted using a furnace heating and Joule heating method, with a specific focus on welding consumables. Comparison of common steel and stainless steel welding consumables to frequently used literature values consistently resulted in a greater resistivity from room temperature to 1200 ^{o}C. The effect of the cold work from the drawing operation during manufacturing was shown to be insignificant through fully annealing stainless steel and steel welding wires. The dominant factor in altering the resistivity of welding consumables can therefore be directly related to the chemical composition of the wire. Table 2.8 below contains a summary of the chemical composition of the literature materials and of the ER309LSi, ER310, and ER70S-6 consumables.

Welding consumables are often alloyed different from base materials to ensure the weld metal meets strength, hardness, corrosion, and toughness requirements. The effect of individual alloying elements on the resistivity of pure Fe is summarized in Figure 2.22. If we consider the composition of AISI 1008 C-Mn steel, the room temperature resistivity will increase ~0.12 μΩm over pure Fe, corresponding with the literature resistivity for AISI 1008. If we consider the higher Mn and Si contents of the ER70S-6 welding wire, a ~0.4 μΩm increase in resistivity is predicted. While the predicted resistivity of ER70S-6 wire using Figure 2.22 is greater than the measured value, the individual element interaction and cumulative increase in resistivity is unknown. The effect of chemical composition was also observed in the austenitic stainless steel welding consumables.

Table 2.8: Summary of base material and welding consumable nominal compositions of the materials discussed in Chapter 2.5. Prefix ER denotes welding electrode.

	Nominal Composition (wt%, Fe balance)						
Material	**C**	**Mn**	**Si**	**Cr**	**Ni**	**Mo**	**V**
AISI 1006	<0.08	0.25-0.4	-	-	-	-	-
AISI 1008	<0.1	0.3-0.5	-	-	-	-	-
AISI 1010	0.08-0.13	0.3-0.6	-	-	-	-	-
AISI 1020	0.18-0.23	0.3-0.6	-	-	-	-	-
AISI 4130	0.28-0.33	0.4-0.6	0.15-0.3	0.8-1.1	-	0.15-0.25	-
AISI 4140	0.38-0.43	0.75-1.0	0.15-0.3	0.8-1.1	-	0.15-0.25	-
Grade 304	0.08	2.0	0.75	18-20	8-10.5	-	-
Grade 304L	0.03	2.0	0.75	18-20	8-12	-	-
Grade 309	0.08	2.0	0.75	22-24	12-15	-	-
Grade 310	0.08	2.0	1.50	24-26	19-22	-	-
Grade 316	0.08	2.0	0.75	16-18	10-14	2-3	-
Grade 316L	0.03	2.0	0.75	18-18	10-14	2-3	-
ER309LSi	<0-03	1-2.5	0.65-1.0	23-25	12-14	<0.75	-
ER310	0.08-0.15	1-2.5	0.3-0.65	25-28	20-22.5	<0.75	-
ER70S-6	0.06-0.15	1.4-1.85	0.8-1.15	<0.15	<0.15	<0.15	<0.03

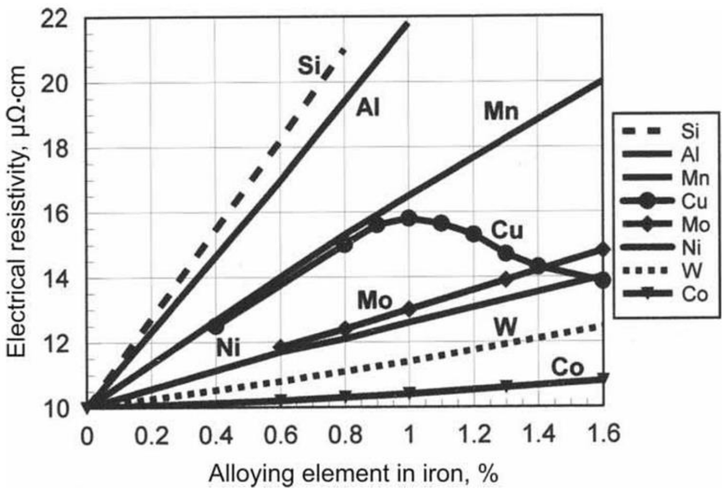

Figure 2.22: Effect of individual alloying elements on resistivity in an iron matrix [113].

Analysis of the tubular Ni-WC Consumable D resistivity at high temperature showed discrepancies between each test and a rapid increase in resistivity around 1000-1200 ^{o}C, depicted in Figure 2.21 and Figure 3.5. The slow heating rate of the stepwise current heating and the powder thermal conductivity (Chapter 2.4) meant that any low melting point powders will melt. This will form a liquid layer between the nickel sheath and the tungsten carbide particles. The effective current carrying area will increase as the liquid film will now conduct a portion of the current and decreasing the resistivity. Liquids however have a higher resistivity than solids. In addition, the liquid layer will not be comprised of pure nickel but rather a combination of alloying/arc stabilizing elements specific to the manufacturer. The liquid layer and relatively long durations (~1-1.5 min) at high temperature may overcome the low heat of formation of tungsten carbide, increasing the tungsten concentration in the liquid. This will also decrease the volume of non-conducting ceramic tungsten carbide particles, altering the resistivity of the wire. The formation of a liquid within the wire powder is documented in Figure 4.9 and Figure 4.10 where the hot-wire electrode was frozen in the weld pool after welding was stopped.

The literature electrical resistivity values for steel, stainless steel, and nickel are summarized in Figure 2.19 to Figure 2.21. While much literature is available for low temperatures, namely the 0-300 K range, and for pure or specialized materials, little data is available at high temperatures for the materials studied in this thesis. As a result, some resistivity's were calculated using the Wiedemann-Franz law. In all cases, the Wiedemann-Franz calculated resistivity's were lower than the other measured literature sources. This deviation was also observed by Basak et al. during high temperature electrical resistivity measurements of Inconel 718, Ti-6Al-4V, and CF8M stainless steel [131]. Careful consideration should be given when considering electrical resistivity's calculated from the Wiedemann-Franz law as they may not be representative of the measured values.

In addition to the Wiedemann-Franz law discrepancies, there was an observed spread in the high temperature resistivity found in literature. This can be attributed to the variation in chemical composition of the individual literature sources, exemplified by the austenitic stainless steel literature data and the effect of individual elements shown in Figure 2.22. The literature values for pure nickel were observed to vary widely, despite being for a pure material. The reasons for the variations in resistivity sourced from literature are unclear. Of note, literature sources typically do not specify the number of tests performed or error (in both temperature and resistivity) for the data presented.

The physical dimensions for calculating the electrical resistivity were taken at room temperature. As the wires reach higher temperatures, they expand according to their characteristic coefficient of thermal expansion, altering the calculated resistivity. Wilthan et al. studied this effect in detail using grade 316 austenitic stainless steel [124]. The change of volume during heating led to a higher resistivity at elevated temperatures, shown in Figure 2.19 by the labels Wilthan_316_IG (initial geometry) and Wilthan_316_CO (corrected geometry accounting for thermal expansion). Accounting for the volume change resulted in approximately 3% increase in resistivity compared to room temperature dimensions. For this reason, the dimensional volume change at high temperatures was neglected during the resistivity calculations of the studied wires.

The spot welding of the 4 thermocouples onto the wire surface did not induce a localized increase in resistivity, creating increased heating and eventual melting at the thermocouple location. In total, more than 75 sections of wire, including those contained within this thesis and other consumables not included here, were tested with the Joule heating test method. The wire was never recorded to have melted at the spot welded thermocouple locations across all consumables, in tubular or solid form. This points to a localized defect or compositional inhomogeneity creating a higher localized resistance at random intervals along the wire length than the 4 spot welded thermocouples. The localized inhomogeneity would increase the rate of heating and therefore cause eventual melting of the consumable.

2.6. Summary of Tubular Ni-WC Consumables

The calculation of the initial wire carbide volume fraction yielded surprising results as only Consumable C, D, and potentially G contain a maximum of 50% by volume of tungsten carbide prior to any loss mechanism that may occur during welding. The consumables which had a thick nickel sheath exhibited a drastic drop in the initial wire carbide fraction, making the sheath thickness a dominant factor in carbide volume fraction. Chemical analysis of the nickel sheath revealed that they are entirely comprised of nickel while the carbide and alloying powder analysis showed immense variability in the carbide size distribution and the amount of alloying elements. All manufacturers added forms of arc stabilizing agents such as F, Na, and K to increase the arc welding stability of the wires.

The approximation of the thermal conductivity of the powder core was completed to determine the role of the carbide powder in affecting the thermal distribution of the wire during welding. The thermal conductivity of the tungsten carbides powders is approximately 0.4 $W \cdot m^{-1} \cdot K^{-1}$ at 295 K. The distance from the electrical contact point to a homogenous temperature of a tubular Ni-WC wire was determined to be much less than the hot-wire electrode extension, satisfying the electrode extension model proposed in Chapter 3. The electrical resistivity of Consumable D was measured from room temperature to 1200 ^{o}C using a Joule heating method. The electrical resistivity of the Ni-sheathed tubular wires is in good agreement with pure Ni literature values.

3. Modelling the Hot-Wire Electrode Extension with GTAW and GMAW Leading Heat Sources

3.1. Introduction

The determination of the heat flux gradient along the electrode extension is necessary to control the welding process. Generally, most thermal welding electrode models are constructed around the Gas Metal Arc Welding (GMAW) process wherein the arc attaches to a molten droplet at the end of the wire. These models typically take into account the effect of Joule heating (I^2R) and conduction from the superheated molten droplet to the solid wire. The relatively short electrode extension in GMAW processes reduces the Joule heating contribution and conduction is primarily responsible for electrode melting. Development of a hot-wire specific model varies from existing GMAW models as it lacks a superheated molten droplet transferring energy to the wire. The hot-wire models need to include additional terms as the weld pool conducts heat to the end of the wire and the nearby welding arc impinges heat on the end or side of the wire.

Little published research is available for predicting melting along the electrode extension in the hot-wire welding process. Shinozaki et al. proposed an electrode extension temperature distribution model for the hot-wire GTA welding process using an incremental step method and temperature dependent material properties [15]–[17]. Shinozaki et al. was able to determine regions of adequate hot-wire current that provided sufficient preheating of the welding wire based on weld bead shape observations, shown in Figure 3.1.

Using a radiation thermometer, Shinozaki et al. were able to verify the model accuracy using a specialized hot-wire torch setup, seen in Figure 3.2. The machined reliefs in the ceramic guide tube allowed the radiation thermometer to gather temperature readings at specified distances from the electrical contact point. The measured temperature distribution is in good agreement with the calculated temperature distribution for mild steel, stainless steel, and titanium, with mild steel shown in Figure 3.1.

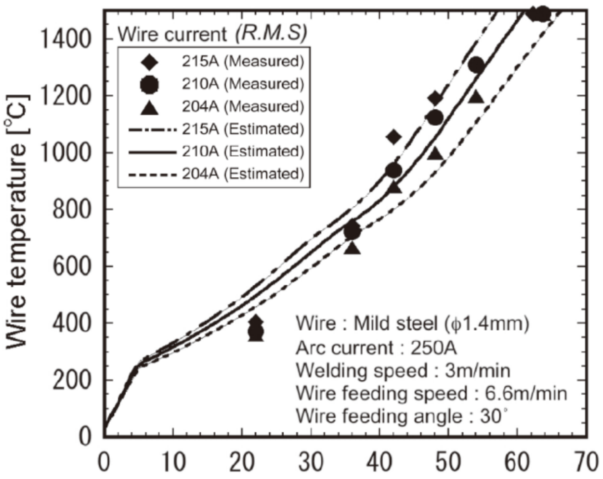

Figure 3.1: Measured and estimated hot-wire GTAW temperature distribution for solid mild steel wire, as observed and calculated by Shinozaki et al. [15]–[17].

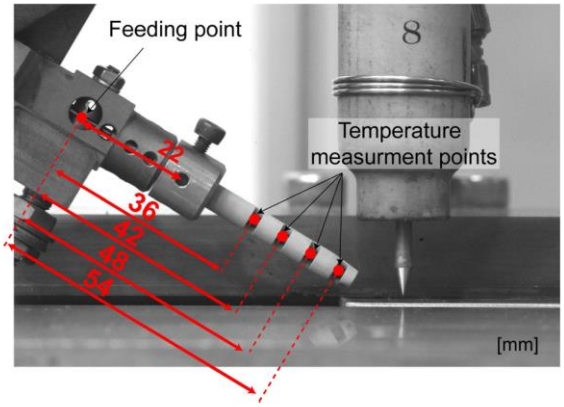

Figure 3.2: Hot-wire assisted GTAW setup with reliefs machined into ceramic guide tube for radiation thermometer measurement location for temperature distribution model verification [15]–[17].

3.2. Mathematical Model

Development of a model for hot-wire technology was based off of previous work done by Lehnhoff and Mendez in which the solid wire heat content distribution was analyzed for Gas Metal Arc Welding. This model deviates from conventional consumable electrode models as it accounts for temperature depending material property variations [132]. Figure 3.3 below is a modified schematic of the electrode extension depicted in Lehnhoff and Mendez and includes the enthalpy profile of the hot-wire. The following work is a modification of the Lehnhoff and Mendez model to account for the change in behaviour when using a tubular consumable.

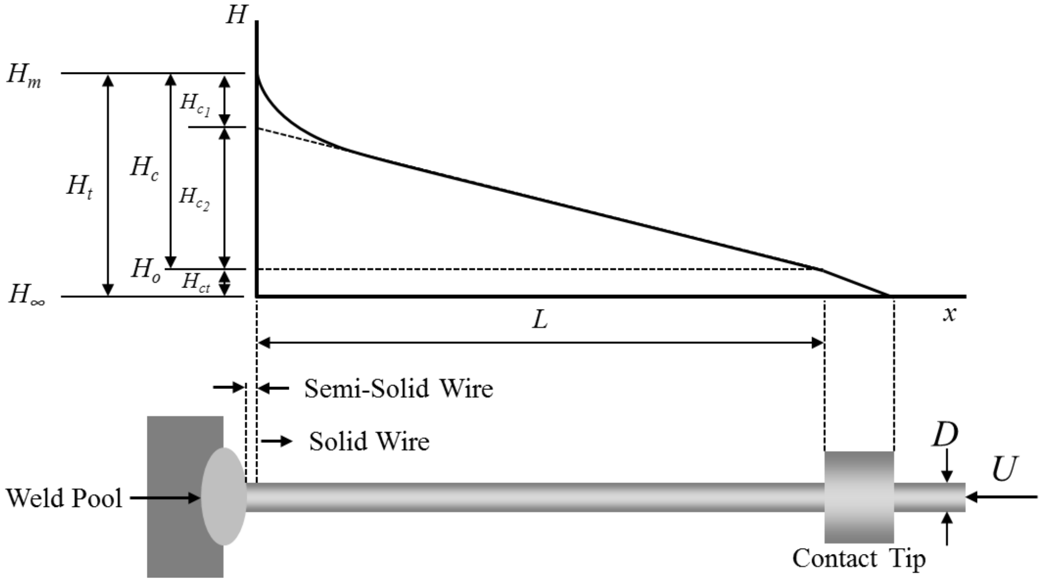

Figure 3.3: Hot-wire electrode extension schematic with corresponding enthalpy curve as a function of electrode length.

The best estimate of the heat from the end of the hot-wire can be given by Equation 3.1 below.

$$\hat{q}^{+} = \left(1 - \widehat{H_{c_2}^{+*}}\right) H_c U$$

Equation 3.1

Where $\widehat{H_{c_2}^{+*}}$ is the normalized improved estimation of the enthalpy increase in H_{c_2}, H_c is the difference in enthalpy from the contact tip to the melting temperature of the consumable, and U is the wire feed speed of the consumable. The enthalpy of the contact tip is approximated at 200 ^{o}C as a result of the contact resistance heating between the wire and electrical contact point, as was measured by Shinozaki et al [15]–[17]. Expanding we see that:

$$H_c = H_m - H_o$$

Equation 3.2

$$H_m = \sum \frac{m_i'}{\rho_i A_{eff}} H_i^m$$

Equation 3.3

$$H_o = \sum \frac{m_i'}{\rho_i A_{eff}} H_i^o$$

Equation 3.4

Where H_m is the volumetric enthalpy of the consumable at the melting temperature of nickel, H_o is the volumetric enthalpy of the consumable at room temperature, m_i' is the linear mass of component i, H_i^m is the enthalpy at the melting temperature of nickel of component i, H_i^o is the enthalpy at room temperature of component i, ρ_i is the density of i, and i is either tungsten carbide or nickel. The effective area, A_{eff}, is the cross sectional area if the wire is considered to be solid.

$$\widehat{H_{c_2}} = \frac{\rho_o' I^2 L}{A_{eff}^2 U}$$

Equation 3.5

The normalized improved estimation of the enthalpy increase in H_{c_2} can be defined as:

$$\widehat{H_{c_2}^{+*}} = 2\left[\frac{e^{\frac{d}{M_1}} - 1}{b\left(1 - e^{\frac{d}{M_1}}\right) + d\left(1 + e^{\frac{d}{M_1}}\right)}\right]$$

Equation 3.6

Where:

$$d = \sqrt{b^2 - 4a}$$

Equation 3.7

$$b = M_2 + 4M_3 = \frac{\Delta\rho_1'}{\rho_o'} + 4\frac{\Delta\rho_2'}{\rho_o'}$$

Equation 3.8

$$a = -4M_3 = -4\frac{\Delta\rho_2'}{\rho_o'}$$

Equation 3.9

$$M_1 = \frac{U H_c A_{eff}^2}{L \rho_o' I^2}$$

Equation 3.10

Where ρ'_o, ρ'_1, and ρ'_2 are electrical resistivity's that are described in Figure 3.4 and Equations 3.11 and 3.12 below. The wire current, I, is calculated using the RMS value using Equation 3.13 below.

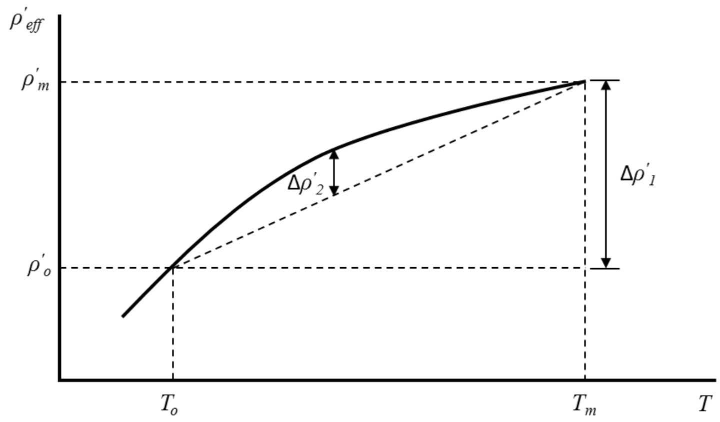

Figure 3.4: Generic electrical resistivity curve with ρ'_o, ρ'_1, and ρ'_2 from room temperature, T_o, to melting temperature, T_m.

Where:

$$\Delta\rho'_1 = \rho'_m - \rho'_o$$

Equation 3.11

$$\Delta\rho_2 = max\left\{\begin{matrix} max\left\{\rho' - \left[\rho'_o + \dfrac{\Delta\rho'_o}{H_C}(H - H_o)\right]\right\} \\ min\left\{\rho' - \left[\rho'_o + \dfrac{\Delta\rho'_o}{H_C}(H - H_o)\right]\right\} \end{matrix}\right\} whichever\ is\ greater\ in\ magnitude$$

Equation 3.12

The resistivity of Consumable D was measured from room temperature to 1200 ^{o}C and compared to that of pure nickel in Chapter 2. As a result of the comparison, the tubular wires exhibited the same trend and magnitude as pure nickel however insufficient data existed at the melting temperature of nickel. The resistivity at the melting temperature of pure nickel was extrapolated from the high temperature region of the conducted resistivity tests, indicated in Figure 3.5.

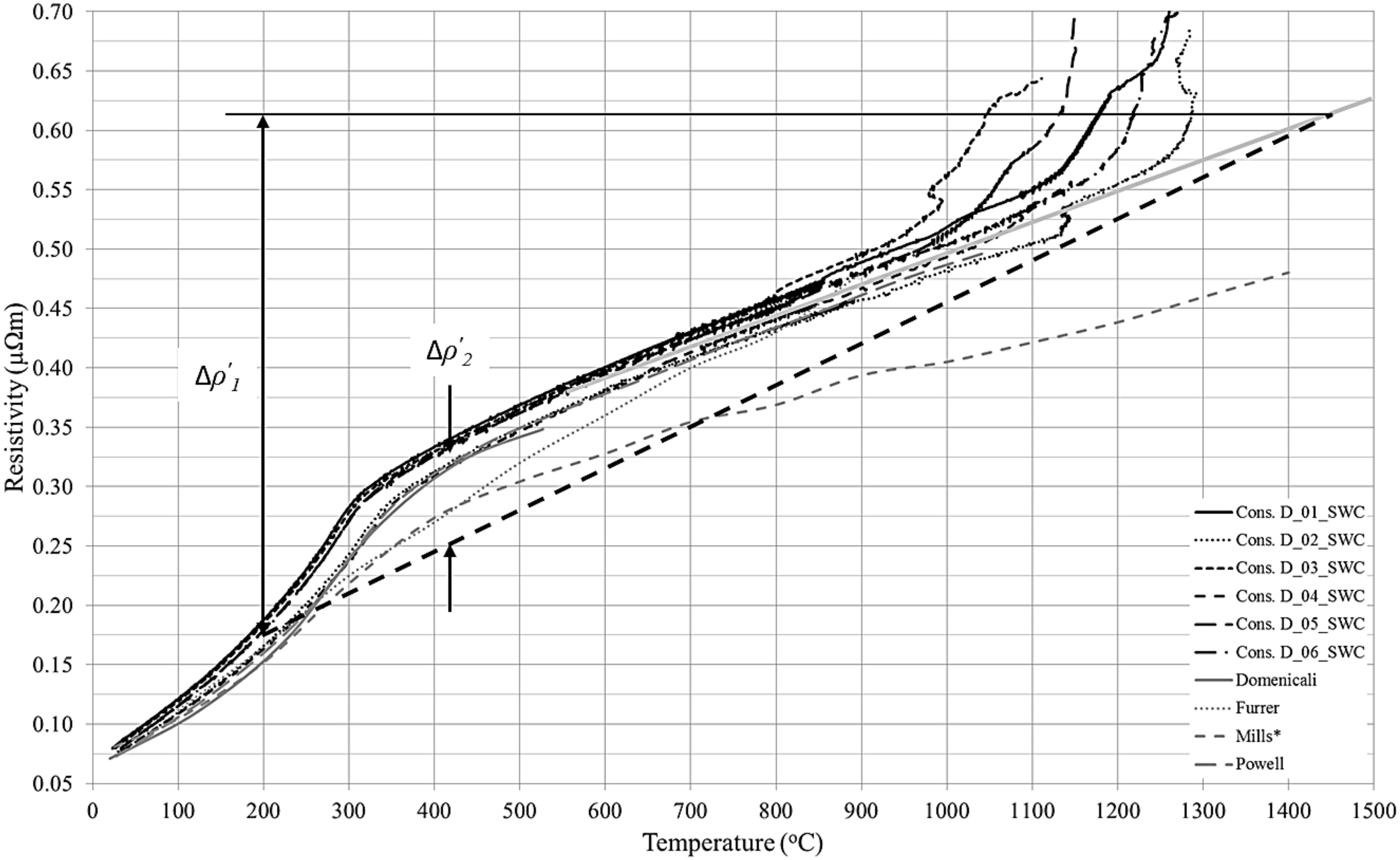

Figure 3.5: Resistivity of Consumable D with extrapolation to melting temperature of pure nickel.

The hot-wire power supply utilized in this thesis uses a pulsed current waveform to reduce the arc blow phenomenon when two strong magnetic fields are in proximity. In order to calculate the hot-wire current, the Root Mean Square of the wire current is calculated using Equation 3.13 below where i is the instantaneous current measurement recorded by data acquisition during welding.

$$I = \sqrt{\overline{\iota^2}}$$

Equation 3.13

The pulsed current of the hot-wire can create an unstable heat flux in portions of the wire as the time between current pulses or heating periods can allow the heat to dissipate and the wire will not achieve melting. Determination of a stable heating condition can be determined as functions of the wire feed speed, pulsing frequency, and thermal diffusivity.

$$D_p = \frac{U}{f} = \frac{50\, {}^{mm}/_{s}}{100\, Hz} = 0.5\, mm$$

Equation 3.14

Where D_p is the distance the wire has travelled between current pulses, U is the wire feed speed, and f is the pulsing frequency of the power supply. Based on the above calculation, the wire has travelled 0.5 mm between current pulses with a wire feed speed of 3 m·min^{-1} (120 ipm). Equation 3.15 below can be used to approximate the time necessary for the heat to diffuse between pulses.

$$t \approx \frac{{D_p}^2}{\propto} \approx \frac{(0.5\, mm)^2}{10^{-5}\, {}^{m^2}/_{s}} \approx 0.025s$$

Equation 3.15

Where t represents the time to completely diffuse the heat created from the current pulse, and α is the approximated thermal diffusivity of the wire. Based on the hot-wire power supply minimum pulsing frequency of 100 Hz, the wire will experience 2 current pulses before the heat will have dissipated from the first pulse. Following this analysis, the pulsed current hot-wire can be approximated as a constant current heated wire.

The basic hot-wire model has been discussed however the effect of the GTAW or GMAW leading heat source will now be discussed.

3.3. Hot-Wire GTAW Model

The Lehnhoff and Mendez model was originally developed for the GMAW process where the arc attached to the molten droplet, transferring considerably less energy directly onto the wire than the hot-wire configuration. Adjustment of the model for the hot-wire configuration was conducted to account for the arc/hot-wire separation distance, d, and the wire insertion angle, θ, and the arc current, I_{Arc}. Solid steel wire was used for the hot-wire consumable due to its consistent melting characteristics. The modified room and melting temperature volumetric enthalpy equations (Equations 3.3 and 3.4) no longer need be applied as the wire is of homogeneous composition. The hot-wire wire feed speed was kept constant at 6 $\text{m}\cdot\text{min}^{-1}$ (240 ipm) and the wire current was adjusted such that a semi-solid melting condition occurred.

The semi-solid condition is characterized by the hot-wire drooping and streaming into the weld pool, identified through high speed video. The hot-wire current during the streaming condition were recorded by data acquisition. GTAW arc currents of 225 A and 275 A, wire insertion angles of 30^{o} and 60^{o}, and arc/hot-wire separation distances of 0, 3, and 5 mm were studied to determine their effect on the hot-wire melting condition by varying the wire current to obtain the streaming condition. The parameters were selected to represent welding configurations and parameters similar to those used in tubular Ni-WC hot-wire welding. Collected high speed video frames of the various test parameters are shown in Figure 3.6 and Figure 3.7 below.

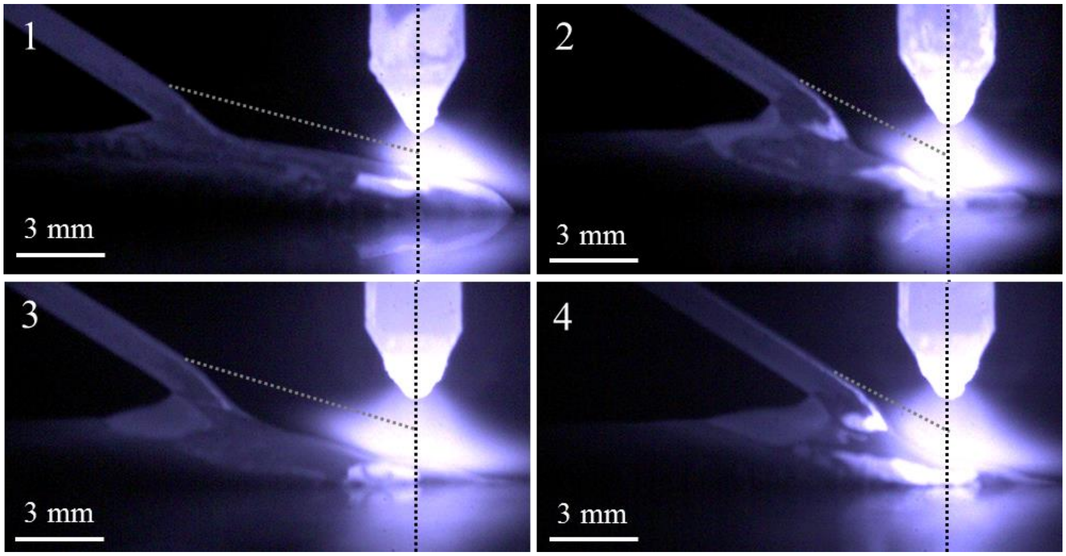

Figure 3.6: High speed video frames of 30^{o} insertion angle calibration tests with semi-solid streaming location indicated.

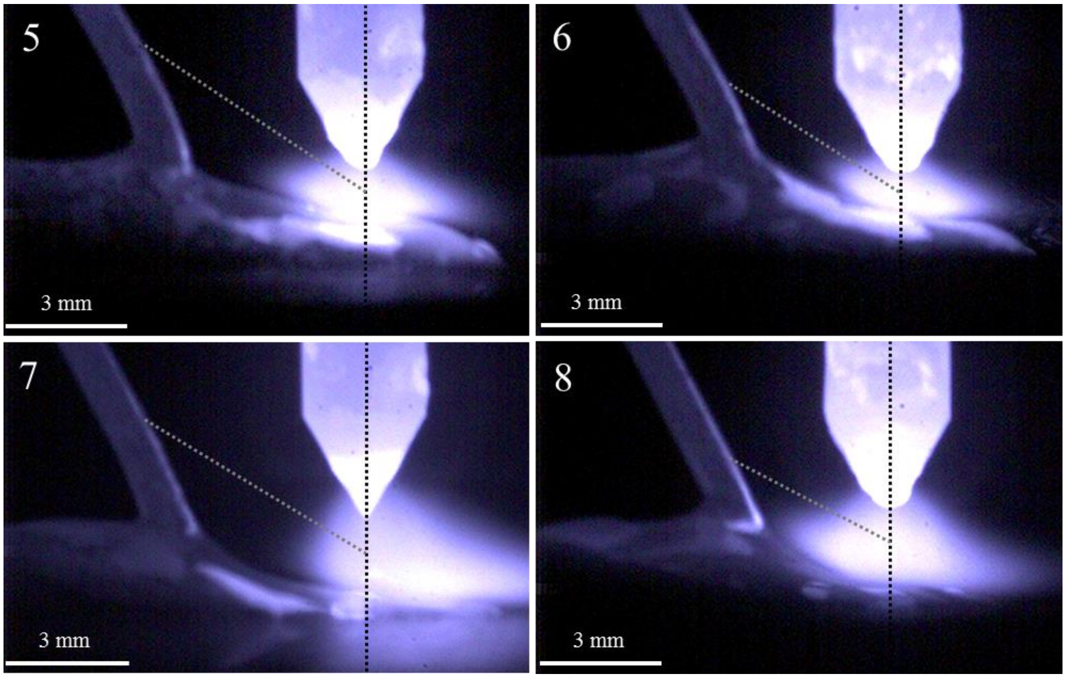

Figure 3.7: High speed video frames of 60^{o} insertion angle calibration tests with semi-solid streaming location indicated.

Analysis of the collected high speed video frames were conducted to determine the arc proximity effect on the hot-wire. Accurate calculation of the amount of Joule heating required measuring the hot-wire electrode extension from the electrical contact point to the semi-solid point, L, using trigonometry and the initial electrode extension, L_o, of 70 mm. The reference point of measurements revolved around the transition between the solid and semi-solid condition along the length of wire. This transition point was identified by the wire deviating from the insertion angle caused by the semi-solid streaming. The characteristic distance, d_1, between the streaming wire start point and the half arc height distance, h, was measured from the high speed video frames. The angle between d_1 and the hot-wire insertion angle, depicted by α, is related to the amount of arc energy transferred to the wire. Figure 3.8 and Figure 3.9 depict the measured parameters α, θ, L, d, d_1, and h. Table 3.1 contains a summary of the welding parameters and measured components of the calibration tests including the measured height of the weld bead, t.

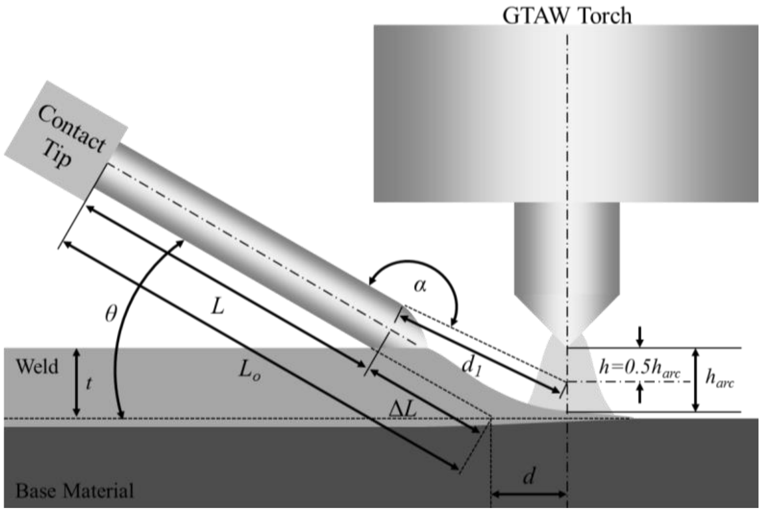

Figure 3.8: Depiction of the measured parameters, α, θ, L, ΔL, L_o, d, d_1, t, and h.

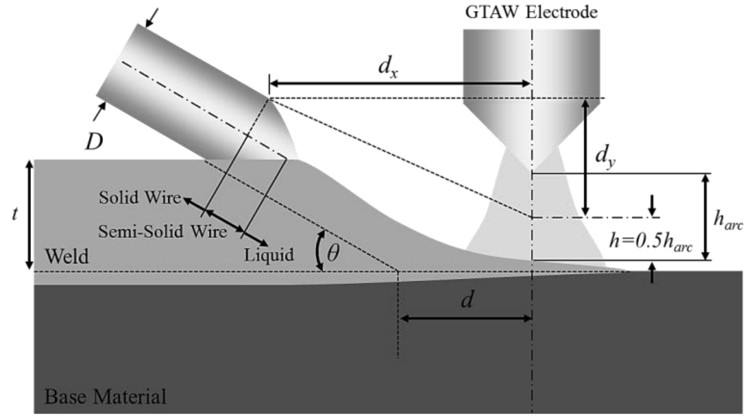

Figure 3.9: Depiction of d_2 and the variables used to calculate $\widehat{d_1}$ and $\hat{\alpha}$.

Table 3.1: Experimental parameters and measured values of the HWGTAW calibration tests depicted in Figure 3.6 and Figure 3.7.

	I_{Arc}	I_{HW}	θ	d	d_1	d_2	d_x	d_y	$\widehat{d_1}$	h	ΔL	L	α	$\hat{\alpha}$	t
Test	(A)	(A)	(°)	(mm)	(mm)	(mm)	(mm)	(mm)	(mm)	(mm)	(mm)	(mm)	(°)	(°)	(mm)
1	225	133.5	30	3.0	8.8	1.7	7.63	2.49	8.02	0.6	6	64	162	168	3
2	225	130.6	30	0	5.6	1.6	4.63	2.49	5.25	1.1	6	64	175	178	3
3	275	130.8	30	3.0	8.2	1.6	5.89	1.49	6.08	1.0	6	64	166	164	2
4	275	126.5	30	0	4.4	1.5	2.89	1.49	3.25	1.1	5	65	175	177	2
5	225	130.8	60	5.0	6.5	2.9	5.74	2.07	6.11	0.5	5	65	156	140	3
6	225	129.2	60	3.0	5.0	1.9	3.74	2.07	4.28	0.5	4	66	152	149	3
7	275	129.4	60	5.0	6.4	3.1	5.17	1.07	5.28	0.8	5	65	150	132	2
8	275	126.5	60	3.0	4.5	1.8	3.17	1.07	3.34	0.8	3	67	146	139	2

While the values of d_1 and α are easily measured from the high speed video frames, they are not easily determined without a camera or prior to welding. It is necessary to estimate these values using experimental setup data or approximated values, such as the weld bead thickness. Equations 3.16 and 3.17 can be used to calculated the estimated d_1 distance, $\widehat{d_1}$, and estimated α angle, $\hat{\alpha}$.

$$\widehat{d_1} = \sqrt{{d_x}^2 + {d_y}^2}$$

Equation 3.16

$$\hat{\alpha} = \tan^{-1}\left(\frac{d_y}{d_x}\right) + (180 - \theta)$$

Equation 3.17

Where d_x and d_y are calculated using Equations 3.18 and 3.19 below.

$$d_x = d + \frac{t}{\tan\theta} - D\sin\theta$$

Equation 3.18

$$d_y = t + D\cos\theta - h$$

Equation 3.19

Calculation of the heat flux at the end of the wire, $\hat{q}^{+}$, was completed using Equation 3.1 above. It is important to note that the Lehnhoff and Mendez model used herein calculates the 1-D heat flux coming from the end of the wire electrode. In the case of a hot-wire setup, the arc heat is impinging on the sides of the wire, altering the temperature distribution of the wire. The effects of the non 1-D heat flow is taken into account in the following work and treated as an additional heat source impinging on the end of the electrode, satisfying the proposed model and predicting the exact semi-solid point of the electrode. This will however provide an inaccurate temperature distribution along the length of the wire but this is secondary to accurately predicting melting of the hot-wire.

The heat flux, $\hat{q}^{+}$, is the amount of energy contributed by the leading heat source to achieving semi-solid melting. High speed video was able to determine the electrode extension at the semi-solid point and data acquisition measured the hot-wire current necessary to achieve semi-solid melting. Table 3.2 summarizes the material properties of the 0.045 in. AWS A5.18 ER70S-6 steel electrode used to calculate the heat flux. The resistivity at melting temperature was approximated by extrapolating the electrical resistivity data from Figure 3.10. The resistivity used for the proposed hot-wire model was completed using the constant current (CC), fast heating tests completed in Chapter 2. The rate of heating from room to semi-solid temperature of the hot-wire at the wire feed speeds utilized in this thesis range from 0.7-1.4 seconds. The semi-solid temperature of 1395 ^{o}C was determined through Scheil calculations using ThermoCalc.

Table 3.2: Summary of ER70S-6 steel wire properties. Resistivity data is extrapolated from Figure 3.10 and volumetric enthalpy is calculated by ThermoCalc.

H_o (10^9 Jm^{-3})	H_m (10^9 Jm^{-3})	ρ'_o (10^{-6} Ωm)	ρ'_m (10^{-6} Ωm)	$\Delta\rho'_1$ (10^{-6} Ωm)	$\Delta\rho'_2$ (10^{-6} Ωm)
-0.368	6.96	0.50	1.51	1.01	0.33

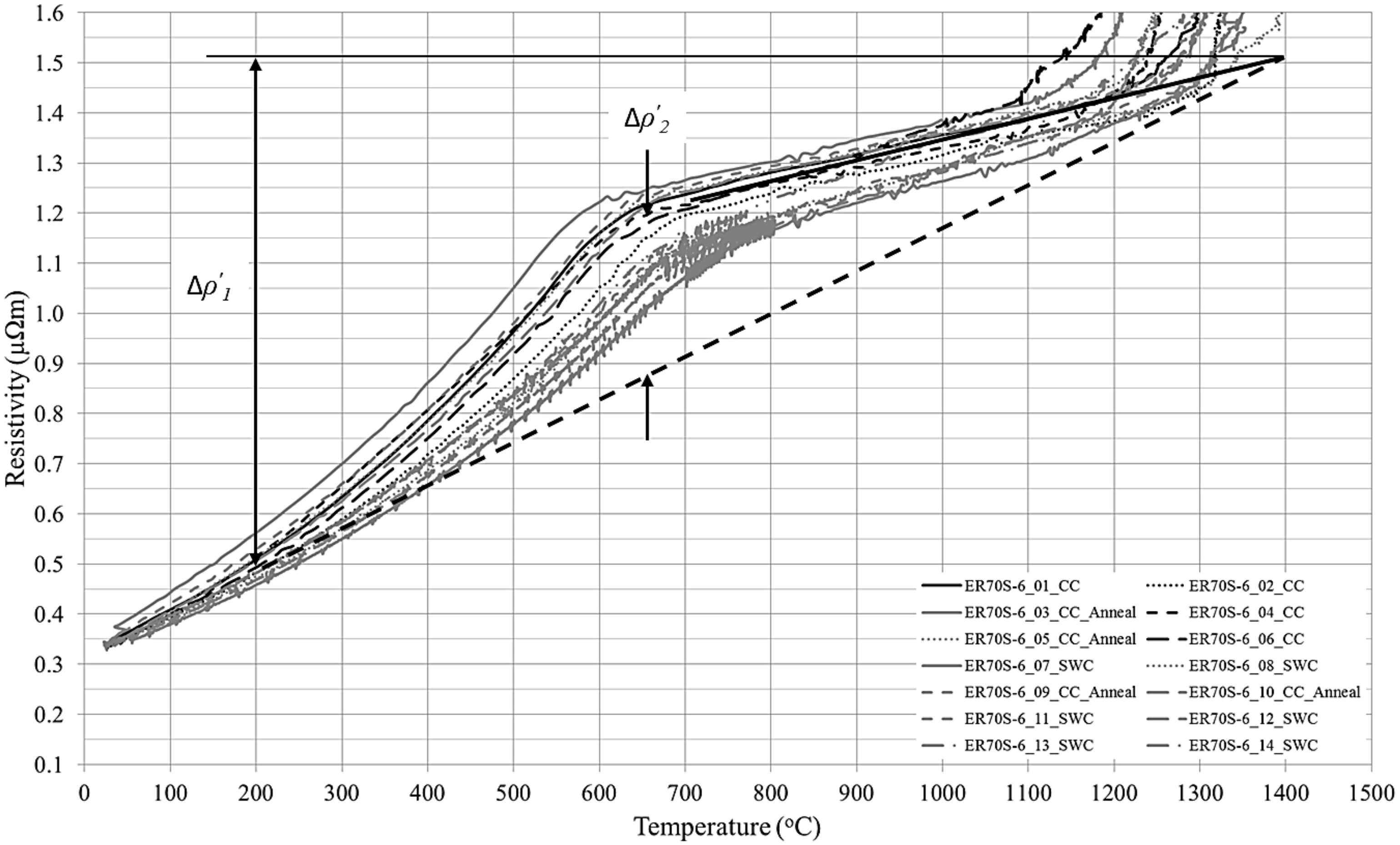

Figure 3.10: Measured electrical resistivity of the AWS A5.18 ER70S-6 welding consumable. Extrapolation to semi-solid temperature indicated.

Prior to welding testing, the model was calibrated by adjusting the hot-wire current to attain a semi-solid streaming condition without the presence of a leading heat source. The semi-solid point was verified with a high speed camera and data acquisition measured the required current, depicted in Figure 3.11. As a result, the proposed model over-calculated the required current to achieve a semi-solid melting condition. The proposed model depends on two dominant material properties: volumetric enthalpy and resistivity. The volumetric enthalpy calculated by ThermoCalc and summarized in Table 3.2 corresponds well with those utilized by Lehnhoff and Mendez [132]. The electrical resistivity at the contact tip and semi-solid temperature was taken from Figure 3.10. Without a correction factor, the current required for the calibration test produced an overheating of the hot-wire or $\widehat{H_{C_2}^{+*}}>1$. The correction factor, $f_{\widehat{H_{C_2}^{+*}}}$, was placed on the unitless volumetric enthalpy term, $\widehat{H_{C_2}^{+*}}$, shown in Equations 3.20 and 3.21. The correction factor is chosen such that the model predicts 100% Joule heating of the hot-wire, producing the semi-solid conditions without a leading heat source. Sufficient current to produce semi-solid melting of a steel wire without a leading heating source is depicted in Figure 3.11.

$$f_{\widehat{H_{C_2}^{+*}}} = 0.573$$

Equation 3.20

$$\hat{q}^{+} = \left(1 - f_{\widehat{H_{C_2}^{+*}}}\widehat{H_{C_2}^{+*}}\right) H_C U$$

Equation 3.21

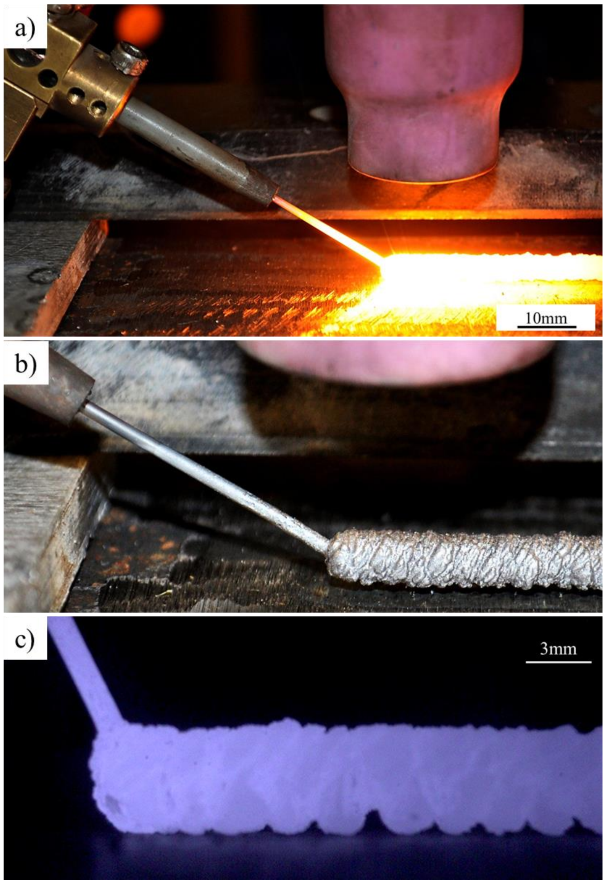

Figure 3.11: Hot-wire model calibration images of a) during wire feeding, b) solidified semi-solid weld bead, and c) high speed video image of sufficient current to produce semi-solid streaming.

Using the corrected heat flux expression from Equation 3.21, the effective heat at the electrode tip, q_{eff}, is calculated using Equation 3.22. The solid steel wire used has a measured diameter of 1.14 mm (0.045”). The effective heat is analogous to the amount of arc heat and weld pool conduction energy that is being transferred to the hot-wire and contributing to melting. Table 3.3 contains the results of the calculated effective heat of the calibration weld beads conducted in Figure 3.6 and Figure 3.7.

$$q_{eff} = A_{eff}\hat{q}^{+}$$

Equation 3.22

Table 3.3: Summary of calculated variables and the effective heat of the hot-wire GTAW calibration Tests 1-8 in Figure 3.6 and Figure 3.7.

Weld	$\widehat{H_{c_2}}$ (10^9 Jm^{-3})	$f_{\widehat{H_{C_2}^{+*}}}\widehat{H_{c_2}^{+*}}$	d	b	a	M_1	$\hat{q}^+$ (10^7 Wm^{-2})	q_{eff} (W)
1	*5.47*	0.991	5.681	4.660	-2.640	1.278	0.619	6.3
2	*5.24*	0.967	5.681	4.660	-2.640	1.336	2.306	23.5
3	*5.25*	0.969	5.681	4.660	-2.640	1.332	2.183	22.3
4	*4.99*	0.938	5.681	4.660	-2.640	1.402	4.357	44.5
5	*5.34*	0.978	5.681	4.660	-2.640	1.311	1.572	16.0
6	*5.37*	0.981	5.681	4.660	-2.640	1.304	1.353	13.8
7	*5.22*	0.965	5.681	4.660	-2.640	1.340	2.426	24.8
8	*5.15*	0.956	5.681	4.660	-2.640	1.360	3.047	31.1

Determination and prediction of the effect of welding parameters, namely the hot-wire insertion angle, θ, GTAW arc current, I_{arc}, and the hot-wire separation distance from the arc, d, was conducted to adapt the proposed model for various welding scenarios. Regressions were calculated using the natural logarithms of the parameters such that a Power Law can be used to express the results. The angles of α and θ were converted to radians in order to use the regression function within Microsoft Excel. Using the measured parameters, d_2 and α, from the high speed frames in Figure 3.6 and Figure 3.7 in conjunction with the arc current, a regression can be made that approximates the effective heat from the arc and weld pool, $\widehat{q_{arc}}$ (Equation 3.23). The correlation between the regression-calculated effective heat from the arc, $\widehat{q_{arc}}$, and the effective heat, q_{eff}, is shown in Figure 3.12.

$$\widehat{q_{arc}} = e^{-13.6838} I_{Arc}^{3.3393} d_1^{-1.1394} \sin \alpha^{-0.2280}$$

Equation 3.23

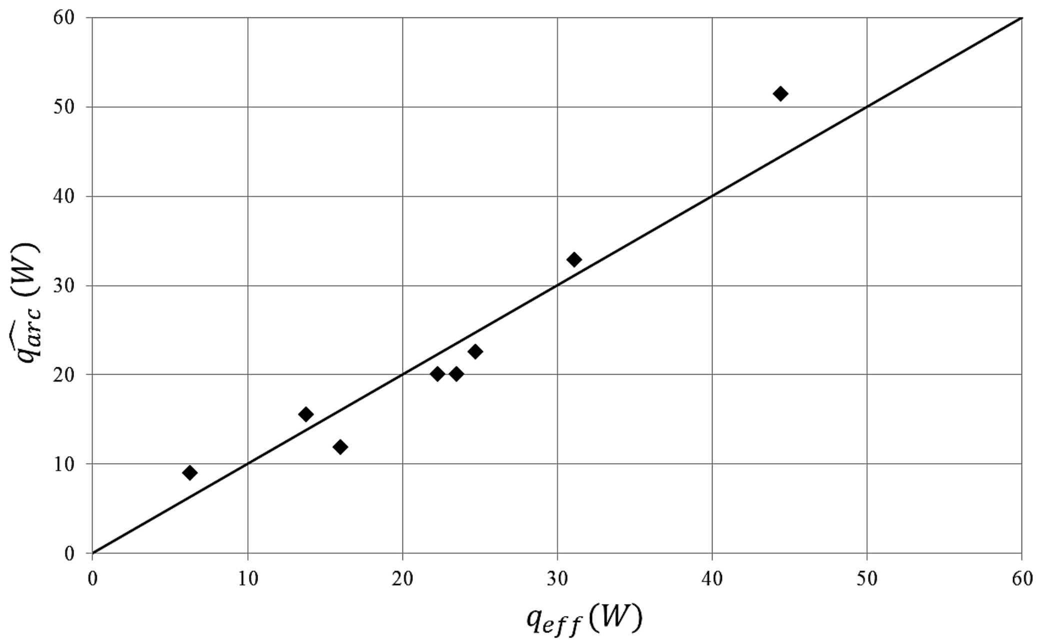

Figure 3.12: Calculated effective heat, q_{eff}, compared to the approximated heat of the arc, $\widehat{q_{arc}}$. R^2 of 0.88.

The parameters d_1 and α are measured parameters and as such are not useful to industrial torch apparatus setup. Correlation between d_1 and α and user determined parameters such as the wire insertion angle, θ, the distance between the hot-wire and the electrode, d, and the weld bead thickness, t, is necessary for a usable approximation of the arc heat flux. The measured d_1 and α from the high speed video frames and summarized in Table 3.1 are normalized against the calculated estimates, $\widehat{d_1}$ and $\hat{\alpha}$ from Equations 3.16 and 3.17. Equations 3.24 and 3.25 below are the result of regressions to determine d_1 and α. The correlation between the normalized d_1 and α and the regressions is shown in Figure 3.13 and Figure 3.14.

$$d_1 = \widehat{d_1} e^{0.5285} d^{-0.0078} \sin\theta^{-0.0062}\, t^{-0.4416}$$

Equation 3.24

$$\alpha = \hat{\alpha} e^{0.2324} d^{0.0137} \sin\theta^{0.1388}\, t^{-0.0651}$$

Equation 3.25

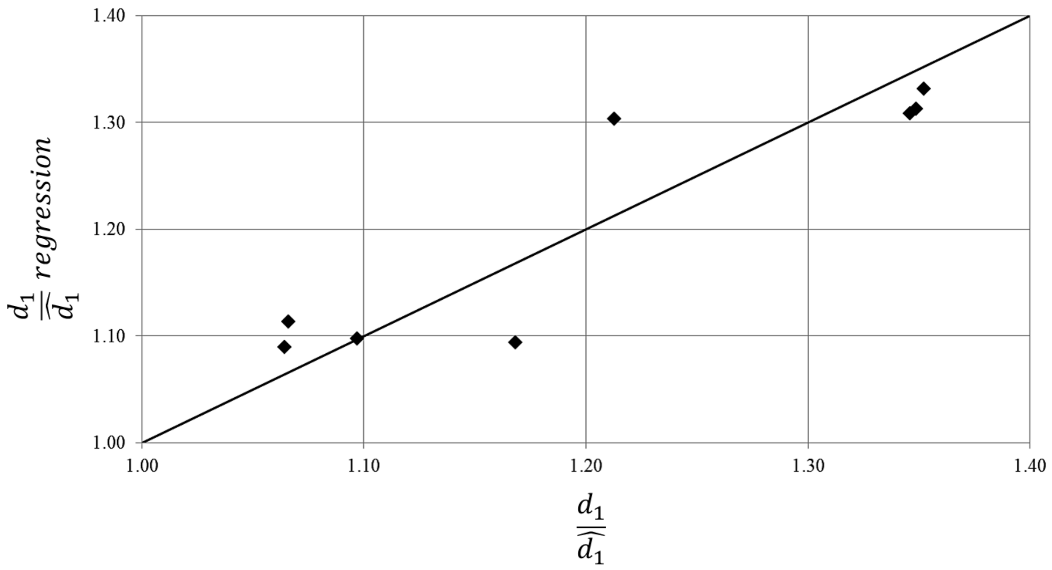

Figure 3.13: Correlation of the normalized d_1 to the regression calculated d_1 with R^2 of 0.83.

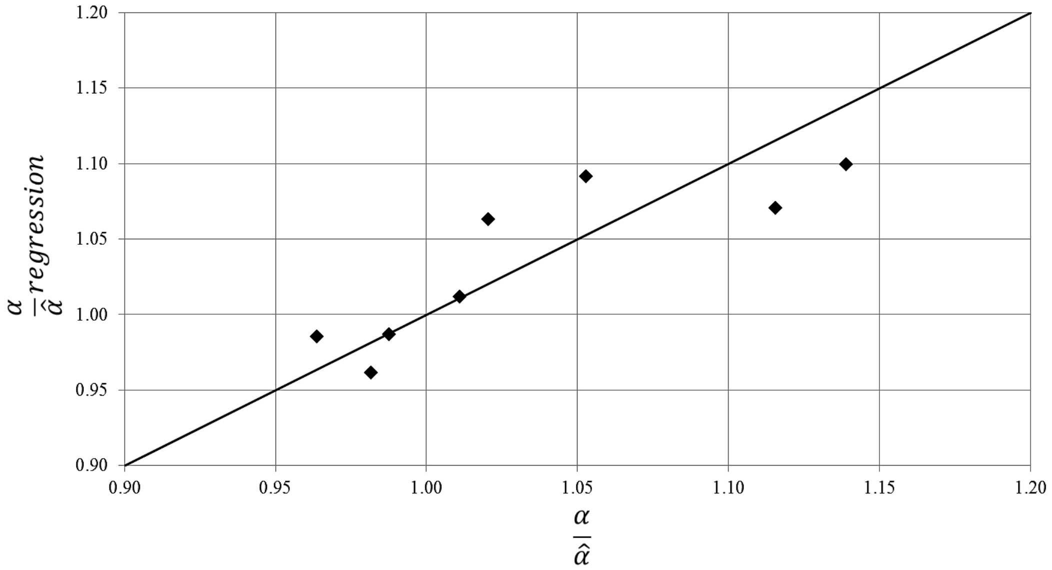

Figure 3.14: Correlation of the normalized α to the regression calculated α with R^2 of 0.73.

3.4. Hot-Wire GMAW Model

Calibration of the hot-wire electrode extension model proposed in Chapter 3.1 required calibration to accommodate the GMAW leading heat source. This was completed in a similar manner to the hot-wire GTAW model wherein a series of tests were performed to quantify the amount of heat impinging on the hot-wire from the leading arc. Adjustment of the model for the hot-wire configuration was conducted to account for the arc/hot-wire separation distance, *d*, and the wire insertion angle, θ, and the arc current, I_{Arc}. Arc current was calculated as the RMS value using Equation 3.13. ER70S-6 solid steel wire was used for the hot-wire consumable due to its consistent melting characteristics. Wire resistivity was utilized from Table 3.2. The modified room and melting temperature volumetric enthalpy equations (Equations 3.3 and 3.4) no longer need to be used as the wire is of homogeneous composition. Wire insertion angles were fixed at 30^o and 60^o and travel speed was kept constant at 0.25 $m \cdot min^{-1}$. The GMAW shielding gas was blended with a rotometer, resulting in an $85Ar\text{-}15CO_2$ mix. Contact-tip-to-workpiece distance (CTWD) was maintained at 18 mm. Short-circuit transfer was utilized in a current range similar to the hot-wire GMAW Ni-WC welds conducted in Chapter 4. The hot-wire wire feed speed (WFS) was calculated as 75% of the GMAW leading arc WFS to prevent cold lap. Table 3.4 summarizes the hot-wire and GMAW experimental parameters.

Table 3.4: Experimental parameters for HWGMAW calibration tests shown in Figure 3.15 and Figure 3.16.

	GMAW			***Hot-Wire***			
Test	***WFS*** ($mmin^{-1}$)	***Voltage*** (V)	I_{Arc} (A)	***WFS*** ($mmin^{-1}$)	I_{HW} (A)	θ (^{o})	***L*** (mm)
1	6.00	20.0	205.0	4.50	117.5	60	65
2	5.00	18.5	178.6	3.75	109.2	60	65
3	4.00	18.0	153.0	3.00	98.3	60	65
4	6.00	20.0	206.0	4.50	121.9	60	65
5	5.00	18.5	183.5	3.75	113.1	60	65
6	4.00	18.0	155.1	3.00	102.4	60	65
7	6.00	20.0	205.7	4.50	127.2	30	64
8	5.00	18.5	179.6	3.75	117.8	30	64
9	4.00	18.0	154.0	3.00	106.6	30	64
10	6.00	20.0	205.2	4.50	128.0	30	64
11	5.00	18.5	180.6	3.75	117.6	30	64
12	4.00	18.0	154.7	3.00	108.1	30	64

Twelve test welds were conducted to determine the heat flux impinging on the wire tip from the leading GMAW arc, shown in Figure 3.15 and Figure 3.16. The solid to semi-solid transition point of the hot-wire was determined through use of high speed video.

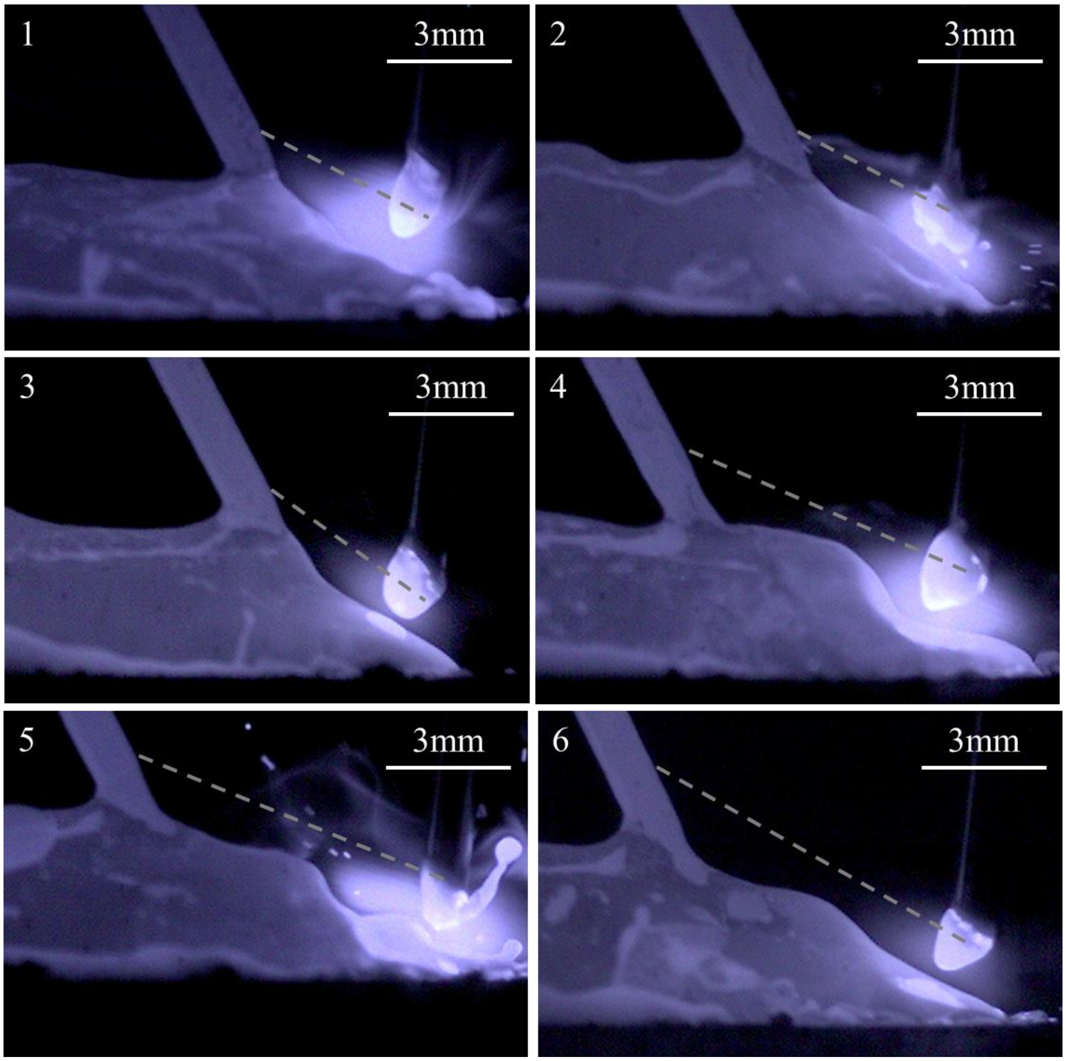

Figure 3.15: High speed video frames of 60^{o} insertion angle calibration tests with semi-solid streaming location indicated.

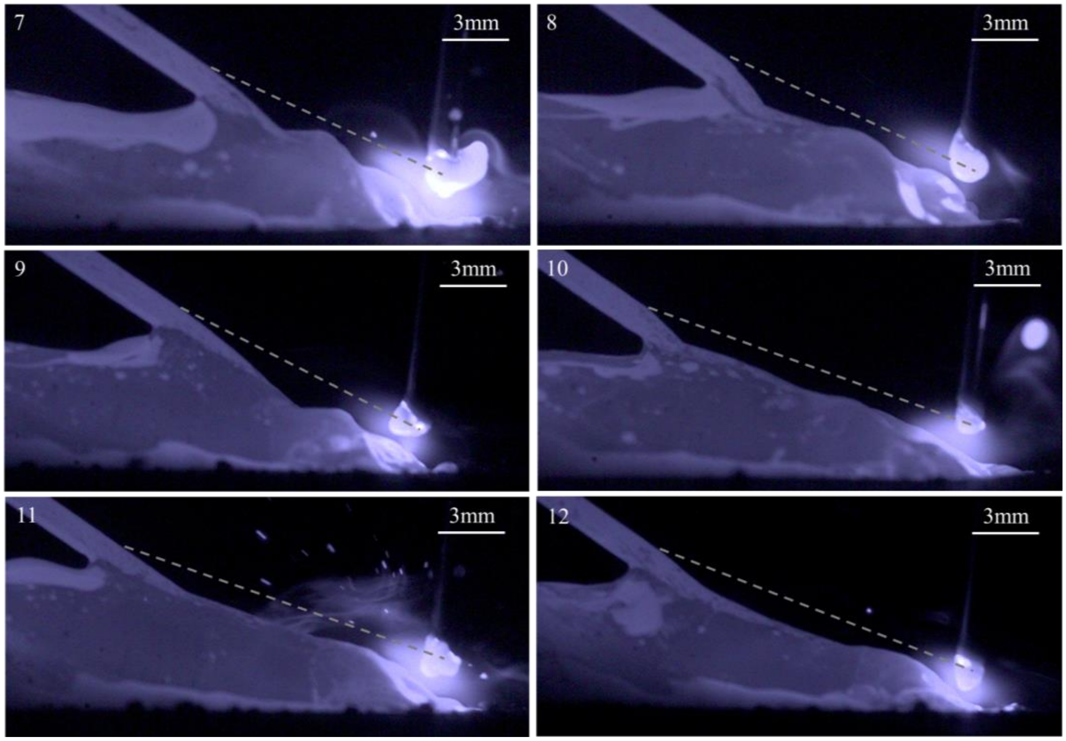

Figure 3.16: High speed video frames of 30^{o} insertion angle calibration tests with semi-solid streaming location indicated.

Analysis of the high speed video frames was conducted to determine the necessary measured and calculated parameters to form a HWGMAW model similar to the HWGTAW model previously discussed. The enthalpy correction factor, $f_{\widehat{H_{C_2}^{+*}}}$, discussed for the HWGTAW model was utilized. Figure 3.17 and Figure 3.18 depict the variables α, θ, L, ΔL, L_o, d, d_1, t, and h, and Table 3.5 summarizes the variables including the estimated $\widehat{d_1}$ and $\hat{\alpha}$ values.

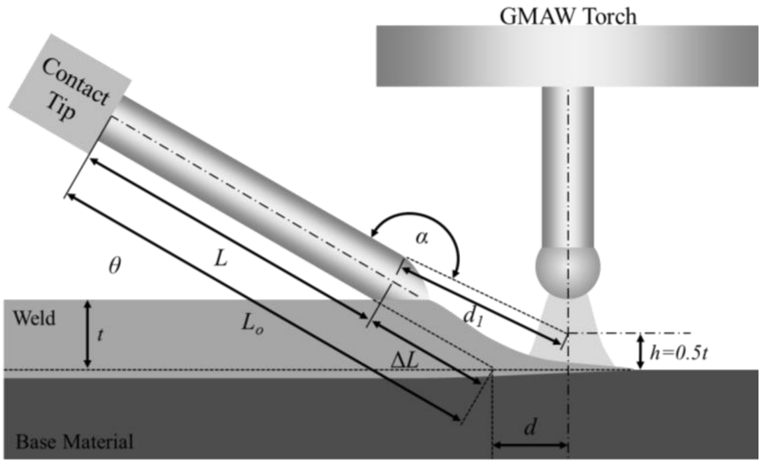

Figure 3.17: Depiction of the measured parameters, α, θ, L, ΔL, L_o, d, d_1, t, and h.

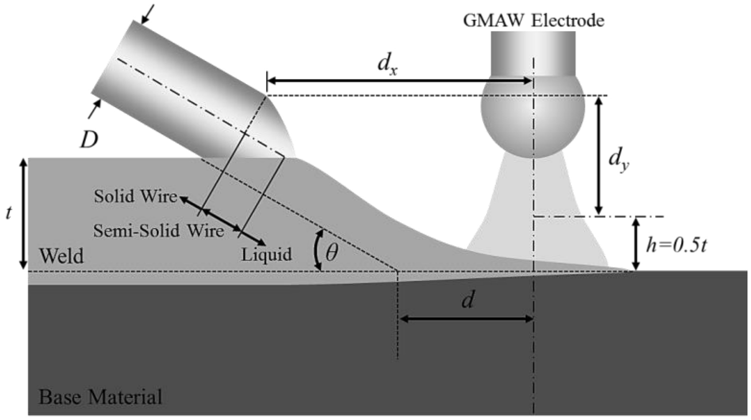

Figure 3.18: Depiction of d_2 and the variables used to calculate $\widehat{d_1}$ and $\hat{\alpha}$.

Table 3.5: Summary of measured and calculated from the HWGMAW calibration tests of Figure 3.15 and Figure 3.16.

	d	d_1	d_2	d_x	d_y	$\widehat{d_1}$	ΔL	L	α	$\hat{\alpha}$	t
Test	(mm)	(mm)	(mm)	(mm)	(mm)	(mm)	(mm)	(mm)	(°)	(°)	(mm)
1	2	4.52	1.14	3.90	3.07	4.96	4.76	60.2	145	158.2	5
2	2	4.26	1.15	3.90	3.07	4.96	4.71	60.3	146	158.2	5
3	2	4.47	1.00	3.32	2.57	4.2	5.33	59.7	154	157.7	4
4	5	7.33	1.39	6.90	3.07	7.55	7.00	58.0	139	144.0	5
5	5	7.92	1.55	6.90	3.07	7.55	8.50	56.5	140	144.0	5
6	5	8.61	1.55	6.32	2.57	6.82	9.80	55.2	146	142.1	4
7	2	11.50	2.19	10.09	3.49	10.68	11.9	52.1	172	169.1	5
8	2	12.09	1.59	10.09	3.49	10.68	12.7	51.3	173	169.1	5
9	2	11.98	1.99	8.36	2.99	8.88	13.1	50.9	174	169.7	4
10	5	15.33	1.93	13.09	3.49	13.55	12.2	51.8	167	164.9	5
11	5	15.29	1.89	13.09	3.49	13.55	12.1	51.9	167	164.9	5
12	5	15.03	2.13	11.36	2.99	11.74	14.5	49.5	169	164.7	4

The effective heat, q_{eff}, was calculated using Equations 3.21 and 3.22, with the results summarized in Table 3.6 for the twelve HWGMAW calibration tests.

Table 3.6: Summary of calculated variables and effective heat flux of the HWGMAW calibration tests.

Weld	$\widehat{H_{c_2}}$ $(10^9\ \mathrm{Jm^{-3}})$	$f_{\widehat{H_{c_2}^{+*}}}\widehat{H_{c_2}^{+*}}$	d	b	a	M_1	$\hat{q}^+$ $(10^6\ \mathrm{Wm^{-2}})$	q_{eff} (W)
1	5.32	0.976	5.681	4.660	-2.640	1.315	12.7	13.0
2	5.52	0.995	5.681	4.660	-2.640	1.269	2.13	2.2
3	5.53	0.997	5.681	4.660	-2.640	1.265	1.19	1.2
4	5.52	0.995	5.681	4.660	-2.640	1.268	2.50	2.5
5	5.55	0.998	5.681	4.660	-2.640	1.261	0.84	0.9
6	5.56	0.999	5.681	4.660	-2.640	1.259	0.31	0.3
7	5.40	0.984	5.681	4.660	-2.640	1.296	8.51	8.7
8	5.46	0.990	5.681	4.660	-2.640	1.281	4.38	4.5
9	5.56	0.999	5.681	4.660	-2.640	1.259	0.40	0.4
10	5.43	0.987	5.681	4.660	-2.640	1.289	6.84	7.0
11	5.51	0.995	5.681	4.660	-2.640	1.270	2.33	2.4
12	5.55	0.998	5.681	4.660	-2.640	1.261	0.63	0.6

Similar to the proposed HWGTAW electrode extension model, the hot-wire GMAW model utilizes measured and calculated parameters that are not utilized in industrial scenarios. Regressions were made so as to estimate the effective arc heat, $\widehat{q_{arc}}$, and relate the calculated $\widehat{d_1}$ and $\hat{\alpha}$ terms to θ, d, and t. As a result, $\widehat{q_{arc}}$ can be estimated using Equation 3.26. The correlation between $\widehat{q_{arc}}$ and the effective heat flux is shown in Figure 3.19.

$$\widehat{q_{arc}} = e^{-52.7140} I_{Arc}^{9.0712} d_1^{-1.1156} \sin \alpha^{-0.9109}$$

Equation 3.26

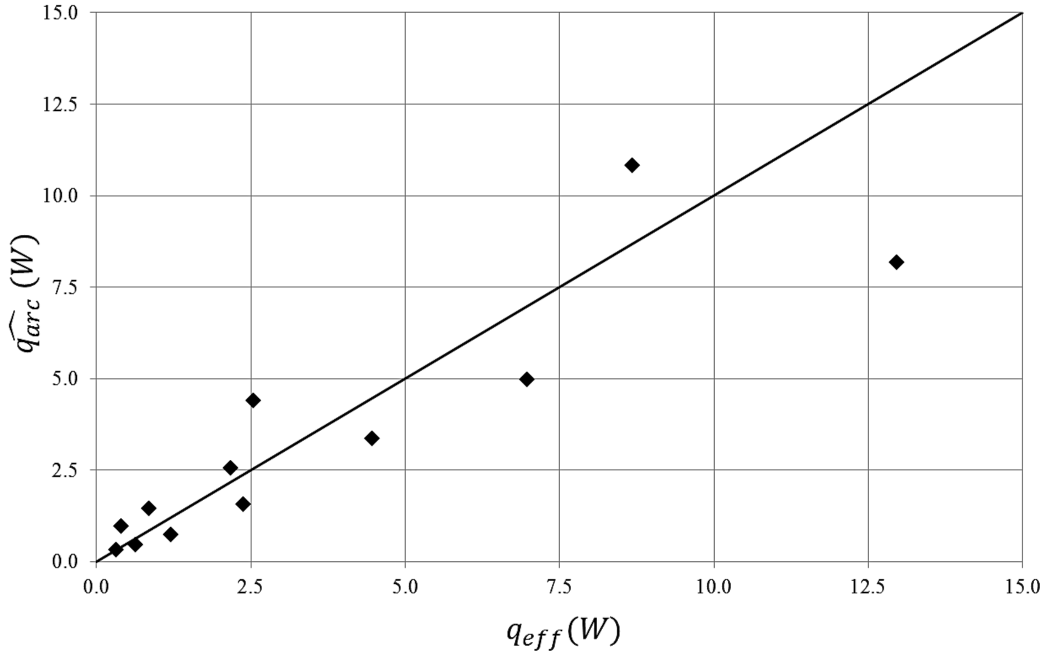

Figure 3.19: Calculated effective heat, q_{eff}, compared to the approximated heat of the arc, $\widehat{q_{arc}}$. R^2 of 0.85.

Correlation between d_1 and α and user determined parameters such as the wire insertion angle, θ, the distance between the hot-wire and the electrode, d, and the weld bead thickness, t, is necessary for a usable approximation of the arc heat. The measured d_1 and α from the high speed video frames and summarized in Table 3.5 are normalized against the calculated estimates, $\widehat{d_1}$ and $\hat{\alpha}$ from Equations 3.16 and 3.17. Equations 3.26 and 3.27 below are the result of regressions to determine d_1 and α. The correlation between the normalized d_1 and α and the regressions is shown in Figure 3.20 and Figure 3.21.

$$d_1 = \widehat{d_1} e^{-3.9928} d^{0.0775} \sin\theta^{-0.28}\, t^{-0.8208}$$

Equation 3.27

$$\alpha = \hat{\alpha} e^{-0.7282} d^{0.0255} \sin\theta^{-0.1044}\, t^{-0.153}$$

Equation 3.28

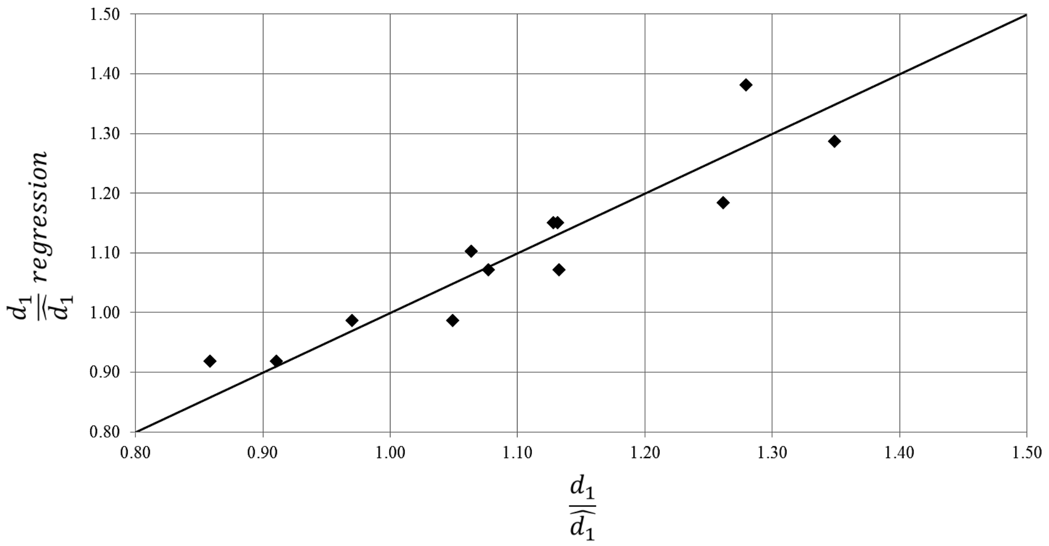

Figure 3.20: Correlation of the normalized d_1 to the regression calculated d_1 with R^2 of 0.87.

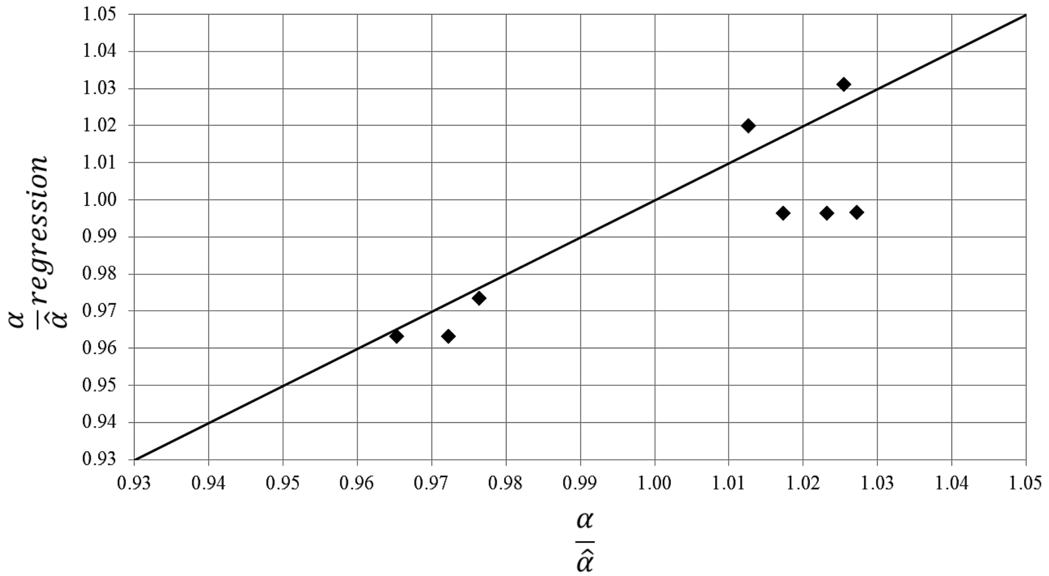

Figure 3.21: Correlation of the normalized α to the regression calculated α with R^2 of 0.78.

3.5. Tubular Ni-WC HWGTAW and HWGMAW Models

The calibration of the proposed hot-wire electrode extension model to account for the effects of hot-wire insertion angle, arc current, and the hot-wire distance from the leading heat source can now be applied to tubular Ni-WC wires. Equations 3.3 and 3.4 will now have to be used to calculate the total volumetric enthalpy as the wires are not homogenous and contain varying amounts of nickel and tungsten carbide. Table 3.7 contains the volumetric enthalpy for the Ni and tungsten carbide components and summarizes the resistivity of the Ni-WC wires.

Table 3.7: Summary of tubular Ni-WC resistivity and volumetric enthalpy. Resistivity extrapolated from Figure 3.5 and volumetric enthalpy calculated from ThermoCalc.

$\boldsymbol{H_{WC}^{o}}$	$\boldsymbol{H_{WC}^{m}}$	$\boldsymbol{H_{Ni}^{o}}$	$\boldsymbol{H_{Ni}^{m}}$	$\boldsymbol{\rho_{o}'}$	$\boldsymbol{\rho_{m}'}$	$\boldsymbol{\Delta\rho_{1}'}$	$\boldsymbol{\Delta\rho_{2}'}$
(10^{6} Jm^{-3})	(10^{9} Jm^{-3})	(10^{6} Jm^{-3})	(10^{9} Jm^{-3})	(10^{-7} Ωm)	(10^{-7} Ωm)	(10^{-7} Ωm)	(10^{-7} Ωm)
-98.4	4.83	7.23	8.89	1.75	6.15	4.4	0.7

The tubular Ni-WC wires do not exhibit the same semi-solid streaming condition that is observed in solid consumables. The lack of a characteristic semi-solid droop makes approximating the hot-wire electrode extension, L, very difficult. The semi-solid point for Ni-WC consumables is assumed to exist at the weld pool free surface.

Selecting the desired leading heat source welding parameters, the arc energy contributing to the hot-wire melting can be approximated by the previously defined HWGTAW and HWGMAW $\widehat{q_{arc}}$ expressions. Calculating the desired hot-wire current can be completed with Equation 3.29, a rearranged form of Equation 3.1, and using a solver to determine the optimum hot-wire current to produce semi-solid melting.

$$\widehat{H_{c_2}^{+*}} = 1 - \frac{\widehat{q_{arc}}}{U H_c A_{eff}}$$

Equation 3.29

3.6. Discussion

The proposed HWGTAW and HWGMAW models have been fundamentally proposed, calibrated through arc-less semi-solid melting, the leading heat source's contribution to hot-wire melting measured, and expressions formed to approximate the effect of the GTAW/GMAW welding parameters and torch setup on the necessary hot-wire current to achieve semi-solid melting. In comparison, the GTAW process provides a greater contribution to the hot-wire melting than the short-circuit GMAW process. This is attributed to the lower process efficiency of GTAW compared to GMAW.

The proposed electrode extension model centres on a few primary material property and experimental terms that have a large impact on the validity and accuracy of the model. A small sensitivity analysis of the effect of small variations in volumetric enthalpy, electrical resistivity, hot-wire electrode extension, electrode diameter, and hot-wire current on the ability of the model to predict melting was conducted. All variables were studied independent of each other. Volumetric enthalpy and electrical resistivity were increased 5%. The wire diameters typically utilized in hot-wire assisted welding applications can range from 0.9-2.0 mm nominal outside diameters. A 1 mm increase in electrode extension was studied as it is on the same order as the wire diameters. The diameter of the solid ER70S-6 steel wire used in the HWGTAW and HWGMAW testing was measured with a digital caliper, with a resolution of 0.02 mm. The hot-wire power supply utilized in this thesis has an average current input resolution of 1 ampere. With the pulsing frequency and range of currents utilized in this thesis, a 1 average ampere change results in approximately 1.42A RMS change in current. Table 3.8 contains the results of the sensitivity study on the effective heat, q_{eff}, where a baseline of 100 W was established for easy comparison.

Table 3.8: Sensitivity study on the effect of variations in volumetric enthalpy, electrical resistivity, electrode extension, electrode diameter, and hot-wire power supply current resolution on effective heat, q_{eff}.

	Baseline	$\boldsymbol{H}$	$\boldsymbol{\rho'}$	$\boldsymbol{L}$	$\boldsymbol{D}$	$\boldsymbol{I_{HW}}$
variation	-	+5%	+5%	+1 mm	+0.02 mm	+1.42 A
q_{eff} (W)	100	136.3	68.6	89.6	146.9	78.5

As a result of the sensitivity analysis, small variations in critical parameters have large implications on calculating the required hot-wire current to achieve semi-solid melting. Volumetric enthalpy, electrical resistivity, and electrode diameter have the largest effect on calculating the amount of Joule heating the hot-wire experiences. Variations in measurements and material properties up to this point have been lumped into a single correction factor, $f_{\widehat{H_{C_2}^{+*}}}$ (Equation 3.20), where the model was calibrated against an arc-less semi-solid melting scenario, depicted in

Figure 3.11. The results of the sensitivity analysis indicate that a combination of small variations in the variables will render the correction factor unnecessary. The exact contribution from each of the 5 studied variables to the correction factor is unknown however.

While effective, the correction factor may only apply to the solid ER70S-6 steel wire utilized during the calibration tests. It is likely that other consumables, such as stainless steel, Ni-based superalloys, and tubular Ni-WC wires will require a consumable specific correction factor that accounts for variations in material properties and measured parameters to ensure proper estimation of the required hot-wire current.

It is important to note that the proposed hot-wire electrode extension model only applies to the range of leading heat source parameters studied. A significant increase or decrease in the GTAW/GMAW current will potentially have a large effect on the estimated arc contribution to hot-wire melting. For example, an increase in current during GMAW can shift the metal transfer from short-circuit to free-flight globular, spray, or pulsed transfer. During the range of short-circuit currents utilized in this thesis, a small amount of arc energy contributes to hot-wire melting. Further testing will need to be conducted to create a spray-transfer specific hot-wire GMAW model.

3.7. Conclusion

The electrode extension model proposed by Lehnhoff and Mendez was used as the basis for approximating the required hot-wire welding parameters to promote sufficient wire melting in tubular Ni-WC wires. The model was calibrated through the use of high speed video and measurement of the current necessary to produce a semi-solid melting condition. The effect of a leading GTAW or GMAW heat source on the melting of the trailing hot-wire was measured. The arc energy influence was related to the hot-wire insertion angle, arc current, and hot-wire separation distance from the electrode.

4. Analysis of Hot-Wire Assisted Ni-WC Overlays

4.1. Introduction

The welding of Ni-WC overlays is very difficult due to the high carbide dissolution rates, large variation in consumables, and hot-wire and arc welding instabilities inherent with the consumables. The following sections outline the experimental setup of the hot-wire, GTAW, and GMAW process, carbide volume fraction and overlay metallurgy results, and ASTM G65 wear test data.

4.2. Experimental Setup

4.2.1. Hot-Wire Assisted GTAW/GMAW

The experimental setup was designed around a purpose-built 400A pulsed hot-wire assist power supply with integrated wire feeder from Babcock-Hitachi Ltd. The power supply can store up to 10 custom consumable profiles, has selectable duty cycle ranges from 30-70%, and can pulse at either 100Hz or 200Hz frequency. Initial wire start-up is controlled by user-selectable wire current, wire feed speed, and current ramp rate. The current and voltage pulsing waveform of the hot-wire power supply is shown in Figure 4.1. The low voltage avoids the formation of an arc by not overcoming the cathode and anode fall voltages. The hot-wire operates in electrode positive polarity which causes magnetic arc blow or deflection in GTAW and arc attraction in GMAW.

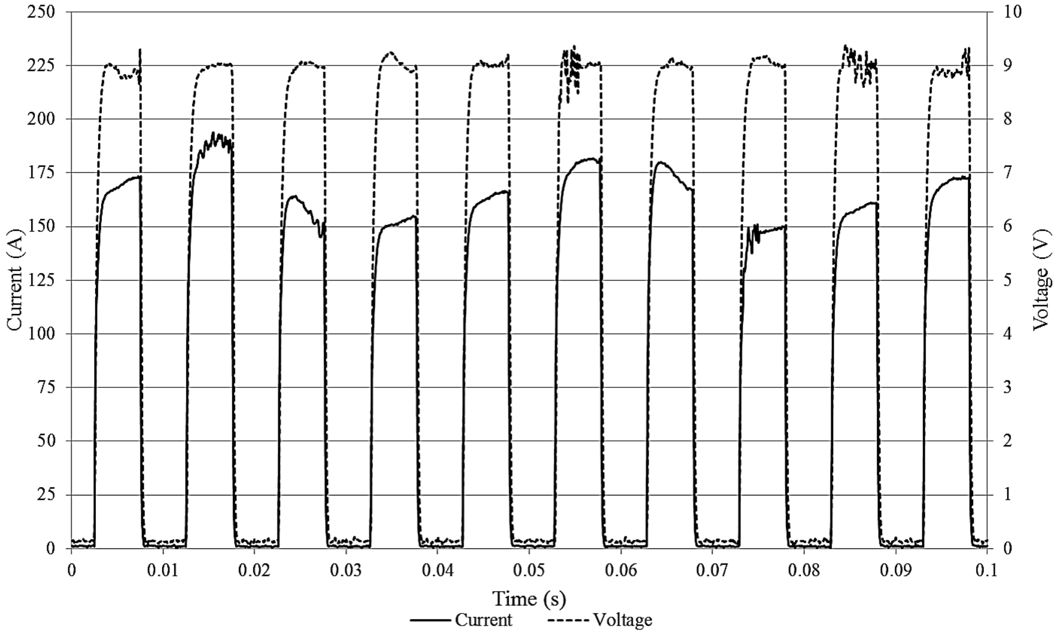

Figure 4.1: Current and voltage waveform of Babcock-Hitachi Ltd. hot-wire power supply. Duty cycle was set at 50% and 0.045 in. ER70S-6 wire was used in the HWGTAW configuration.

The GTAW power supply is a 700A Miller Dynasty unit operating in DCEN polarity with a water-cooled Weldcraft WP-27 torch utilizing a 3.2 mm (0.125 inch) 2% thoriated tungsten electrode. The GMAW power supply is a Lincoln Electric PowerWave 455M/STT and S500 with a PowerFeed 10M wire feeder connected to a Tregaskiss Tough Gun 180° air-cooled 500A automation torch. Contact-tip-to-workpiece distance (CTWD) was maintained at 18 mm through all GMAW and HWGMAW testing. All GMAW and HWGMAW testing was completed using constant voltage mode (Program #5 in software version Z073102i). Knurled drive rollers were used to feed the stiff, kink and crush prone tubular Ni-WC consumables. Both the GTAW and GMAW torches were fixed to a stationary mount above a motorized variable speed lathe bed to facilitate high speed videography. To minimize thermal distortions, the substrate plates were held rigid with a clamping system.

To control the insertion location of the hot-wire, 2-axis (X-Y) screw dovetails were used to position the wire centrally behind the arc and control the distance between the hot-wire and the arc. The wire insertion angle was controlled using angled brackets. Figure 4.2 and Figure 4.3 provide an overall view of the HWGMAW setup.

Pure argon was used to shield the GTAW arc and weld pool while the gas mixtures employed in GMAW were mixed with an Omega FL-6GP-40ST-40ST-40ST tri-tube rotometer for precise control over custom gas blends. Shielding gas flow rates were kept constant at 35 SCFH during GTAW and GMAW operations.

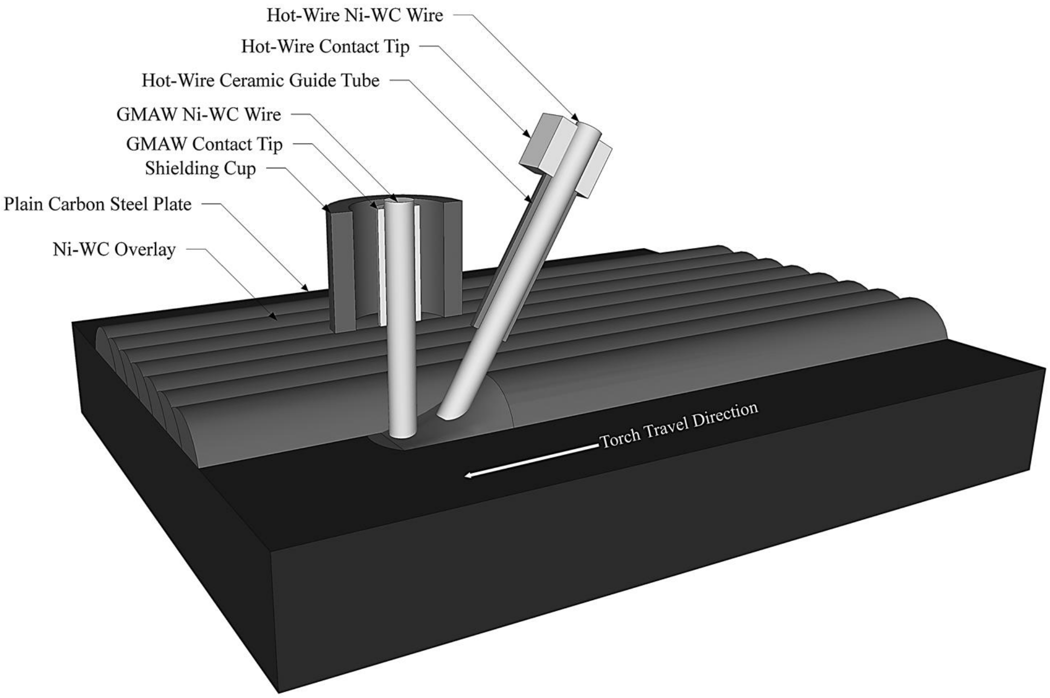

Figure 4.2: Overall schematic of a multi-pass hot-wire GMAW setup.

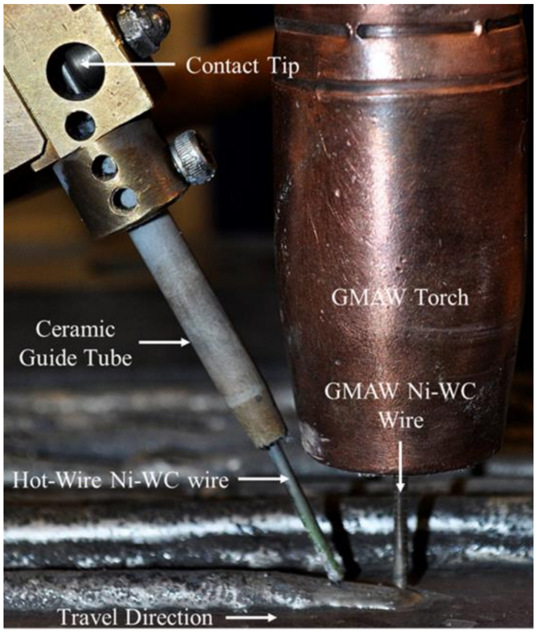

Figure 4.3: HWGMAW torch setup with two Ni-WC wires and 60^o insertion angle.

4.2.2. Data Acquisition and High Speed Videography

The collection of data and observation of welding phenomenon is crucial to analyzing and understanding the welding process. The collection of current, voltage, and wire feed speed was handled by a custom data acquisition system. The system was built around a National Instruments USB-6351 acquisition system that collects and synchronizes the sensor signals and transfers the raw binary data via USB to a computer. Signal acquisition rate was controlled via LabView software and is typically collected at 10 kHz per channel to obtain the required data during the welding operation. Current and voltage sensing for the GTAW/GMAW arc and the hot-wire was handled by LEM HTA 600S Hall Effect sensors and LEM LV 25-P voltage sensors respectively.

The collected binary signals were converted to digital signals using LabView software. The digital signals for the selected sensors could then be analyzed in various software suites such as Microsoft Excel, MATLAB, or Python. During initial trials of the data acquisition system, the hot-wire current and voltage signals were collected from the signal outputs from the Babcock-Hitachi power supply. Figure 4.4 contains a comparison of the power supply and purpose-built data acquisition current outputs. Increased signal noise was observed with the power supply sensors compared to the LEM sensors previously discussed. Following this analysis, the data acquisition system was expanded to collect the hot-wire current and voltage signals in addition to the GTAW/GMAW current and voltage.

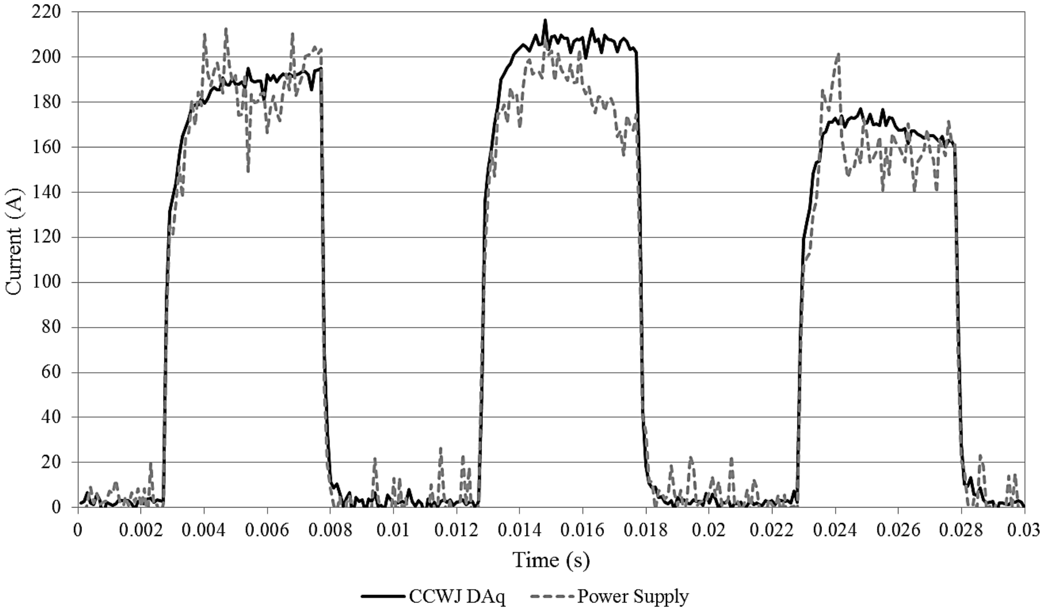

Figure 4.4: Comparison of pulsed hot-wire current waveforms captured with the CCWJ data acquisition or Babcock-Hitachi Ltd. power supply.

High speed videography was accomplished using a Phantom Miro eX4 or Phantom V210, a Nikon 180 mm f2.8D lens with 83 mm of extension tubes. Filtering of the arc light was accomplished using long-wave pass filters which work by cutting out the light with shorter wavelengths while allowing light with longer wavelengths to pass and be absorbed by the camera sensor. To remove the majority of the welding arc light, long-wave pass filters of 800 nm or 850 nm were used to collect the near-infrared emissions of the weld pool and decrease the arc light intensity.

4.2.3. Quantitative Carbide Volume Fraction Measurements

The volume fraction of tungsten carbide in the weld metal is a critical factor in the wear performance of the overlay. The fraction of carbide is typically measured either using existing software packages that were not designed specifically for carbide overlays or with manual techniques.

Measurement of tungsten carbide volume fractions in the weld deposits can be characterized two ways: overall tungsten carbide volume fraction in the weld deposit, f_c, and tungsten carbide transfer efficiency, η_c. The overall tungsten carbide volume fraction, calculated using Equation 4.1, is measured considering the total area of the weld metal, A_W, and the total area of tungsten carbide, A_{WC}, accounting for weld penetration and dilution with the substrate. Tungsten carbide transfer efficiency, calculated using Equation 4.2, is a function of the reinforcement area, A_R, the total carbide area, A_{WC}, and the initial wire carbide volume fraction, $f_{c,max}$.

The carbide transfer efficiency is an important measure when determining the total amount of tungsten carbide lost to dissolution or non-wetting during welding. It is essential to measure the tungsten carbide area, A_{WC}, using the entire weld cross section and total area of tungsten carbides. Use of a high magnification image for measuring the tungsten carbide area is not representative of the overall carbide distribution throughout the weld overlay. Figure 4.5 indicates the relative regions of the weld deposit used for calculating the tungsten carbide volume fraction and transfer efficiencies.

$$f_c = \frac{A_{WC}}{A_W}$$

Equation 4.1

$$\eta_c = \frac{A_{WC}/A_R}{f_{c,max}}$$

Equation 4.2

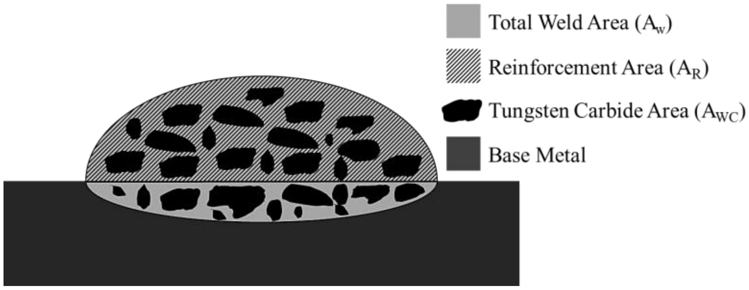

Figure 4.5: General schematic depicting the regions of the weld used in calculating f_c and η_c.

Measurement of the tungsten carbide area (A_{WC}) was completed using custom image analysis software designed specifically for characterizing Ni-WC overlays at the Canadian Centre for Welding and Joining. Carbide area measurement is conducted on the entire weld bead, creating a representative measurement of the true carbide fraction of the overlay accounting for dilution or any carbide settling that may have occurred. In order to obtain sufficient pixel density of the carbide-matrix-carbide interface region, high magnification (ex. 75X) inverted light microscope images are rastered over the entire weld cross section. The many images, ranging from 20 to over 100 individual images based on weld size, are then stitched, merged, and blended together. This typically results in an image ranging from 40 to over 100 megapixels, yielding sufficient carbide-matrix interface pixel density for accurate carbide identification.

Using an un-etched overlay cross section, the image analysis software converts the stitched color image to a binary black and white image wherein the carbides are separated from the matrix based on contrast differences. Once separated and highlighted, the image processing software performs morphological eroding and dilating operations to separate multiple individual carbide images that may have looked like a single larger carbide during the initial contrast separation stages. The morphological operations are important when creating size distribution histograms of the surviving tungsten carbides in the weld deposit. Distinguishing individual or linked carbides is aided by coloring separated carbides a unique color. Once colored, the image is visually examined for evidence of linked carbides. It is important to note that a particular color does not correspond with a specific carbide size.

The most influential operation is lower bound carbide area thresholding. Carbide area thresholding selectively eliminates particular size ranges from measurement. During welding, excessive weld pool temperatures can lead to carbide dissolution and re-precipitation of smaller deleterious tungsten-carbon containing phases. These re-precipitated phases decrease the erosion and erosion-corrosion performance of the overlay. The lower bound carbide area threshold is chosen based on high magnification microscopy to determine the upper bounded size of the re-precipitated carbides. Re-precipitated carbides typically are small (<20-30μm) and very angular while primary carbides are larger (50-200μm) and are more ovoid in shape. In oil sands mining applications, small carbides do not measurably increase wear performance in the Ni-WC material system and are eliminated from measurement [78]. The effect of lower bound size thresholding is demonstrated in Figure 4.6. The CCWJ-designed image analysis software is also capable of displaying individual carbide areas. This allows further analysis of the carbide size distribution and creation of a histogram, shown in Figure 4.7. The carbide sizes shown are the result of assuming the tungsten carbides are spherical, allowing easy calculation of the carbide diameters. In reality, this assumption is invalid but the influence of carbide size distribution on wear resistance is not the main focus of this work.

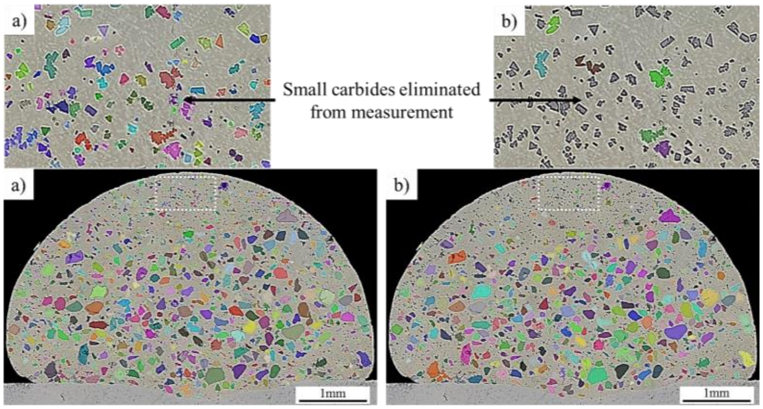

Figure 4.6: Effect of lower bound area threshold on carbide fraction. Image a) shows a weld cross section without lower bound area thresholding resulting in f_c of 31.5%. Image b) shows use of a lower bound threshold eliminating carbides <35µm from measurement resulting in a f_c of 26.8%.

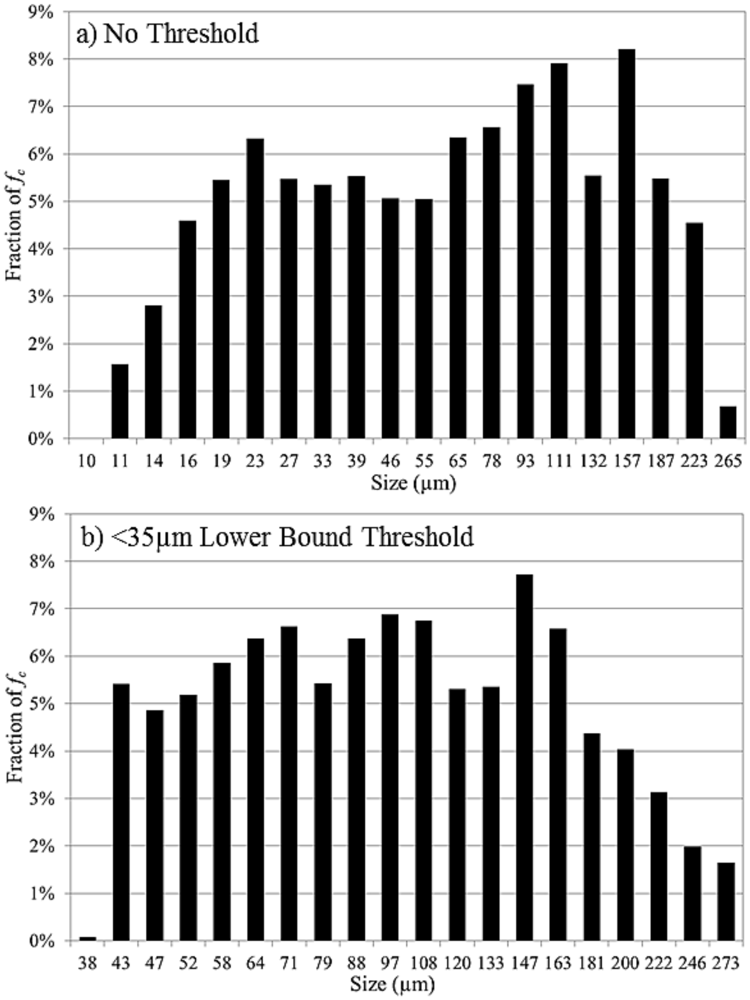

Figure 4.7: Carbide size distribution with a) no lower bound threshold and b) <35µm lower bound threshold corresponding to Figure 4.6.

4.3. Hot-Wire Assisted GTAW

The use of hot-wire assisted GTAW (HWGTAW) utilizing tubular Ni-WC wires has the ability to reduce the weld pool temperature and decrease the dissolution of the temperature sensitive tungsten carbides. The GTAW arc serves as a heat source to melt the base material and metallurgically fuse the weld metal to the substrate. The Ni-WC hot-wire does require a small amount of arc heat to provide a consistent melting condition as any Ni sheath thickness inconsistencies provide localized current density spikes. These spikes will cause the hot-wire to prematurely melt, breaking contact with the weld pool. Typically, the hot-wire current predicted using the electrode extension model proposed in Chapter 3 can be decreased slightly (ie. 1-2 A) to avoid premature melting.

The insertion location of the hot-wire is an essential factor in the welding stability and bead quality. Increasing the hot-wire distance from the arc, d, causes the wire to contact the weld pool solidification tail. Inserting the wire too close to the arc will cause higher carbide dissolution and premature wire melting, making the process similar to cold-wire GTAW. The hot-wire insertion angle, θ, plays a critical role in the retention of tungsten carbide following welding. Inserting the wire at a 60^{o} angle exposes the top of the nickel sheath to the arc heat, leading to premature sheath melting. A 30^{o} insertion angle moves the top of the nickel sheath away from the arc heat, keeping the nickel sheath intact and guiding the carbides directly into the weld pool, shown in Figure 4.8. The premature nickel sheath melting exposes the loose carbides to the turbulent arc plasma gases and arc heat, increasing carbide loss and dissolution. The adequate range of hot-wire current is larger at 30^{o} compared to 60^{o} as the wire can contact the bottom of the weld and skip underneath the arc, where it will be melted. The 60^{o} angle requires finer control of the current as insufficient current can cause the hot-wire to stub along the bottom of the weld pool.

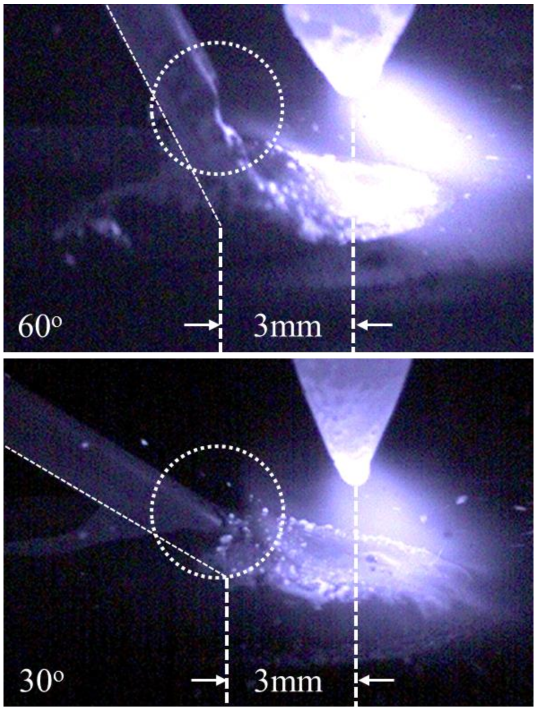

Figure 4.8: Effect of hot-wire insertion angle on the premature melting of the nickel sheath. A 60° insertion angle brings the top-side sheath into close proximity to the arc causing premature melting and carbide loss.

To view the interaction of the hot-wire in the weld pool, the GTAW current, hot-wire feeding, and welding travel are simultaneously halted. This creates a weld overlay with the hot-wire frozen in place. Longitudinally cutting the weld down the axis of the wire resulted in the cross section shown in Figure 4.9 and Figure 4.10. In Figure 4.9, the intact nickel sheath contacting the bottom of the weld pool is the result of insufficient hot-wire current which can lead to the wire wandering in the weld pool, increased carbide dissolution as the carbides are underneath the arc, and the electrode skipping into the GTAW electrode. With sufficient hot-wire current, the wire will completely melt before contacting the bottom of the weld pool, shown in Figure 4.10. Proper hot-wire melting improves bead shape consistency by eliminating wire wandering and decreases carbide dissolution. Closer inspection of the wire interior revealed extremely fine eutectic Ni_3B surrounding the carbides which formed as a result of the low melting temperature alloying additions. The reason for the formation of Ni_3B is unclear as the boron carbide powders identified in Chapter 2 have a very high melting temperature (~2700 °C). As seen in Figure 4.9 and Figure 4.10, the tungsten carbides are surrounding by a liquid prior to the weld pool. The effects of the prolonged contact time between carbide and liquid phases are unknown on carbide dissolution.

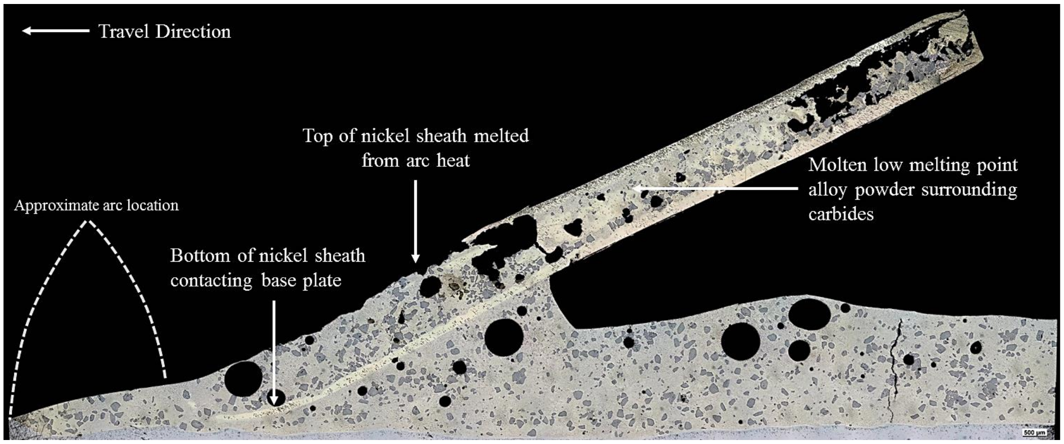

Figure 4.9: HWGTAW of Consumable A depicting the hot-wire frozen into the weld pool. High quantities of low melting point alloys of Al, Mg, and Si are suspected to be encasing the tungsten carbides inside the hot-wire.

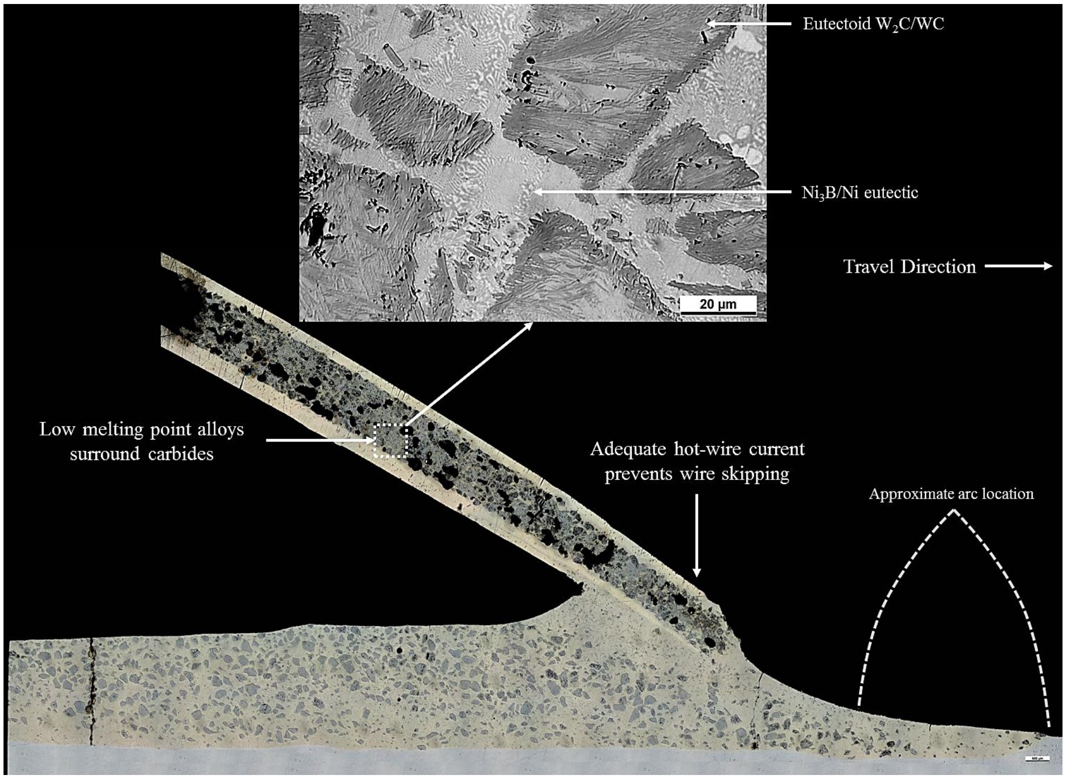

Figure 4.10: HWGTAW of Consumable F depicting the hot-wire frozen into the weld pool. Sufficient hot-wire current prevents wire from contacting bottom of weld pool and low melting point alloys surround the carbides in the powder core.

Table 4.1 below contains the GTAW and hot-wire welding parameters used during welding of Figure 4.11-Figure 4.16. The following welding parameters were utilized for all overlays: travel speed was kept constant at 0.5 m·min^{-1} (20 ipm), arc length fixed 3 mm (0.125 in.), 3 mm (0.125 in.) 2% thoriated electrode with 60^{o} grind, hot-wire insertion angle of 30^{o}, and a fixed hot-wire distance, *d*, of 3 mm (0.125 in.). Wire feed speed was kept constant at 3 m·min^{-1} and a hot-wire electrode extension, L_o, of 70 mm during all tests. Arc current had to be increased with Consumable E to maintain an acceptable bead shape compared to other wires. Overlays could not be completed using Consumable G due to wire feeding problems encountered with the hot-wire feeding system. The weld cross sections for Consumables A-F is shown in Figure 4.11-Figure 4.16 with their respective carbide volume fractions (f_c) measurements.

Table 4.1: GTAW and hot-wire welding parameters used for Consumables A-F in Figure 4.11-Figure 4.16.

Consumable	**GTAW Current** (A)	**HW Current** (A, RMS)
A	200	157
B	200	161
C	200	143
D	200	144
E	215	170
F	200	158

Figure 4.11: Consumable A with f_c of 9%.

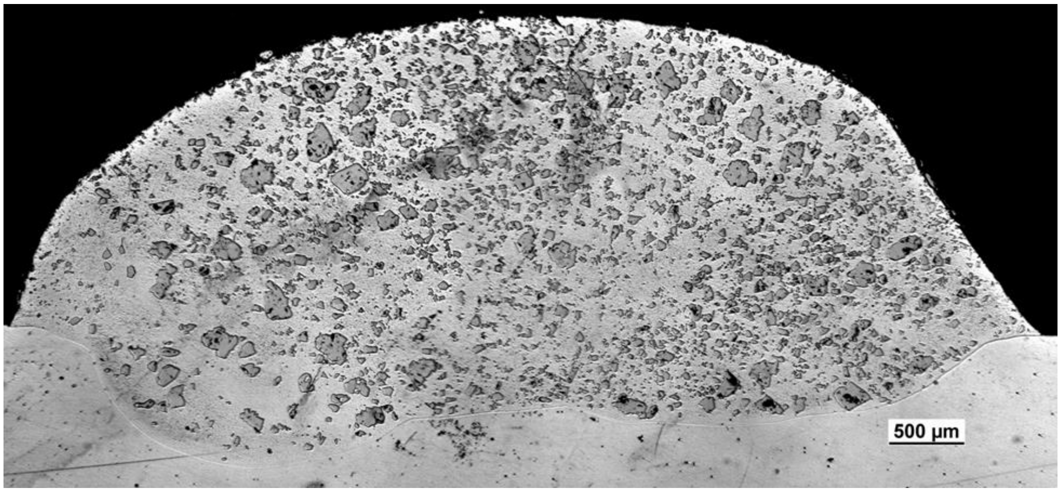

Figure 4.12: Consumable B with f_c of 30%.

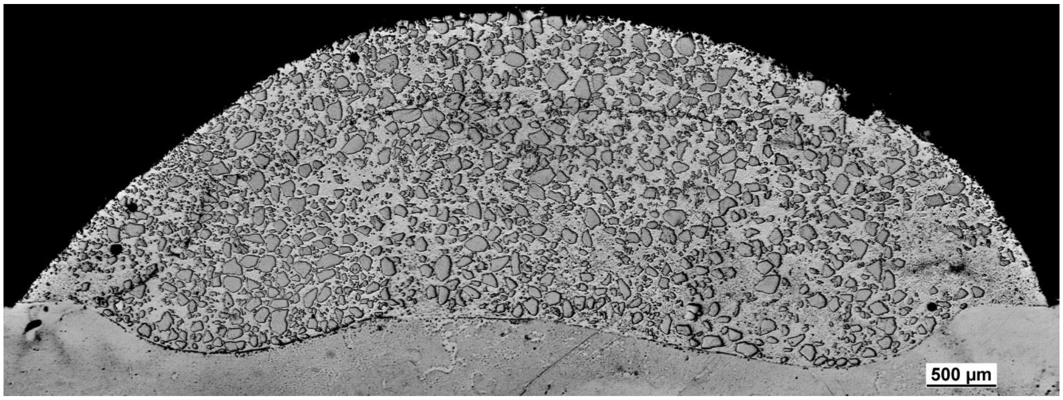

Figure 4.13: Consumable C with f_c of 49%.

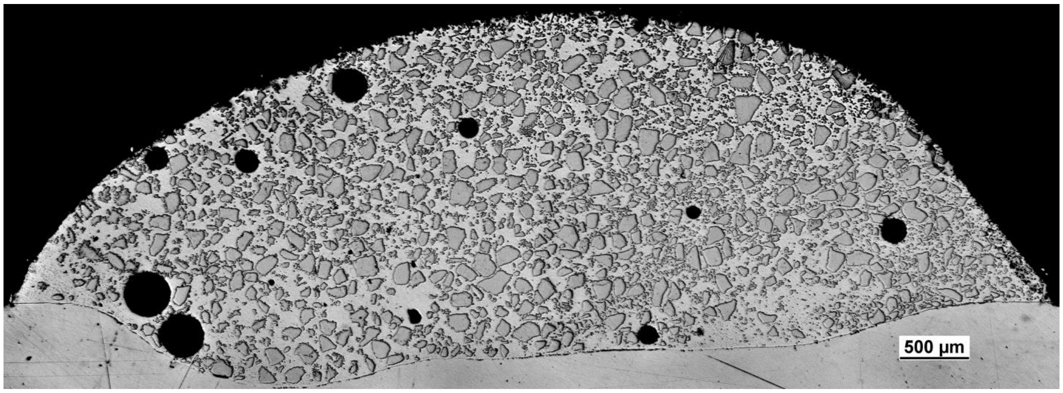

Figure 4.14: Consumable D with f_c of 48%.

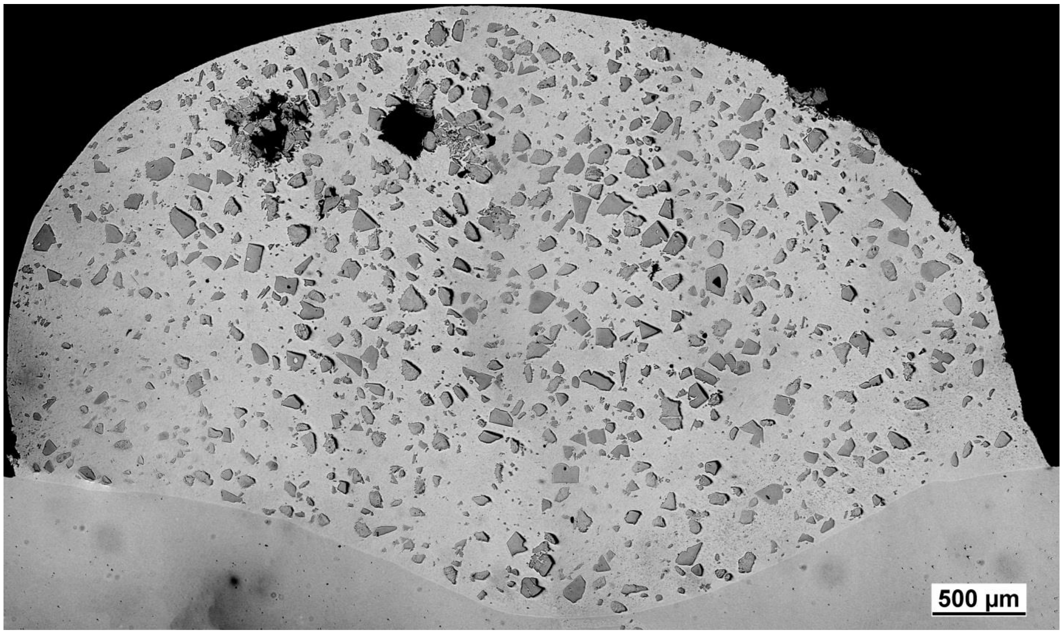

Figure 4.15: Consumable E with f_c of 22%.

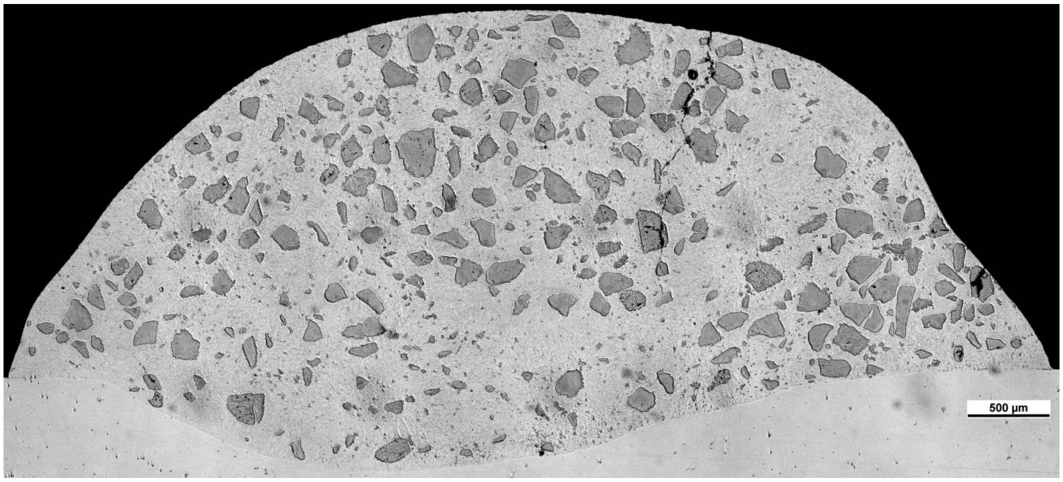

Figure 4.16: Consumable F with f_c of 24%.

The Ni-WC overlays shown in Figure 4.11-Figure 4.16 indicate that the volume fraction of carbides in the overlays can vary considerably with similar welding parameters. Consumables C and D produced high volume fraction overlays at a deposition rate of 3.3 kghr^{-1} (7.2 lbhr^{-1}) which is comparable to industrial scale PTAW deposition rates. The volume fraction of the Ni-WC overlays produced using HWGTAW are high enough to be considered as a viable option to PTAW.

The hot-wire GTAW process does however have one major drawback. During welding, the GTAW tungsten electrode becomes contaminated and eventually causes the arc to become unstable. This contamination buildup can occur in as little as 30 cm of weld, shown in Figure 4.17. Following contamination, the GTAW electrode has to be re-ground before welding operations can continue. It was observed that contamination varied between Consumables however contamination was typically lower when using a thick nickel sheathed Consumable.

Analysis of HWGTAW high speed videos indicated that contamination was the result of weld pool oscillations. The tubular consumables carry a certain volume of air into weld pool due to their powder core. The escaping weld pool air bubbles create an inflection and a weld pool surface reverberation that ejects a Ni-WC droplet that can contact the GTAW electrode, as shown in Figure 4.18 and Figure 4.19. This phenomenon is akin to a drop of water being vertically ejected from a perturbed water surface. Furthermore, the changing magnetic fields between the pulsed hot-wire and GTAW electrode can cause a deflection in the droplet trajectory, shown in Figure 4.18.

Figure 4.17: GTAW electrode contamination from Consumable D after approximately 30 cm of welding.

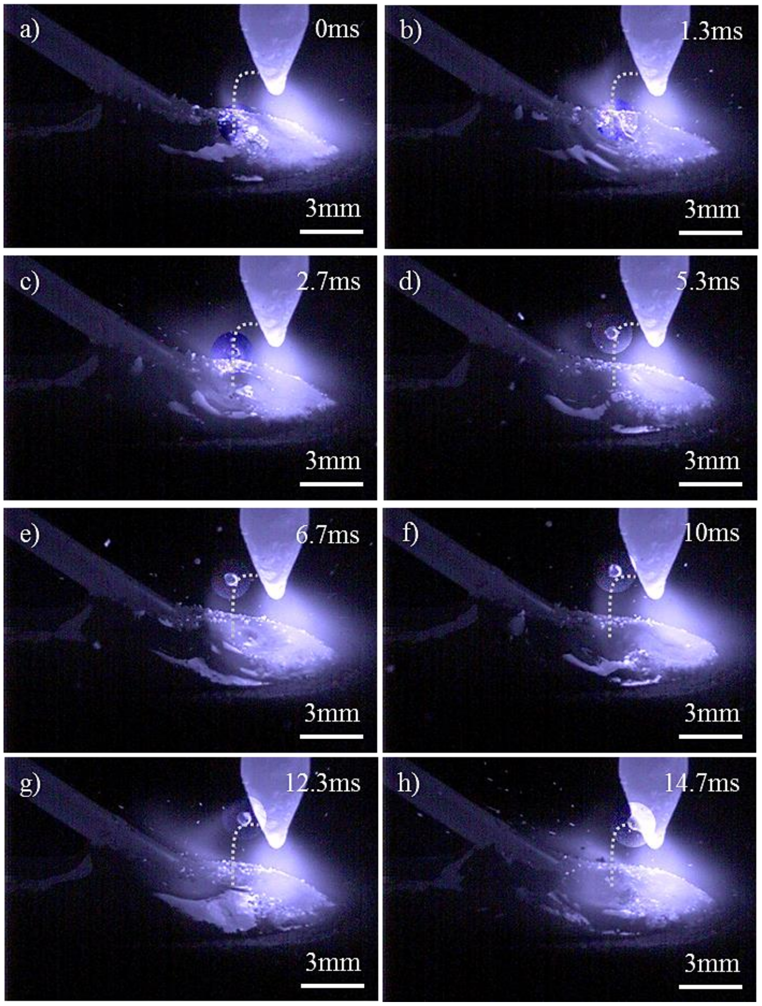

Figure 4.18: GTAW electrode contamination during welding of Consumable F. Ejected vertical droplet trajectory changes at 6.7 ms due to hot-wire pulse creating a magnetic field that drives the droplet towards GTAW electrode.

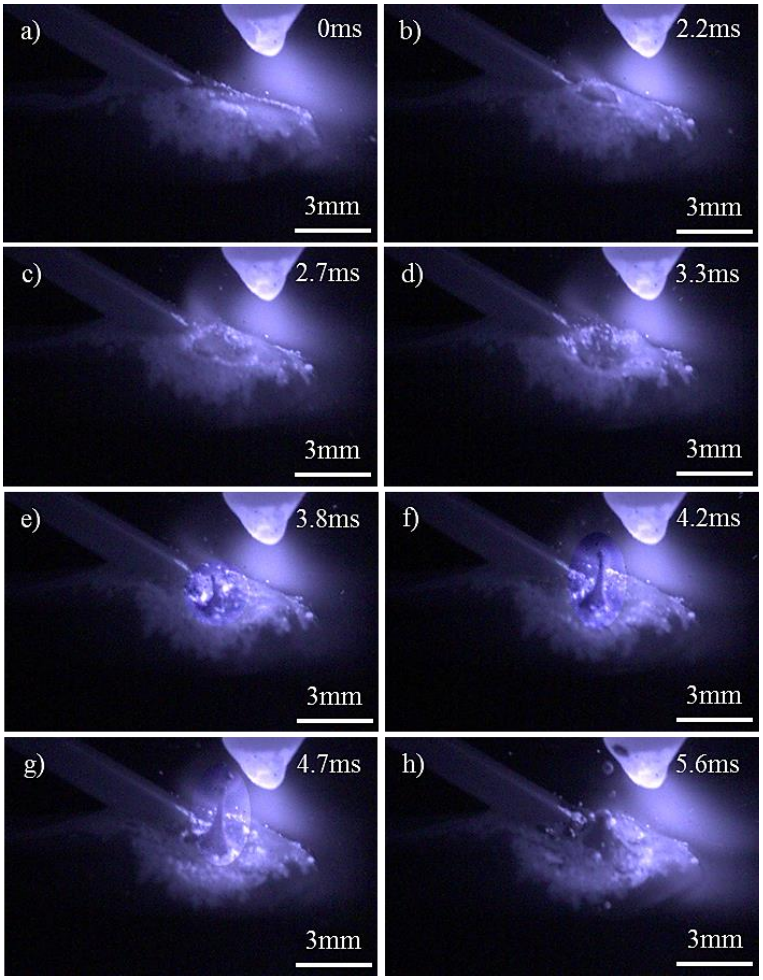

Figure 4.19: Escaping air bubble induces a weld pool surface reverberation that ejects a molten Ni-WC droplet, leading to GTAW electrode contamination during welding of Consumable F.

To determine the contamination constituents, AES was conducted on a longitudinally cut electrode that was polished to 0.5µm finish. Figure 4.20 below shows the SEM image of the contaminated GTAW electrode and Table 4.2 contains the measured atomic compositions. The chemical makeup of the contamination layer is tungsten and carbon based with trace amounts of iron and nickel. The presence of copper detected in Points 2 and 4 is of unknown origins while the high concentrations of thorium and oxygen in Point 6 indicates that the 2% thoriated electrode additions are from thorium oxide stringers.

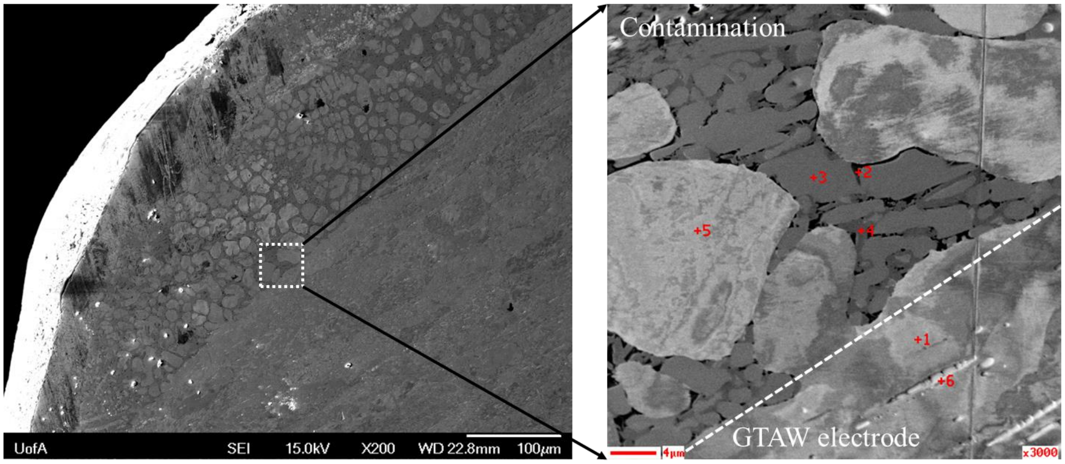

Figure 4.20: AES analysis of GTAW electrode contaminated with Consumable D.

Table 4.2: Atomic composition of the AES analysis conducted on contaminated electrode in Figure 4.18.

	Atomic Composition (at%)						
Point	**W**	**C**	**O**	**Fe**	**Cu**	**Ni**	**Th**
1	89.7	7.7	1.9	0.7	0	0	0
2	4.2	15.0	1.8	0	79	0	0
3	90.6	4.1	5.3	0	0	0	0
4	57.3	24.6	1.8	1.8	4.7	9.9	0
5	89.2	8.6	2.1	0	0	0	0
6	6.8	6.1	68.5	0	0	0	18.6

4.4. GMAW with Ni-WC Consumables

The contamination of the GTAW electrode made the process unstable and not industrially viable despite its excellent overlay metallurgy. The use of hot-wire assisted GMAW was researched to determine the feasibility of the process for industrial usage. Individual characterization of the Ni-WC GMAW process was completed to determine optimum carbide transfer efficiencies prior to the addition of a Ni-WC hot-wire.

Parametric studies of shielding gas compositions, welding parameters, metal transfer modes, and welding consumables were conducted to determine the optimum carbide transfer efficiencies. Analysis was conducted using data acquisition, high speed video, and carbide volume fraction image analysis. Initial GMAW studies were conducted using Consumable F operating in DCEP and short-circuit and free-flight globular metal transfer modes. Fifteen welds with current ranges from 122-240 A and argon-based shielding gases were investigated with high speed video and metallurgically characterized, summarized in Table 4.3. The tungsten carbide transfer efficiencies, η_c, showed a marked difference between metal transfer modes, with short-circuit retaining higher fractions of carbides than free-flight transfer. In globular transfer, it was observed that there was separate transfer of the nickel sheath and carbide powders. The following sections will discuss carbide loss mechanisms, including the newly documented non-wetting of tungsten carbide, and optimizing the GMAW process prior to the addition of the hot-wire.

Table 4.3: Summary of Consumable F GMAW welding parameters.

Weld	**Shielding Gas**	**WFS (ipm)**	**Current (A)**	**Voltage (V)**	**Transfer Mode**	**f_c (%)**	**η_c (%)**
1	95Ar-5CO_2	120	156	19.5	Short-Circuit	17.5	60.4
2	95Ar-5CO_2	185	235	29	Globular	7.03	28.3
3*	95Ar-5CO_2	185	240	31	Globular	6.4	25.6
4	70Ar-30CO_2	120	147	20	Short-Circuit	13.8	49.9
5	70Ar-30CO_2	185	225	32.5	Globular	2.7	13.6
6	98Ar-2O_2	120	163	17	Short-Circuit	26.3	83.5
7	98Ar-2O_2	185	234	28.1	Globular	13.3	49.3
8	85Ar-15O_2	120	180	12	Short-Circuit	24.4	83.2
9	85Ar-15O_2	185	237	27.5	Globular	7.3	28.7
10*	85Ar-15O_2	185	235	29	Globular	5.8	20.0
11	95Ar-5O_2	80	125	16.1	Short-Circuit	26.8	79.0
12	95Ar-5O_2	80	122	16.1	Short-Circuit	23.5	75.4
13	95Ar-5O_2	120	166	17.5	Short-Circuit	23.8	81.1
14	95Ar-5O_2	140	183	18	Short-Circuit	21.3	71.3
15	95Ar-5O_2	165	208	18.9	Short-Circuit	19	64.0

*: 2-layer welds where substrate is a previously deposited Ni-WC weld bead with same parameters.

4.4.1. Non-Wetting of Tungsten Carbide to a Ni Weld Pool

Carbide loss mechanisms have traditionally been attributed to only dissolution, where the hot welding arc and weld pool overcome tungsten carbides low heat of formation [73]. The dissolution loss mechanism is extensively documented and discussed in PTAW, laser cladding, and GMAW literature (see Chapter 1.3.3). The following work will present a new loss mechanism, observed directly for the first time, to explain the traditionally low carbide volume fractions in Ni-WC overlays deposited by GMAW. The non-wetting of tungsten carbide is observed in free-flight globular and short-circuit metal transfers. The non-wetting tungsten carbide agglomerates were characterized to determine the constituents of the non-wetting powder.

Free-flight metal transfer is characterized by the non-axial transfer of molten droplets across the welding arc. In Ni-WC free-flight metal transfer, the carbide powder is transferred separately from the molten nickel droplet. The powder transfers across the arc in small agglomerates as the low melting temperature alloy additions hold multiple tungsten carbides together. The falling agglomerated carbides strike the surface of the nickel weld pool and do not wet to the liquid surface, leading to rejection and lower carbide volume fraction in the deposit. The non-wetting behaviour is observed during single (Welds 2, 5, 7, and 9) or multi-layer (Welds 3 and 10) welding where the substrate is either a steel plate or a previously deposited Ni-WC bead.

Figure 4.21 contains a series of high speed video frames that tracks an agglomerated carbide leaving the wire and transfers across the arc where it contacts the weld pool and is rejected due to the non-wetting behaviour. The carbide non-wetting and rejections occur repeatedly during the welding operations, lowering the carbide volume fraction in the deposit.

The globular metal transfer weld deposits showed considerable tungsten carbide dissolution typically associated with fast kinetics overcoming the low heat of formation of tungsten carbide [73]. The combined carbide loss mechanisms of dissolution and non-wetting resulted in deposited tungsten carbide volume fractions of 3-13% and transfer efficiencies of 14-37%, demonstrated in Figure 4.22. It should be noted that pure free-flight globular transfer (ie. sufficiently high current and voltage) was used to complete the weld deposits shown. A lower current and voltage will result in intermittent short-circuits and can potentially reduce the amount of carbide dissolution and increase the retained carbide volume fraction.

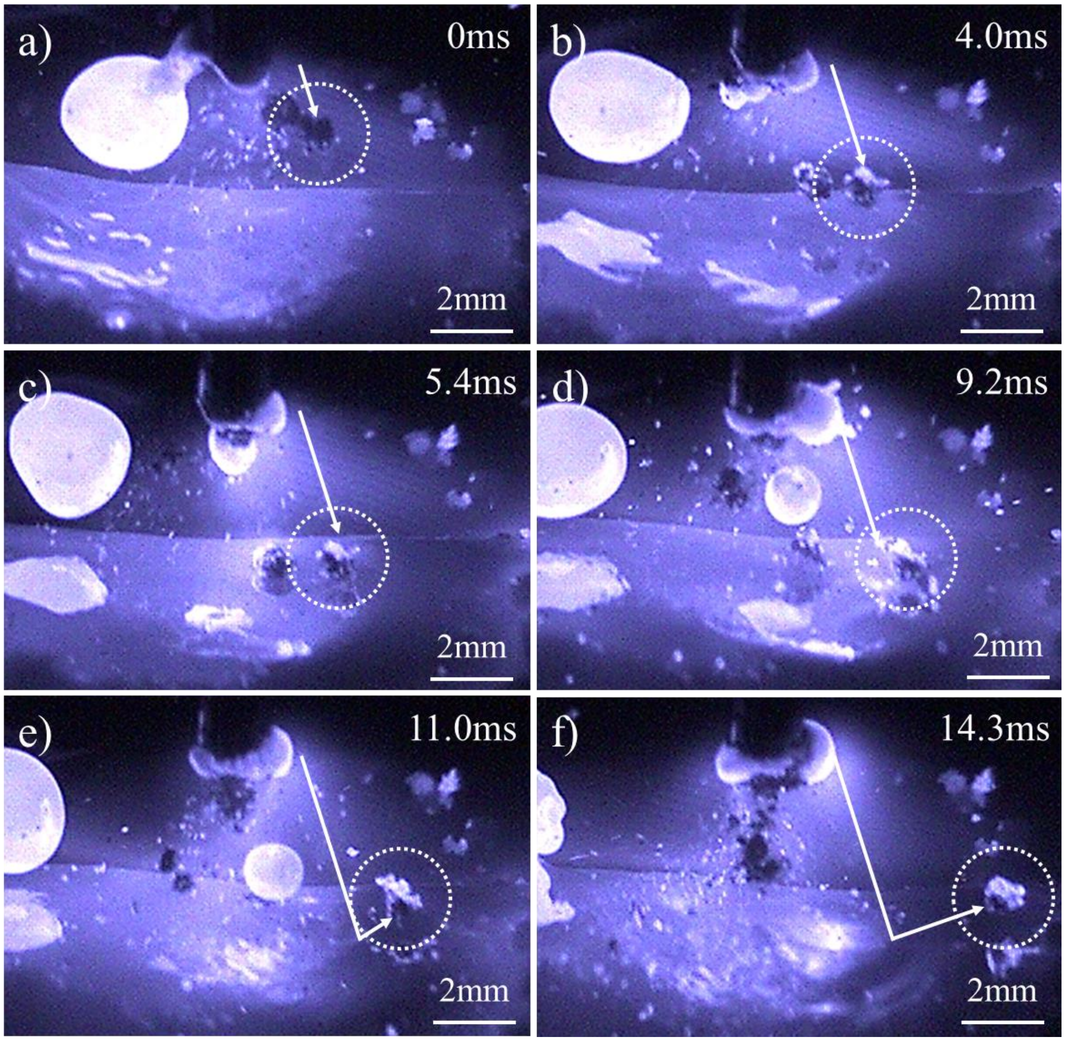

Figure 4.21: Tungsten carbide powder and agglomerates bouncing off the nickel weld pool (Weld 3). The dashed circle and arrow highlights the trajectory of an individual agglomerate of powders. Frames a) to c) show the agglomerate approaching the free surface. Frame c) was taken very close to the time of impact on the free surface and Frame d) shows the agglomerate reflection after contact with the weld pool surface. Frames e) and f) show the agglomerate leaving the weld pool free surface and is not entrained in weld overlay.

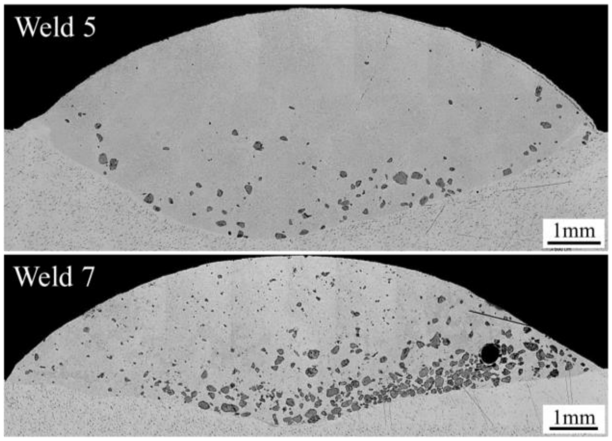

Figure 4.22: Typical globular free-flight Ni-WC deposits. Weld 5 resulted in f_c=3% and η_c=14% and Weld 7 resulted in f_c=13% and η_c=37%.

The non-wetting phenomenon is also observed during short-circuit metal transfer mode, however to a lesser extent. Although the wire periodically contacts the weld pool and injects the carbides directly into the weld pool during the short-circuiting periods, a portion of the carbides can be seen sitting on the weld pool surface.

High speed video analysis shows that these surface non-wetting carbides result from the droplet formation period of the short-circuit transfer, where loose carbides fall out of the wire and remain on the weld pool surface. Immediately following the droplet formation and the arc extinguishment (short-circuit) periods, the rising current and arc pressure of the arc re-ignition phase expels the non-wetting carbides off the weld pool surface. Figure 4.23 contains high speed video frames from Weld 15 tracking a non-wetting carbide agglomerate discharged from the weld pool free surface during short-circuit metal transfer.

While the majority of carbides are directly injected into the weld pool during the short-circuit period, a portion of the carbides are blown away from the weld pool. As a result, typical GMAW deposits can contain lower carbide volume fractions than originally desired, demonstrated in Figure 7. The short-circuit deposits showed no evident carbide dissolution and contained a measured tungsten carbide volume fraction of 14-26% and a carbide transfer efficiency of 40-83%. The tungsten carbide transfer efficiency indicates that a minimum of 20% of the carbides are lost to non-wetting during welding for the consumables and parameters studied.

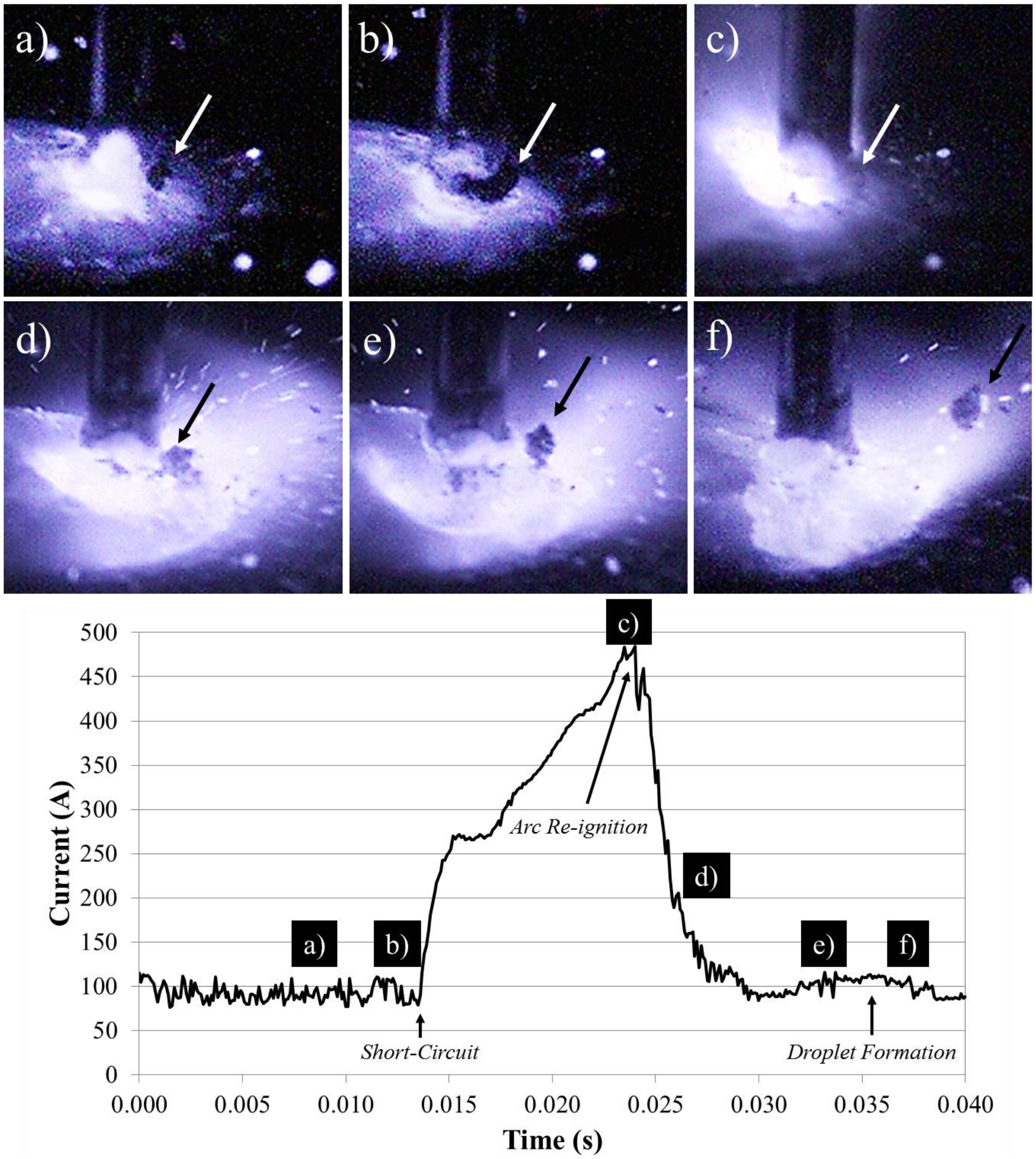

Figure 4.23: Non-wetting carbide agglomerate expelled from weld pool free surface in short-circuit GMAW (Weld 15). Frame a) shows carbide agglomerate leaving the wire core during the droplet formation period. During the short-circuit period shown in Frame b), the agglomerate is not entrained into the weld pool prior to arc re-ignition of Frame c). The non-wetting carbide agglomerate is tracked in Frames d), e), and f) as it is blown off the weld pool free surface.

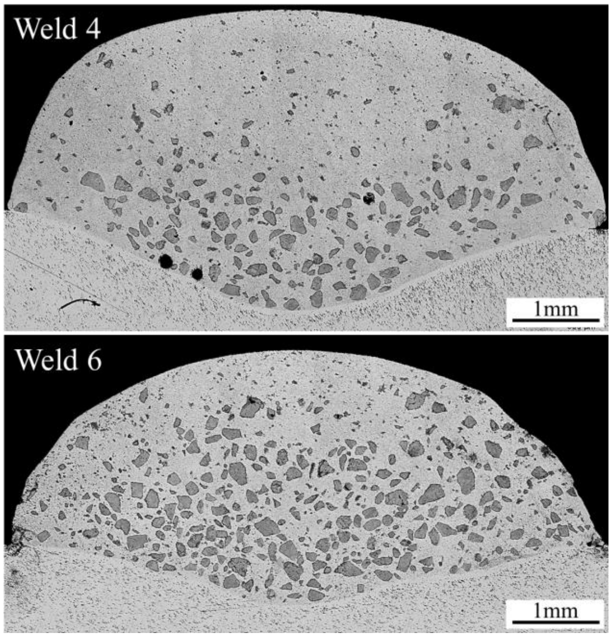

Figure 4.24: Typical short-circuit Ni-WC deposits. Weld 4 resulted in a f_c=14% and η_c=40% and Weld 6 resulted in a f_c=26% and η_c=83%.

Following the discovery of the non-wetting behaviour, a general map of tungsten carbide loss mechanisms can be formed, summarized in Figure 4.25. In the short-circuit transfer welds conducted, carbide dissolution was not observed. The higher currents and voltages of free-flight globular transfer provided sufficient kinetic driving force to cause carbide dissolution. In all metal transfer modes, the non-wetting phenomenon contributed to the low carbide volume fractions in the weld deposits.

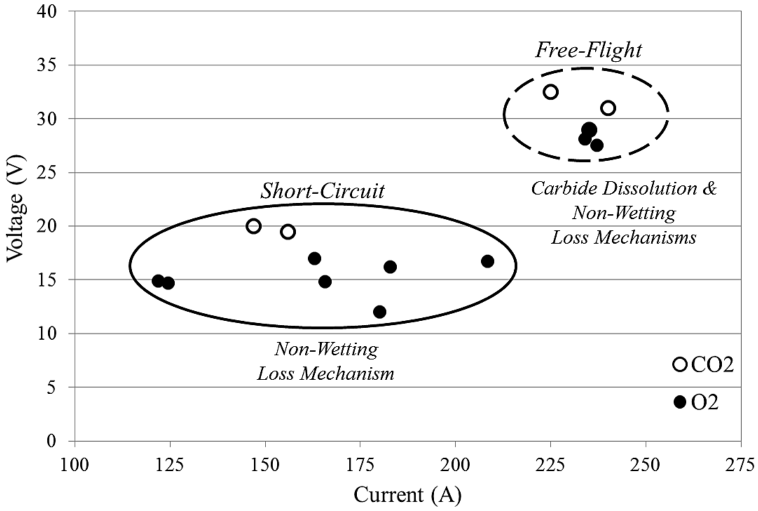

Figure 4.25: Tungsten carbide loss mechanisms during short-circuit and free-flight metal transfer modes for Consumable F.

Characterization of the ejected non-wetting powder and spatter was completed by collecting the spatter off an alcohol cleaned steel plate surface following welding. The spatter was collected by gently brushing any loose particles off the plate surface. Analysis of the spatter was completed using a Zeiss EVO MA 15 scanning electron microscope equipped with a Bruker Silicon Drift Detector for Energy Dispersive X-ray (EDX) analysis.

High speed video analysis of Weld 3 (corresponding to Figure 4.21) revealed high amounts of rejected non-wetting powders and low carbide volume fractions in the weld deposit. Characterization of the non-wetting powders and spatter collected from Weld 3, a two-layer free flight metal transfer weld shielded with 95Ar-5CO_2 shielding gas, was completed and summarized in Figure 4.26 and Table 4.4. Stereomicroscopy and SEM indicates that the non-wetting powders are primarily agglomerates (~0.5-1 mm) comprised of much smaller individual tungsten carbide and alloying powder particles (shown in Figure 2.9).

Closer inspection of the individual particles in the agglomerates using EDX showed the presence of tungsten carbide and boron alloying particles summarized in Table 4.4. Portions of the agglomerates are observed to be partially melted tungsten carbides likely due to their proximity to the hot welding arc, depicted by

Particles 1, 3, 5, and 6. While some particles are observed to be partially melted, other particles do not appear to be melted. Particles 8-10 in Figure 4.26 appear to retain their original morphology following welding. While Particles 8-10 are boron alloying particles and Na-F-K arc stabilizing powders, several individual tungsten carbides seen in Figure 4.26b) and Figure 4.26d) are observed to retain their original morphology following welding when compared to Figure 2.9. The surface of Particle 10, a B_4C alloying particle, shows distinct film-like regions of high tungsten concentrations, resulting from direct contact with molten tungsten carbide. The high concentration of oxygen measured on nearly all particles is a result of the particles oxidizing in the CO_2 containing welding arc and further oxidizing once the particles have travelled outside the GMAW shielding gas envelope on the plate surface. The presence of relatively low amounts of Ni on the particle surfaces indicates low wetting between the rejected powders and nickel weld pool.

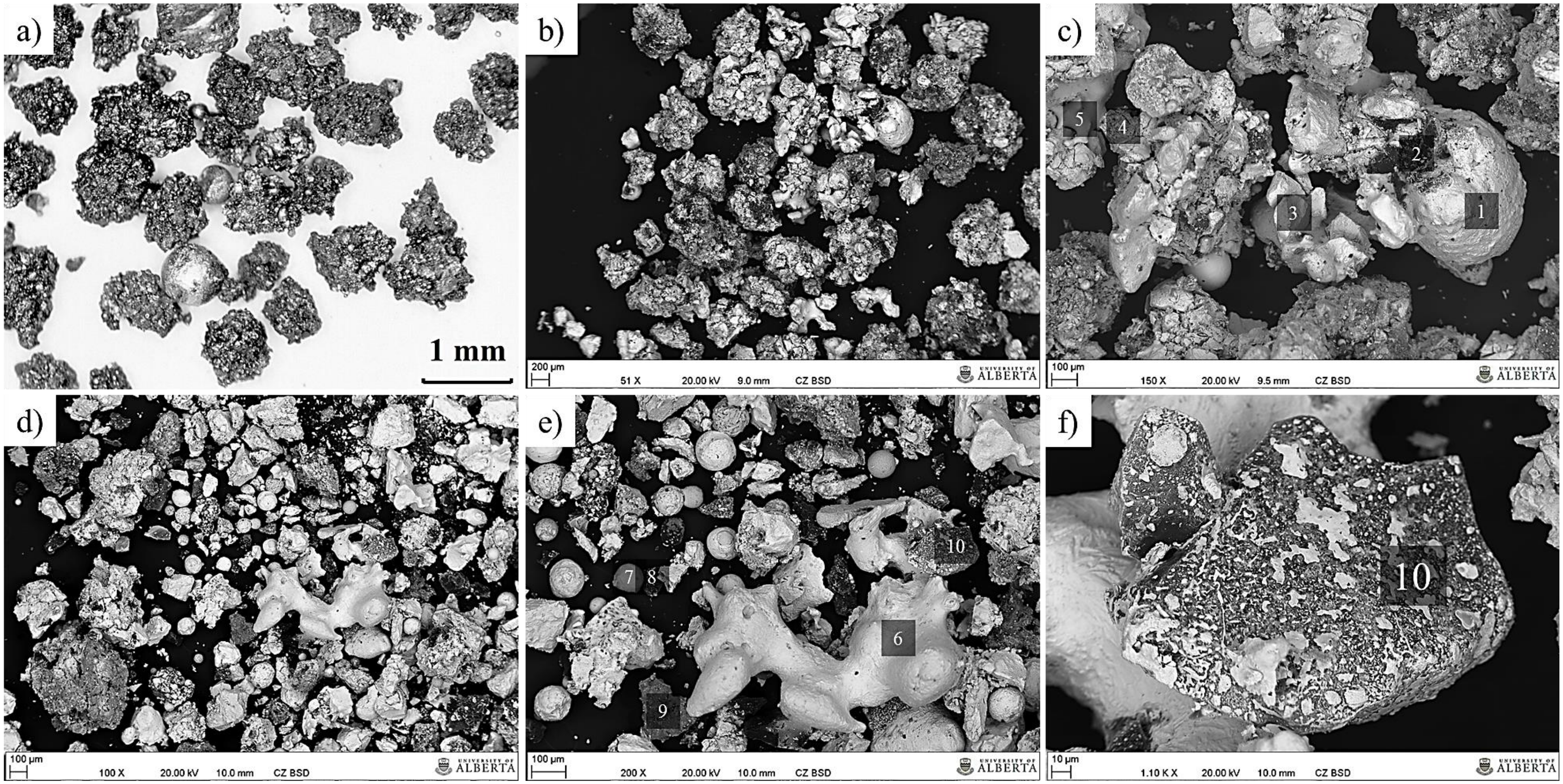

Figure 4.26: Characterization of non-wetting powders and weld spatter from Weld 3. Image a) is a stereomicroscope image of the collected powders while b)-f) contains backscattered SEM images of the spatter and agglomerates. Individual particle EDX measurements and suggested particle morphologies can be found in Table 4.4.

Table 4.4: Summary of Weld 3 EDX measurements of individual non-wetting powder particles (Particles 1-10) depicted in Figure 4.26.

	Powder Composition (at%)									
Particle	**W**	**C**	**O**	**Ni**	**Fe**	**B**	**Na**	**F**	**K**	**Suggested Particle**
1	20.5	28.2	45.3	-	-	-	1.7	2.4	0.6	Tungsten Carbide
2	1.2	17.3	-	-	-	82.3	-	-	-	B_4C Alloying Powder
3	42.7	30.5	26.8	-	-	-	-	-	-	Tungsten Carbide
4	14.2	7.10	68.6	1.9	0.4	-	1.7	4.0	2.1	Tungsten Carbide
5	11.3	21.7	65.8	0.7	-	-	-	-	0.5	Tungsten Carbide
6	31.5	15.7	49.5	2.5	0.9	-	-	-	-	Tungsten Carbide
7	30.0	18.9	23.8	-	-	27.3	-	-	-	Tungsten/Boron Carbide
8	-	15.8	2.0	0.9	-	81.0	-	-	-	B_4C Alloying Powder
9	0.9	5.4	35.1	6.7	0.4	-	16.6	31.0	3.8	Na/F Based Particle
10	3.0	10.6	10.2	1.1	-	74.8	-	-	-	B_4C Alloying Powder

The non-wetting of tungsten carbide is driven by the surface interactions between the carbides and weld pool. The fact that tungsten carbide readily dissociates in molten metal indicates a high chemical reactivity. A high chemical reactivity is usually associated with good wetting between the two species [133]. The lack of wetting between the falling carbide agglomerates and the nickel surface is consistent with an oxide layer on the weld pool free surface [134]. Oxidizing additions to the shielding gas are used to stabilize the highly mobile cathode spot in GMAW. This will form an oxide layer on the weld pool surface which may interfere with the wetting of tungsten carbide and nickel.

Tungsten carbide is approximately twice the density of nickel and is often observed sinking and settling to the bottom of the weld during PTAW welding with powder consumables [55], [101]. During laser cladding with Ni-WC powder, tungsten carbides have been observed to enter the weld pool without non-wetting problems [135]. This indicates that the surface interactions between tungsten carbide and molten Ni in GMAW are very different than PTAW or laser processes. The lack of non-wetting in PTAW and laser can be a result of particle impingement velocity. In laser and PTAW applications, the particles are accelerated towards the weld pool with a mechanical and gas feeding system. Analysis of high speed videos completed at the Canadian Centre for Welding and Joining of laser and PTAW processes shows that the impingement velocity might be sufficient to overcome the weld pool free surface force balance as non-wetting is not observed [136]. Furthermore, PTAW and laser processes utilize inert pure argon shielding gas to protect the molten nickel pool. The lack of active oxidizing compounds may also prevent the formation of an oxide layer on the weld pool surface, promoting carbide entrainment. The falling tungsten carbide particles and agglomerates in GMAW may not have sufficient force to overcome the surface tension of the weld pool surface.

To increase the deposit carbide fraction, it is imperative that the wetting between the weld pool and tungsten carbides be increased or the kinetic energy of the impinging carbide agglomerate. This can involve surface modification of the tungsten carbide, such as applying a thin metallic coating (ex. Ni) [137]. In aluminum matrix material systems, modification of the ceramic particle surface with a metal has been shown to increase wetting [134]. The metallic coating may aid in wetting as the particle-liquid interface will be of the same material.

4.4.2. Optimizing Carbide Fraction in GMAW Ni-WC

Analysis of the carbide volume fractions and transfer efficiencies of the 15 welds completed in Table 4.3 revealed several trends. Perhaps the most discernable is the correlation between welding current and carbide transfer efficiency. As welding current increases, the carbide transfer efficiencies exhibit a marked decline. This has been shown to be related to the amount of tungsten carbide dissolution and/or non-wetting depending on the metal transfer mode. However, within the short-circuit transfer regimes, the carbide transfer efficiencies do vary considerably. A distinct increase in η_c is observed when utilizing an O_2-containing shielding gas compared to Ar-CO_2, despite similar welding parameters. Traditionally, the addition of an oxidizing gas such as CO_2 to argon-rich gas mixtures can stabilize the GMAW welding arc. However in the Ni-WC material system, CO_2 cannot provide sufficient arc stabilization compared to O_2. Molten nickel is resistant to oxidation, therefore emitting less electrons and de-stabilizing the cathode spots. The addition of O_2 increases the oxidation rate of the nickel weld pool, increasing arc stability during the droplet formation period.

This phenomenon was observed non-qualitatively with high speed video however analysis of the current/voltage signals collected during welding provides some insight into metal transfer stability. Fast Fourier Transforms (FFT) is a relatively simple method to determining dominant frequencies inside large complex data sets. For example, if we consider short-circuit metal transfer where the voltage fluctuates during welding. Anytime the molten droplet contacts the weld pool, the arc is extinguished and the voltage drops to near-zero and then rapidly increases when the arc is re-established. This voltage fluctuation repeats itself at a frequency characteristic of the welding process and parameters. FFT analysis can be easily performed on large data sets within programs such as MATLAB.

To determine the effect of shielding gas on metal transfer stability and carbide transfer efficiencies, 5 seconds of voltage signals (corresponding to 50000 data points) of Weld 4 and Weld 15 were compared using FFT analysis. The O_2 bearing weld a more dominant metal transfer frequency set compared to the CO_2 bearing gas, shown in Figure 4.27. Dominant frequencies (ie. higher individual signal peaks) are indicative of consistent short-circuit events. The CO_2 bearing metal transfer exhibited no such dominant peaks, signifying random and inconsistent metal transfer. While FFT is a useful tool, one must consider the magnitude of the current during the arc re-ignition phase of short-circuit transfer.

Let us consider a comparison between Weld 13 and Weld 15. Both are short-circuit transfers with an Ar-O_2 shielding gas, and both have similar FFT frequencies and signal peaks yet there is a marked difference in carbide transfer efficiency (81% and 64% respectively). The lower wire feed speed of Weld 13 results in lower peak currents during the arc re-ignition phase, providing a less explosive force to expel any non-wetting tungsten carbides. The higher wire feed speeds of Weld 15 dictate that a higher peak current is necessary to re-establish the arc and prevent stubbing, providing a more rapid and explosive force.

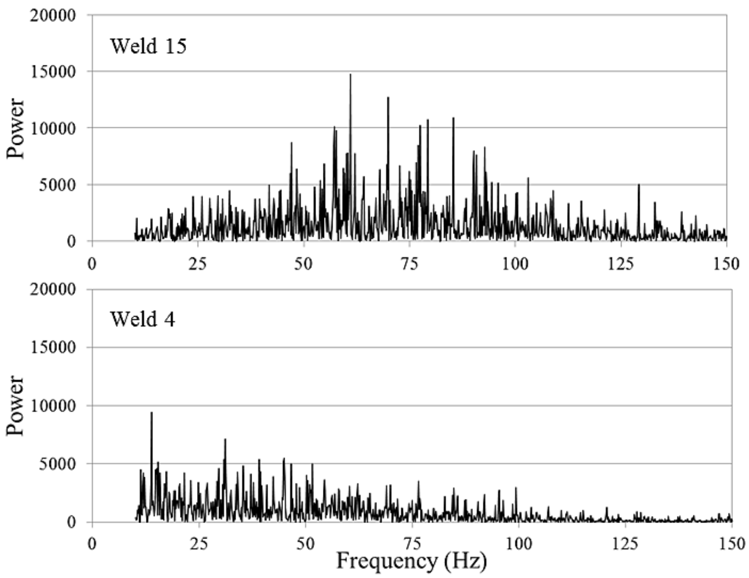

Figure 4.27: FFT comparison of O_2 bearing shielding gas (Weld 15, 85Ar-15O_2) to CO_2 bearing shielding gas (Weld 4, 70Ar-30CO_2).

The large variance between the consumables studied posed wire-specific welding difficulties. Previous welding studies utilized Consumable F which had a low initial carbide volume fraction (~35%) and a thick nickel sheath. Consumable D with a thin nickel sheath and high initial wire carbide volume fraction was further studied to determine optimum parameters to maximize GMAW carbide fraction prior to the hot-wire addition. Welding parameters were 3 m·min^{-1} wire feed speed, 16.5 V, 0.5 m·min^{-1} travel speed, 18 mm CTWD, and 85Ar-15O_2 shielding gas.

The weldability of Consumable D is drastically lower than the thicker sheathed Consumable F. The welding arc could no longer be stabilized with 2% O_2 but required 15%O_2 to maintain a stable short-circuit. Due to the thin nickel sheath, small changes in welding parameters have a drastic effect on the metal transfer mode. Whereas the stable short-circuit region for Consumable F stretched from 80-165 ipm WFS, Consumable D was only able to attain a stable short-circuit transfer between 110-130 ipm WFS due to high current density of its thin Ni sheath.

Carbide volume fraction analysis of the weld bead from Consumable D with no lower bound size threshold resulted in an exceptional 41% carbides, shown in Figure 4.28. Further analysis of the carbides and the carbide size distribution histogram showed high concentrations of small undesirable carbides, depicted in Figure 4.29. Applying a minimum size threshold to the volume fraction measurements, the carbide volume fraction dropped to 24%. Due to the small stable transfer region and high carbide losses of thin sheathed consumables, thicker sheathed consumables were used for GMAW prior to hot-wire additions.

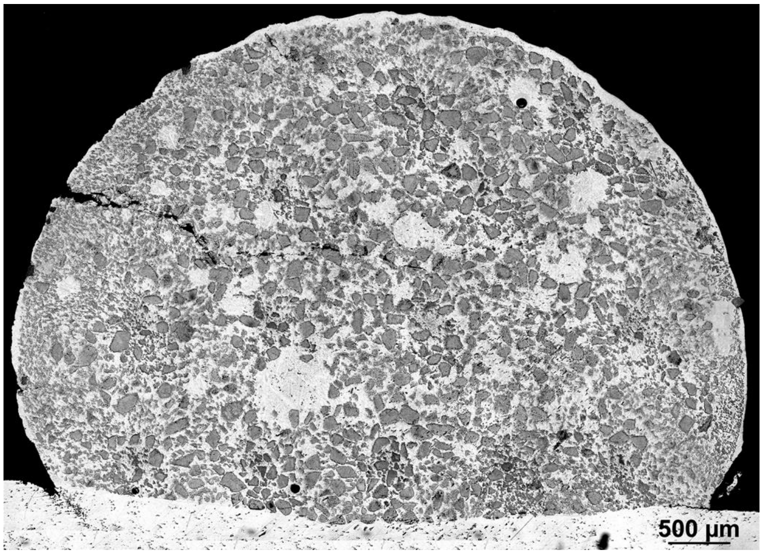

Figure 4.28: Short-circuit GMAW of Consumable D using 85Ar-15O_2 shielding gas. No carbide size threshold resulted in a f_c=41% and η_c=87% however large quantities of re-precipitated carbide led to a f_c=24% and η_c=51% after <25µm size thresholding.

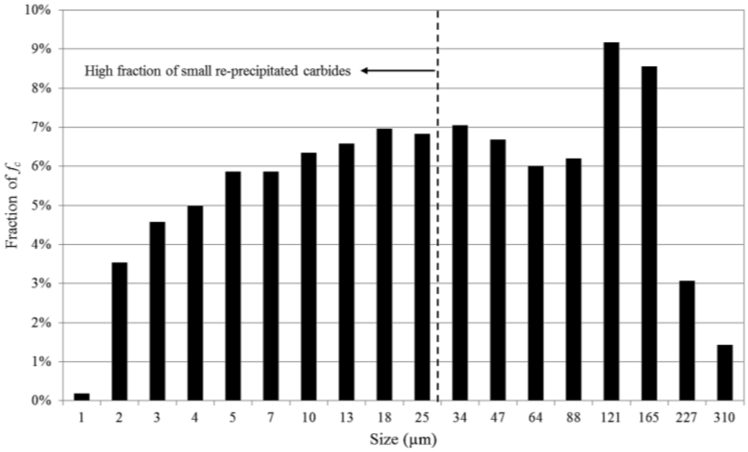

Figure 4.29: Un-thresholded carbide size distribution of Consumable D shown in Figure 4.28. High fractions of undesirable carbides falsely increase measured carbide volume fraction while not improving wear resistance.

4.5. Hot-Wire GMAW

Utilizing the understanding gained with the GMAW process with Ni-WC wires, the hot-wire electrode was added to the rear of the weld pool. The similar polarities between the hot-wire and GMAW will cause arc attraction. The arc attraction is mainly observed during globular free-flight transfer and is not readily observed in short-circuit GMAW. Initial HWGMAW testing was completed using an insertion angle of 30^{o} and globular transfer GMAW. Globular transfer was necessary to achieve sufficient heat input to the weld to provide a satisfactory bead shape without cold lap at the weld toes. The globular transfer increased the non-wetting carbide loss and led to increased carbide dissolution despite the higher thermal mass of the weld pool from the hot-wire addition, shown in Figure 4.30.

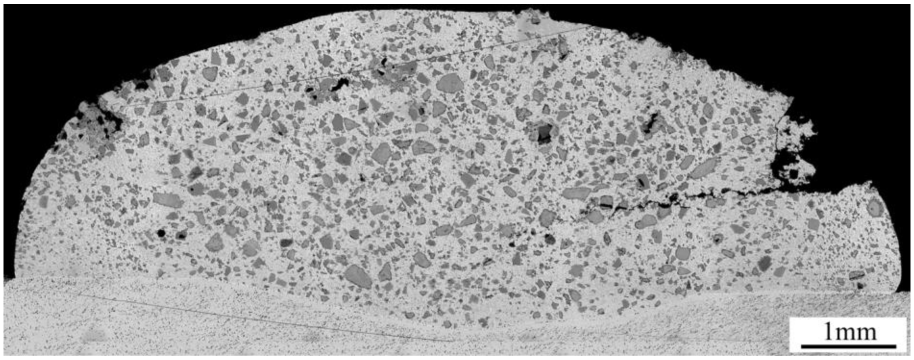

Figure 4.30: Globular free-flight HWGMAW using Consumable E hot-wire electrode and Consumable F GMAW electrode. High heat input caused severe carbide dissolution despite an optimal bead profile.

To circumvent the high levels of carbide dissolution, short-circuit GMAW was employed. The small weld pool of short-circuit metal transfer necessitated the use of a steep insertion angle of 60^o to prevent the wire from contacting the weld pool tail. Consumable F was used as the GMAW electrode at a wire feed speed of 3 $m \cdot min^{-1}$ (120 ipm) while Consumable D was used as the hot-wire at 2 $m \cdot min^{-1}$ (80 ipm) WFS and an average current of 91 A. The two Ni-WC wires utilized in the short-circuit HWGMAW study contained different carbide volume fractions. Using the initial wire carbide volume fractions calculated in Chapter 2 and a transfer efficiency of 81%, the maximum carbide fraction the test parameters could achieve is 33% accounting for non-wetting losses. To ensure sufficient oxidation and arc stability during multi-layer welding where a previous Ni-WC bead is the substrate, $85\%Ar\text{-}15\%O_2$ GMAW shielding gas was utilized. The travel speed was kept constant at 0.5 $m \cdot min^{-1}$ and the hot-wire electrode extension of 65 mm was maintained.

A stringer weld bead cross section produced with HWGMAW using Consumable D and F is shown in Figure 4.31. The carbide volume fraction of the weld was measured at 29% with a lower bound size threshold. While this value is lower than the predicted 33%, the calculated $f_{c,max}$ of Consumable D is completed using the mass of carbides and not accounting for the size distribution of the carbides. This means that lower bound thresholding the overlay cross section will remove some of the small carbides present in Consumable D. The HWGMAW overlay carbide volume fraction was measured at 36% with no threshold. While it is slightly higher than the predicted 33%, the carbides are small and will not measurably increase the wear resistance of the overlay. The effect of thresholding on Figure 4.31 is shown in Appendix 5.

Study of the carbide distribution in the longitudinal weld direction was completed on the HWGMAW weld bead. This was accomplished in the same manner as the HWGTAW welds of Figure 4.9 and Figure 4.10. The hot-wire GMAW process produces a homogeneous distribution of carbides along the length of the weld, with a clear increase in carbide fraction at hot-wire insertion location, depicted in

Figure 4.32. Based on the excellent results obtained by HWGMAW, the production of single and double layer ASTM G65 Dry Sand/Rubber Wheel abrasion test coupons were welded for testing.

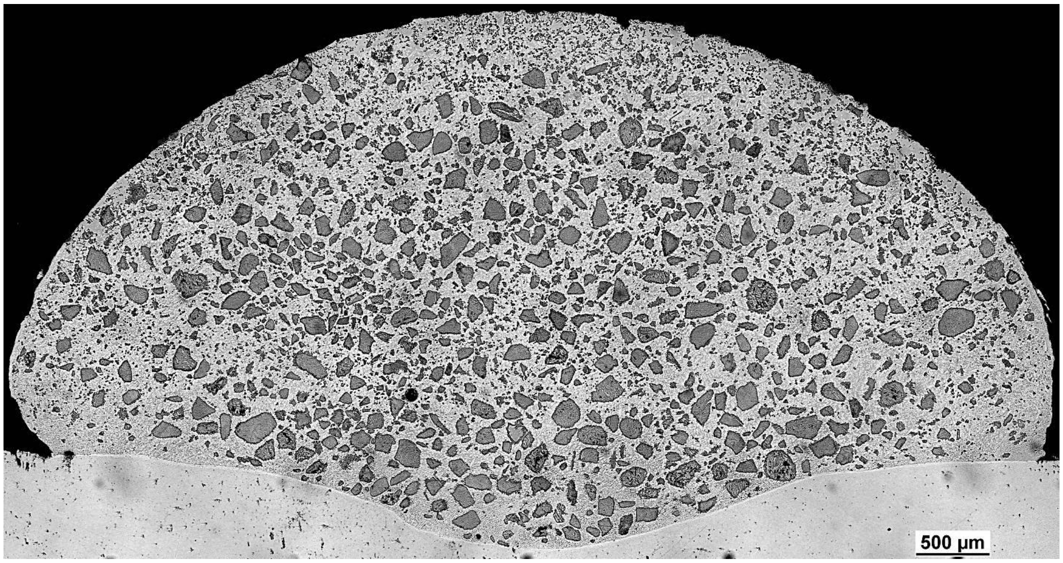

Figure 4.31: HWGMAW cross section with f_c of 29%.

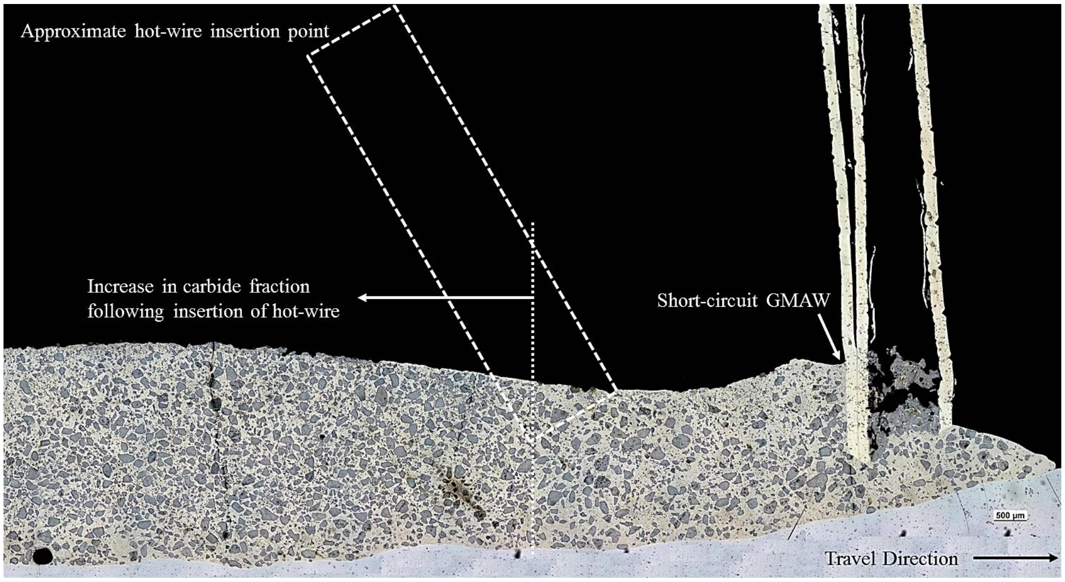

Figure 4.32: HWGMAW longitudinal cross section with Consumable F GMAW electrode frozen in the weld pool and Consumable D hot-wire electrode insertion location approximated. A marked increase in carbide fraction is observed following the hot-wire insertion.

4.6. Microstructural Analysis

4.6.1. Tubular Ni-WC Wire Overlays

The performance of Ni-WC overlays in-service is directly linked to the carbide volume fraction and matrix phases. The chemical composition and welding parameters have a strong influence the carbide dissolution and the formation of undesirable secondary phases. Determination of the level of dissolution and re-precipitation of tungsten containing phases were conducted using optical microscopy, EPMA, AES, and SEM/EDS methods on HWGTAW, GMAW, and HWGMAW overlays.

The use of chemical etchants can preferentially attack and stain phases containing elements of interest. Figure 4.33 demonstrates the effects of Murakami's and Kalling's Reagents on free-flight globular welds to identify and differentiate tungsten-containing phases that are indicative of dissolution. Murakami's Reagent was utilized to preferentially attack and stain re-precipitated phases containing elevated levels of tungsten. The constituents of Murakami's Reagent also preferentially attack the W_2C phase in relation to WC, revealing the complex lamellar structure of the carbides. Kalling's Reagent is an excellent etchant to reveal primary and re-precipitated tungsten carbides as it chemically attacks the nickel matrix. Eutectoid carbides typically partially dissolve during welding. Upon cooling, the tungsten-rich region surrounding the carbides re-precipitates as a W-Ni-Fe dissolution band which has been shown to decrease wear resistance. Kalling's Reagent exposes the small regions of nickel between the primary carbide and the W-Ni-Fe dissolution band.

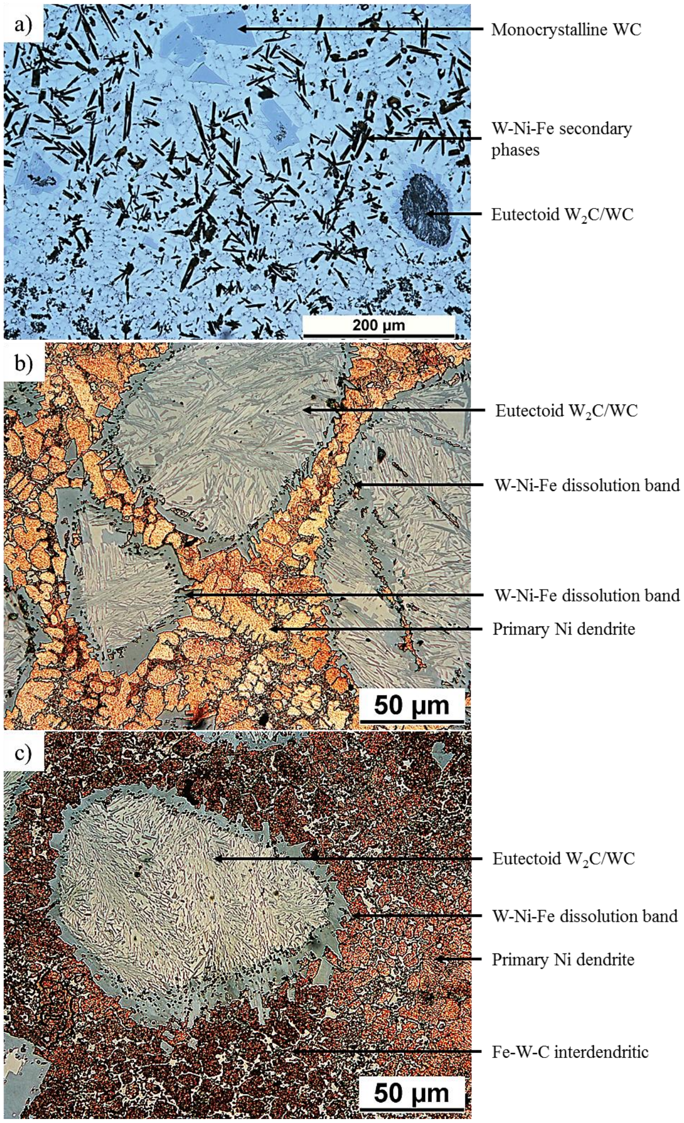

Figure 4.33: Etched tubular Ni-WC free-flight globular metal transfer overlays: a) Consumable E and etched with Murakami's Reagent, and Consumable F etched with Kalling's Reagent in b) and c). Carbide dissolution is clearly indicated.

While etching is a suitable method for determining the structure of a material, it is not always necessary for Ni-WC overlays. The large difference in hardness (~350-3000HV) between the matrix and carbides often produces inconsistent polishing wear rates. The matrix and carbide phases are also easily distinguishable from one another. Figure 4.34 compares un-etched optical microscopy to backscattered SEM images. While the phases are not exactly the same due to polishing between imaging, the W-containing phases are easily recognized in the optical microscopy images.

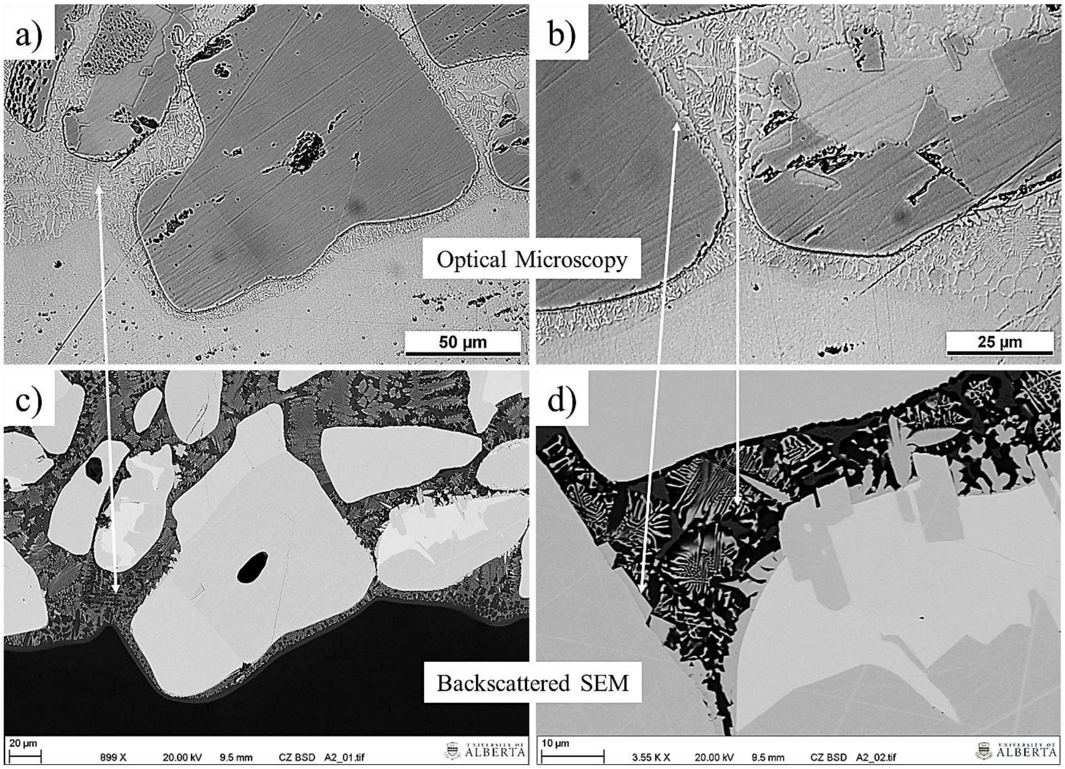

Figure 4.34: Comparison between un-etched optical microscopy to backscattered SEM. W-containing phases clearly visible on carbide periphery and eutectic lamellae with optical microscopy of PTA welded NiCrBSi overlay with WC carbides.

Determination of the chemical compositions of individual phases from HWGTAW welds of Consumable A and D were completed using Electron Probe Micro Analysis (EPMA). Consumable A contains chromium and a lower initial carbide volume fraction while Consumable D exhibits high carbide volume fraction, no chromium, and proprietary carburized W_2C/WC carbides which limit dissolution. EPMA mapping was completed by analyzing carbon, boron, silicon, tungsten, nickel, iron, and chromium. The data collected for boron and carbon were dismissed as there was insufficient signal for reliable interpretation. Backscattered electron SEM images are shown along with the corresponding EPMA elemental maps for reference in Figure 4.35 and Figure 4.36, while Appendix 6 contains other analyzed regions of Consumable A and D.

Analysis of Consumable A, shown in Figure 4.35, indicates a nickel matrix containing Fe, W, Cr, and Si. The partially dissolved carbides have increased the tungsten concentration in the matrix, leading to formation of W-Cr-Fe-Ni re-precipitated phases dispersed throughout the weld bead as feathery star-shaped phases. Surrounding the partially dissolved carbides, small phases containing W, Ni, Fe and Cr are observed, known to be hard and brittle and decreasing the wear resistance [55].

EPMA of Consumable D showed a drastically different matrix compared to Consumable A, exemplified in Figure 4.36. The matrix showed no quantifiable amount of chromium and silicon, reinforcing the powder analysis completed in Section 2, and decreasing the amount of carbide dissolution. The proprietary WC coating surrounding the W_2C/WC eutectoid carbides significantly decreased the carbide dissolution, indicated by the negligible levels of tungsten in the matrix. The presence of iron in the nickel matrix was observed to have a negligible effect on carbide dissolution despite the evidence shown in literature [70]–[72]. Dissolution was not observed in other analyzed regions, shown in Appendix 6.

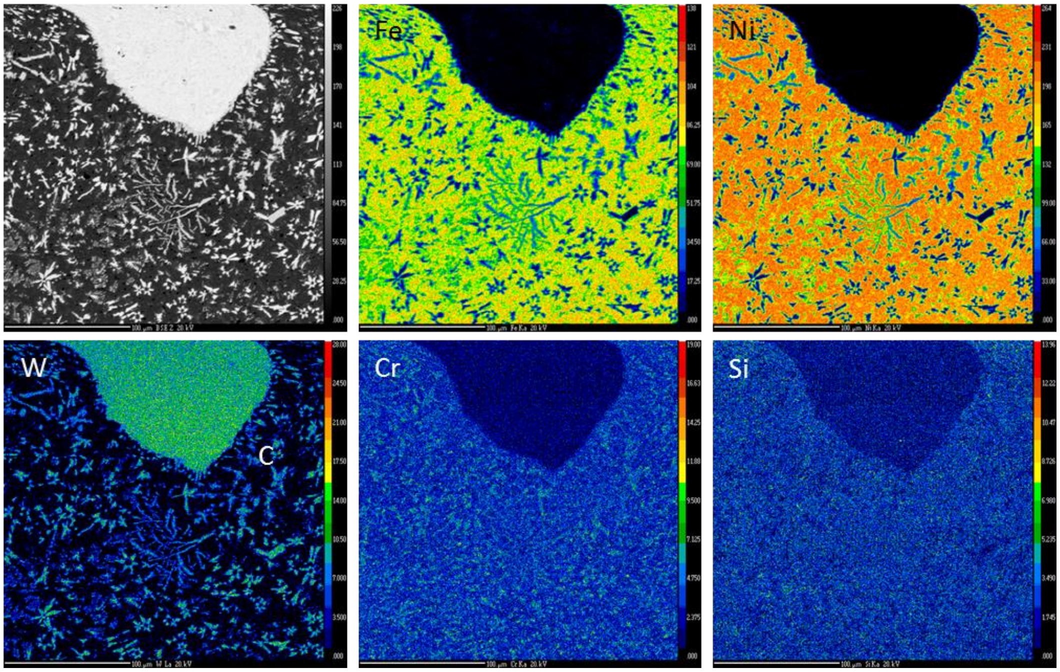

Figure 4.35: EPMA elemental map of Consumable A welded with HWGTAW showing high carbide dissolution and re-precipitation of Ni-W-Cr-Fe secondary phases.

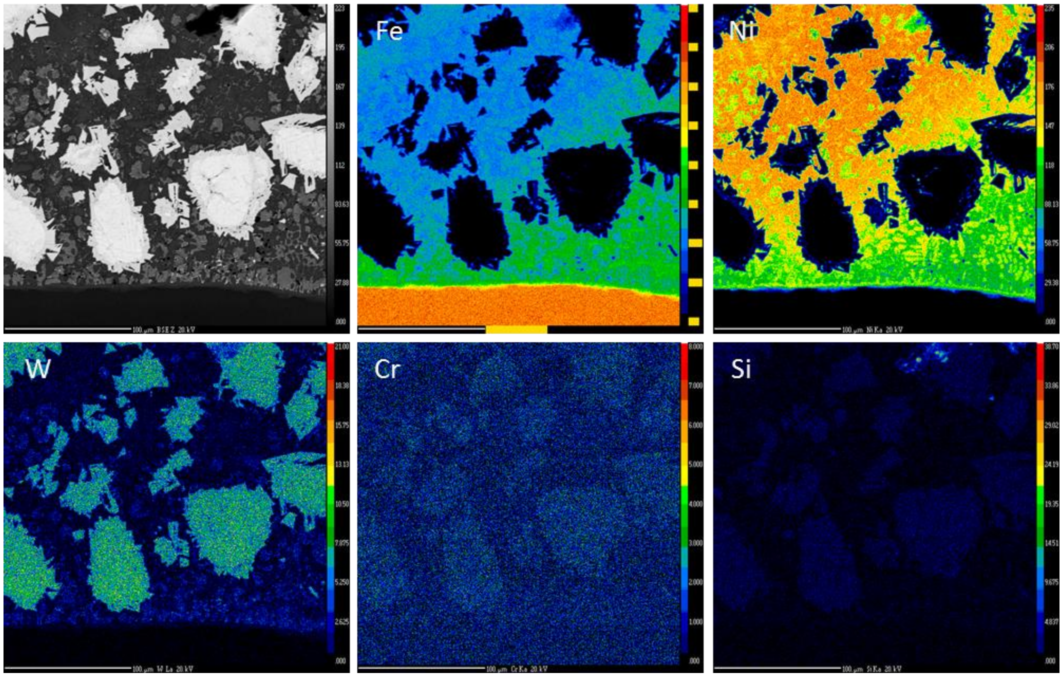

Figure 4.36: EPMA elemental analysis of Consumable D welded with HWGTAW showing no carbide dissolution along the fusion line.

To determine the exact constituents of each phase in Consumable D, Auger Electron Spectroscopy (AES) was utilized. AES has excellent resolution and chemical analysis accuracy as it analyzes the top ~10nm of substrate whereas the interaction volume of SEM is ~1µm. To increase the accuracy of carbon concentration analysis, a carbon correction factor of 1.30 was used. This factor was determined by analyzing the carbon concentration of a known monocrystalline WC particle where the atomic concentration ratio of carbon:tungsten is approximately 1:1. Interpretation of the chemical composition data collected yielded a matrix structure containing eutectic nickel borides (Ni_3B), primary nickel eutectic lamellae, and various Ni-W-Fe-C eutectic phases, summarized in Table 4.5. The regions surrounding the carburized carbides are nearly devoid of tungsten, indicating low levels of dissolution and success of the proprietary WC layer.

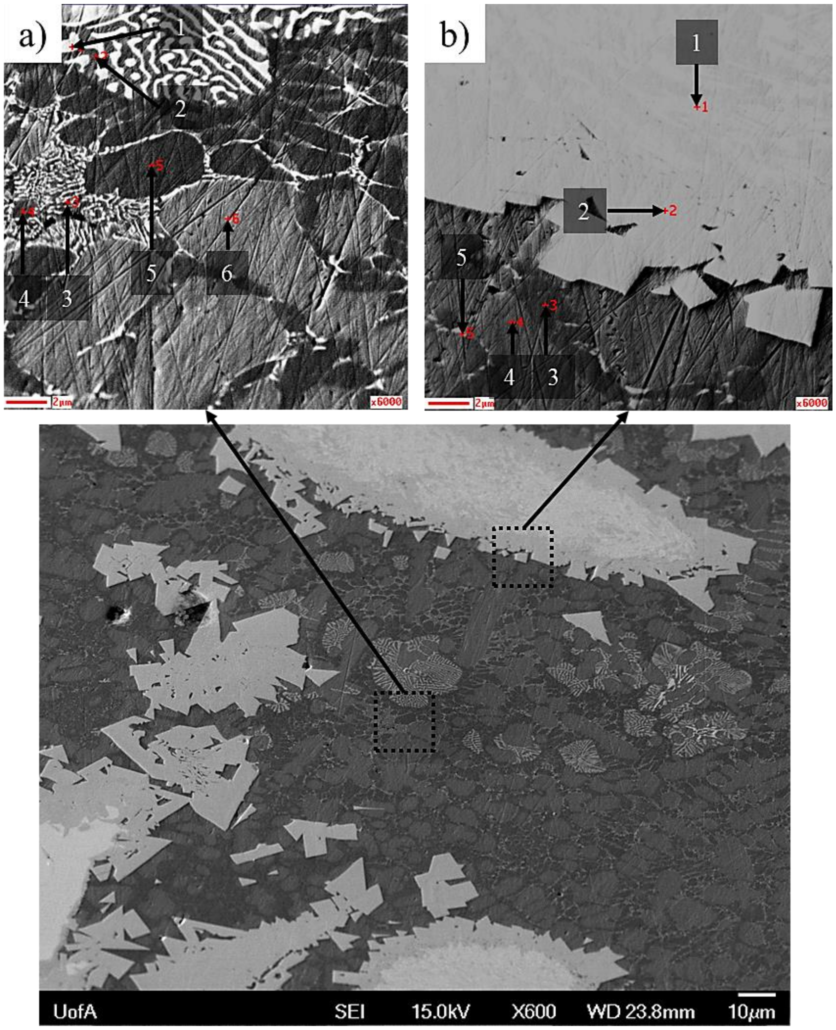

Figure 4.37: AES matrix and carbide analysis of HWGTAW welded Consumable D. Chemical analysis of specific phases is shown in Table 4.5.

Table 4.5: AES atomic concentrations of analyzed phases in images a) and b) of Figure 4.37 from HWGTAW Consumable D.

		Atomic Concentration (%)					
Image	Point	C	W	Ni	Fe	Si	B
a)	1	2.9	48.8	25.5	22.8	0	0
	2	5.0	3.4	63.8	27.8	0	0
	3	33.8	38.7	16.1	11.4	1.9	0
	4	8.8	2.9	51.2	17.2	0	19.8
	5	7.8	2.4	53.9	16.1	0	19.7
	6	6.7	3.5	65.6	24.3	0	0
b)	1	33.5	66.5	0	0	0	0
	2	43.6	56.4	0	0	0	0
	3	6.6	2.7	50.9	17.7	0	22.1
	4	4.9	2.5	62.7	29.9	0	0
	5	5.3	17.0	53.8	24.0	0	0

The short-circuit HWGMAW overlays were examined with optical microscopy and SEM/EDX to determine the level, if any, of carbide dissolution. The cold weld pool afforded by Joule heating the trailing Ni-WC wire can lead to portions of un-melted Ni sheath dispersed throughout the overlay. While indicative of a cold weld pool and rapid cooling rates, the un-melted sheath sections are very soft and wear considerably faster than the surrounding matrix and tungsten carbides. For reference, the Ni sheath of Consumable D is ~100 µm thick. To determine the presence of dissolution surrounding the tungsten carbides, SEM/EDX line scans were conducted across the carbide-matrix interface of HWGMAW welds. The EDX line scans did not show the presence of carbide dissolution bands or tungsten in the surrounding matrix, shown in Figure 4.39 and Figure 4.40.

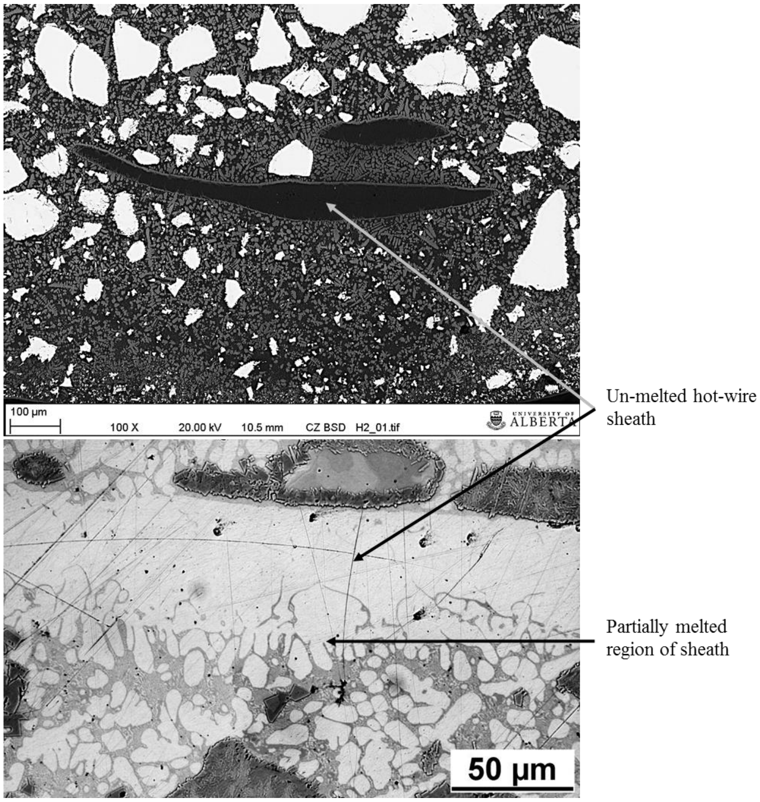

Figure 4.38: Portions of un-melted hot-wire Ni sheath observed with optical microscopy and backscattered SEM from short-circuit HWGMAW weld.

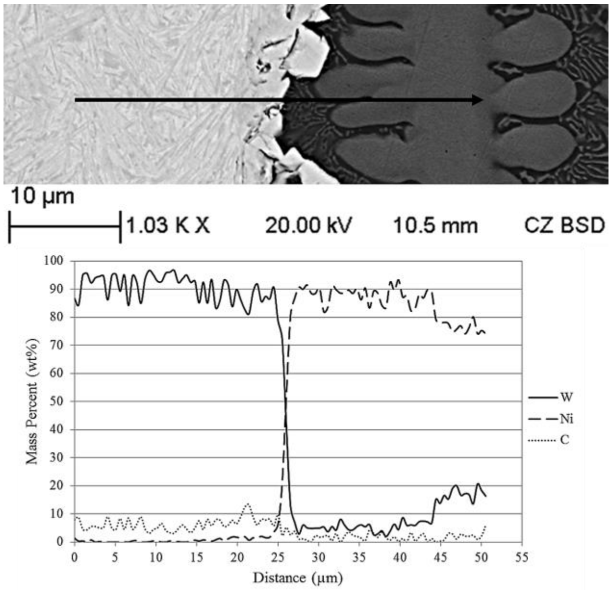

Figure 4.39: EDX line scans of W, Ni, and C across the carbide-matrix interface. No carbide dissolution bands are present in short-circuit HWGMAW overlays.

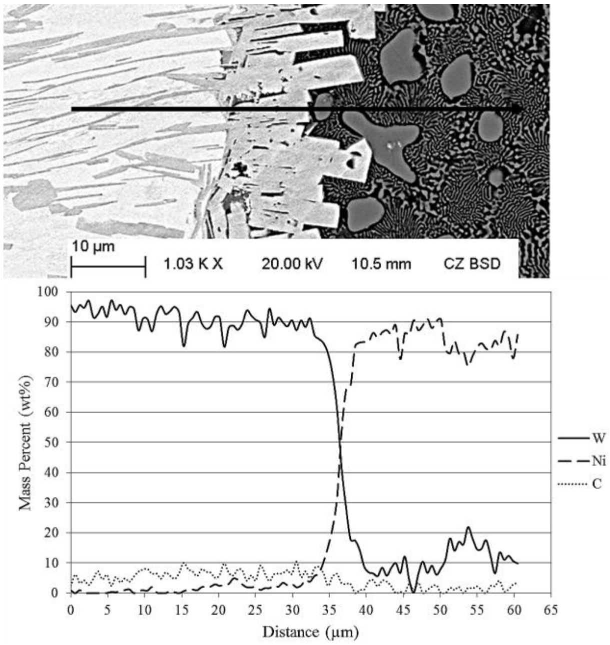

Figure 4.40: EDX line scans of W, Ni, and C across the carbide-matrix interface. No carbide dissolution bands are present in short-circuit HWGMAW overlays.

4.6.2. Matrix and Carbide Hardness

The matrix and carbide hardness have a large effect on the wear resistance of the overlay. Hardness is often used as a metric to assess the relative wear resistance of overlays. The intricacies of the hardness and wear resistance of a Ni-WC overlay were discussed in detail in Chapter 1. The matrix and carbide hardness of HWGTAW, GMAW, and HWGMAW overlays are summarized below.

The carbide and bulk matrix hardness measurements shown in Table 4.6 (HWGTAW) and Table 4.7 (GMAW and HWGMAW) are the average of 6 or more hardness indents taken throughout the weld. Consumables C and D, which contained high levels of boron and through optical microscopy large amounts of interdendritic Ni_3B eutectic, had a harder matrix than the other consumables. Consumables B and E contained low levels of alloying elements from the EDS analysis which resulted in a soft nickel matrix. Carbide hardness measurements varied considerably between consumables. Manufacturers using monocrystalline WC, Consumables B and E, recorded significantly lower hardness compared to the eutectoid carbides of Consumables A, C, D, E, and F. The monocrystalline carbides had an increased likelihood to fracture under the same load conditions as the eutectoid carbides, making hardness measurements difficult. The hardness values listed in Table 4.7 correspond to the ASTM G65 overlays wear tested in Section 4.7. Consumable F was utilized for the GMAW electrode and Consumable D for the hot-wire electrode.

Table 4.6: Vicker's microhardness of the matrix and carbides in HWGTAW welded Consumables A-F. Matrix testing used a load of 1kg while carbide hardness was completed using 100g.

	Consumable					
Location	**A**	**B**	**C**	**D**	**E**	**F**
Matrix	508±49	469±26	630±49	636±65	457±20	547±15
Carbide	1926±203	1408±251	2232±199	2357±71	1183±318/1860±269*	2373±169

*: Hardness measurements for monocrystalline WC and W_2C/WC eutectoid carbides respectively

Table 4.7: Vicker's microhardness of matrix and carbides of single (-1) and double (-2) layer GMAW and HWGMAW welds. Matrix testing used a load of 1kg while carbide hardness was completed using 200g.

		Hardness			
Location	Layer	**GMAW-1**	**GMAW-2**	**HWGMAW-1**	**HWGMAW-2**
Matrix	1	524±12	512±8	639±22	556±11
	2	-	604±40	-	766±54
Carbide	-	2307±165	2361±112	2397±165	2375±142

4.7. Wear Performance of Tubular Ni-WC Wire Overlays

Utilizing the information gained throughout this study, GMAW and short-circuit HWGMAW wear test coupons were produced on a 0.375 in. mild steel plate. The coupons were welded in accordance with ASTM G65 Dry Sand/Rubber Wheel samples sizes and surface ground down to provide a flat surface. Wear resistance is characterized by performing two ASTM G65 Procedure A tests in the same wear scar. The coupons were removed after the first Procedure for mass loss measurement and tested again in the same scar for the second set of rotations. Single and double layer coupons were welded to simulate industrial overlay thickness requirements. To avoid excessive relief cracking/checking and chipping, the coupons were not allowed to cool down between subsequent weld passes. Analysis of the weld cross sections revealed little difference in penetration, microstructure, and carbide dissolution between the initial and final weld beads despite the increasing interpass temperatures. Consumable F was utilized for the GMAW electrode while the high initial wire carbide volume fraction of Consumable D was chosen for the hot-wire electrode. The GMAW welding parameters were kept constant between the GMAW and HWGMAW overlays for consistency.

The carbide volume fraction of the GMAW and HWGMAW wear coupons was measured using the entire weld cross section, accounting for denuded regions between adjacent weld passes. Re-precipitated carbides were omitted from the volume fraction measurements through lower bound thresholding. The weld cross sections with the highlighted measured primary carbides are shown in Appendix 7. The ASTM G65 wear tests results are summarized in Figure 4.41 and compared to industry-standard 14%Cr and a Cr-free matrix PTAW overlays [55].

Comparing the GMAW overlays, the increase in wear resistance of the double layer coupon is clear. This is a result of the smaller denuded regions between adjacent weld passes, decreasing preferential wear of the matrix. The HWGMAW overlays show a clear increase in wear resistance compared to the GMAW overlays, attributed to the higher carbide volume fraction. Compared to industry-standard PTAW overlays, the HWGMAW coupons exhibited higher mass loss and decreased wear resistance. The volume fraction of carbide in the HWGMAW is insufficient to decrease the inter-carbide distance to decrease the mass loss of the nickel matrix. However, the mass loss of the HWGMAW process is comparable to a PTAW overlay produced with a high chromium matrix. The deposition rate of the HWGMAW process utilized was 5.4 kghr^{-1} (11.9 lbhr^{-1}), which 60% higher than the PTAW overlays [55]. Figure 4.43-4.53 contain the weld cross sections and optical and SEM wear scar analysis.

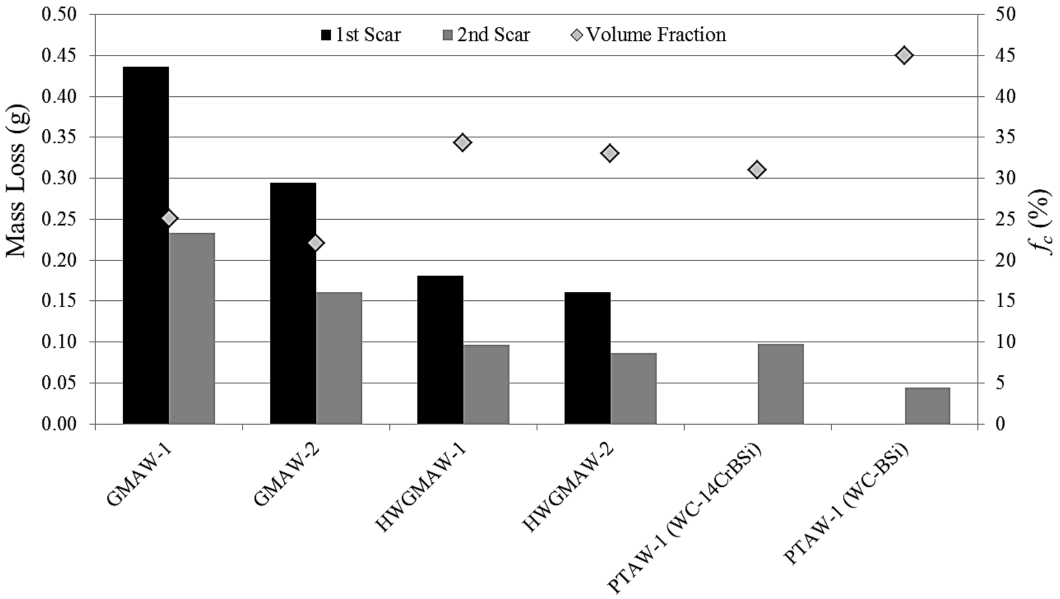

Figure 4.41: ASTM G65 wear test comparisons of GMAW, HWGMAW, and PTAW [55]. (-1) denotes single layer while (-2) denotes a double layer Ni-WC overlay.

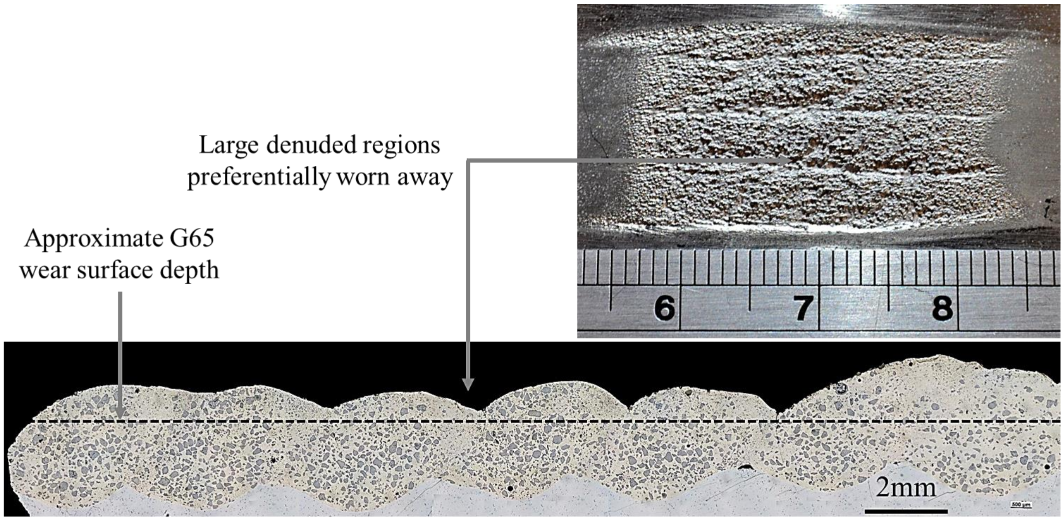

Figure 4.42: Single layer GMAW of Consumable F with corresponding wear scar depicting large denuded zones between adjacent welds, leading to increased mass loss. f_c=25%.

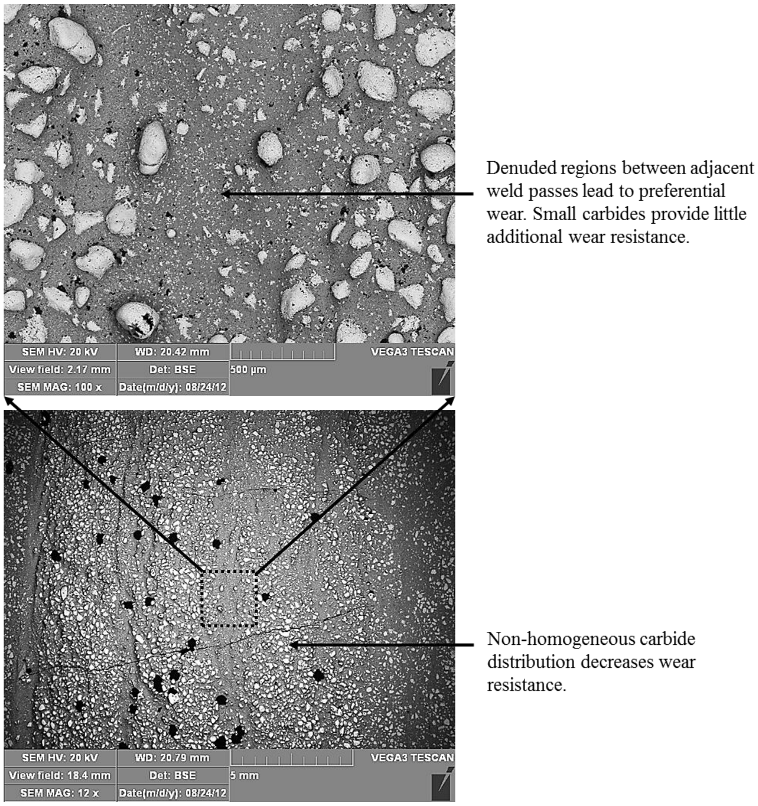

Figure 4.43: Backscattered electron SEM image of wear scar surface of single layer GMAW.

Large inter-particle spacing leads to excessive matrix wear rates.

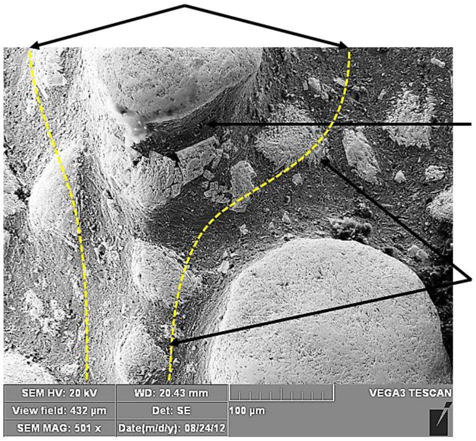

Lack of brittle re-precipitated phases surrounding carbide periphery increases carbide tear-out resistance, improving wear resistance. Carbides are very prominent above matrix surface.

Small primary carbides increase wear resistance but are fractured easier from larger abrasive sand.

Figure 4.44: SEM image of wear scar surface of single layer GMAW. Large inter-particle spacing increases matrix wear rate while lack of brittle phases surrounding carbides resist carbide fracture and pull out.

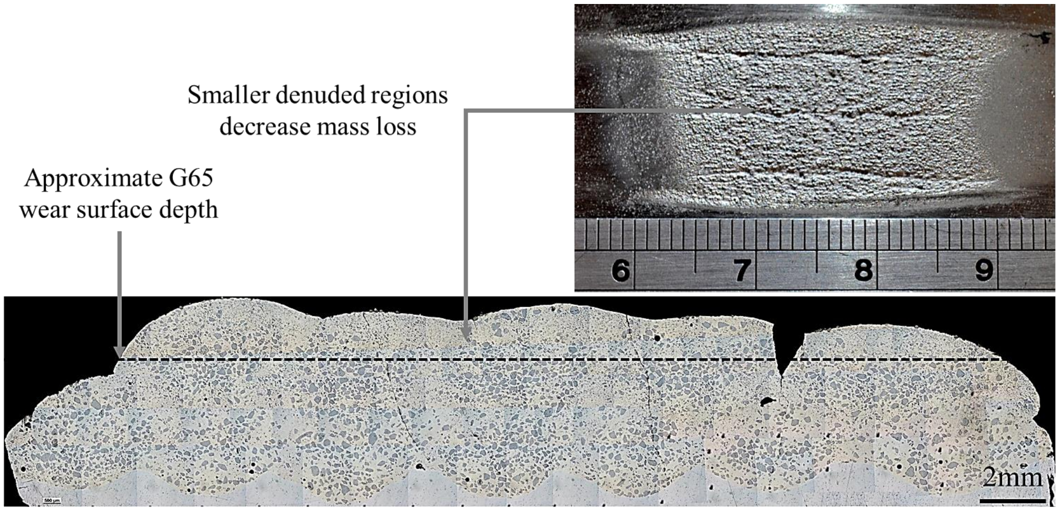

Smaller denuded regions decrease mass loss

Approximate G65 wear surface depth

Figure 4.45: Double layer GMAW of Consumable F with corresponding wear scar. Increased carbide fraction and more homogeneous distribution decreases mass loss compared to single layer GMAW. f_c=22%.

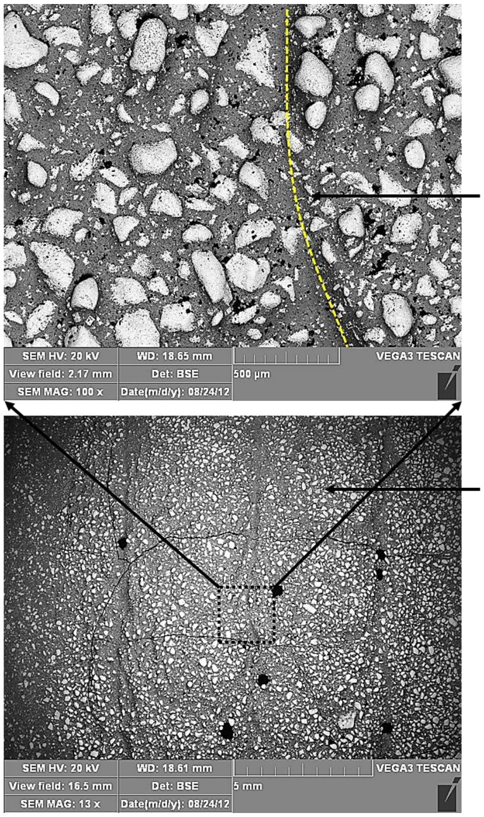

Smaller denuded regions between adjacent weld passes decrease preferential wear.

Higher carbide fraction and more homogeneous distribution compared to single pass GMAW improves wear resistance.

Figure 4.46: Backscattered electron SEM image of wear scar surface of double layer GMAW. Smaller denuded regions between adjacent welds increase wear resistance compared to single layer GMAW.

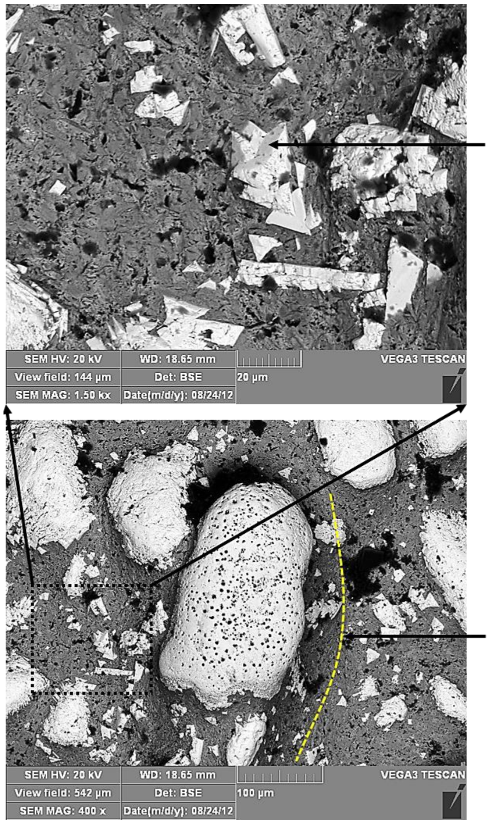

Re-precipitated monocrystalline WC or small primary carbide fines fracturing during wear test.

High inter-particle spacing leads to increased matrix wear rate.

Figure 4.47: Backscattered electron SEM image of wear scar surface of double layer GMAW showing small tungsten carbide phases fracturing during wear testing.

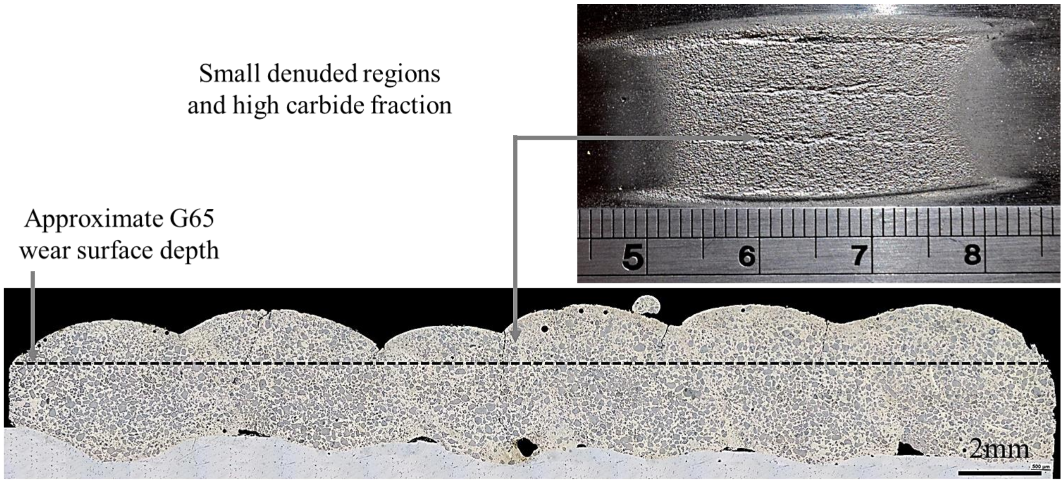

Small denuded regions and high carbide fraction

Approximate G65 wear surface depth

Figure 4.48: Single layer of HWGMAW with high carbide volume fraction. Small denuded zones and near-homogeneous carbide distribution led to preferential mass loss between adjacent welds. f_c=34%.

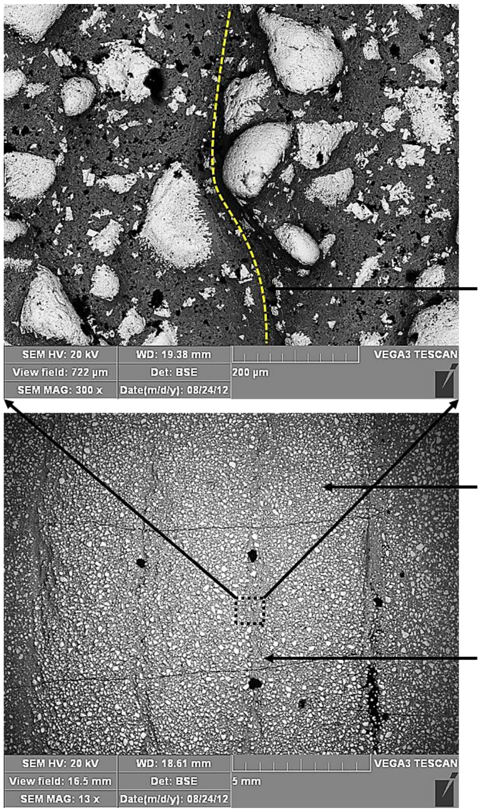

Preferential wear due to insufficient inter-particle spacing between weld passes.

Homogeneous carbide distribution and inter-particle spacing improves wear resistance.

Small denuded zones between adjacent weld passes still provide regions for preferential wear.

Figure 4.49: Backscattered electron SEM image of wear scar surface of single layer HWGMAW. Near-homogeneous carbide distribution and higher volume fraction compared to GMAW decreases mass loss. Small denuded regions still exist between adjacent welds.

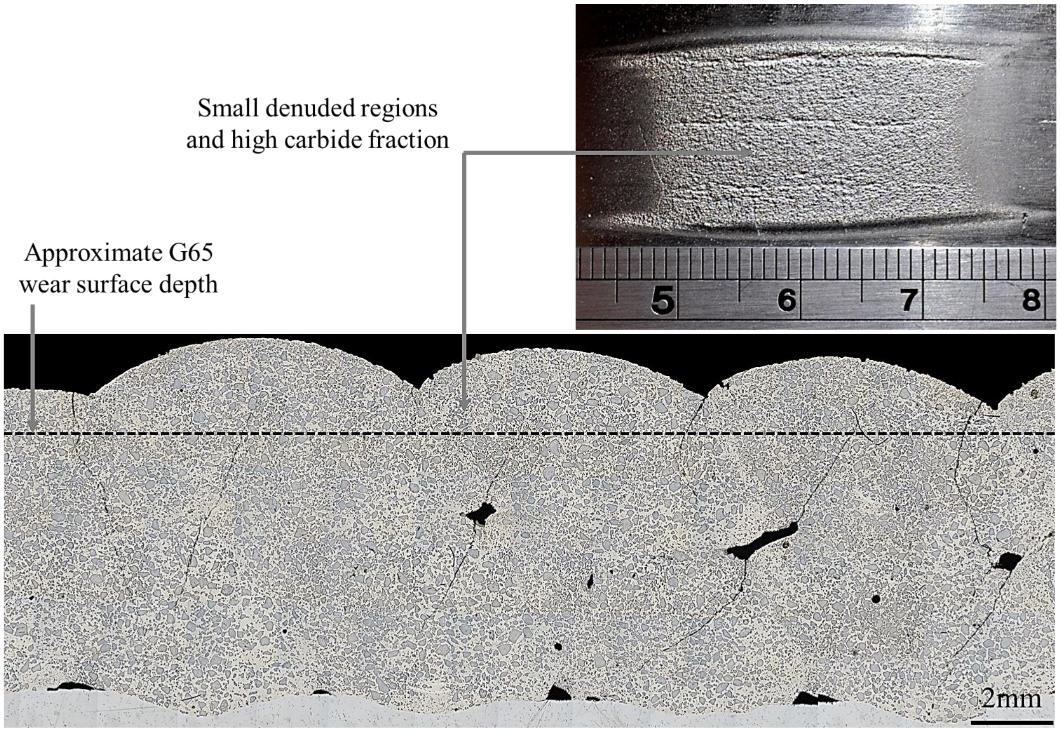

Figure 4.50: Double layer of HWGMAW with high carbide volume fraction. Homogeneous carbide distribution and small denuded zones decrease mass loss. f_c=33%.

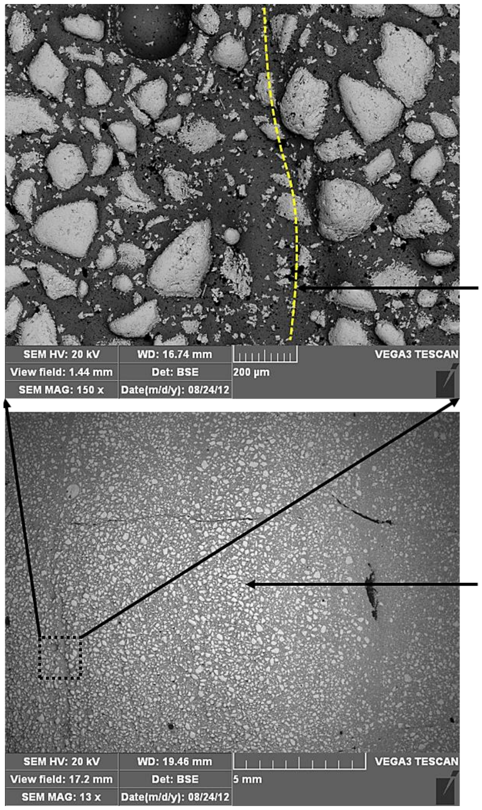

Preferential wear due to insufficient inter-particle spacing between weld passes.

Homogeneous carbide distribution and inter-particle spacing improves wear resistance.

Figure 4.51: Backscattered electron SEM image of wear scar surface of double layer HWGMAW. Nearly homogeneous carbide distribution with smaller denuded regions compared to single layer HWGMAW.

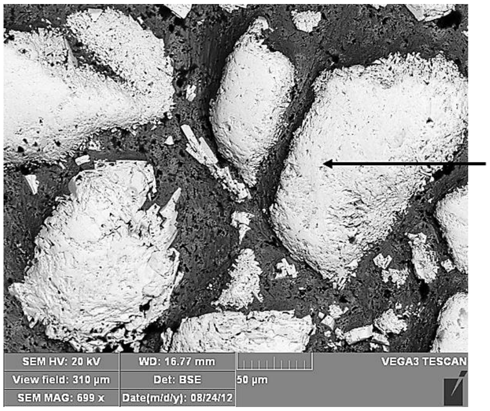

Sufficient inter-particle spacing outside the adjacent pass regions increase wear resistance.

Figure 4.52: Backscattered electron SEM image of wear scar surface of double layer HWGMAW with short inter-particle spacing that reduces matrix wear.

4.8. Conclusion

The use of hot-wire assist technology in conjunction with GTAW and GMAW for production of Ni-WC overlays is discussed. The HWGTAW process produced overlays with high carbide volume fraction and little carbide dissolution. The process however was unstable due to escaping air bubbles projecting Ni-WC droplets onto the GTAW electrode. The electrode contamination prompted the use of HWGMAW utilizing two Ni-WC consumables. To maximize the retained carbide fraction, the GMAW process was characterized prior to the hot-wire addition. The traditional carbide loss mechanism is a result of carbide dissolution from the high arc and weld pool temperatures. It was shown that tungsten carbide non-wetting to the molten Ni weld pool is an new, previously undocumented loss mechanism in short-circuit and free-flight metal transfer. Globular transfer exhibits non-wetting and dissolution mechanisms while short-circuit exhibited only non-wetting losses within the range of parameters studied. Due to the excessive carbide dissolution of globular transfer, short-circuit GMAW was employed with the hot-wire addition. The short-circuit metal transfer of tubular Ni-WC wires requires specific advancements in shielding gas composition and complex waveform design to further improve stability and carbide retention. Two ASTM G65 Dry Sand/Rubber Wheel Procedure A tests in the same wear scar resulted in a mass loss of 0.086g with an overall carbide volume fraction of 33% at a deposition rate of 5.4 $kghr^{-1}$.

The hot-wire process has the ability to produce high hardness matrix microstructures with low carbide dissolution. Optical microscopy, EPMA, AES, SEM/EDX quantification of HWGTAW, GMAW, and HWGMAW overlays yielded low concentrations of tungsten in the matrix and surrounding the tungsten carbides, indicating low dissolution. Measurement of carbide volume fraction was completed using the entire weld bead, eliminating regional variances due to weld pool movement and settling phenomenon.

5. Discussion

Through the course of the work presented, a number of assumptions and new findings are reported. The tubular nickel sheathed, tungsten carbide cored wires were characterized prior to welding. In literature, the unique chemical composition and initial wire carbide volume fraction are taken at face value from the manufacturer. As a result of the powder characterization and carbide fraction measurements conducted, the manufacturer consumable reports are often not accurate and can skew subsequent overlay observations. The hot-wire electrode extension model relies heavily on accurate material property data. The electrical resistivity of steel, stainless steel, and Ni-WC welding consumables was measured from room temperature to 1200 ^{o}C. It is determined that welding consumables, due to their unique chemical compositions, exhibit different electrical resistivity's compared to literature values. As a result, researchers working on electrode extension models for wire based processes such as hot-wire, GMAW, FCAW, MCAW should measure their consumable-specific resistivity.

The hot-wire electrode extension model proposed in this work has for the first time, accounted for the energy of the leading heat source and the effect of welding torch parameters on predicting the current necessary to achieve semi-solid melting. While successful, a number of critical assumptions were used during its inception. The model assumes that all energy from the leading heat source is impinging on the hot-wire tip. In actuality, the arc energy is dispersed over the "top-side" of the electrode and altering the temperature distribution along the wire length. While this may not have a significant effect on solid consumables, this may cause increased melting of powders inside Ni-WC wires. Hot-wire Ni-WC wires have been observed to contain a liquid phase inside the wire prior to the weld pool (Figure 4.9 and Figure 4.10). This will alter the resistivity of the wire near the end of the electrode. The current Ni-WC electrode extension model underestimates the Joule heating required to melt the wire. The electrical resistivity of the Ni-WC wires, extrapolated as the same slope as pure nickel to the melting temperature, may be lower than the actual high temperature resistivity of a Ni-WC wire. This can explain the discrepancy observed between the model predicted and real-world hot-wire currents. As an addendum, the effect of other variables such as volumetric enthalpy and wire area has a large impact on the predicted welding current.

6. Conclusions and Recommendations

6.1. Conclusions

Hot-wire assist technology has a very bright future for the deposition of Ni-WC overlays. The tubular Ni-WC wires and powders were characterized and large variances in powder composition, nickel sheath thickness, and initial carbide volume fraction were observed with few consumables meeting the required minimum carbide volume fraction set by oil sands operators. A hot-wire specific electrode extension model for solid and tubular wires was developed to predict necessary current to achieve the semi-solid temperature near the weld pool surface. The model quantified the energy contribution of the nearby GTAW and GMAW welding arcs to melting of the hot-wire. The use of hot-wire GTAW was discounted due to excessive electrode contamination preventing industrial scale overlay production. Hot-wire GMAW was determined to be a feasible deposition process exhibiting no carbide dissolution, good ASTM G65 Dry Sand/Rubber Wheel abrasion test results, and an equivalent or higher deposition rate than PTAW.

The hot-wire process is relatively inexpensive when compared to PTAW, the traditional deposition method currently in use, making it ideal for use in small fabrication shops and field repairs of worn components. Hot-wire GMAW is also very versatile and robust when compared to PTAW/laser cladding processes. The smaller torch apparatus can be used to weld relatively small inner diameter parts where PTAW torches cannot access. The cold weld pool of short-circuit HWGMAW also can lend it for use in out-of-position welding, decreasing the fixturing necessary to overlay new or damaged parts. The deposition rate of the HWGMAW process was 5.4 $kg \cdot hr^{-1}$ compared to the much lower industrial rate of ~4 $kg \cdot hr^{-1}$ for PTAW and laser cladding. The HWGMAW results depicted in Chapter 4 are from initial studies and further optimization of welding parameters and consumables can increase the retained carbide volume fraction and wear resistance while maintaining a competitive deposition rate.

6.2. Recommendations

Hot-wire assist technology when paired with GMAW can produce good quality Ni-WC overlays at high productivities. The consumables utilized in this work were primarily of 1.6 mm nominal OD. Increasing the wire diameter (ex: 2.0 mm) will potentially increase the carbide volume fractions and deposition rates. Future research on increasing the volume fractions contained within the tubular Ni-WC consumables will enhance the wear resistance of the overlays. Following the development of new consumables, optimized short-circuit metal transfer through the use of computer-controlled waveforms will maximize the carbide transfer efficiency of the process. Minimization of tungsten carbide non-wetting to molten Ni should be attempted via carbide surface modification or altering the properties of the Ni weld pool free surface. A wire straightener, while not utilized in this work, should be used to reduce weld bead geometry inconsistencies from the wire cast.

While the work presented focussed on the Ni-WC material system, the proposed hot-wire electrode extension model and the wire electrical resistivity test methods can be used for other applications. Welding and manufacturing of steel, stainless steel, and duplex stainless steel components can take advantage of the increased deposition rates of the hot-wire addition to either the GTAW or GMAW process.

References

[1] M. Anderson, S. Chiovelli, and S. Hoskins, “Improving Reliability and Productivity at Syncrude Canada Ltd. Through Materials Research: Past, Present, and Future,” *CIM Bull.*, vol. 97, no. October, pp. 1–6, 2004.

[2] J. F. Flores and A. Neville, “Materials Selection in the Oilsands Industry Based on Materials Degradation Mechanisms,” *Eng. Constr.*, pp. 42–45, 2009.

[3] D. Harper, M. Gill, K. W. D. Hart, and M. Anderson, “Plasma Transferred Arc Overlays Reduce Operating Costs in Oil Sand Processing.”

[4] NRCC, *A Strategy for Tribology in Canada: Enhancing Reliability and Efficiency through the Reduction of Wear and Friction*. NRC, 1987.

[5] H. Roth, “Private Communication.” Syncrude Canada Ltd., 2012.

[6] P. F. Mendez, N. Barnes, K. Bell, S. D. Borle, S. S. Gajapathi, S. D. Guest, H. Izadi, A. K. Gol, and G. Wood, “Welding processes for wear resistant overlays,” *J. Manuf. Process.*, Jul. 2013.

[7] A. F. Manz, “Consumable electrode arcless electric working,” US 3,122,6291964.

[8] AlabamaLaser, “Laser Cladding.” [Online]. Available: http://www.alspi.com/lasercladding.htm. [Accessed: 20-Feb-2012].

[9] M. Yamamoto, K. Shinozaki, T. Myoga, T. Kanazawa, and H. Arashin, “Development of Ultra-High-Speed GTA Welding Process Using Pulse-Heated Hot-Wire,” *IIW Doc. XII-1927-07*.

[10] K. Hori, H. Watanabe, T. Myoga, and K. Kusano, “Development of hot-wire TIG welding methods using pulsed current to heat filler wire - research on pulse heated hot-wire TIG welding processes,” *Weld. Int.*, vol. 18, no. 6, pp. 456–468, 2004.

[11] S. Ueguri, Y. Tabata, T. Shimizu, and T. Mizuno, “Control of deposition rates in hot wire TIG welding,” *Weld. Int.*, vol. 1, no. 8, pp. 736–742, Jan. 1987.

[12] D. J. Crement, “Narrow Groove Welding of Titanium Using the Hot-Wire Gas Tungsten Arc Process,” *Weld. J.*, vol. April, pp. 71–76, 1993.

[13] K. Kusano and H. Watanabe, “Recent trends in development of high-efficiency TIG welding; high-deposition TIG welding and ultranarrow-gap TIG welding,” *Weld. Int.*, vol. 16, no. 12, pp. 986–991, Jan. 2002.

[14] S. X. Lv, Z. W. Xu, H. T. Wang, and S. Q. Yang, “Investigation on TIG cladding of copper alloy on steel plate,” *Sci. Technol. Weld. Join.*, vol. 13, no. 1, pp. 10–16, Jan. 2008.

[15] K. Shinozaki, M. Yamamoto, K. Kadoi, T. Nagashima, and T. Kanazawa, “Melting phenomenon of hot-wire GTA and hot-wire laser welding process,” *IIW Doc. XII -1994-10*, 1994.

[16] K. Shinozaki, M. Yamamoto, K. Mitsuhata, T. Nagashima, T. Kanazawa, and H. Arashin, “Bead formation and wire temperature distribution during ultra-high-speed GTA welding using pulse-heated hot-wire,” *Weld. World*, vol. 55, no. 3–4, pp. 12–18, 2011.

[17] K. Shinozaki, M. Yamamoto, Y. Nagamitsu, T. Uchida, K. Mitsuhata, T. Nagashima, and T. Kanazawa, “Melting Phenomenon during Ultra-High-Speed GTA Welding Method using Pulse-heated Hot-wire,” *Q. J. Japan Weld. Soc.*, vol. 27, no. 2, p. 22s–26s, 2009.

[18] T. Tsuyama, “Development of Submerged Arc Welding Method Using Hot-Wire,” *Doc. XII 2120-13*, pp. 1–20.

[19] T. Tsuyama, K. Nakai, M. Akiyama, B. Takahashi, T. Sakamoto, and S. Kobayashi, “Effects of Microstructure on Mechanical Property in Weld Metal Formed with the Hot-Wire Method Applying Ordinal CO2 Gas Shielded Arc Welding Method,” *J. Iron Steel Inst. Japan*, vol. 99, no. 7, pp. 468–474, 2013.

[20] T. Tsuyama, K. Nakai, K. Noumaru, T. Sakamoto, and S. Kobayashi, “Effect of hot-wire on microstructure and mechanical property in weld metal formed with CO 2 gas shielded arc welding method F-MAG SN490B F-MAG F-MAG,” *Q. J. Japan Weld. Soc.*, vol. 31, no. 2, pp. 104–111, 2013.

[21] K. Kadoi, K. Shinozaki, M. Yamamoto, K. Owaki, K. Inose, and D. Takayangi, “Development of High-efficiency / High-quality Hot-wire Laser Fillet,” *Q. J. Japan Weld. Soc.*, vol. 29, no. 3, p. 62s–65s, 2011.

[22] W. Liu, S. Liu, J. Ma, and R. Kovacevic, “Real-time monitoring of the laser hot-wire welding process,” *Opt. Laser Technol.*, vol. 57, pp. 66–76, Apr. 2014.

[23] T. Ohnishi, Y. Kawahito, M. Mizutani, and S. Katayama, “Butt welding of thick, high strength steel plate with a high power laser and hot wire to improve tolerance to gap variance and control weld metal oxygen content,” *Sci. Technol. Weld. Join.*, vol. 18, no. 4, pp. 314–322, 2013.

[24] R. Phaoniam, K. Shinozaki, M. Yamamoto, K. Kadoi, S. Tsuchiya, and A. Nishijima, “Development of a highly efficient hot-wire laser hybrid process for narrow-gap welding—welding phenomena and their adequate conditions,” *Weld. World*, vol. 57, pp. 607–613, May 2013.

[25] M. Yamamoto, K. Shinozaki, K. Kadoi, D. Fujita, and T. Inoue, “Development of Hot-wire Laser Welding Method for Lap Joint of Steel Sheet with Wide Gap,” *Q. J. Japan Weld. Soc.*, vol. 29, no. 3, p. 58s–61s, 2011.

[26] M. Yarmuch, “Effect of Welding Parameters on the Plasma Transferred Arc Welding (PTAW) Process for Autogenous Beads and 410SS-WC Overlays,” University of Alberta, 2005.

[27] J. A. Browning, “Plasma - A Substitute for the Oxy-Fuel Flame,” *Weld. J.*, vol. 38, no. 9, pp. 870–875, 1959.

[28] P. F. Mendez, M. A. Ramirez, G. Trapaga, and T. W. Eager, “Order of Magniture Scaling of the Cathode Region in a Axisymmetric Transferred Electric Arc,” *Metall. Trans. B*, vol. 32, no. 3, pp. 547–554, 2001.

[29] P. F. Mendez, M. A. Ramirez, G. Trapaga, and T. W. Eager, “Scaling Laws in the Welding Arc,” in *Mathematical Modelling of Weld Phenomena 6*, 2002, pp. 43–61.

[30] M. Weglowski, “Determination of GTA and GMA welding arc temperatures,” *Weld. Int.*, vol. 19, no. 3, pp. 186–192, Mar. 2005.

[31] D. R. Milner, G. R. Salter, and J. B. Wilkinson, “Arc Characteristics and their Significance in Welding,” *Br. Weld. J.*, vol. 7, no. 2, pp. 73–88, 1960.

[32] G. K. Hicken, “Gas Tunsgten Arc Welding,” in *Welding Handbook, Vol. 2: Welding Processes*, 8th Ed., AWS, pp. 74–107.

[33] W. Lucas, “Choosing a Shielding Gas-Part 2,” *Weld. J.*, vol. 60, no. 6, pp. 269–276, 1992.

[34] B. Irving, “Trying to Make Some Sense Out of Shielding Gases,” *Weld. J.*, vol. 73, no. 5, pp. 65–70, 1995.

[35] B. Raj, V. Shankar, and A. K. Bhaduri, *Welding Technology for Engineering*. Narosa Publishing House, 2006, p. 116.

[36] M. S. Wêglowski, Y. Huang, and Y. M. Zhang, "Effect of welding current on metal transfer in GMAW," *Mater. Sci. Eng.*, vol. 33, no. 1, pp. 49–56, 2008.

[37] J. H. Waszink and L. H. J. Graat, "Experimental Investigation of the Forces Acting on a Drop of Weld Metal," *Weld. J.*, vol. 62, no. 4, pp. 108–116, 1983.

[38] J. J. Lowke, "Globular and Spray Transfer in MIG Welding," *Weld. World*, vol. 55, no. 3–4, 2011.

[39] A. Klimpel and T. Kik, "Erosion and abrasion wear resistance of GMA wire surfaced nanostructural deposits," *Mater. Sci. Eng.*, vol. 30, no. 2, pp. 121–124, 2008.

[40] L. J. Li and C. Bin Gui, "Effect of Dissolving of WC/W_2C on the Interface Microstructure of Iron Matrix Hardfacing Alloys," *Adv. Mater. Res.*, vol. 306–307, pp. 819–822, Aug. 2011.

[41] A. Klimpel, L. A. Dobrzanski, A. Lisiecki, and D. Janicki, "The study of properties of Ni-WC wires surfaced deposits," *J. Mater. Process. Technol.*, vol. 164, pp. 1046–1055, May 2005.

[42] L. J. Li and L. Dai, "Microstructures and Properties of Tungsten Carbide Particle-Reinforced Composites Fabricated by Overlaying Welding with Flux-Cored Wire," *Adv. Mater. Res.*, vol. 228–229, pp. 548–551, Apr. 2011.

[43] A. Klimpel, A. Lisiecki, A. St. Klimpel, and A. Rzeznikiewicz, "Robotized GMA surfacing of cermetal deposits," *J. Achiev. Mater. Manuf. Eng.*, vol. 18, no. 1–2, pp. 395–398, 2006.

[44] P. Vespa, P. T. Pinard, R. Gauvin, and M. Brochu, "Analysis of WC/Ni-Based Coatings Deposited by Controlled Short-Circuit MIG Welding," *J. Mater. Eng. Perform.*, vol. 21, no. 6, pp. 865–876, Jun. 2012.

[45] E. Badisch and M. Kirchgaßner, "Influence of welding parameters on microstructure and wear behaviour of a typical NiCrBSi hardfacing alloy reinforced with tungsten carbide," *Surf. Coatings Technol.*, vol. 202, no. 24, pp. 6016–6022, Aug. 2008.

[46] L. Choi, T. Wolfe, M. Yarmuch, and A. Gerlich, "Effect of Welding Parameters on Tungsten Carbide - Metal Matrix Composites Produced by

GMAW Effect of Welding Parameters on Tungsten Carbide - Metal Matrix Composites Produced by GMAW," in *CWA Annual Conference*, 2011.

[47] K. M. Scott, "Heat Transfer and Calorimetry of Tubular Ni/WC Wires Deposited with GMAW," University of Alberta, 2011.

[48] E. Soderstrom, K. Scott, and P. Mendez, "Calorimetric Measurement of Droplet Temperature in GMAW," *Weld. J.*, vol. 90, no. 4, pp. 77–84, 2011.

[49] M. Ushio, A. Raja, and F. Matsuda, "Melting Characteristics of Flux Cored Wire," *Japan Weld. Res. Inst.*, vol. 13, no. 1, pp. 1–6, 1984.

[50] R. Shimura, H. Nagasaki, Y. Totsuka, and S. Nakamura, "Development of Seamless flux cored wire for high strength steel," *Doc. VII-2033-11*.

[51] K. Srinivasan and V. Balasubramanian, "Effect of surface tension metal transfer on fume formation rate during flux-cored arc welding of HSLA steel," *Int. J. Adv. Manuf. Technol.*, vol. 56, no. 1–4, pp. 125–134, Feb. 2011.

[52] C. M. D. Starling and P. J. Modenesi, "Metal transfer evaluation of tubular wires," *Weld. Int.*, vol. 21, no. 6, pp. 412–420, Jun. 2007.

[53] E. Bauné, C. Bonnet, and S. Liu, "Assessing metal transfer stability and spatter severity in flux cored arc welding," *Sci. Technol. Weld. Join.*, vol. 6, no. 3, pp. 139–148, Jun. 2001.

[54] H.-Y. Liu, Z.-X. Li, H. Li, and Y.-W. Shi, "Study on metal transfer modes and welding spatter characteristics of self-shielded flux cored wire," *Sci. Technol. Weld. Join.*, vol. 13, no. 8, pp. 777–780, Nov. 2008.

[55] T. Liyanage, "Microstructure and Properties of Ni-Alloy and Ni-WC Composite Overlays," University of Alberta, 2010.

[56] B. V Cockeram, "The fracture toughness and toughening mechanisms of nickel-base wear materials," *Metall. Mater. Trans. A-Physical Metall. Mater. Sci.*, vol. 33, no. 1, pp. 33–56, Jan. 2002.

[57] C. B. Finch, O. B. Cavin, and P. F. Becher, "Crystal Growth and Properties of Trinickel Boride, Ni3B," *J. Cryst. Growth*, vol. 67, pp. 556–558, 1984.

[58] Q. Y. Hou, Y. Z. He, Q. a. Zhang, and J. S. Gao, "Influence of molybdenum on the microstructure and wear resistance of nickel-based alloy coating obtained by plasma transferred arc process," *Mater. Des.*, vol. 28, no. 6, pp. 1982–1987, Jan. 2007.

[59] Z. Huang, Q. Hou, and P. Wang, “Microstructure and properties of Cr3C2-modified nickel-based alloy coating deposited by plasma transferred arc process,” *Surf. Coatings Technol.*, vol. 202, no. 13, pp. 2993–2999, Mar. 2008.

[60] T. Hejwowski, “Erosive and abrasive wear resistance of overlay coatings,” *Vacuum*, vol. 83, no. 1, pp. 166–170, Sep. 2008.

[61] P. K. Liao and K. E. Speak, “B-Ni (Boron-Nickel),” in *Binary Alloy Phase Diagrams*, 2nd Ed., T. B. Massalski, Ed. 1990, pp. 508–510.

[62] I. C. Grigorescu, C. DiRauso, R. DriraHalouani, B. Lavelle, R. DiGiampaolo, and J. Lira, “Phase characterization in Ni alloy hard carbide composites for fused coatings,” *Surf. Coat. Technol.*, vol. 76–77, no. 1–3, pp. 494–498, Dec. 1995.

[63] K. I. Portnoi, V. M. Romashov, V. M. Chubarov, M. K. Levinskaya, and S. E. Salibekov, “Phase Diagram of the System Nickel-Boron,” *Sov. Powder Metall. Met. Ceram.*, vol. 6, no. 2, pp. 99–103, 1967.

[64] Y. H. Shieh, J. T. Wand, H. C. Shih, and S. T. Wu, “Alloying and Post-Heat-Treatment of Thermal-Sprayed Coatings of Self-Fluxing Alloys,” *Surf. Coat. Technol.*, vol. 58, no. 1, pp. 73–77, Jun. 1993.

[65] K. Oikawa, R. Saito, K. Kobayashi, J. Yaokawa, and K. Anzai, “Phase Equilibria in Ni-Rich Portion of Ni-Si System,” *Mater. Trans.*, vol. 48, no. 9, pp. 2259–2262, 2007.

[66] M. Lindholm and B. O. Sundman, “A Thermodynamic Evaluation of the Nickel-Silicon System,” *Metall. Mater. Trans. A-Physical Metall. Mater. Sci.*, vol. 27, no. 10, pp. 2897–2903, 1996.

[67] J. W. Baker and M. S. Patel, “Protective Coatings by Powder and Flame Deposition Processes,” in *8th International Thermal Spray Conference*, 1976, p. 159.

[68] T. Liyanage, G. Fisher, and a. P. Gerlich, “Microstructures and abrasive wear performance of PTAW deposited Ni–WC overlays using different Ni-alloy chemistries,” *Wear*, vol. 274–275, pp. 345–354, Jan. 2012.

[69] R. Polak, S. Ilo, and E. Badisch, “Relation Between Inter-Particle Distance (L-IPD) and Abrasion in Multiphase Matrix-Carbide Materials,” *Tribol. Lett.*, vol. 33, no. 1, pp. 29–35, Jan. 2009.

[70] S. S. Babu, R. P. Martukanitz, K. D. Parks, and S. A. David, “Toward Prediction of Microstructural Evolution during Laser Surface Alloying,” *Metall. Mater. Trans. A*, vol. 33A, pp. 1189–1200, 2002.

[71] S. Zhou, X. Dai, and T. Zhang, “Effect of binder metals on structure and properties of WC ceramic-metal composite coatings by laser-induction hybrid rapid cladding,” *J. Compos. Mater.*, vol. 47, no. 12, pp. 1549–1559, Jun. 2012.

[72] J. Yang, F. Liu, X. Miao, and F. Yang, “Influence of laser cladding process on the magnetic properties of WC–FeNiCr metal–matrix composite coatings,” *J. Mater. Process. Technol.*, vol. 212, no. 9, pp. 1862–1868, Sep. 2012.

[73] T. Iwai, I. Takahashi, and M. Handa, “Gibbs Free-Energies of Formation of Molybdenum Carbide and Tungsten Carbide from 1173 to 1573 K,” *Metall. Trans. A-Physical Metall. Mater. Sci.*, vol. 17, no. 11, pp. 2031–2034, Nov. 1986.

[74] M. Gauthier, *Engineered Materials Handbook*. ASM International, 1995.

[75] C. Gerk and K. D. Wernicke, “Dual-Phase Hard Material Comprising Tungsten Carbide, Process for the Production Thereof and Its Use,” US 7,541,0902009.

[76] M. Jones and U. Waag, “The influence of carbide dissolution on the erosion-corrosion properties of cast tungsten carbide/Ni-based PTAW overlays,” *Wear*, vol. 271, no. 9–10, pp. 1314–1324, Jul. 2011.

[77] D. Yu, T. Xing-long, L. Yu-xi, Y. Jian-gao, and H. Bai-yun, “Influence of fabricating process on microstructure and properties of spheroidal cast tungsten carbide powder,” *Trans. Nonferrous Met. Soc. China*, vol. 15, no. 2, pp. 270–274, 2005.

[78] G. Fisher, T. Wolfe, and K. Meszaros, “The Effects of Carbide Characteristics on the Performance of Tungsten Carbide-Based Composite Overlays, Deposited by Plasma-Transferred Arc Welding,” *J. Therm. Spray Technol.*, vol. 22, no. 5, pp. 764–771, Jan. 2013.

[79] DurumVerschleiss-SchutzGMBH, “FTC and SFTC technical brochure.” 2013.

[80] M. D. Demetriou, N. M. Ghoniem, and A. S. Lavine, “Computation of metastable phases in tungsten-carbon system,” *J. Phase Equilibria*, vol. 23, no. 4, pp. 305–309, Aug. 2002.

[81] M. D. Demetriou, N. M. Ghoniem, and A. S. Lavine, “Modeling of graphitization kinetics during peritectic melting of tungsten carbide,” *Acta Mater.*, vol. 50, no. 20, pp. 4995–5004, Mar. 2002.

[82] V. Z. Kublii and T. Y. Velikanova, “Ordering in the Carbide W2C and Phase Equilibria in the Tungsten-Carbon System in the Region of its Existence,” *Powder Metall. Met. Ceram.*, vol. 43, no. 11–12, pp. 630–644, 2004.

[83] A. S. Kurlov and A. I. Gusev, “Tungsten carbides and W-C phase diagram,” *Inorg. Mater.*, vol. 42, no. 2, pp. 121–127, Feb. 2006.

[84] T. V Massalski, P. R. Subramanian, H. Okamoto, and L. Kasprzak, Eds., “C-W Phase Diagram,” in *ASM Handbook*, 2nd Ed., ASM International, 1990.

[85] H. Okamoto, “C-W (Carbon-Tungsten),” *J. Phase Equilibria Diffus.*, vol. 29, no. 6, pp. 543–544, Oct. 2008.

[86] F. A. C. Oliveira, J. C. Fernandes, J.-M. Badie, B. Granier, L. G. Rosa, and N. Shohoji, “High meta-stability of tungsten sub-carbide W2C formed from tungsten/carbon powder mixture during eruptive heating in a solar furnace,” *Int. J. Refract. Met. Hard Mater.*, vol. 25, no. 1, pp. 101–106, Jan. 2007.

[87] P. J. Pappafava, “The Manufacturing Process for Cemented Tungsten Carbides.” General Carbide Corporation, Greensburg, USA.

[88] C. Just, S. Ilo, and E. Badisch, “Influence of processing conditions on the carbide/matrix interface in sintered composite layers,” *Surf. Coatings Technol.*, vol. 205, no. 1, pp. 35–42, Sep. 2010.

[89] M. Jones and R. J. Llewellyn, “Erosion-Corrosion Assessment of Tungsten Carbide-Based Plasma-Transferred Arc-Welded Overlays,” *Corrosion*, vol. 68, no. 2, pp. 1–14, 2012.

[90] S. Ilo, C. Just, E. Badisch, J. Wosik, and H. Danninger, “Effects of interface formation kinetics on the microstructural properties of wear-resistant metal–matrix composites,” *Mater. Sci. Eng. A*, vol. 527, no. 23, pp. 6378–6385, 2010.

[91] C. Katsich and E. Badisch, “Effect of carbide degradation in a Ni-based hardfacing under abrasive and combined impact/abrasive conditions,” *Surf. Coatings Technol.*, vol. 206, no. 6, pp. 1062–1068, Dec. 2011.

[92] C. Just, E. Badisch, and J. Wosik, "Influence of welding current on carbide/matrix interface properties in MMCs," *J. Mater. Process. Technol.*, vol. 210, no. 2, pp. 408–414, Jan. 2010.

[93] K. Van Acker, D. Vanhoyweghen, R. Persoons, and J. Vangrunderbeek, "Influence of tungsten carbide particle size and distribution on the wear resistance of laser clad WC/Ni coatings," *Wear*, vol. 258, no. 1–4, pp. 194–202, Jan. 2005.

[94] R. Gassmann, "Laser cladding with (WC + W2C)/Co-Cr-C and (WC + W2C)/Ni-B-Si composites for enhanced abrasive wear resistance," *Mater. Sci. Technol.*, vol. 12, no. August, pp. 691–696, 1996.

[95] D. M. Janicki, "High Power Diode Laser Cladding of Wear Resistant Metal Matrix Composite Coatings," *Solid State Phenom.*, vol. 199, pp. 587–592, Mar. 2013.

[96] P. Wu, H. M. Du, X. L. Chen, Z. Q. Li, H. L. Bai, and E. Y. Jiang, "Influence of WC particle behavior on the wear resistance properties of Ni–WC composite coatings," *Wear*, vol. 257, no. 1–2, pp. 142–147, Jul. 2004.

[97] S. Zhou and X. Dai, "Laser induction hybrid rapid cladding of WC particles reinforced NiCrBSi composite coatings," *Appl. Surf. Sci.*, vol. 256, no. 14, pp. 4708–4714, May 2010.

[98] J. F. Flores, A. Neville, N. Kapur, and A. Gnanavelu, "Corrosion and Erosion-Corrosion Processes of Metal-Matrix Composites in Slurry Conditions," *J. Mater. Eng. Perform.*, vol. 21, no. 3, pp. 395–405, Mar. 2012.

[99] J. F. Flores, A. Neville, N. Kapur, and A. Gnanavelu, "Erosion–corrosion degradation mechanisms of Fe–Cr–C and WC–Fe–Cr–C PTA overlays in concentrated slurries," *Wear*, vol. 267, no. 11, pp. 1811–1820, 2009.

[100] J. F. Flores, A. Neville, N. Kapur, and A. Gnanavelu, "An experimental study of the erosion-corrosion behavior of plasma transferred arc MMCs," *Wear*, vol. 267, no. 1–4, pp. 213–222, Jun. 2009.

[101] T. B. B. Wolfe, "Homogeneity of Metal Matrix Composites Deposited by Plasma Transferred Arc Welding," University of Alberta, 2010.

[102] M. Zhao, A. Liu, M. Guo, D. Liu, Z. Wang, and C. Wang, "WC reinforced surface metal matrix composite produced by plasma melt injection," *Surf. Coatings Technol.*, vol. 201, no. 3–4, pp. 1655–1659, Oct. 2006.

[103] K. W. D. Hart, D. Harper, and M. J. Gill, “Case studies in wear resistance using HVOF, PTAW and Spray Fusion surfacing,” in *1st International Thermal Spray Conference, ASM International*, 2000, vol. Montreal,, pp. 1117–1125.

[104] M. Jones and R. J. Llewellyn, “Erosion–corrosion assessment of materials for use in the resources industry,” *Wear*, vol. 267, no. 11, pp. 2003–2009, Oct. 2009.

[105] J. F. Flores, A. Neville, N. Kapur, and A. Gnanavelu, “Assessing the resistance of metal matrix composites and their microstructural integrity under erosion-corrosion,” *Wear*, vol. 271, no. 9–10, pp. 1331–1340, Jul. 2011.

[106] E. I. Kivineva, D. L. Olson, and D. K. Matlock, “Particulate-Reinforced Metal Matrix Composite as a Weld Deposit,” *Weld. J.*, vol. March, pp. 83–92, 1995.

[107] M. Gubisch, Y. Liu, S. Krischok, G. Ecke, L. Spiess, J. A. Schaefer, and C. Knedlik, “Tribological characteristics of WC1-x, W2C and WC tungsten carbide films,” *Tribol. Interface Eng. Ser.*, vol. 48, pp. 409–417, 2005.

[108] ASMTE1479, “Standard Practice for Describing and Specifying Inductively-Coupled Plasma Atomic Emission Spectromers.”

[109] E. Tsotsas and H. Martin, “Thermal conductivity of packed beds: A review,” *Chem. Eng. Process. Process Intensif.*, vol. 22, no. 1, pp. 19–37, Jul. 1987.

[110] Y. Ozaki and R. H. Zee, “Investigation of thermal and hydrogen effects on emissivity of refractory metals and carbides,” *Mater. Sci. Eng. A*, vol. 202, no. 1–2, pp. 134–141, Nov. 1995.

[111] J. F. Shackelford and W. Alexander, Eds., *CRC Materials Science and Engineering Handbook*, 3rd Ed. CRC Press, 2000, p. 279.

[112] F. P. Incroprera, D. P. DeWitt, T. L. Bergman, and A. S. Lavine, *Introduction to Heat Transfer*, 5th Ed. John Wiley & Sons, 2007.

[113] D. U. Furrer and S. L. Semiatin, “Simulation of Induction Heating Prior to Hot Working and Coating,” in *ASM Handbook*, vol. 22, 2009, pp. 475–500.

[114] C. A. Reeves, “Electrical Conductivity and Mechanical Property Measurements on a Cold Worked Austenitic Stainless Steel,” University of Tennessee, 1972.

[115] W. D. Callister, *Materials Science and Engineering An Introduction*, 7th Ed. 2007.

[116] S. Seetharaman, Ed., *Fundamentals of Metallurgy*. Woodhead Publishing Limited, 2005.

[117] G. S. Kumar, G. Prasad, and R. O. Pohl, “Experimental determinations of the Lorenz number,” *J. Mater. Sci.*, vol. 28, pp. 4261–4272, 1993.

[118] A. Cezairliyan and A. P. Miiller, “Thermophysical Measurements on Low Carbon 304 Stainless Steel Above 1400 K by a Transient (Subsecond) Technique,” *Int. J. Thermophys.*, vol. 1, no. 1, pp. 83–95, 1980.

[119] A. F. Clark, G. E. Childs, and G. H. Wallace, “Electrical Resistivity of some Engineering Alloys at Low Temperatures,” *Cryogenics (Guildf).*, vol. 10, no. 4, pp. 295–305, 1970.

[120] R. H. Bogaard, P. D. Desai, H. H. Li, and C. Y. Ho, “Thermophysical properties of stainless steels,” *Thermochim. Acta*, vol. 218, pp. 373–393, May 1993.

[121] K. C. Mills, *Recommended values of thermophysical properties for selected commercial alloys*. Woodhead Publishing Limited, 2002.

[122] NIDI, “Mechanical and Physical Properties of Austenitic Chromium-Nickel Stainless Steel at Ambient Temperatues, Publ. No: 2978.”

[123] M. Rouby and P. Blanchard, “Physical and Mechanical Properties of Stainless Steels,” *les Ed. Phys.*, pp. 111–158, 1993.

[124] B. Wilthan, H. Reschab, R. Tanzer, W. Schützenhöfer, and G. Pottlacher, “Thermophysical Properties of a Chromium–Nickel–Molybdenum Steel in the Solid and Liquid Phases,” *Int. J. Thermophys.*, vol. 29, no. 1, pp. 434–444, Nov. 2007.

[125] C. A. Domenicali and F. A. Otter, “Thermoelectric Power and Electrical Resistivity of Dilute Alloys of Silicon in Copper, Nickel, and Iron,” *J. Appl. Phys.*, vol. 26, no. 4, pp. 377–380, 1955.

[126] R. W. Powell, R. P. Tye, and M. J. Hickman, “The Thermal Conductivity of Nickel,” *Int. J. Heat Mass Transf.*, vol. 8, pp. 679–688, 1965.

[127] E. A. Eldridge and H. W. Deem, “Report on physcial properties of metals and alloys from cryogenic to elevated temperatures,” *ASTM Spec. Tech. Publ. N. 296*, 1961.

[128] *ASM Handbook, Vol. 1*, 10th Ed. ASM International, 1990.

[129] M. F. Rothman, Ed., *High Temperature Property Data: Ferrous Alloys*. ASM International, 1988.

[130] P. M. Unterweiser, H. E. Boyer, and J. J. Kubbs, Eds., *Heat Treater's Guide: Standard Practices and Procedures for Steel*. 1982.

[131] D. Basak, R. a. Overfelt, and D. Wang, "Measurement of Specific Heat Capacity and Electrical Resistivity of Industrial Alloys Using Pulse Heating Techniques," *Int. J. Thermophys.*, vol. 24, no. 6, pp. 1721–1733, Nov. 2003.

[132] G. R. Lehnhoff and P. F. Mendez, "Scaling of non-linear effects in heat transfer of a continuously fed melting wire," *Int. J. Heat Mass Transf.*, vol. 54, no. 11–12, pp. 2651–2660, May 2011.

[133] G. Kaptay, "On the interfacial force between ceramic particles and moving solid-liquid interface during solidification of metal matrix composites," in *Proc. of the EUROMAT*, 1997, pp. 435–438.

[134] A. Mortensen, "Interfacial Phenomena in the Solidification Processing of Metal Matrix Composites," *Mater. Sci. Eng. A-Structural Mater. Prop. Microstruct. Process.*, vol. 135, pp. 1–11, Mar. 1991.

[135] D. Hamre, "Laser Applied Tungsten Carbide Wear Protection (Laser Cladding)," in *CWA Seminar "Weld Overlays for Wear Protection"*, 2013, CWA Seminar.

[136] G. Kaptay, "Interfacial Phenomena during Melt Processing of Ceramic Particle-Reinforced Metal Matrix Composites Part I. Introduction (Incorporation) of Solid Particles into Melts," *Mater. Sci. Forum*, vol. 215–216, pp. 459–466, 1996.

[137] L. Luo, Y. Wu, J. Li, and Y. Zheng, "Preparation of nickel-coated tungsten carbide powders by room temperature ultrasonic-assisted electroless plating," *Surf. Coatings Technol.*, vol. 206, no. 6, pp. 1091–1095, Dec. 2011.

Appendix

1. Nomenclature

Chapter	Term	Description
2	m'_X	Linear mass (g·cm^{-1}) of *x*, where *x* is carbide powder or nickel sheath.
	$f_{c,max}$	Initial wire carbide volume fraction or the maximum upper bound carbide fraction in the wire prior to welding.
	$f_{c,core}$	Wire core carbide fraction or packing factor of carbides in tubular wire interior.
	$\sigma_{f_{c,max}}$	Calculated error of measuring $f_{c,max}$.
	λ_{2P}	Unitless bulk thermal conductivity coefficient of powders accounting for packing factor, inter-particle radiation, powder shape factor, and particle thermal conductivity.
	λ_C	Core conductivity coefficient accounting for radiation, fluid conduction, particle-particle contact conduction, powder deformation factor.
	H_{WC}^m, H_{WC}^o	Melting and room temperature volumetric enthalpies of tungsten carbide calculated with ThermoCalc.
3	*	Superscript depicting a normalized term or function.
	$^+$	Superscript depicting an improved estimation of the term or function.
	$\hat{}$	Accent depicting an estimated value or term.
	$\hat{q}^+$	Heat flux at the end of the electrode from leading heat source and weld pool.
	$\widehat{H_{c_2}^{+*}}$	Normalized improved estimation of the enthalpy increase along the Joule heating portion of the electrode extension accounting for non-linearity's in temperature dependent electrical resistivity.
	L	Hot-wire electrode extension from contact tip to semi-solid transition point.
	L_o	Initial hot-wire electrode extension from contact tip to workpiece (ie. CTWD).

	α	Angle between h and the semi-solid transition point on the top-side of the hot-wire electrode.
	θ	Hot-wire insertion angle relative to the workpiece.
	d	Hot-wire separation distance between the centre of the leading heat source and the hot-wire when the hot-wire is touching the workpiece prior to welding.
	d_1	Distance between the semi-solid transition point on the hot-wire electrode top surface and h.
	h	GTAW: half height of the arc length between the weld pool surface and the electrode tip. GMAW: half height of the weld bead thickness.
	t	Weld bead thickness.
	d_x	Horizontal distance between the leading heat source electrode and the hot-wire semi-solid transition point.
	d_y	Vertical distance between h and the hot-wire semi-solid transition point.
	$f_{\widehat{H_{C_2}^{+*}}}$	Correction factor accounting for inaccuracies in volumetric enthalpy, hot-wire electrode diameter, electrode extension, hot-wire current, and electrical resistivity. Calculated from reaching the semi-solid temperature with sufficient hot-wire current without a leading heat source and comparing the observed energy to the uncorrected model.
	$\widehat{q_{arc}}$	Heat from the leading heat source calculated with the HWGTAW/HWGMAW regressions.
4	f_c	Overall area fraction of tungsten carbide in the total weld deposit considering the dilution with the substrate. Area fraction is approximated as equivalent to volume fraction.
4	η_c	Tungsten carbide transfer efficiency of the GMAW process neglecting dilution with the substrate. Provides a metric for comparing the amount of tungsten carbide lost to dissolution and non-wetting.

2. Ni-WC Wire Cross Sections

2.1. Consumable A

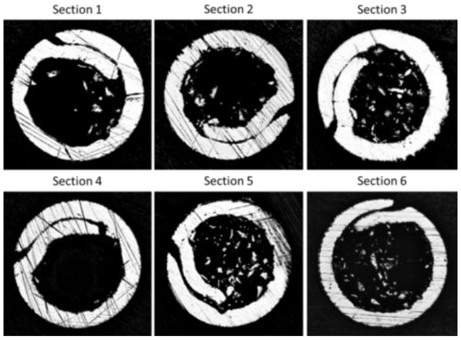

2.2. Consumable B

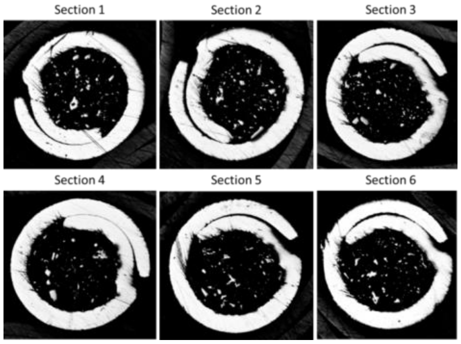

2.3. Consumable C

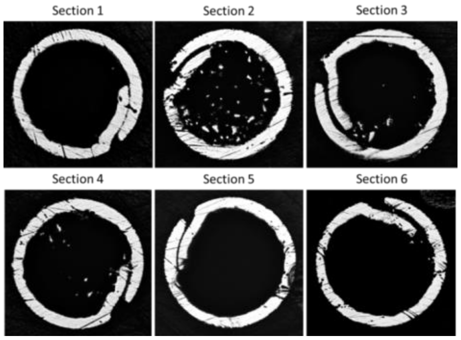

2.4. Consumable D

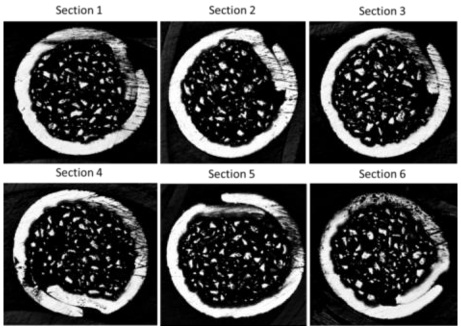

2.5. Consumable E

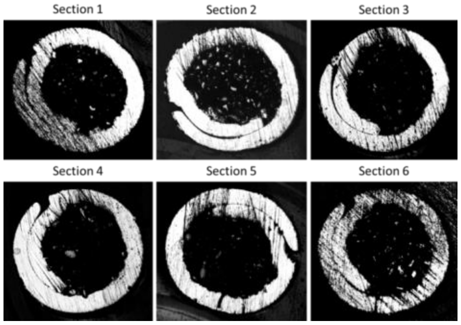

2.6. Consumable F

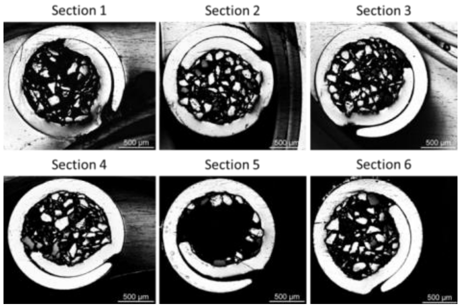

2.7. Consumable G

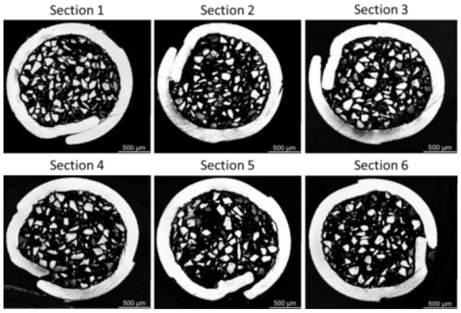

2.8. Nickel Sheath Area Measurements

Consumable	**A**	**B**	**C**	**D**	**E**	**F**	**G**
Section 1 (mm^2)	0.885	1.023	0.683	0.779	1.114	0.991	1.151
Section 2 (mm^2)	0.973	1.020	0.711	0.777	1.029	0.963	1.168
Section 3 (mm^2)	1.072	1.030	0.727	0.761	1.025	0.981	1.148
Section 4 (mm^2)	1.008	1.039	0.670	0.780	1.052	0.955	1.103
Section 5 (mm^2)	0.950	1.035	0.694	0.745	1.047	0.933	1.223
Section 6 (mm^2)	0.806	1.034	0.660	0.775	1.067	0.972	1.129

2.9. Internal Area Measurements: As-Polished

Consumable	**A**	**B**	**C**	**D**	**E**	**F**	**G**
Section 1 (mm^2)	0.953	0.924	1.271	1.312	0.903	0.987	1.878
Section 2 (mm^2)	0.899	0.922	1.218	1.217	0.962	0.990	1.892
Section 3 (mm^2)	0.894	0.942	1.188	1.246	0.995	0.983	1.888
Section 4 (mm^2)	0.859	0.907	1.369	1.292	0.931	1.001	2.069
Section 5 (mm^2)	0.927	0.918	1.277	1.271	0.962	0.980	2.024
Section 6 (mm^2)	1.204	0.884	1.331	1.263	0.925	0.994	2.045

2.10. Internal Area Measurements: Adjusted

Consumable	**A**	**B**	**C**	**D**	**E**	**F**	**G**
Section 1 (mm^2)	0.923	0.865	1.224	1.201	0.881	0.922	1.829
Section 2 (mm^2)	0.863	0.867	1.167	1.166	0.931	0.940	1.822
Section 3 (mm^2)	0.858	0.865	1.133	1.155	0.979	0.932	1.768
Section 4 (mm^2)	0.832	0.845	1.283	1.235	0.879	0.957	1.958
Section 5 (mm^2)	0.873	0.863	1.232	1.182	0.929	0.942	1.914
Section 6 (mm^2)	1.160	0.835	1.275	1.178	0.869	0.947	1.980
% difference from As-Polished Area	4.0	6.4	4.5	6.4	3.7	5.0	4.4

$$\% \, Change\ in\ Area = 1 - \frac{Adjusted\ Area}{As - Polished\ Area} \ x\ 100\%$$

2.11. Nickel Sheath Area Verification

$$calculated\ nickel\ sheath\ linear\ density = \ {\rho_{S_C}}' = \rho_S A_S$$

Where ρ_S is the density of nickel (8.91 g/cm^3) and A_S is the average measured area of the nickel sheath using the Measurement tool in Adobe Photoshop. The calculated nickel sheath linear density was compared to the measured sheath linear density using the variance of the measured sheath area.

Consumable	ρ'_S (g/cm)	A_S (mm^2)	$\rho'_{S,c}$ (g/cm)	***Agrees*** (Y/N)
A	0.087	0.949 ± 0.085	0.077-0.092	**Y**
B	0.088	1.030 ± 0.007	0.091-0.092	**N**
C	0.065	0.691 ± 0.023	0.060-0.064	**N**
D	0.069	0.769 ± 0.013	0.067-0.070	**Y**
E	0.094	1.056 ± 0.030	0.091-0.097	**Y**
F	0.092	0.966 ± 0.019	0.084-0.088	**N**
G	0.101	1.154 ± 0.037	0.100-0.106	**Y**

2.12. Carbide and Alloying Powder Extraction Efficiency Verification

The error of the mass scale used for measuring the mass of carbide powder is 0.01 grams. During the removal of the carbide powder, a few carbide particles were lost. The average carbide diameter was assumed to be 100 µm with a density of 16.475 gcm^{-3}. This calculation below nullifies the potential extraction error as a result of the sheath and powder separation process as over 1159 particles were not lost, making the scale error dominant.

$$No.of\ Carbide\ Particles = \frac{\dfrac{Scale\ Error\ (g)}{Carbide\ Density\ \left({}^{g}/_{cm^3}\right)}}{Volume\ of\ Carbide\ Particle\ (cm^3)} = \frac{\dfrac{0.01}{16.475}}{\dfrac{4}{3}\pi(0.05^3)} = 1159$$

3. Powder ICP Analysis

3.1. Consumable A – Testing Facility 1

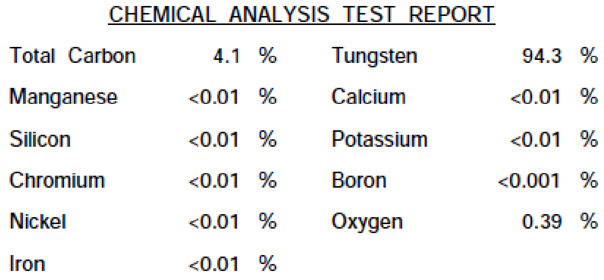

CHEMICAL ANALYSIS TEST REPORT

Total Carbon	4.1	%	Tungsten	94.3	%
Manganese	<0.01	%	Calcium	<0.01	%
Silicon	<0.01	%	Potassium	<0.01	%
Chromium	<0.01	%	Boron	<0.001	%
Nickel	<0.01	%	Oxygen	0.39	%
Iron	<0.01	%			

3.2. Consumable A – Testing Facility 2

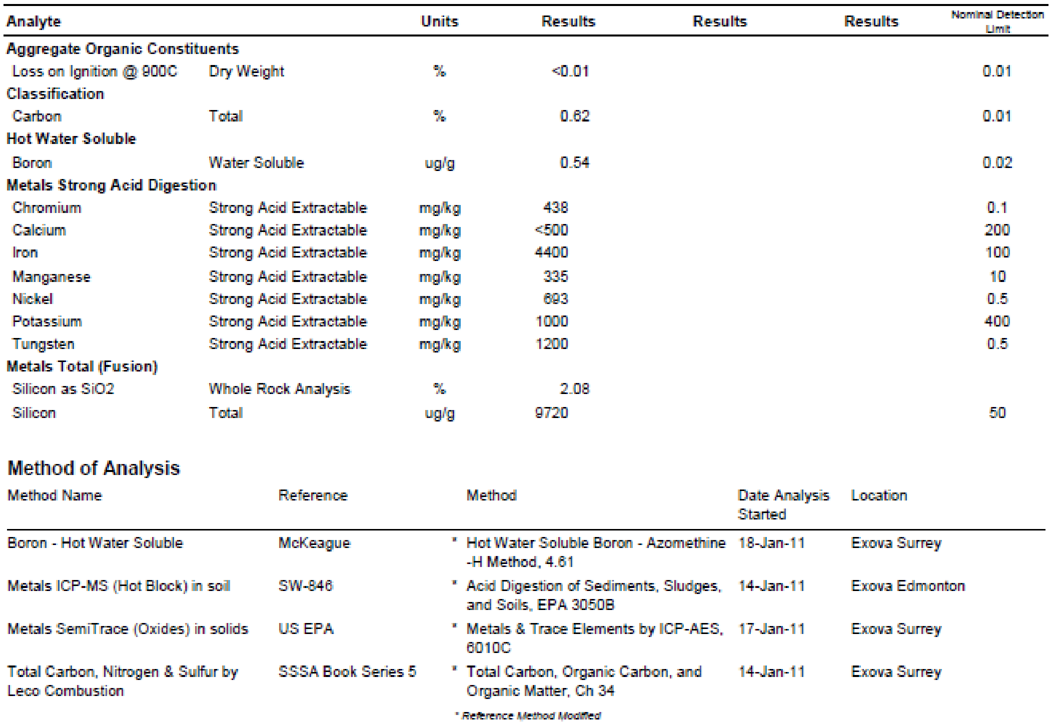

Analyte		Units	Results	Results	Results	Nominal Detection Limit
Aggregate Organic Constituents						
Loss on Ignition @ 900C	Dry Weight	%	<0.01			0.01
Classification						
Carbon	Total	%	0.62			0.01
Hot Water Soluble						
Boron	Water Soluble	ug/g	0.54			0.02
Metals Strong Acid Digestion						
Chromium	Strong Acid Extractable	mg/kg	438			0.1
Calcium	Strong Acid Extractable	mg/kg	<500			200
Iron	Strong Acid Extractable	mg/kg	4400			100
Manganese	Strong Acid Extractable	mg/kg	335			10
Nickel	Strong Acid Extractable	mg/kg	693			0.5
Potassium	Strong Acid Extractable	mg/kg	1000			400
Tungsten	Strong Acid Extractable	mg/kg	1200			0.5
Metals Total (Fusion)						
Silicon as SiO2	Whole Rock Analysis	%	2.08			
Silicon	Total	ug/g	9720			50

Method of Analysis

Method Name	Reference	Method	Date Analysis Started	Location
Boron - Hot Water Soluble	McKeague	* Hot Water Soluble Boron - Azomethine -H Method, 4.61	18-Jan-11	Exova Surrey
Metals ICP-MS (Hot Block) in soil	SW-846	* Acid Digestion of Sediments, Sludges, and Soils, EPA 3050B	14-Jan-11	Exova Edmonton
Metals SemiTrace (Oxides) in solids	US EPA	* Metals & Trace Elements by ICP-AES, 6010C	17-Jan-11	Exova Surrey
Total Carbon, Nitrogen & Sulfur by Leco Combustion	SSSA Book Series 5	* Total Carbon, Organic Carbon, and Organic Matter, Ch 34	14-Jan-11	Exova Surrey

** Reference Method Modified*

3.3. Consumable B

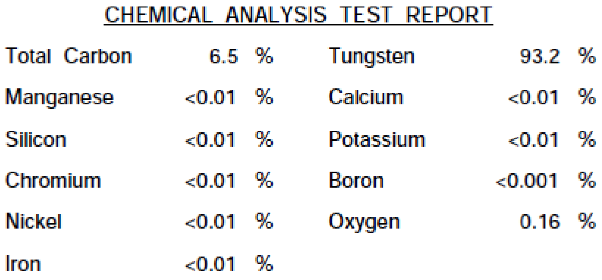

CHEMICAL ANALYSIS TEST REPORT

Total Carbon	6.5	%	Tungsten	93.2	%
Manganese	<0.01	%	Calcium	<0.01	%
Silicon	<0.01	%	Potassium	<0.01	%
Chromium	<0.01	%	Boron	<0.001	%
Nickel	<0.01	%	Oxygen	0.16	%
Iron	<0.01	%			

3.4. Consumable C

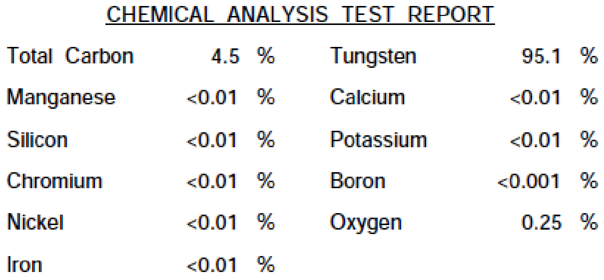

CHEMICAL ANALYSIS TEST REPORT

Total Carbon	4.5	%	Tungsten	95.1	%
Manganese	<0.01	%	Calcium	<0.01	%
Silicon	<0.01	%	Potassium	<0.01	%
Chromium	<0.01	%	Boron	<0.001	%
Nickel	<0.01	%	Oxygen	0.25	%
Iron	<0.01	%			

3.5. Consumable D

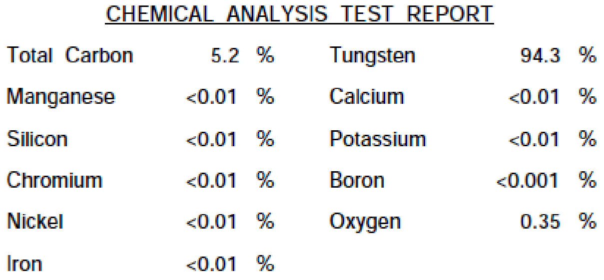

CHEMICAL ANALYSIS TEST REPORT

Total Carbon	5.2	%	Tungsten	94.3	%
Manganese	<0.01	%	Calcium	<0.01	%
Silicon	<0.01	%	Potassium	<0.01	%
Chromium	<0.01	%	Boron	<0.001	%
Nickel	<0.01	%	Oxygen	0.35	%
Iron	<0.01	%			

4. Powder EDS Analysis

4.1. Consumable A

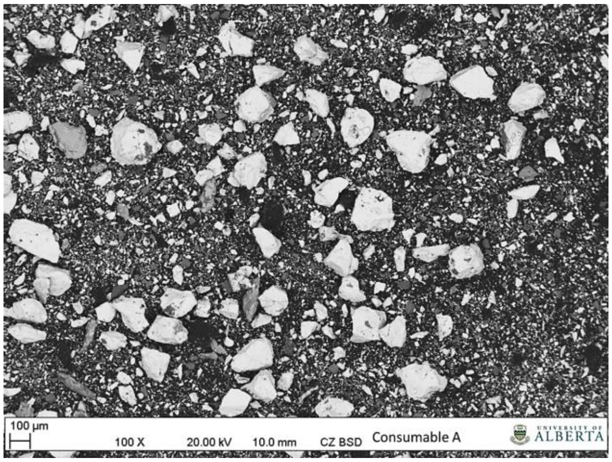

4.1.1. Point #2

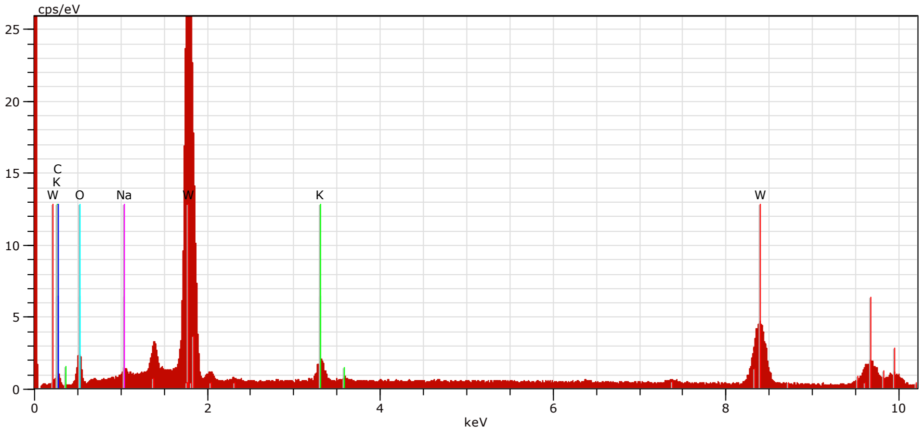

Consumable A
HV:20.0kV Puls th.:13.30kcps

```
El AN  Series   unn. C norm. C Atom. C  Error
                [wt.%]  [wt.%]  [at.%]  [wt.%]
---------------------------------------------
C   6  K-series   3.95    4.04   22.58    1.0
O   8  K-series   8.86    9.06   38.01    1.6
Na 11  K-series   1.44    1.48    4.31    0.1
K  19  K-series   2.84    2.91    5.00    0.1
W  74  L-series  80.61   82.51   30.11    2.3
---------------------------------------------
        Total:   97.70  100.00  100.00
```

4.1.2. Point #3

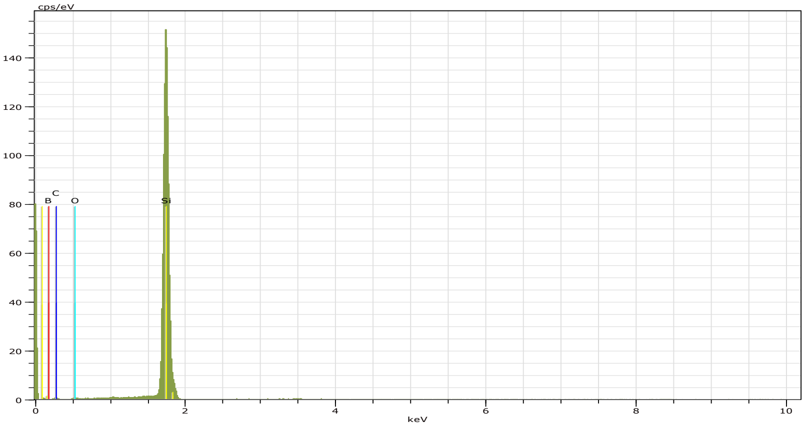

Consumable A
HV:20.0kV   Puls th.:18.30kcps

4.1.3. Point #4

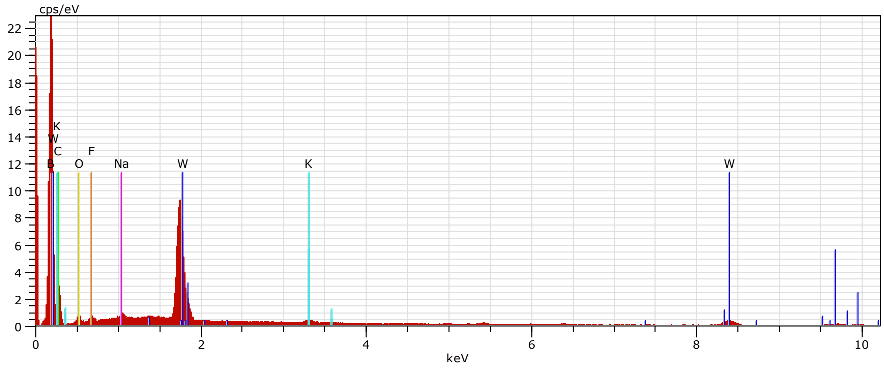

Consumable A
HV:20.0kV   Puls th.:5.46kcps

```
El AN  Series   unn. C norm. C Atom. C  Error
                [wt.%]  [wt.%]  [at.%] [wt.%]
---------------------------------------------
B   5  K-series  75.51   75.51   80.21    8.8
C   6  K-series  18.91   18.91   18.08    2.7
O   8  K-series   1.51    1.51    1.09    0.3
F   9  K-series   0.53    0.53    0.32    0.1
Na  11 K-series   0.15    0.15    0.07    0.0
K   19 K-series   0.07    0.07    0.02    0.0
W   74 L-series   3.31    3.31    0.21    0.1
---------------------------------------------
        Total: 100.00  100.00  100.00
```

4.1.4. Point #5

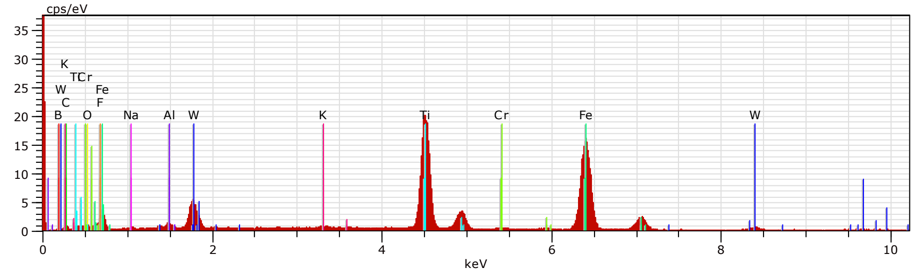

Consumable A
HV:20.0kV   Puls th.:12.32kcps

```
El AN  Series   unn. C norm. C Atom. C  Error
                [wt.%]  [wt.%]  [at.%] [wt.%]
---------------------------------------------
B   5  K-series   6.42    5.92   20.37    2.2
C   6  K-series   3.39    3.12    9.67    0.8
O   8  K-series   2.96    2.73    6.35    0.7
F   9  K-series   2.20    2.03    3.98    0.5
Na 11  K-series   1.16    1.07    1.73    0.1
Al 13  K-series   1.17    1.08    1.48    0.1
K  19  K-series   0.38    0.35    0.33    0.0
Ti 22  K-series  31.86   29.37   22.82    0.9
Cr 24  K-series   0.43    0.40    0.29    0.0
Fe 26  K-series  51.64   47.60   31.71    1.4
W  74  L-series   6.88    6.34    1.28    0.3
---------------------------------------------
        Total: 108.49  100.00  100.00
```

4.1.5. Point #6

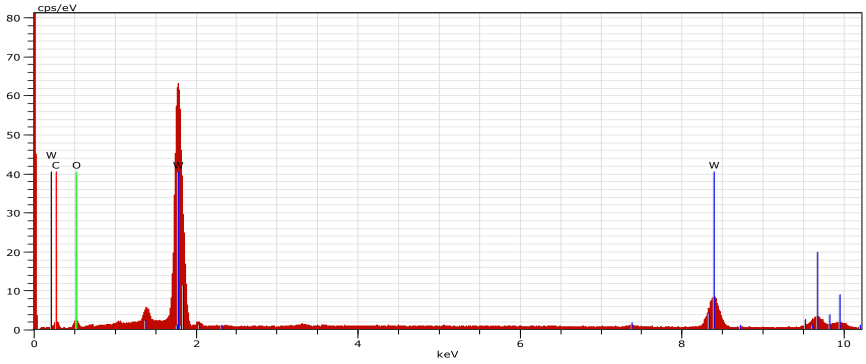

Consumable A
HV:20.0kV   Puls th.:23.08kcps

```
El AN  Series   unn. C norm. C Atom. C  Error
                [wt.%]  [wt.%]  [at.%] [wt.%]
---------------------------------------------
C   6  K-series   7.29    7.42   43.40    1.5
O   8  K-series   5.20    5.30   23.25    1.1
W  74  L-series  85.75   87.28   33.35    2.4
---------------------------------------------
        Total:  98.25  100.00  100.00
```

4.1.6. Point #7

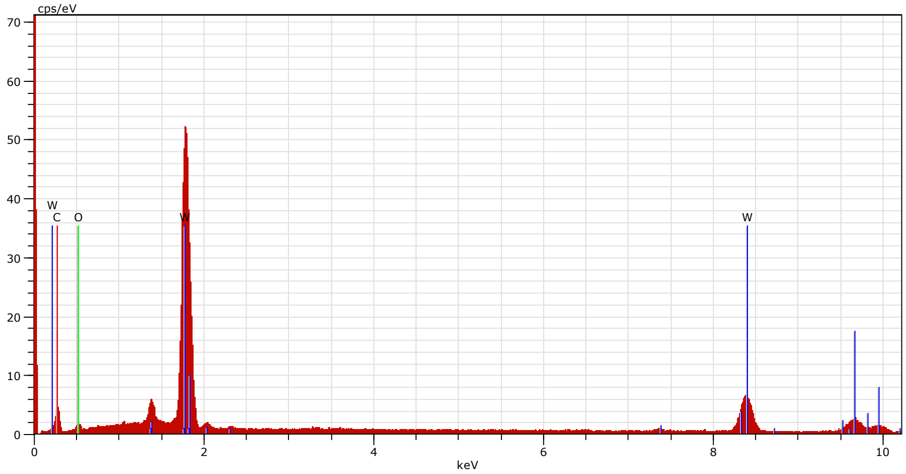

Consumable A
HV:20.0kV   Puls th.:19.98kcps

```
El AN  Series   unn. C norm. C Atom. C  Error
                [wt.%]  [wt.%]  [at.%] [wt.%]
---------------------------------------------
C   6  K-series  15.36   16.05   65.15    2.6
O   8  K-series   4.33    4.53   13.79    0.9
W  74  L-series  76.01   79.42   21.06    2.2
---------------------------------------------
        Total:   95.71  100.00  100.00
```

4.2. Consumable B

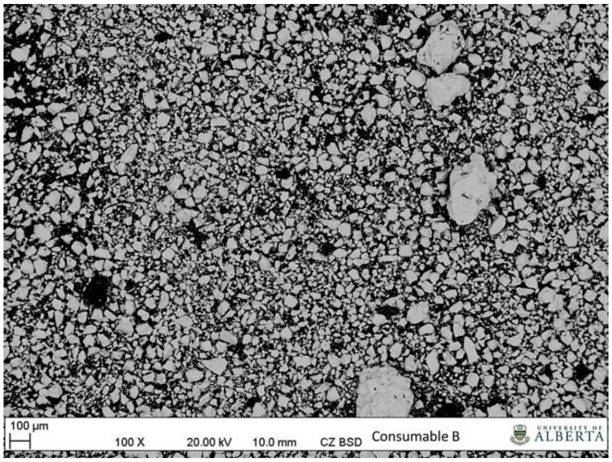

4.2.1. Point #2

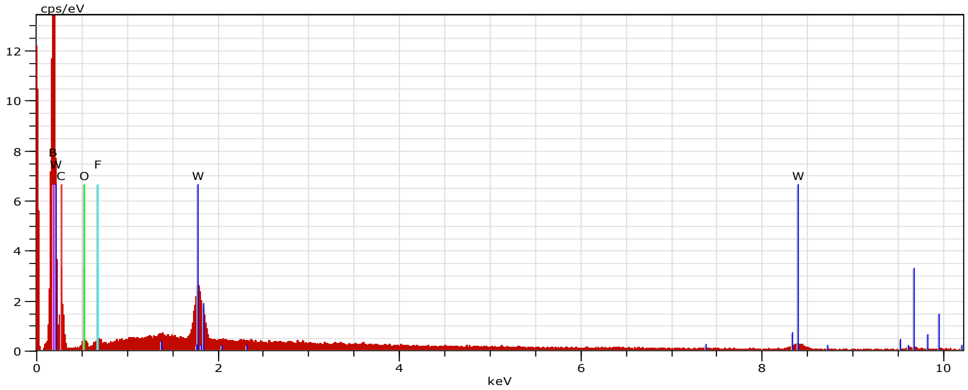

Consumable B
HV:20.0kV   Puls th.:3.69kcps

```
El AN  Series   unn. C norm. C Atom. C  Error
                [wt.%]  [wt.%]  [at.%] [wt.%]
---------------------------------------------
B   5  K-series  77.12   77.12   81.44    9.6
C   6  K-series  18.17   18.17   17.27    3.0
O   8  K-series   1.15    1.15    0.82    0.3
F   9  K-series   0.46    0.46    0.28    0.1
W   74 L-series   3.11    3.11    0.19    0.1
---------------------------------------------
        Total: 100.00  100.00  100.00
```

4.2.2. Point #3

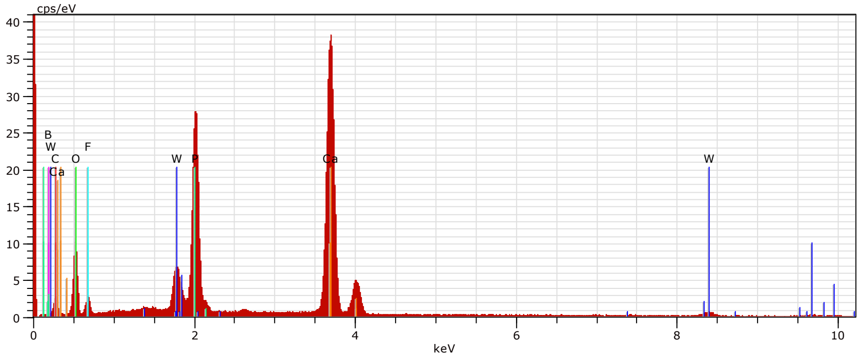

Consumable B
HV:20.0kV   Puls th.:15.83kcps

```
El AN  Series   unn. C norm. C Atom. C  Error
                [wt.%]  [wt.%]  [at.%] [wt.%]
---------------------------------------------
B   5  K-series   0.00    0.00    0.00    0.0
C   6  K-series   8.39    8.08   15.49    1.6
O   8  K-series  32.96   31.76   45.68    4.6
F   9  K-series   7.51    7.24    8.76    1.3
P  15  K-series  13.86   13.36    9.93    0.6
Ca 20  K-series  35.10   33.83   19.42    1.1
W  74  L-series   5.94    5.73    0.72    0.2
---------------------------------------------
        Total: 103.77  100.00  100.00
```

4.2.3. Point #4

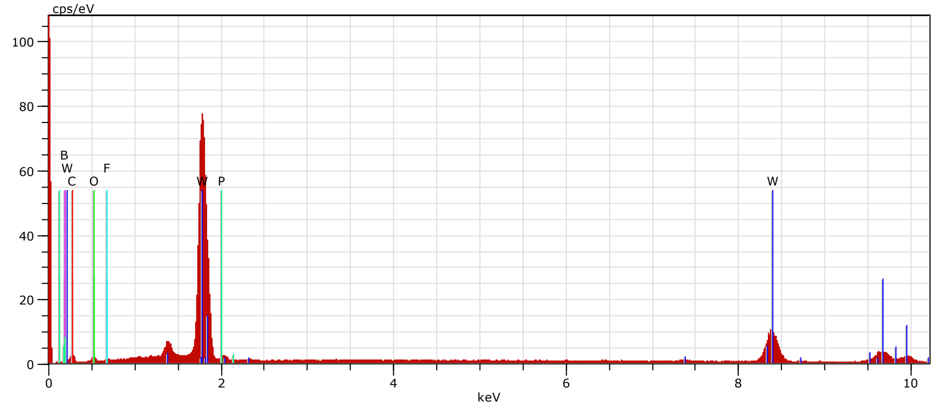

```
Consumable B
HV:20.0kV        Puls th.:27.96kcps

El  AN   Series   unn. C norm. C Atom. C  Error
                  [wt.%]  [wt.%]  [at.%] [wt.%]
-----------------------------------------------
B   5   K-series   0.00    0.00    0.00    0.0
C   6   K-series   7.55    7.68   46.63    1.6
O   8   K-series   3.28    3.34   15.20    0.8
F   9   K-series   0.83    0.84    3.22    0.3
P   15  K-series   0.00    0.00    0.00    0.0
W   74  L-series  86.67   88.14   34.95    2.5
-----------------------------------------------
        Total:    98.33  100.00  100.00
```

4.2.4. Point #5

Elemental EDS counts were too low for accurate measurement.

4.2.5. Point #6

Elemental EDS counts were too low for accurate measurement.

4.3. Consumable C

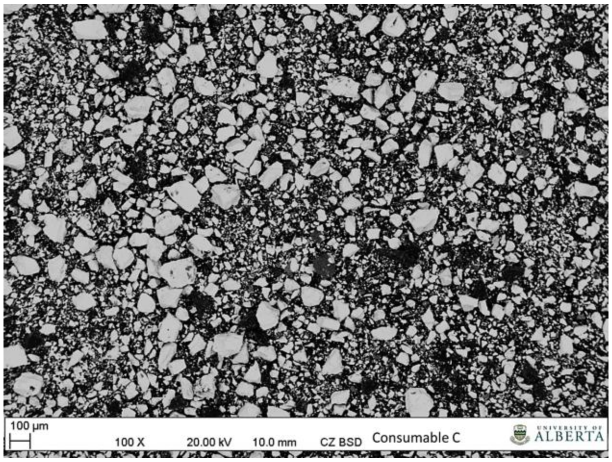

4.3.1. Point #2

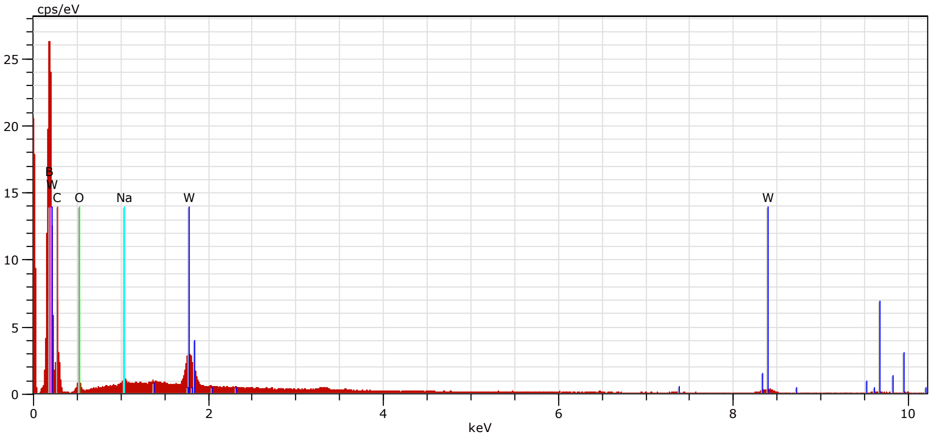

```
Consumable C
HV:20.0kV        Puls th.:5.18kcps

El AN  Series   unn. C norm. C Atom. C  Error
                [wt.%]  [wt.%]  [at.%] [wt.%]
---------------------------------------------
B   5  K-series  77.49   77.49   81.28    9.3
C   6  K-series  18.62   18.62   17.58    2.9
O   8  K-series   1.31    1.31    0.93    0.3
Na 11  K-series   0.11    0.11    0.05    0.0
W  74  L-series   2.47    2.47    0.15    0.1
---------------------------------------------
        Total:  100.00  100.00  100.00
```

4.3.2. Point #3

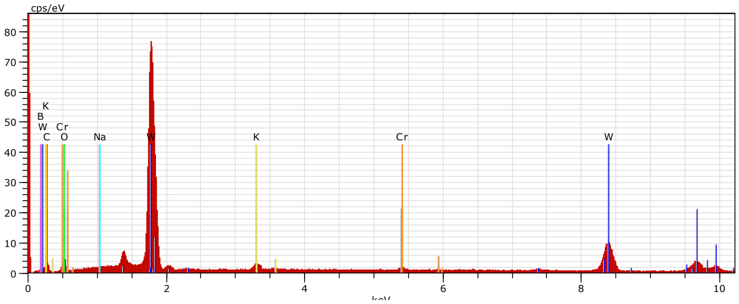

```
Consumable C
HV:20.0kV        Puls th.:28.35kcps

El AN  Series   unn. C norm. C Atom. C  Error
                [wt.%]  [wt.%]  [at.%] [wt.%]
---------------------------------------------
B   5  K-series   8.23    8.48   35.63    2.3
C   6  K-series   6.41    6.62   25.01    1.4
O   8  K-series   5.88    6.07   17.21    1.1
Na 11  K-series   0.11    0.12    0.23    0.0
K  19  K-series   2.03    2.10    2.44    0.1
Cr 24  K-series   0.86    0.89    0.78    0.1
W  74  L-series  73.42   75.73   18.70    2.1
---------------------------------------------
        Total:   96.96  100.00  100.00
```

4.3.3. Point #4

Elemental EDS counts were too low for accurate measurement.

4.3.4. Point #5

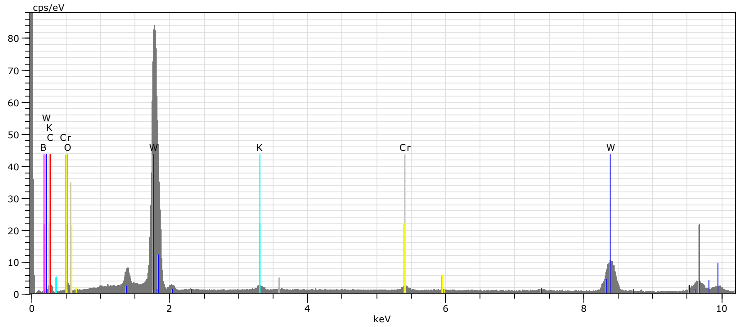

```
Consumable C
HV:20.0kV       Puls th.:30.38kcps

El AN  Series   unn. C norm. C Atom. C  Error
                [wt.%]  [wt.%]  [at.%] [wt.%]
---------------------------------------------
B   5  K-series   4.30    4.32   23.61    1.6
C   6  K-series   5.66    5.68   27.95    1.3
O   8  K-series   4.99    5.00   18.49    1.0
K  19  K-series   1.18    1.19    1.79    0.1
Cr 24  K-series   1.46    1.47    1.67    0.1
W  74  L-series  82.06   82.35   26.49    2.3
---------------------------------------------
        Total:   99.65  100.00  100.00
```

4.3.5. Point #6

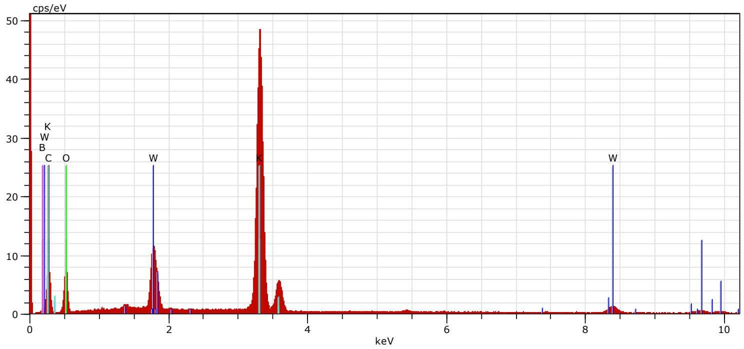

```
Consumable C
HV:20.0kV       Puls th.:14.76kcps

El AN  Series   unn. C norm. C Atom. C  Error
                [wt.%]  [wt.%]  [at.%] [wt.%]
---------------------------------------------
B   5  K-series   5.68    6.05   12.36    1.6
C   6  K-series  14.29   15.21   27.97    2.2
O   8  K-series  24.29   25.86   35.70    3.5
K  19  K-series  37.22   39.62   22.38    1.2
W  74  L-series  12.46   13.26    1.59    0.4
---------------------------------------------
        Total:   93.93  100.00  100.00
```

Point #7

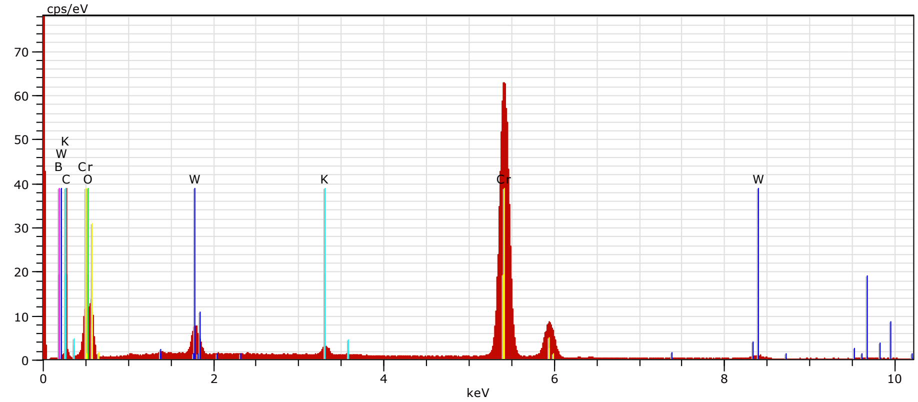

```
Consumable C
HV:20.0kV            Puls th.:22.98kcps

El AN  Series  unn. C norm. C Atom. C  Error
               [wt.%]  [wt.%]  [at.%] [wt.%]
---------------------------------------------
B   5  K-series   4.08    4.12   14.86    1.6
C   6  K-series   3.39    3.43   11.13    0.8
O   8  K-series   4.75    4.80   11.70    0.8
K  19  K-series   1.09    1.10    1.10    0.1
Cr 24  K-series  78.79   79.59   59.73    2.2
W  74  L-series   6.90    6.97    1.48    0.3
---------------------------------------------
        Total:   98.99  100.00  100.00
```

4.4. Consumable D

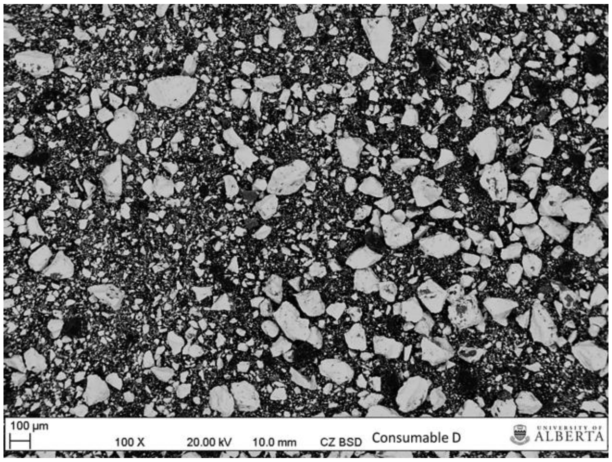

4.4.1. Point #2

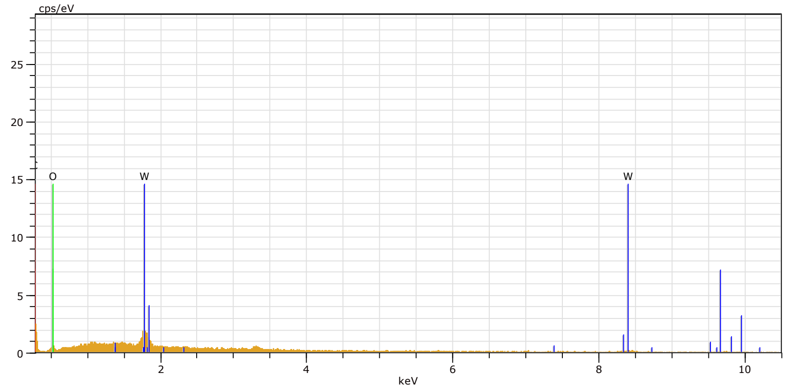

Consumable D
HV:20.0kV Puls th.:4.79kcps

```
El AN  Series   unn. C norm. C Atom. C  Error
                [wt.%]  [wt.%]  [at.%] [wt.%]
---------------------------------------------
B   5  K-series  79.76   79.76   82.26   10.0
C   6  K-series  18.40   18.40   17.08    3.2
O   8  K-series   0.87    0.87    0.60    0.3
W  74  L-series   0.97    0.97    0.06    0.1
---------------------------------------------
        Total: 100.00  100.00  100.00
```

4.4.2. Point #3

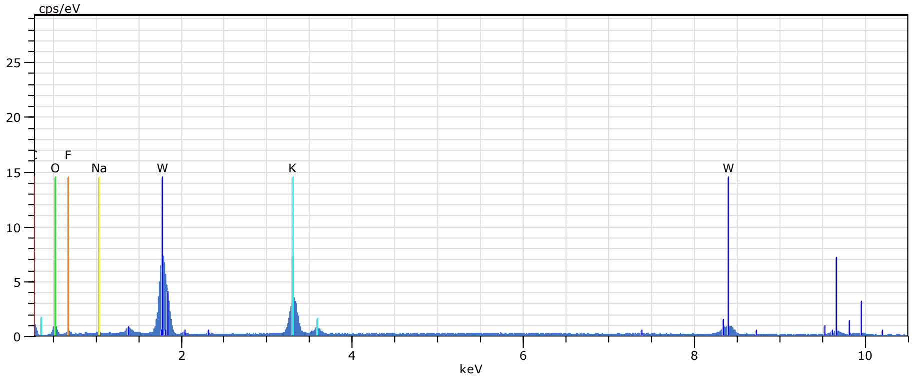

Consumable D
HV:20.0kV Puls th.:4.59kcps

```
El AN  Series   unn. C norm. C Atom. C  Error
                [wt.%]  [wt.%]  [at.%] [wt.%]
---------------------------------------------
B   5  K-series   7.70   17.96   35.95    2.1
C   6  K-series   7.25   16.92   30.49    1.5
O   8  K-series   4.22    9.84   13.31    0.9
F   9  K-series   1.27    2.97    3.39    0.3
Na 11  K-series   0.89    2.08    1.96    0.1
K  19  K-series   8.85   20.64   11.42    0.3
W  74  L-series  12.68   29.58    3.48    0.4
---------------------------------------------
        Total:  42.85  100.00  100.00
```

4.4.3. Point #4

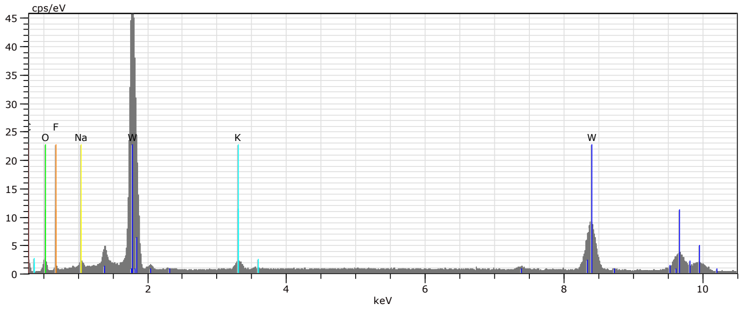

Consumable D
HV:20.0kV   Puls th.:20.67kcps

```
El AN  Series   unn. C norm. C Atom. C  Error
                [wt.%]  [wt.%]  [at.%]  [wt.%]
---------------------------------------------
B   5  K-series   4.50    4.70   22.98    1.5
C   6  K-series   6.43    6.71   29.55    1.3
O   8  K-series   4.53    4.73   15.63    0.9
F   9  K-series   0.95    0.99    2.75    0.3
Na  11 K-series   1.26    1.32    3.03    0.1
K   19 K-series   2.32    2.43    3.28    0.1
W   74 L-series  75.79   79.13   22.77    2.1
---------------------------------------------
        Total:  95.78  100.00  100.00
```

4.4.4. Point #5

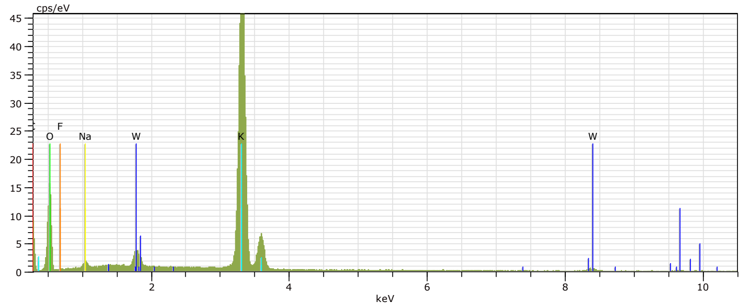

Consumable D
HV:20.0kV   Puls th.:15.04kcps

```
El AN  Series   unn. C norm. C Atom. C  Error
                [wt.%]  [wt.%]  [at.%]  [wt.%]
---------------------------------------------
B   5  K-series  10.35    9.01   15.21    2.5
C   6  K-series  19.37   16.85   25.61    2.8
O   8  K-series  43.00   37.41   42.69    5.7
F   9  K-series   0.99    0.86    0.82    0.3
Na  11 K-series   0.74    0.64    0.51    0.1
K   19 K-series  36.43   31.70   14.80    1.1
W   74 L-series   4.06    3.53    0.35    0.2
---------------------------------------------
        Total: 114.93  100.00  100.00
```

4.4.5. Point #6

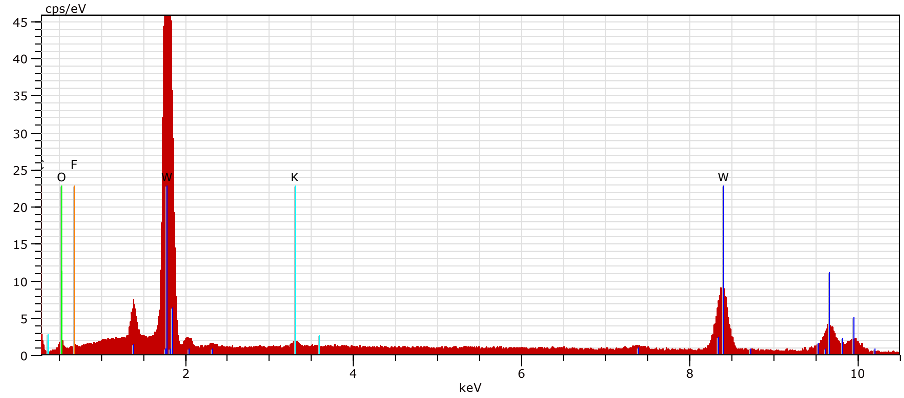

Consumable D
HV:20.0kV Puls th.:25.65kcps

```
El AN   Series   unn. C norm. C Atom. C  Error
                 [wt.%]  [wt.%]  [at.%] [wt.%]
-----------------------------------------------
B   5  K-series   4.82    4.96   26.09     1.7
C   6  K-series   7.23    7.44   35.25     1.5
O   8  K-series   2.82    2.91   10.33     0.7
F   9  K-series   0.47    0.48    1.45     0.2
K  19  K-series   0.71    0.73    1.06     0.1
W  74  L-series  81.10   83.48   25.82     2.3
-----------------------------------------------
        Total:   97.15  100.00  100.00
```

4.5. Consumable E

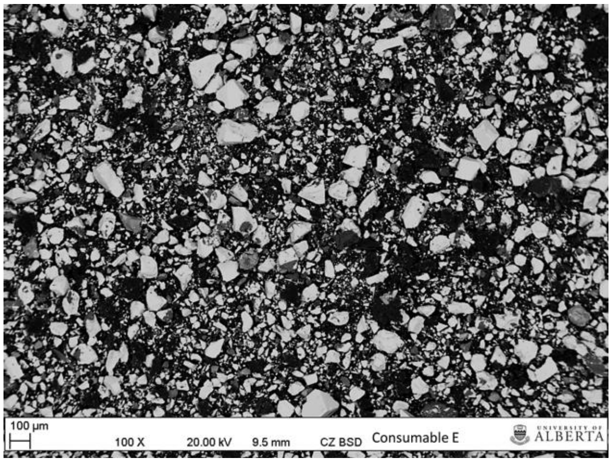

4.5.1. Point #2

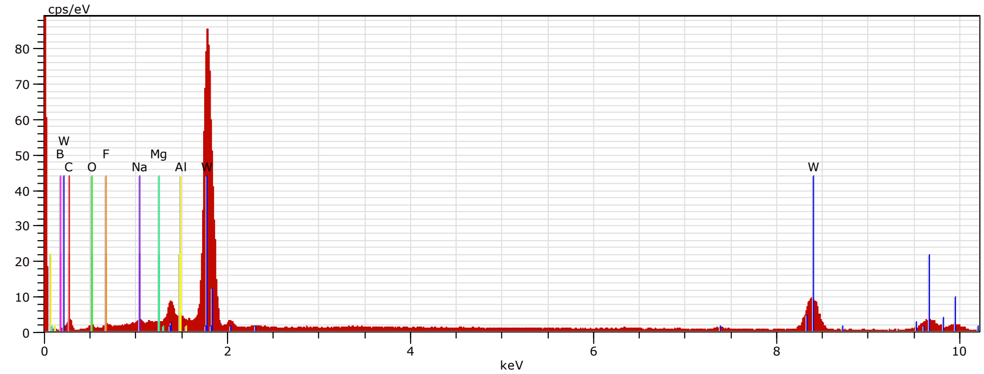

Consumable E
HV:20.0kV Puls th.:30.48kcps

```
El AN  Series   unn. C norm. C Atom. C  Error
                [wt.%]  [wt.%]  [at.%] [wt.%]
---------------------------------------------
B   5  K-series   4.66    4.90   21.58    1.7
C   6  K-series   9.40    9.89   39.20    1.9
O   8  K-series   2.72    2.86    8.52    0.7
F   9  K-series   1.96    2.06    5.16    0.5
Na  11 K-series   1.16    1.22    2.52    0.1
Mg  12 K-series   0.47    0.50    0.97    0.1
Al  13 K-series   1.09    1.14    2.02    0.1
W   74 L-series  73.58   77.43   20.04    2.1
---------------------------------------------
        Total:   95.04  100.00  100.00
```

4.5.2. Point #3

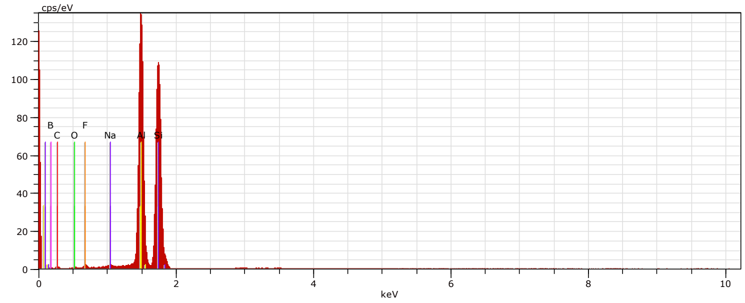

Consumable E
HV:20.0kV Puls th.:28.91kcps

```
El AN  Series   unn. C norm. C Atom. C  Error
                [wt.%]  [wt.%]  [at.%] [wt.%]
---------------------------------------------
B   5  K-series  40.11   24.06   40.88   11.7
C   6  K-series  13.83    8.29   12.68    3.5
O   8  K-series   2.72    1.63    1.87    0.7
F   9  K-series   2.74    1.64    1.59    0.6
Na  11 K-series   0.85    0.51    0.41    0.1
Al  13 K-series  50.58   30.34   20.65    2.4
Si  14 K-series  55.90   33.53   21.93    2.4
---------------------------------------------
        Total:  166.72  100.00  100.00
```

4.5.3. Point #4

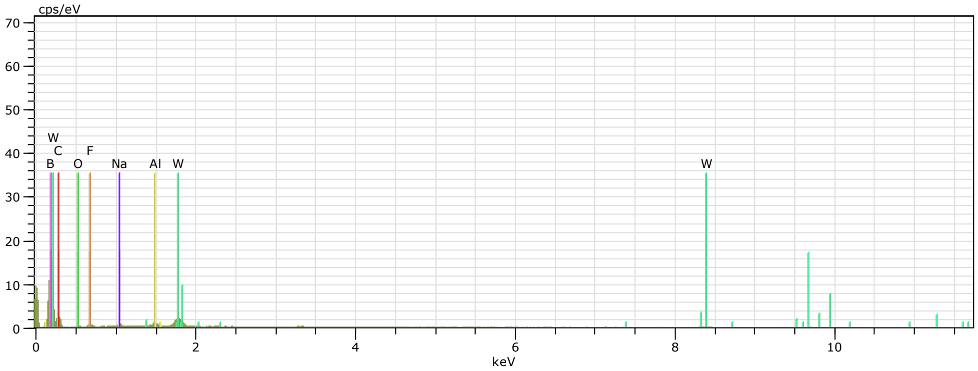

Consumable E
HV:20.0kV   Puls th.:3.56kcps

```
El AN  Series   unn. C norm. C Atom. C  Error
                [wt.%]  [wt.%]  [at.%] [wt.%]
---------------------------------------------
B   5  K-series  73.87   73.87   77.24    9.6
C   6  K-series  22.66   22.66   21.33    3.9
O   8  K-series   1.05    1.05    0.74    0.3
F   9  K-series   0.79    0.79    0.47    0.2
Na 11  K-series   0.14    0.14    0.07    0.0
Al 13  K-series   0.17    0.17    0.07    0.0
W  74  L-series   1.31    1.31    0.08    0.1
---------------------------------------------
        Total: 100.00  100.00  100.00
```

4.5.4. Point #5

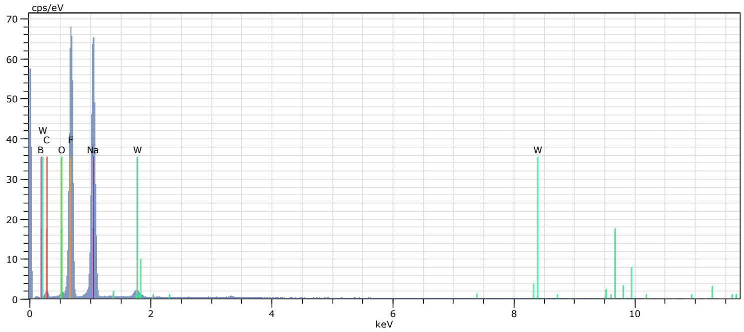

Consumable E
HV:20.0kV   Puls th.:14.02kcps

```
El AN  Series   unn. C norm. C Atom. C  Error
                [wt.%]  [wt.%]  [at.%] [wt.%]
---------------------------------------------
B   5  K-series  14.09    9.70   16.26    4.2
C   6  K-series  11.61    7.99   12.06    2.2
O   8  K-series   2.03    1.40    1.58    0.4
F   9  K-series  60.71   41.80   39.86    6.9
Na 11  K-series  55.58   38.27   30.16    3.6
W  74  L-series   1.21    0.83    0.08    0.1
---------------------------------------------
        Total: 145.24  100.00  100.00
```

4.5.5. Point #6

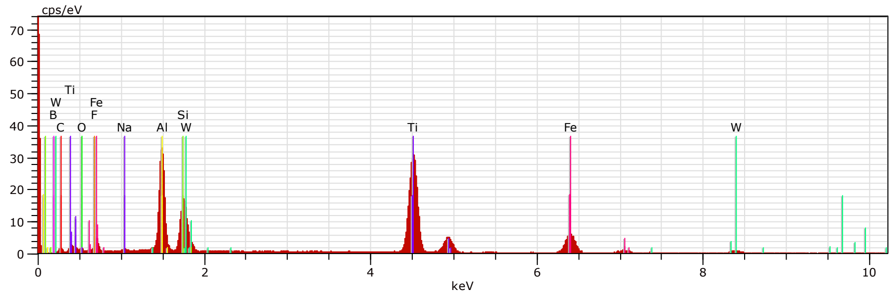

Consumable E
HV:20.0kV   Puls th.:18.52kcps

```
El AN  Series   unn. C norm. C Atom. C  Error
                [wt.%]  [wt.%]  [at.%] [wt.%]
---------------------------------------------
B   5  K-series   7.84    7.28   18.95    2.8
C   6  K-series   8.37    7.76   18.19    1.7
O   8  K-series   4.67    4.33    7.62    1.0
F   9  K-series   2.39    2.22    3.29    0.6
Na 11  K-series   0.88    0.82    1.00    0.1
Al 13  K-series  16.95   15.73   16.41    0.8
Si 14  K-series   5.97    5.54    5.55    0.3
Ti 22  K-series  39.33   36.50   21.46    1.1
Fe 26  K-series  13.83   12.83    6.47    0.4
W  74  L-series   7.54    6.99    1.07    0.3
---------------------------------------------
        Total: 107.76  100.00  100.00
```

Point #7

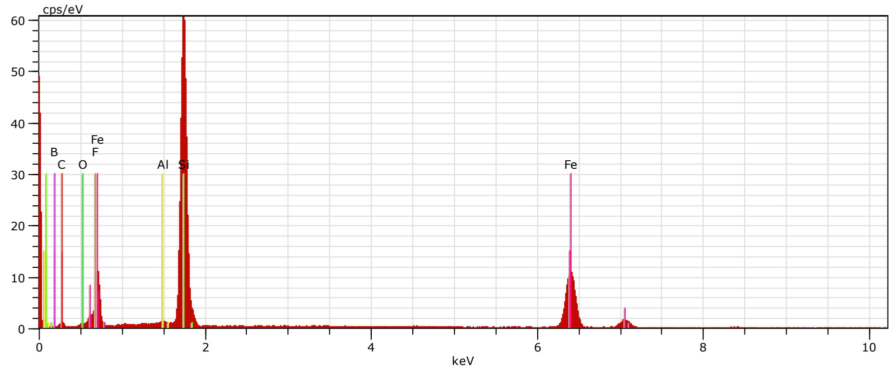

Consumable E
HV:20.0kV   Puls th.:13.20kcps

```
El AN  Series   unn. C norm. C Atom. C  Error
                [wt.%]  [wt.%]  [at.%] [wt.%]
---------------------------------------------
B   5  K-series  17.22   16.95   33.86    5.0
C   6  K-series  11.64   11.46   20.60    2.4
O   8  K-series   2.54    2.50    3.38    0.6
F   9  K-series   2.37    2.33    2.65    0.5
Al 13  K-series   0.73    0.72    0.57    0.1
Si 14  K-series  35.65   35.10   26.98    1.5
Fe 26  K-series  31.42   30.94   11.96    0.9
---------------------------------------------
        Total: 101.56  100.00  100.00
```

4.5.6. Point #8

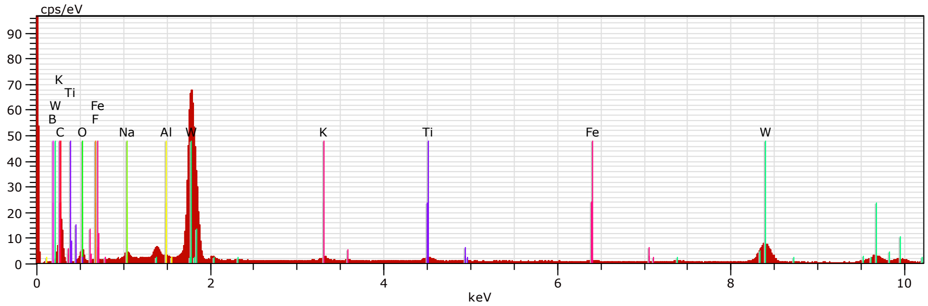

```
Consumable E
HV:20.0kV        Puls th.:27.42kcps

El AN  Series   unn. C norm. C Atom. C  Error
                [wt.%]  [wt.%]  [at.%] [wt.%]
---------------------------------------------
B   5  K-series   3.95    4.18   10.36    1.3
C   6  K-series  26.95   28.52   63.59    3.9
O   8  K-series   6.85    7.25   12.14    1.2
F   9  K-series   1.21    1.28    1.81    0.3
Na 11  K-series   1.66    1.76    2.05    0.1
Al 13  K-series   0.38    0.40    0.40    0.1
K  19  K-series   0.93    0.98    0.67    0.1
Ti 22  K-series   1.45    1.53    0.86    0.1
Fe 26  K-series   0.70    0.74    0.36    0.1
W  74  L-series  50.40   53.34    7.77    1.4
---------------------------------------------
        Total:   94.49  100.00  100.00
```

4.6. Consumable F

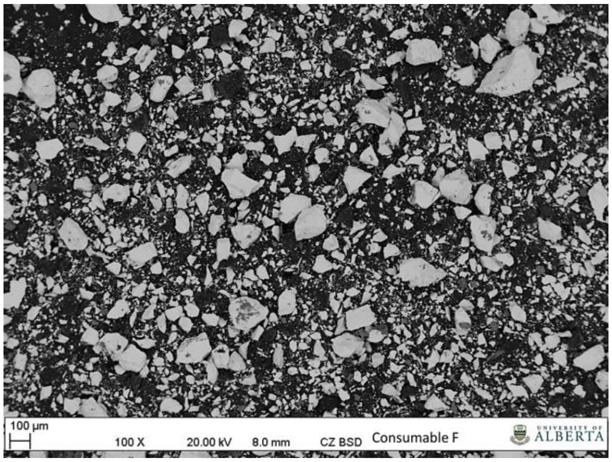

4.6.1. Point #2

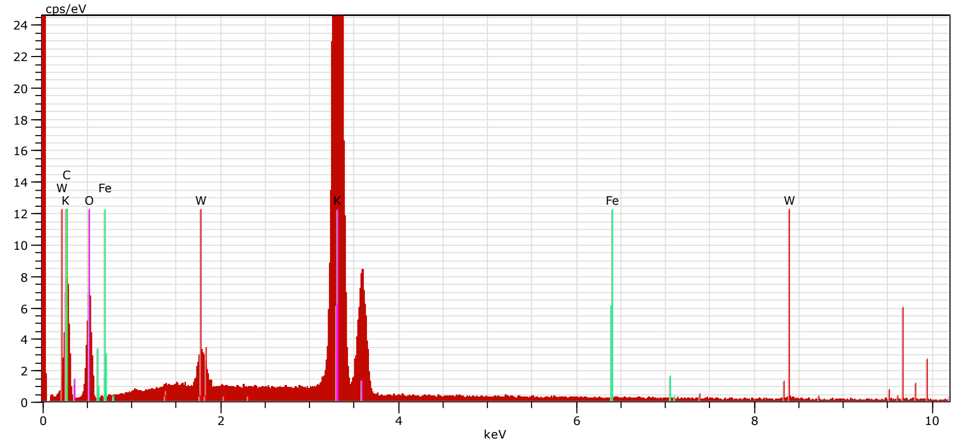

Consumable F
HV:20.0kV Puls th.:15.79kcps

```
El AN  Series   unn. C norm. C Atom. C  Error
                [wt.%]  [wt.%]  [at.%] [wt.%]
---------------------------------------------
C   6  K-series   7.45    9.41   18.38    1.2
O   8  K-series  25.92   32.71   47.98    3.8
K  19  K-series  44.03   55.57   33.35    1.4
Fe 26  K-series   0.01    0.01    0.00    0.0
W  74  L-series   1.82    2.30    0.29    0.1
---------------------------------------------
        Total:   79.23  100.00  100.00
```

4.6.2. Point #3

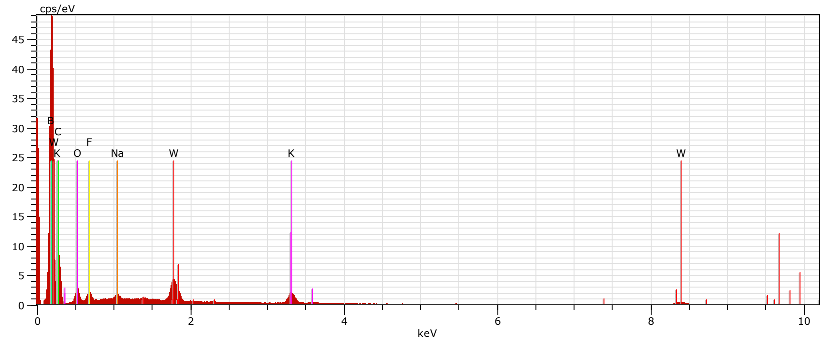

Consumable F
HV:20.0kV Puls th.:8.17kcps

```
El AN  Series   unn. C norm. C Atom. C  Error
                [wt.%]  [wt.%]  [at.%] [wt.%]
---------------------------------------------
B   5  K-series  72.28   72.28   76.29    8.3
C   6  K-series  22.37   22.37   21.25    3.0
O   8  K-series   2.35    2.35    1.67    0.4
F   9  K-series   0.85    0.85    0.51    0.2
Na 11  K-series   0.16    0.16    0.08    0.0
K  19  K-series   0.31    0.31    0.09    0.0
W  74  L-series   1.69    1.69    0.11    0.1
---------------------------------------------
        Total:  100.00  100.00  100.00
```

4.6.3. Point #4

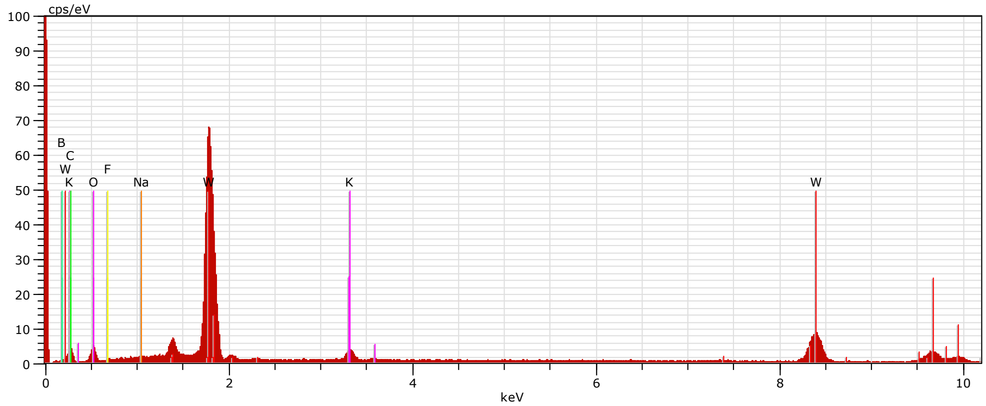

Consumable F
HV:20.0kV Puls th.:25.66kcps

```
El AN  Series   unn. C norm. C Atom. C  Error
                [wt.%]  [wt.%]  [at.%] [wt.%]
---------------------------------------------
B   5  K-series   8.56    8.49   30.95    2.3
C   6  K-series   8.48    8.42   27.62    1.7
O   8  K-series   8.35    8.28   20.40    1.5
F   9  K-series   1.06    1.06    2.19    0.3
Na  11 K-series   0.66    0.66    1.13    0.1
K   19 K-series   2.58    2.56    2.58    0.1
W   74 L-series  71.11   70.54   15.12    2.0
---------------------------------------------
        Total: 100.81  100.00  100.00
```

4.6.4. Point #5

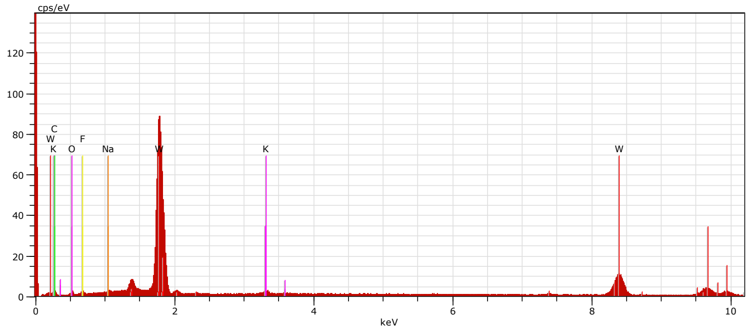

Consumable F
HV:20.0kV Puls th.:32.35kcps

```
El AN  Series   unn. C norm. C Atom. C  Error
                [wt.%]  [wt.%]  [at.%] [wt.%]
---------------------------------------------
C   6  K-series   5.53    5.92   35.78    1.3
O   8  K-series   3.26    3.49   15.84    0.8
F   9  K-series   2.18    2.33    8.91    0.5
Na  11 K-series   0.95    1.02    3.21    0.1
K   19 K-series   1.18    1.26    2.34    0.1
W   74 L-series  80.26   85.97   33.92    2.3
---------------------------------------------
        Total:  93.35  100.00  100.00
```

4.6.5. Point #6

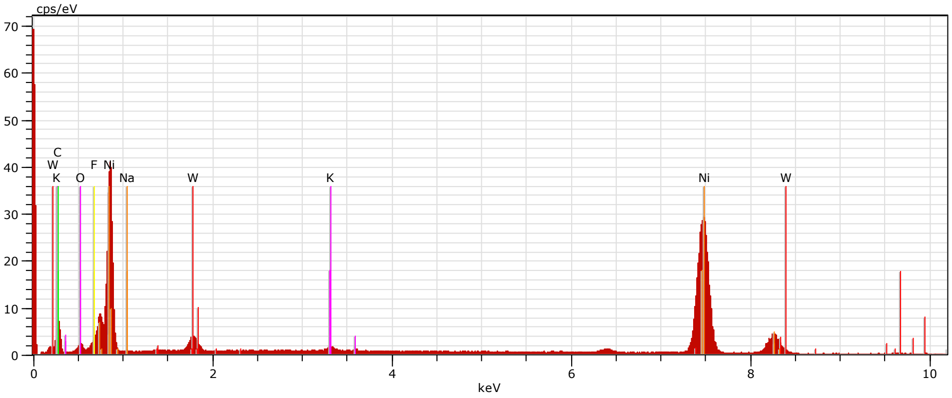

Consumable F
HV:20.0kV   Puls th.:19.12kcps

```
El AN  Series  unn. C norm. C Atom. C  Error
               [wt.%]  [wt.%]  [at.%] [wt.%]
---------------------------------------------
C   6  K-series  13.90   17.61   48.20     2.2
O   8  K-series   1.84    2.33    4.80     0.4
F   9  K-series   1.54    1.95    3.37     0.3
Na 11  K-series   0.48    0.61    0.87     0.1
K  19  K-series   0.58    0.74    0.62     0.1
Ni 28  K-series  58.81   74.50   41.74     1.6
W  74  L-series   1.79    2.27    0.41     0.1
---------------------------------------------
        Total:   78.94  100.00  100.00
```

4.7. Consumable G

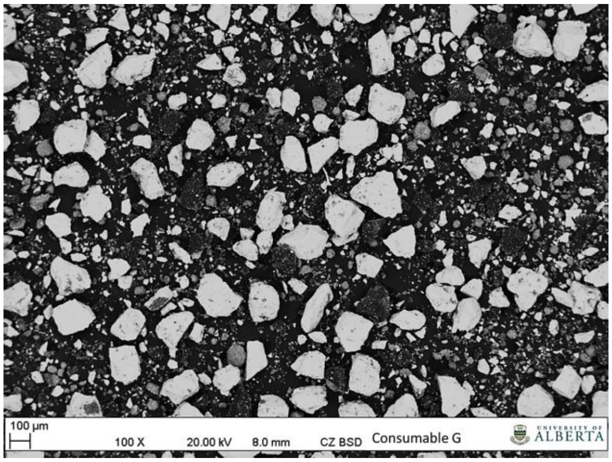

4.7.1. Point #2

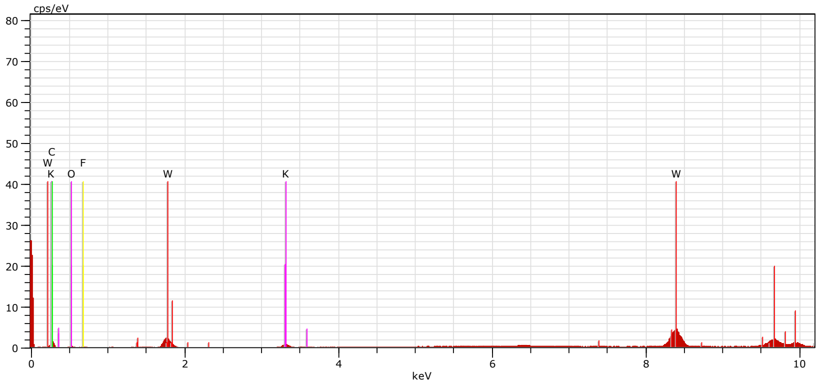

Consumable G
HV:20.0kV   Puls th.:6.10kcps

```
El AN   Series   unn. C norm. C Atom. C  Error
                 [wt.%]  [wt.%]  [at.%] [wt.%]
-----------------------------------------------
C   6  K-series   9.04    8.68   44.46    1.6
O   8  K-series   2.13    2.04    7.85    0.5
F   9  K-series   0.49    0.48    1.54    0.2
K  19  K-series  13.82   13.27   20.88    0.5
W  74  L-series  78.66   75.53   25.27    2.2
-----------------------------------------------
        Total:  104.15  100.00  100.00
```

4.7.2. Point #3

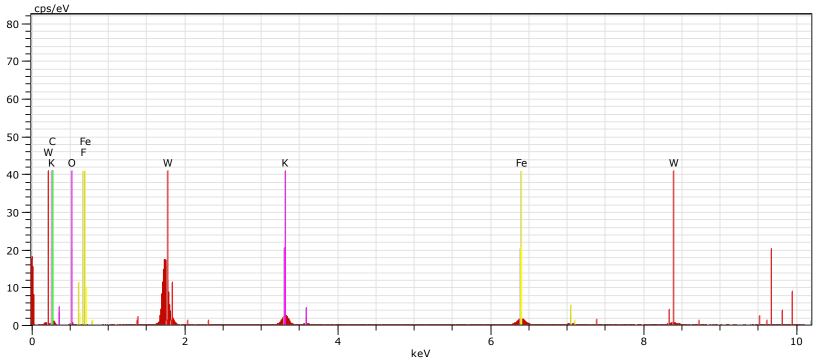

Consumable G
HV:20.0kV   Puls th.:4.70kcps

```
El AN   Series   unn. C norm. C Atom. C  Error
                 [wt.%]  [wt.%]  [at.%] [wt.%]
-----------------------------------------------
C   6  K-series  10.59   19.22   50.95    1.8
O   8  K-series   3.91    7.10   14.14    0.8
F   9  K-series   0.40    0.73    1.23    0.2
K  19  K-series  11.30   20.50   16.70    0.4
Fe 26  K-series  10.97   19.91   11.35    0.3
W  74  L-series  17.93   32.54    5.64    0.6
-----------------------------------------------
        Total:   55.11  100.00  100.00
```

4.7.3. Point #4

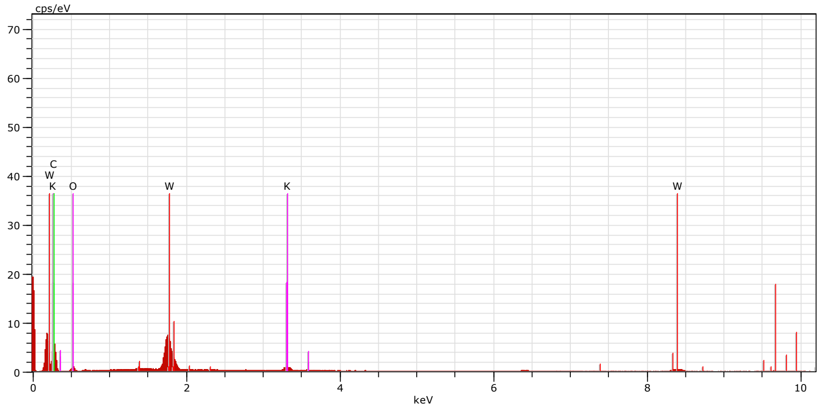

Consumable G
HV:20.0kV Puls th.:4.96kcps

```
El AN  Series   unn. C norm. C Atom. C  Error
                [wt.%]  [wt.%]  [at.%] [wt.%]
---------------------------------------------
C   6  K-series  25.01   52.60   80.55    3.5
O   8  K-series   6.27   13.19   15.16    1.2
K  19  K-series   1.12    2.35    1.10    0.1
W  74  L-series  15.16   31.87    3.19    0.5
---------------------------------------------
        Total:   47.56  100.00  100.00
```

5. Electrical Resistivity: Furnace Heating Method

5.1. Consumable A

Current: 5A
Length: 1.2192m

Temperature (K)	Voltage (V)	Resistance (Ω)
295.2	0.46234	0.092468
318.4	0.51531	0.103062
369.3	0.60444	0.120888
428.5	0.74793	0.149586
470.8	0.85102	0.170204
523	0.99833	0.199666
577	1.18122	0.236244
626	1.37401	0.274802
671	1.53729	0.307458
726	1.69977	0.339954
778	1.82906	0.365812
842	1.98787	0.397574
869	2.04501	0.409002
929	2.16672	0.433344
981	2.24118	0.448236
1029	2.32506	0.465012
1074	2.39266	0.478532
1125	2.48749	0.497498
1171	2.57664	0.515328
1231	2.68904	0.537808
1273	2.79868	0.559736
1325	2.95306	0.590612
1341	3.00764	0.601528

5.2. Consumable B

Current: 5A

Length: 1.2192m

Temperature (K)	Voltage (V)	Resistance (Ω)
295.2	0.4517	0.09034
318.6	0.51958	0.103916
369.3	0.66474	0.132948
429.9	0.90757	0.181514
471.6	1.05309	0.210618
524	1.26611	0.253222
578	1.50392	0.300784
627	1.65548	0.331096
670	1.74402	0.348804
727	1.85412	0.370824
777	1.92994	0.385988
842	2.03308	0.406616
865	2.06542	0.413084
933	2.17104	0.434208
983	2.23413	0.446826
1033	2.30484	0.460968
1075	2.34883	0.469766
1128	2.41766	0.483532
1173	2.47115	0.49423
1233	2.55434	0.510868
1275	2.61123	0.522246
1326	2.69643	0.539286
1337	2.71789	0.543578

5.3. Consumable C

Current: 5A

Length: 1.2192m

Temperature (K)	Voltage (V)	Resistance (Ω)
295.2	0.55412	0.110824
324.3	0.63927	0.127854
393.3	0.83001	0.166002
437.5	0.97101	0.194202
480	1.14227	0.228454
532	1.33331	0.266662
608	1.67336	0.334672
630	1.80804	0.361608
686	2.05485	0.41097
721	2.16945	0.43389
774	2.31392	0.462784
824	2.43443	0.486886
875	2.53664	0.507328
927	2.63472	0.526944
967	2.71113	0.542226
1029	2.79932	0.559864
1073	2.88855	0.57771
1122	2.98409	0.596818
1171	3.07476	0.614952
1221	3.17582	0.635164
1270	3.28716	0.657432
1319	3.41628	0.683256
1365	3.54468	0.708936
1383	3.60631	0.721262

5.4. Consumable D

Current: 5A
Length: 1.2192m

Temperature (K)	Voltage (V)	Resistance (Ω)
324.3	0.63	0.126
349.1	0.698	0.1396
372	0.74677	0.149354
396.1	0.80838	0.161676
420.2	0.87962	0.175924
445	0.95378	0.190756
471.5	1.04881	0.209762
496	1.13305	0.22661
524	1.2451	0.24902
548	1.16112	0.232224
576	1.45938	0.291876
604	1.58722	0.317444
627	1.72601	0.345202
659	1.88332	0.376664
679	1.97244	0.394488
703	2.02042	0.404084
733	2.12967	0.425934
745	2.26	0.452
776	2.235	0.447
829	2.40355	0.48071
880	2.56788	0.513576
930	2.66787	0.533574
990	2.76635	0.55327
1014	2.8485	0.5697
1065	2.90785	0.58157
1122	2.99881	0.599762
1172	3.0995	0.6199
1225	3.1999	0.63998
1271	3.28511	0.657022
1333	3.43321	0.686642
1373	3.51861	0.703722

5.5. ER310 Stainless Steel

Current: 5A

Length: 0.6096m

Cross Sectional Area: 1.021E-06 m^2

Temperature (K)	Voltage (V)	Resistance (Ω)
295.2	2.54471	0.508942
328.1	2.62897	0.525794
395.7	2.72888	0.545776
439.5	2.76386	0.552772
483	2.80222	0.560444
537	2.84557	0.569114
607	2.91413	0.582826
631	2.93192	0.586384
685	3.01882	0.603764
721	3.02877	0.605754
770	3.09122	0.618244
827	3.11812	0.623624
883	3.17752	0.635504
926	3.20555	0.64111
970	3.23745	0.64749
1026	3.31802	0.663604
1076	3.33808	0.667616
1126	3.35001	0.670002
1173	3.37801	0.675602
1223	3.39921	0.679842
1272	3.44096	0.688192
1320	3.46255	0.69251
1363	3.48038	0.696076
1384	3.50519	0.701038

6. HWGMAW Stringer Bead Threshold Comparison

6.1. No Threshold

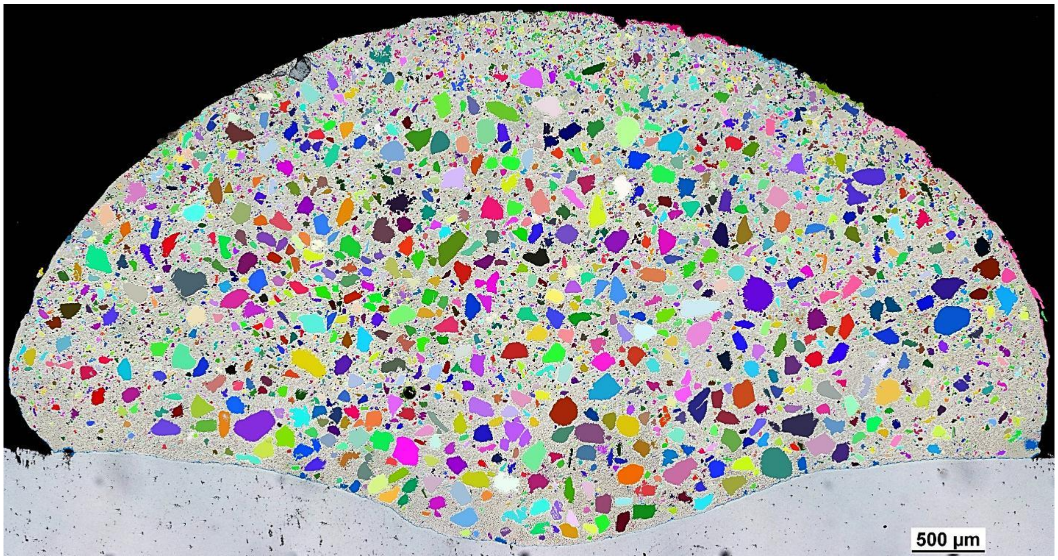

6.2. Threshold

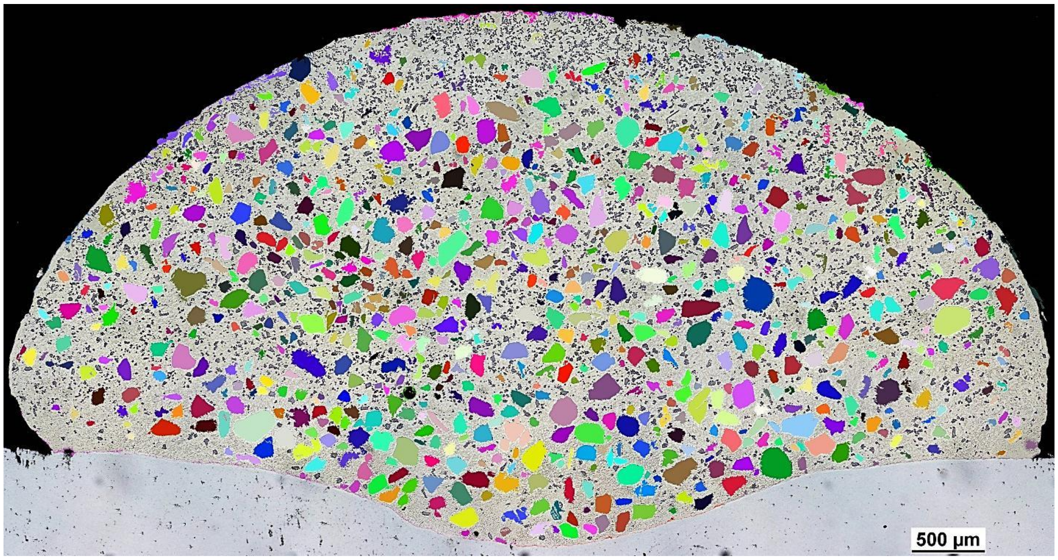

7. EPMA of HWGTAW Overlays

7.1. Consumable A

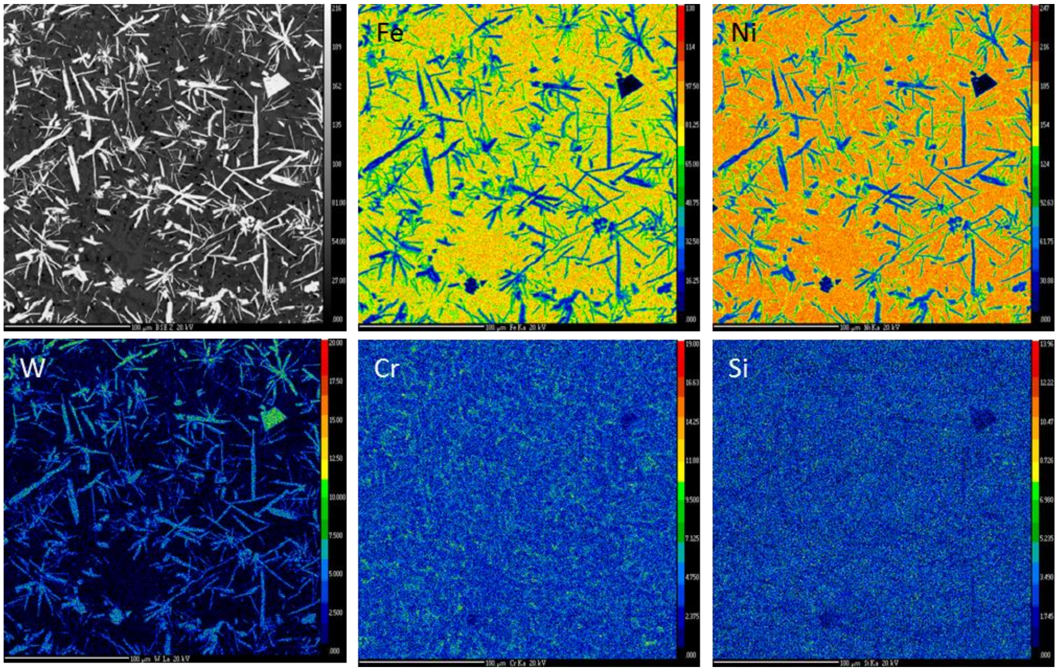

7.2. Consumable D

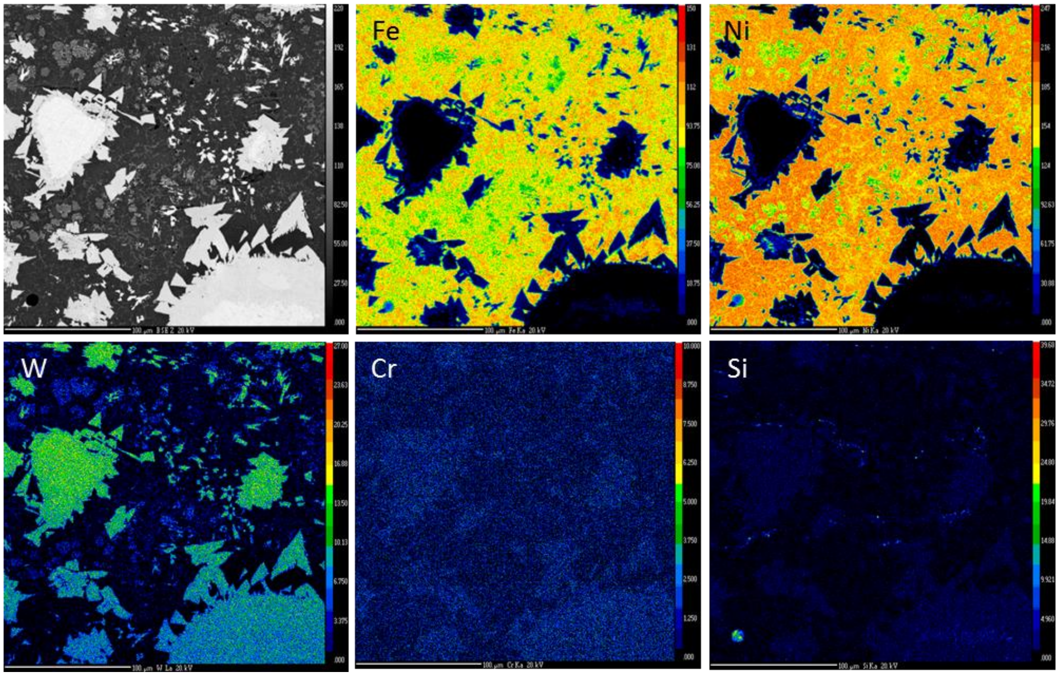

8. ASTM G65 Wear Test Coupon Images

8.1. GMAW-1

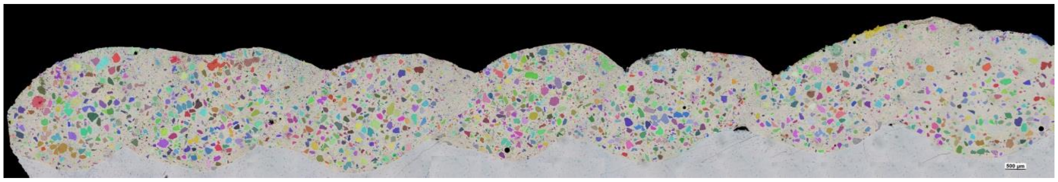

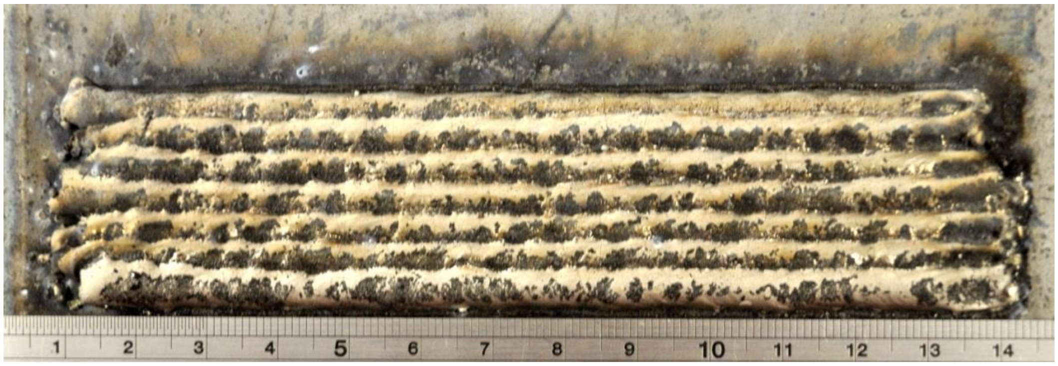

8.2. GMAW-2

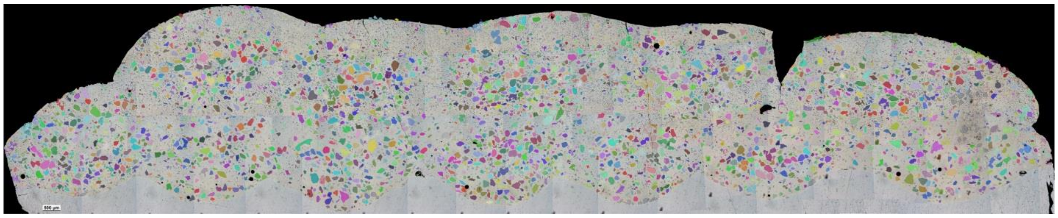

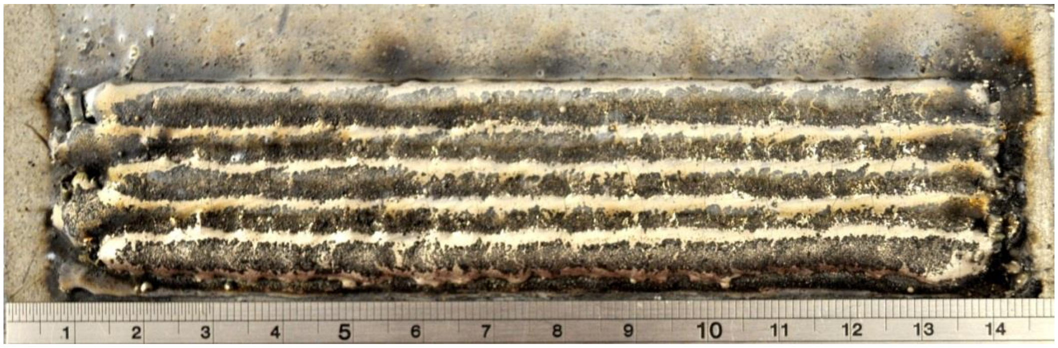

8.3. HWGMAW-1

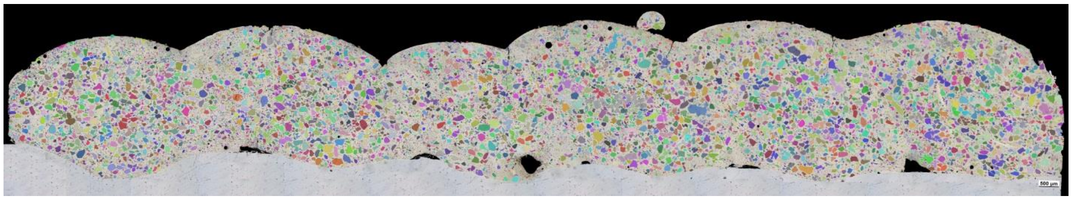

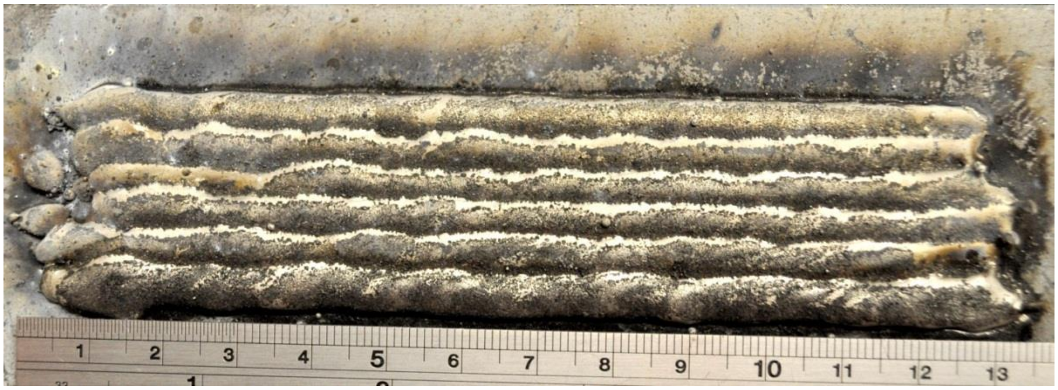

8.4. HWGMAW-2